



HAL
open science

Study of tokamak plasma disruptions and runaway electrons in a metallic environment

Sundaresan Sridhar

► **To cite this version:**

Sundaresan Sridhar. Study of tokamak plasma disruptions and runaway electrons in a metallic environment. Plasma Physics [physics.plasm-ph]. Université d'Aix-Marseille, 2020. English. NNT : . tel-03671885

HAL Id: tel-03671885

<https://cea.hal.science/tel-03671885>

Submitted on 18 May 2022

HAL is a multi-disciplinary open access archive for the deposit and dissemination of scientific research documents, whether they are published or not. The documents may come from teaching and research institutions in France or abroad, or from public or private research centers.

L'archive ouverte pluridisciplinaire **HAL**, est destinée au dépôt et à la diffusion de documents scientifiques de niveau recherche, publiés ou non, émanant des établissements d'enseignement et de recherche français ou étrangers, des laboratoires publics ou privés.

DOCTORAL THESIS

Defended at Aix-Marseille University
on 3 November 2020 by

Sundaresan SRIDHAR

Study of tokamak plasma disruptions and runaway electrons in a metallic environment

Discipline

Energy, Radiation, Plasma

Speciality

Nuclear Fusion

Doctoral School

ED352 - Physics and Sciences of Matter

Laboratory

Institute for Magnetic Fusion Research (IRFM),
CEA - Cadarache,
13108 Saint-Paul-lez-Durance, France

Jury Members

• Jose Ramon MARTIN SOLIS • UC3M	• Reviewer
• Gabriella PAUTASSO • IPP, MPI	• Reviewer
• Jérôme BUCALOSSO • IRFM, CEA	• President of Jury
• Pascale HENNEQUIN • LPP, CNRS	• Examiner
• Michael LEHNEN • ITER Organisation	• Examiner
• Istvan PUSZTAI • Chalmers University	• Examiner
• Peter BEYER • PIIM, CNRS	• Thesis Director
• Cédric REUX • IRFM, CEA	• Thesis Supervisor

This work received financial support from the ITER Organization through Implementing Agreement No. 69 of the Site Support Agreement (ref. IO/4300001586). The views and opinions expressed herein do not necessarily reflect those of the ITER Organization.

This work has been carried out within the framework of the EUROfusion Consortium and has received funding from the Euratom research and training programme 2014-2018 and 2019-2020 under grant agreement No 633053. The views and opinions expressed herein do not necessarily reflect those of the European Commission.

Affidavit

I, undersigned, Sundaresan, SRIDHAR, hereby declare that the work presented in this manuscript is my own work, carried out under the scientific direction of Prof. Peter BEYER (PIIM-CNRS, AMU) and Dr. Cédric REUX (CEA-IRFM), in accordance with the principles of honesty, integrity and responsibility inherent to the research mission. The research work and the writing of this manuscript have been carried out in compliance with both the french national charter for Research Integrity and the Aix-Marseille University charter on the fight against plagiarism.

This work has not been submitted previously either in this country or in another country in the same or in a similar version to any other examination body.

Cadarache, 03-11-2020



Sundaresan SRIDHAR



Cette œuvre est mise à disposition selon les termes de la [Licence Creative Commons Attribution - Pas d'Utilisation Commerciale - Pas de Modification 4.0 International](https://creativecommons.org/licenses/by-nc-nd/4.0/).

Contents

Résumé	7
Abstract	14
1 Introduction to Nuclear Fusion and Tokamaks	16
1.1 Nuclear Fusion	17
1.2 Nuclear Fusion Power	18
1.2.1 Thermonuclear fusion power P_{fusion}	18
1.2.2 α -particle heating	19
1.2.3 Energy loss and confinement time	19
1.2.4 Power balance	19
1.3 Approaches to nuclear fusion	20
1.3.1 Inertial confinement fusion (ICF)	21
1.3.2 Inertial electrostatic fusion (IEF)	21
1.3.3 Magnetized target fusion (MTF)	22
1.3.4 Magnetic confinement fusion (MCF)	22
1.4 Physics and engineering principles of tokamaks	25
1.4.1 Magnetic configuration of the tokamak	26
1.4.2 Present tokamak parameters	27
1.4.3 Tokamak performance	30
2 Tokamak Disruptions and Runaway Electrons	31
2.1 Phases of Tokamak Disruptions	31
2.2 Causes and Operational Limits of Tokamak Disruptions	33
2.2.1 Troyon beta limit	33
2.2.2 Current limit (low- q limit) disruption	34
2.2.3 Density or radiative limit disruption	35
2.3 Consequences of Tokamak Disruptions	36
2.3.1 Thermal loads	36
2.3.2 Electromagnetic loads	38
2.4 Runaway Electrons	42
2.4.1 Dreicer primary mechanism	43
2.4.2 Hot-tail primary mechanism	47
2.4.3 Other seeding mechanisms	48
2.4.4 Secondary avalanche mechanism	49
2.5 Disruption Mitigation Systems	50

2.5.1	Massive gas injection (MGI)	51
2.5.2	Shattered pellet injection (SPI)	51
2.5.3	DMS systems of the various tokamaks	51
2.6	Scope of this thesis	62
3	Characterization of the Cold Background Plasma	64
3.1	Electron density of background plasmas	65
3.2	Electron temperature of background plasmas	68
3.2.1	VUV spectroscopy in the JET tokamak	70
3.2.2	VUV spectrum processing	71
3.2.3	Synthetic line ratios	77
3.2.4	T_e -profile estimation	82
3.3	Database analysis of background plasmas	85
3.3.1	Analysis of Ar MGI as trigger injections	87
3.3.2	Quantitative analysis of Ar MMI as trigger injections	89
3.3.3	Analysis of Ar SPI as trigger injection	95
3.3.4	Analysis of discharges with Ar MMI as killer injection	100
3.3.5	Conclusions	103
4	0D/1D Power balance	104
4.1	Bolometer system in JET	105
4.2	Simple 0D model	107
4.3	1D power balance : Interactions overview	108
4.4	Estimation of power terms	109
4.4.1	Power terms of the RE beam	109
4.4.2	Power terms of the confined background plasma	120
4.4.3	Heat conduction from the background plasma of the open field line region to the wall	125
4.5	1D Power balance of JET-ILW and DIII-D discharges	128
4.5.1	RE beam power terms	130
4.5.2	Confined background plasma power terms	131
4.5.3	Open field line background plasma power terms	133
4.5.4	Conclusions	133
5	1D Diffusion model	135
5.1	Description of the 1D diffusion model	135
5.1.1	Diffusion of species	137
5.1.2	Atomic processes	141
5.1.3	Estimation of species and free electron density profiles	143
5.1.4	Estimation of RE density profile	144
5.1.5	Estimation of T_e profile	145
5.1.6	Conservation of Ar and D atoms	146
5.2	Sensitivity analysis of the 1D diffusion model	146
5.2.1	Initial guesses of the parameters	147

5.2.2	Inclusion of higher ionization states	152
5.2.3	Inclusion of electron impact ionization	153
5.2.4	Impact of RE direct ionization	155
5.2.5	Conservation of Ar and D atoms	156
5.2.6	Change of wall radius R_w	157
5.2.7	Iteration time step	159
5.2.8	Rate calculations from atomic model	161
5.3	Simulation of argon background plasma	164
5.4	Summary	168
5.5	Analysis of D ₂ SPI in JET tokamak	168
5.5.1	Simulation of the D ₂ SPI experiments	171
5.5.2	Non-thermal radiation and 1D diffusion model	180
5.5.3	Conclusions	184
	Summary and Perspectives	185
	Bibliography	188
	A VUV spectra analysis for D₂ SPI experiments	201
	Acknowledgments	205

Résumé

Informations Générales

Parmi les sources d'énergie étudiées pour subvenir aux futurs de l'humanité, la fusion nucléaire est considérée comme l'un des candidats les plus prometteurs. Actuellement les dispositifs de fusion de type tokamaks ont atteint des performances proches de celles nécessaires à réacteur industriel de fusion.

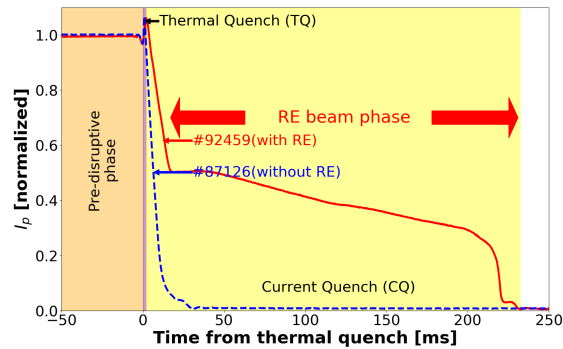


Figure 0.1.: Illustration de la perturbation du plasma tokamak pour les décharges JET #92459 (avec RE, solide rouge) et #87126 (sans RE, pointillé bleu). Le courant plasma I_p est normalisé avec le courant plasma plat.

Dans les tokamaks, les disruptions sont des événements majeurs dans lesquels l'énergie du plasma est perdue en un très court instant. Les plus importantes d'entre-elles, peuvent amener à l'endommagement de la structure du tokamaks comme le montre la figure 0.1. Les disruptions constituent une menace majeure pour les futurs tokamaks, y compris ITER. Trois conséquences sont liées aux disruptions: dépôts thermiques localisés, forces de électromagnétiques (EM) et électrons découplés (RE). Ces derniers, de par leur énergie (quelques 10 MeV), peuvent endommager des composants internes du tokamak. Ainsi, la prévention et le contrôle de ces électrons découplés sont d'une importance essentielle.

Atténuation des électrons découplés

La stratégie actuelle consiste à éviter la génération d'électrons découplés à l'aide d'une injection massive de matière (MMI) telle que deutérium ou d'espèces nobles à haut Z (Ne, Ar, Kr, Xe). Si leur génération ne peut pas être évitée, une deuxième MMI sera utilisée pour atténuer le faisceau d'électrons découplés. Le matériau peut être injecté par injection massive de gaz (MGI) ou par injection de glaçons brisés

(SPI, solution actuellement adoptée par ITER). Après la première MMI utilisée pour empêcher la génération de RE, un plasma de fond dense et froid d'impuretés MMI est formé.

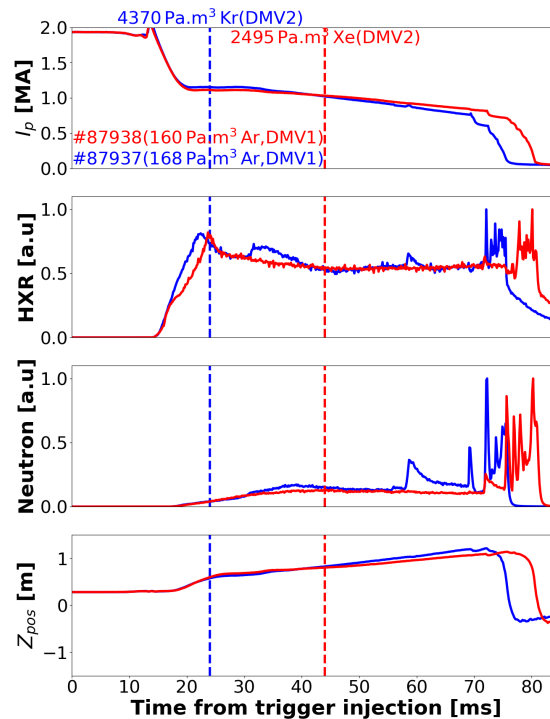


Figure 0.2.: Traces temporelles du courant plasma I_p , monitions de rayons X durs (HXR) et neutrons des décharges #87937 et #87938 montrant une atténuation infructueuse du faisceau RE. Le faisceau RE est déclenché en utilisant $\sim 160 \text{ Pa.m}^3$ d'argon de DMV1 dans les deux décharges.

En sa présence, le deuxième MMI visant à atténuer l'emballement du faisceau d'électrons peut être inefficace en raison d'une mauvaise pénétration dans ce plasma de fond, comme observé dans le tokamak JET et montré dans la figure 0.2. Par conséquent, comprendre la physique de l'interaction entre le faisceau d'électrons découplés et le 2nd MMI en présence du plasma de fond froid est une étude essentielle pour définir un scénario fiable d'atténuation des faisceaux d'électrons découplés. Cette étude sera au centre de cette thèse de doctorat.

Caractérisation expérimentale du plasma de fond

Le plasma de fond est caractérisé par sa température électronique. Sa mesure a demandé le développement d'une méthode basée sur , des données de spectroscopie VUV. Dans cette méthode, des rapports entre des lignes de visées synthétiques sont construits en utilisant le coefficient d'émission de photons (PEC) du modèle atomique ADAS et le profil de température du plasma de fond est estimé en définissant les rapports de lignes expérimentales avec les rapports de lignes synthétiques. Un exemple de profil estimé T_e est illustré dans la figure 0.3.

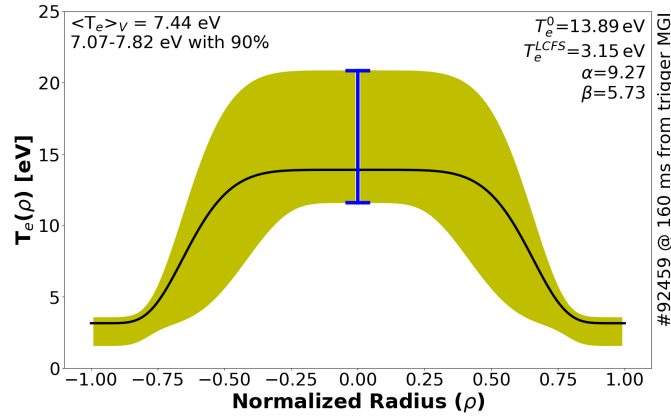


Figure 0.3.: Estimation du profil T_e de la décharge #92459, 160 ms à partir de l'injection de déclenchement.

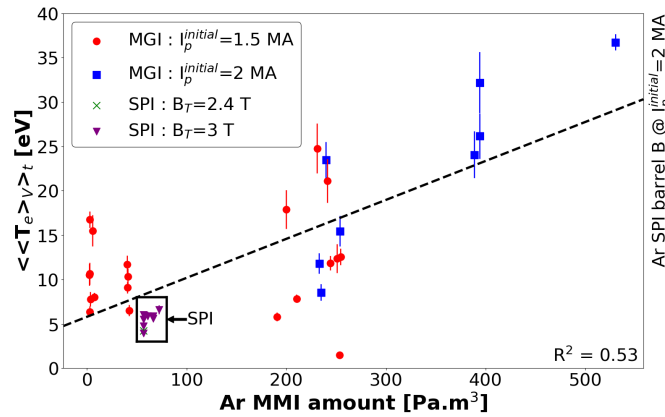


Figure 0.4.: Dépendance de la température moyenne du plasma de fond en temps et en volume $\langle \langle T_e \rangle_V \rangle_t$ de la quantité d'Ar MMI utilisée pour déclencher le plasma de fond pour les décharges MGI et SPI.

Le plasma de fond dans le tokamak JET est plus chaud ($T_e = 6-18$ eV) que sur les autres tokamaks (DIII-D, $T_e \approx 1-2$ eV). La température électronique du plasma de fond augmente avec la quantité de gaz utilisée pour déclencher la disruption et la densité électronique à l'extérieur de la dernière surface magnétique fermée comme le montre la figure 0.4. Dans le cas où la disruption est déclenchée par une injection d'Argon, sa température électronique ne dépend pas de la température électronique du plasma avant la disruption, mais se révèle faiblement corrélée avec la densité électronique précédant la disruption. De plus, les glaçons non fragmentés produisent un plasma de fond plus chaud. Quand un SPI d'argon est utilisé pour atténuer le faisceau d'électrons découplés, un plasma de fond plus chaud est créé que si un MGI avait été utilisé.

0D/1D bilan de puissance des systèmes plasma d'arrière-plan

Un bilan de puissance 0D / 1D du faisceau d'électrons découplés et du plasma de fond est effectuée pour valider les mesures de température.

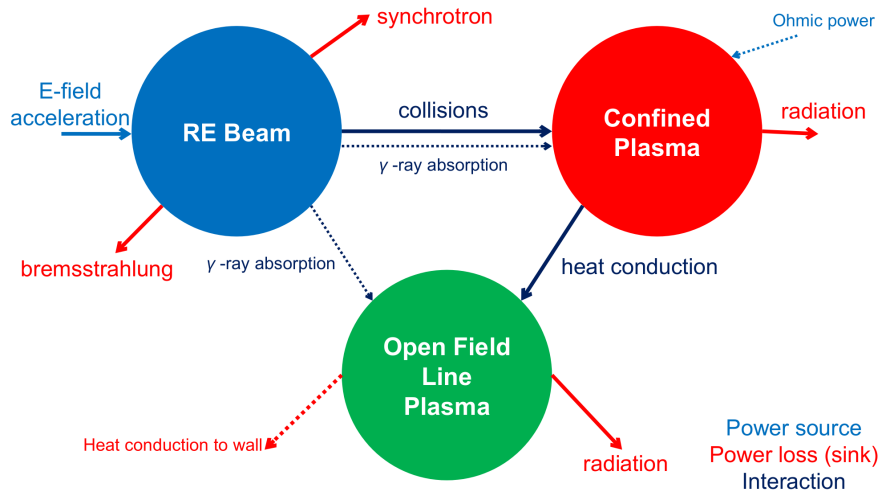


Figure 0.5.: Illustration des systèmes post-perturbation.

Le bilan de puissance est dominé par les processus physiques tels que les effets collisionnels, les rayonnements synchrotron et bremsstrahlung, l'accélération par le champ électrique, le rayonnement de raie du plasma de fond comme le montre la figure 0.5. La température de fond du plasma prédite par le modèle d'équilibre de puissance 0D est en bon accord avec les mesures de la spectroscopie VUV.

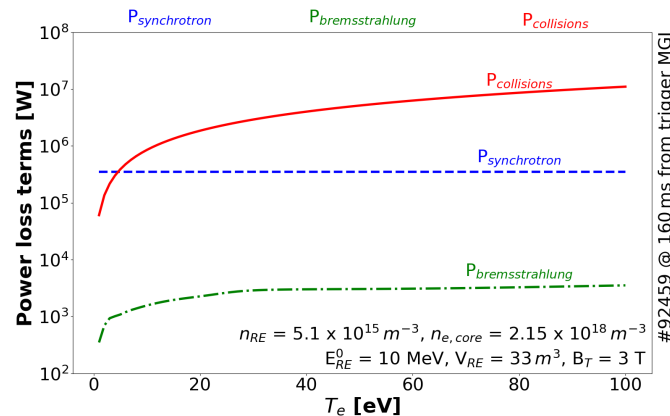


Figure 0.6.: Comparaison des termes de perte de puissance du faisceau RE (synchrotron, bremsstrahlung et transfert de puissance collisionnel) en fonction de la température électronique du plasma de fond. On suppose une énergie centrale constante de la distribution d'énergie RE E_{RE}^0 .

Le transfert d'énergie entre les électrons découplés et le plasma de fond s'avère être le source d'alimentation principale chauffant le plasma de fond à des températures élevées comme le montre la figure 0.6.

Background plasma powers in Confined region (MW)		#92459	#92454	DIII-D
(+)	$P_{collision}$	1.7 (0.72-2.54)	3.72 (3.67-6.87)	5.99
(+)	$P_{ohmic} (\times 10^{-3})$	0.09 (0.04-0.13)	0.16 (0.16-0.27)	0.47
(-)	$P_{radiated}$	2.05 (0.68-2.31)	44.45 (42.45-160.73)	6.45
	$P_{radiated}$ (bolometer)	2.61	10.61	~1
(-)	$P_{conduction}$	TBD	TBD	TBD

Table 0.1.: Bilan de puissance des plasmas de fond confinés pour les décharges JET-ILW et la décharge DIII-D supposée (les termes entre parenthèses indiquent la barre d'erreur due aux incertitudes du profil T_e).

		#92459	#92454	DIII-D
$\langle T_e \rangle_V$	[eV]	7.44 ± 0.37	3.21 ± 0.12	2
$P_{collision}$	[MW]	1.7 (0.72-2.54)	3.72 (3.67-6.87)	5.97
$N_{e,core}$	$[\times 10^{19}]$	7.16	83	28.8
$\frac{P_{collision}}{N_{e,core}}$	$[\times 10^{-14} \text{ W/e}^-]$	2.37 (1-3.55)	0.45 (0.44-0.83)	2.07

Table 0.2.: Puissance collisionnelle transférée par électron libre du plasma de fond pour les décharges JET-ILW et la décharge DIII-D supposée (les termes entre parenthèses indiquent la barre d'erreur due aux incertitudes du profil T_e).

Une puissance de collision plus élevée transférée par électron libre dans le plasma de fond peut être responsable d'une température d'électrons plus élevée, comme indiqué dans le tableau 0.2.

Simulation du plasma de fond à l'aide d'un modèle de diffusion 1D

Les résultats d'un modèle de diffusion radiale 1D, adapté au tokamak JET, sont présentés. La diffusion 1D dépend des hypothèses initiales telles que la densité de chaque espèce et la géométrie des composants face au plasma. Le flux de travail du modèle de diffusion 1D est illustré dans la figure 0.7.

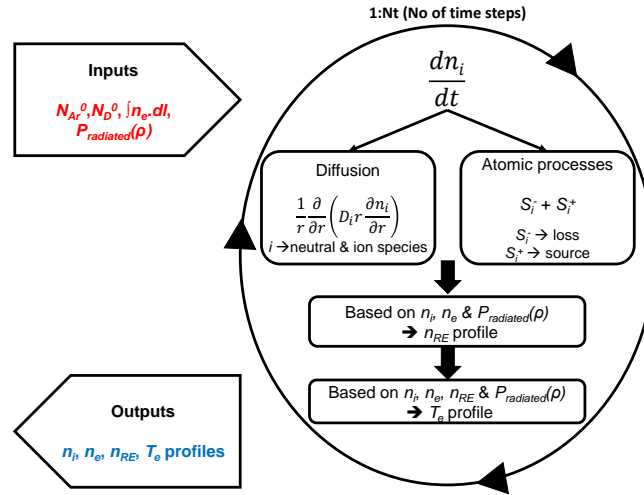


Figure 0.7.: Flux de travail du modèle de diffusion 1D

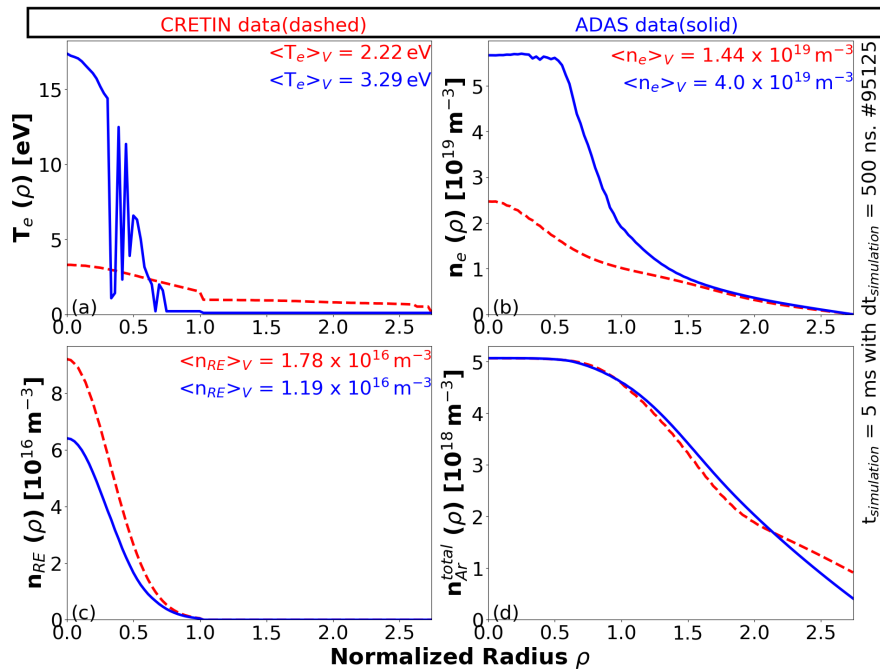


Figure 0.8.: Profils de (a) température T_e , (b) densité électronique n_e , (c) densité RE n_{RE} et (d) densité totale d'argon n_{Ar} , après 5 simulation ms avec $dt=500$ ns. Rayon du mur $R_w=1,92$ m pour toutes les simulations.

Le modèle de diffusion 1D prédit une température et une densité électronique plus élevées lorsque les coefficients issues du modèle atomique ADAS sont utilisés par rapport à ceux du modèle atomique CRETIN (utilisé par défaut dans le code) comme le montre la figure 0.8. Par rapport à la température estimée à partir de la spectroscopie VUV, la température simulée du plasma de fond en d'argon est beaucoup plus faibles et elle montre une dépendance inverse de la diminution de la quantité d'argon.

Lorsque le SPI de deutérium dans le plasma d'argon de fond est simulé, une goutte dans la ligne d'argon, la luminosité après l'entrée du deutérium SPI est prévue, cohérente avec des mesures VUV expérimentales .

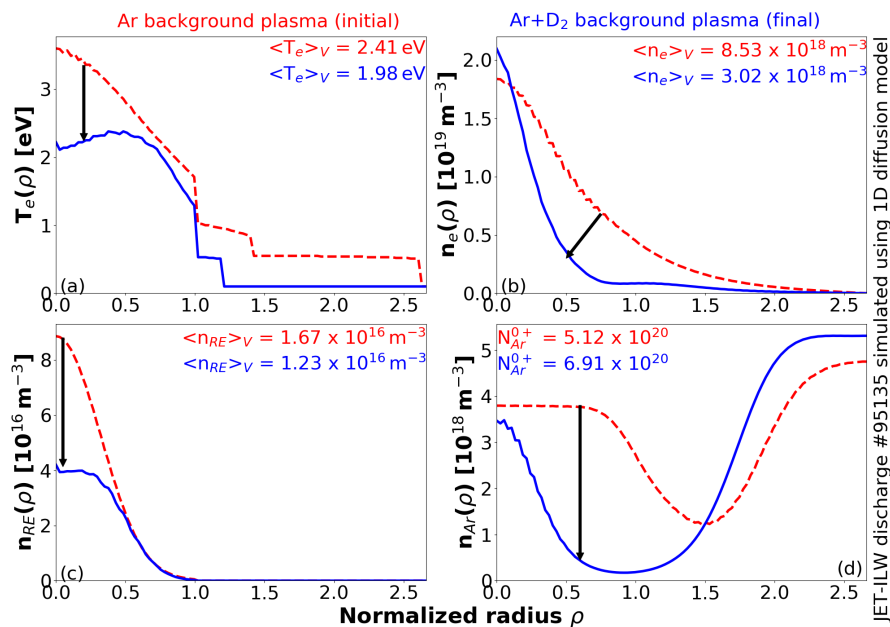


Figure 0.9.: Simulation du plasma d'arrière-plan d'argon (rouge, pointillé) et du plasma de fond Ar+D₂ (bleu, solide) dans le tokamak JET, montrant (a) le profil de température, (b) le profil de densité d'électrons libres, (c) profil de densité RE et (d) profil de densité Ar totale. Simulé à l'aide du modèle de diffusion 1D.

Cependant, le modèle prédit une augmentation de la densité électronique après un SPI en deutérium, incompatible avec les mesures expérimentales. Le modèle prévoyait une baisse de température après l'entrée du SPI de deutérium, mais elle n'est pas suffisamment faible pour atteindre les conditions de recombinaison de l'argon comme le montre la figure 0.9. D'autre part, le modèle prédit une faible température et densité électronique, soutenant l'hypothèse de la recombinaison de l'argon dans DIII-D.

La sur estimation de la densité électronique et de la température peut être due à la présence d'une puissance rayonnée plus élevée (une des entrées du modèle) dans JET (1-4 MW), que dans DIII-D (100 kW). Une grande partie du rayonnement non thermique dû aux électrons découplés explique cette observation sur JET par rapport au DIII-D. En utilisant les données PrismSPECT dans le code de diffusion 1D, le rayonnement non thermique peut être pris en compte dans le code. Cela peut nous aider à mieux simuler les conditions du plasma de fond après l'entrée D₂ SPI. C'est un travail en cours de réalisation.

Abstract

Nuclear fusion is regarded as one of the most promising candidates for humankind's future energy sources. Tokamaks are the devices currently closest to achieve reactor-relevant fusion power. The nuclear fusion power increases with the size of the tokamak and a large plasma current is required for better confinement. In tokamaks, disruptions are unfavorable events in which the plasma energy is lost in a very short timescale causing damage to the tokamak's structures. Disruption loads increase with energy and plasma current. Thus, they are a major threat to the robust operation of future large tokamaks, including ITER. There are three consequences of disruptions: thermal loads, electromagnetic (EM) loads and runaway electrons (RE). Runaway electron beams carry the risk of in-vessel component damage. In larger machines, higher plasma current increases the runaway formation. The prevention, control and mitigation of the runaway electrons are areas that are considered as hot topics in nuclear fusion research.

The current strategy for runaway electrons is to avoid their generation by a massive material injection (MMI) of deuterium or high-Z noble species (Ne, Ar, Kr, Xe). If their generation cannot be avoided, a second MMI will be used to mitigate the generated RE beam. Material can be injected via either Massive Gas Injection (MGI) or Shattered Pellet Injection (SPI, currently adopted by ITER). After the first MMI to prevent RE generation, a cold dense background plasma of MMI impurities is formed. In its presence, the second MMI aimed at mitigating the runaway electron beam may be inefficient due to poor penetration, as observed in the JET tokamak. Therefore, understanding the physics of the interaction between the runaway electron beam and the mitigation MMI in the presence of a cold background plasma is an essential study for a reliable runaway electron beam mitigation scenario. This study will be the focus of this PhD thesis.

The background plasma is characterized through its electron temperature. For this, a method based on VUV spectroscopy is developed. In this method, synthetic line ratios are constructed using Photon-Emissivity Coefficient from the ADAS atomic model and the background plasma temperature profile is estimated by fitting the experimental line ratios with the synthetic line ratios. Background plasma in the JET tokamak is hotter ($T_e \approx 6-18$ eV) than on other tokamaks (DIII-D, $T_e \approx 1-2$ eV). The electron temperature of the background plasma increases with the gas amount used to trigger the disruption and electron density in the far scrape-off layer. When the background plasma is created using argon SPI, the electron temperature have no de-

pendence on the pre-disruptive plasma temperature but is found to weakly correlate with the pre-disruption electron density. In addition, intact SPI pellets produce hotter background plasma. When argon SPI is used as a mitigation injection, it produces hotter background plasma than MGI.

A 0D/1D power balance of the runaway electron beam and the background plasma is performed to confirm the temperature measurements. In the power balance, the dominant physical processes like collisional power transfer, synchrotron and bremsstrahlung radiation, electric field acceleration, line radiation of the background plasma are considered. The background plasma temperature predicted by the 0D power balance model is in good agreement with measurements from VUV spectroscopy. The collisional power transfer between the runaway electrons and the background plasma is found to be the primary power source heating the background plasma to high temperatures.

The results of a 1D radial diffusion code, adapted for the JET tokamak, are presented. The model is sensitive to initial guesses of the species densities and the geometrical wall radius. The 1D diffusion model predicts higher electron temperature and density when rate coefficients from ADAS atomic model are used compared to CRETIN atomic model (used in the code by default). As compared to the temperature estimated from VUV spectroscopy, the simulated argon background plasma temperatures are much lower and they decrease when the argon amount increases. When a deuterium SPI in argon background plasma is simulated, a drop in the argon line brightness after the entry of deuterium SPI is predicted, consistent with experimental VUV measurements. However, the model predicts an increase in electron density after deuterium SPI entry, inconsistent with experimental measurements. The model predicts a drop in temperature after deuterium SPI entry but not low enough for the argon recombination conditions. On the other hand, the model predicts low electron temperature and density, supporting argon recombination in DIII-D. The over-prediction of electron density and temperature may be due to the presence of higher radiated power (one of model's inputs) in JET ($\sim 1-4$ MW) than on DIII-D (≤ 100 kW). A large fraction of non-thermal radiation due to the runaway electrons is considered to explain this observation in JET compared to DIII-D.

1. Introduction to Nuclear Fusion and Tokamaks

The discovery of fire has ignited one of the most important revolutions of the human species, the revolution of energy. Since the ancient times, humanity has aimed at harvesting energy. The various energy sources can be grouped into two major divisions: non-renewable and renewable energy sources. Fossil fuels like coal, petroleum and natural gas are non-renewable resources, as they will soon be depleted. This is because they are consumed much more quickly than the time they required to form naturally. In addition, combustion of these fossil fuels also give out greenhouse gases like carbon dioxide, which aggravates global warming. Energy resources like hydro-electricity, solar, tidal and wind are called renewable energy sources as the resources will not be depleted on a human timescale.

During the 20th century, Nuclear Fission reactions have been introduced as an energy source in which energy is harvested by splitting up heavy atomic nuclei such as plutonium and uranium. In comparison to fossil fuel generation, nuclear fission produced very low emission of greenhouse gases and thus less pollution. Due to the long-lived nuclear waste, nuclear fission poses serious radioactive threat. In addition, extreme risks of radioactive meltdown was witnessed through Chernobyl incident and Fukushima disaster, which prompted for safer practices. According to IEA report ([IEA](#)), ~10% of the global electricity production comes from nuclear sources. About 65% of the global electricity production is from fossil fuels whereas renewable resources account for ~25%.

At present, the scientific community is working on the next step in the energy production: Nuclear Fusion. Due to the high specific energy and the abundance of fuels: deuterium and tritium, which can be extracted from the sea water. Tritium is "bred" when neutrons escaping the plasma interacts with lithium contained in the tokamak blanket wall (more information can be found on ([ITERb](#))), nuclear fusion can be a reliable source of energy generation in the future. Tritium atoms are short-lived radioactive waste with limited risk of proliferation. Due to the absence of harmful greenhouse exhausts and no risk of nuclear meltdown like nuclear fission power plants, nuclear fusion is a very promising candidate for future's energy production.

1.1. Nuclear Fusion

Nuclear fusion is a process in which two or more nuclei combine to form one or more nuclei. Due to the difference in the binding energies, the mass of the product(s) is lower than the mass of the reactants. This difference in mass is converted into energy, from Einstein's mass-energy relation ($E = \Delta mc^2$). In the core of the stars, nuclear fusion reaction occurs at extreme conditions of temperature and pressure. For instance, in small stars like the Sun, the proton-proton cycle (Frieman 1953) is predominant in which two protons fuse to form a helium nuclei with a release of 26.7 MeV energy per fusion cycle in addition to two electrons and one electron neutrino. The conditions in the sun are 15 million kelvin and 265 billion bar of pressure.

For the fusion process to occur, the nuclei of the reactant atoms should overcome Coulomb repulsion and must be in a close proximity to each other. For this, the reactant atoms should have high velocities and thus high temperature and pressure are a necessity. Nuclear fusion of atomic nuclei at very high temperatures is called thermonuclear fusion. Under these extreme conditions, electrons are stripped from the atoms. The positively charged ions along with the free electrons form the fourth state of matter called "plasma". Even though plasma is uncommon in the vicinity of the earth, 99% of the universe comprises of plasma.

Fusion of heavier atoms requires very high energies to overcome Coulomb repulsion due to the presence of higher number of protons. In stars, fusion of heavier atoms (up to iron) can be observed. Moreover, heavier atoms have higher binding energy per nucleon (from the Aston's curve (Aston 1936)) and thus the energy yield per fusion cycle is very low. Therefore, fusion of lighter atoms (such as hydrogen and its isotopes, helium, etc) are more efficient in energy generation due to their lower binding energy per nucleon as compared to heavier atoms.

•	${}^2_1\text{D}$	+	${}^3_1\text{T}$	\rightarrow	${}^4_2\text{He}$	(3.5 MeV)	+	n^0	(14.1 MeV)	
•	${}^2_1\text{D}$	+	${}^2_1\text{D}$	\rightarrow	${}^3_1\text{T}$	(1.01 MeV)	+	p^+	(3.02 MeV)	(50%)
				\rightarrow	${}^3_2\text{He}$	(0.82 MeV)	+	n^0	(2.45 MeV)	(50%)
•	${}^3_2\text{He}$	+	${}^3_2\text{He}$	\rightarrow	${}^4_2\text{He}$		+	2p^+		+12.9 MeV
•	${}^2_1\text{D}$	+	${}^3_2\text{He}$	\rightarrow	${}^4_2\text{He}$	(3.6 MeV)	+	p^+	(14.7 MeV)	
•	p^+	+	${}^{11}_5\text{B}$	\rightarrow	$3{}^4_2\text{He}$					+8.7 MeV

A reaction's "cross-section" denotes the probability that a nuclear fusion reaction will happen. Nuclear fusion reactions of lighter atoms are listed above whereas their dependence of the cross-sections on the energy is shown in the figure 1.1. From the figure, it is obvious that the most promising approach is the fusion of deuterium and tritium (D-T reaction) due to higher cross-sections even at lower temperatures as compared to other reactions. The fusion of two deuterium atoms (D-D reaction) require very high temperatures.

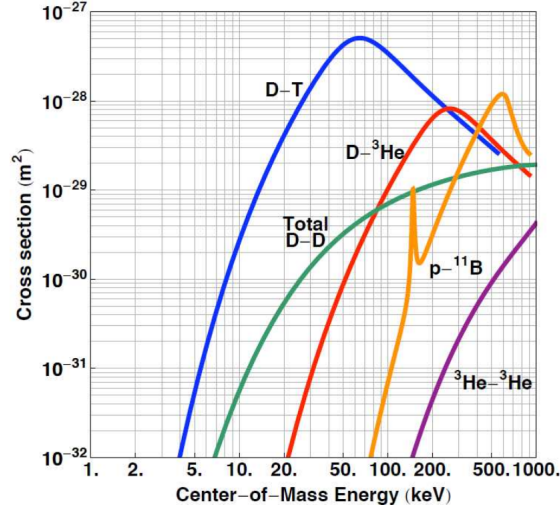


Figure 1.1.: Reaction rates for different nuclear fusion reactions (UWM)

The commercial realization of the nuclear fusion energy production is hindered by material, technological and engineering constraints. In the D-T reaction, approximately 80% of the energy (14.1 MeV per fusion cycle) is carried by the neutrons. One of the major challenges is to find a suitable material to withstand the assault of these energetic neutrons and successfully convert their kinetic energy into thermal and thus electrical energy. Another important challenge is the limited tritium supply in the world. Technology to breed tritium is a major challenge. In addition, tritium being a radioactive component increases the safety constraints of the nuclear fusion reactor.

1.2. Nuclear Fusion Power

For the nuclear fusion power, a power balance can be considered from (Lawson 1957) as,

$$P_{net} = P_{fusion} - P_{loss} \quad (1.1)$$

where P_{fusion} is the thermonuclear power and P_{loss} is the total power lost from the thermonuclear plasma. Power can be lost through radiation and conduction.

1.2.1. Thermonuclear fusion power P_{fusion}

For D-T fusion reaction, the thermonuclear power per unit volume can be defined as,

$$p_{fusion} = n_D n_T \langle \sigma v \rangle \xi \quad (1.2)$$

where n_D and n_T are deuterium and tritium densities, $\langle \sigma v \rangle$ is the rate of the fusion reaction and ξ is the energy released per fusion reaction. The total ion density $n = n_D + n_T$. The fusion power given in equation 1.3 is maximum for equal densities

of deuterium and tritium, i.e, $n_D = n_T = n/2$ for a given value of n . Thus, the equation 1.2 becomes,

$$p_{fusion} = \frac{1}{4} n^2 \langle \sigma v \rangle \cdot \xi \quad (1.3)$$

1.2.2. α -particle heating

In the D-T fusion reaction, about 80% of the energy is carried by the energetic neutrons. The remaining energy ($\xi_\alpha = 3.5$ MeV) is carried by the α -particles. These α -particles may lose their energy due to collisions with the plasma whereas the neutrons escape without interactions. Thus, the thermonuclear power per unit volume due to the α -particle heating may be defined from equation 1.3,

$$p_\alpha = \frac{1}{4} n^2 \langle \sigma v \rangle \xi_\alpha \quad (1.4)$$

and the total α -heating power, integrated over the plasma volume V , is defined as,

$$P_\alpha = \int p_\alpha dV = \frac{1}{4} \overline{n^2 \langle \sigma v \rangle} \xi_\alpha V \quad (1.5)$$

Here, the overline over the quantity $n^2 \langle \sigma v \rangle$ indicates the average value.

1.2.3. Energy loss and confinement time

In thermonuclear plasma, the total energy of the plasma W consisting of stripped ions and the electrons is defined as,

$$W = \int 3nT dV = 3n\bar{T}V \quad (1.6)$$

where n is the density and T is the temperature of the plasma. The rate at which the plasma energy is lost P_{loss} can thus be defined as,

$$P_{loss} = \frac{W}{\tau_e} = \frac{3n\bar{T}V}{\tau_e} \quad (1.7)$$

where the term τ_e is the energy confinement time. It can be defined as the time taken by the plasma to lose all its energy.

1.2.4. Power balance

For the D-T fusion plasma, when adequate confinement conditions are reached, the plasma is sustained by the α -particle heating. Thus, the power balance from the equation 1.1 reads,

$$P_\alpha = P_{loss} \quad (1.8)$$

$$\frac{1}{4} n^2 \langle \sigma v \rangle \xi_\alpha V = \frac{3n\bar{T}V}{\tau_e}$$

assuming constant values of density and temperature. For a self-sustaining plasma, the condition is

$$n\tau_e > \frac{12T}{\langle \sigma v \rangle \xi_\alpha} \quad (1.9)$$

For the temperature range 10-20 keV, the reaction rate $\langle \sigma v \rangle$ within 10% uncertainty can be expressed as (Wesson 2004),

$$\langle \sigma v \rangle = 1.1 \times 10^{-24} T^2 [\text{m}^3 \text{s}^{-1}], T \text{ in keV} \quad (1.10)$$

Thus, using $\xi_\alpha = 3500 \text{ keV}$ (3.5 MeV) and reaction rate from equation 1.10 in the equation 1.9,

$$nT\tau_e > 3 \times 10^{21} \text{ m}^{-3} \text{ keV s} \quad (1.11)$$

assuming flat density and temperature profile. Assuming a parabolic profile, the condition becomes (Wesson 2004),

$$nT\tau_e > 5 \times 10^{21} \text{ m}^{-3} \text{ keV s} \quad (1.12)$$

The equation 1.12 is called as the Lawson criterion (Lawson 1957). The product of the following quantities: density n , temperature T and the confinement time τ_e are called the fusion triple product. There are different ways to achieve nuclear fusion by choosing different parameters to maximize the triple product. For instance, by confining the fusion plasma for long duration, the Lawson criterion can be satisfied. On the other hand, the criterion can be satisfied even with shorter duration plasmas by increasing the density. In the next section 1.3, the different fusion approaches will be discussed in detail.

1.3. Approaches to nuclear fusion

For a successful nuclear fusion reactor, the Lawson criterion (equation 1.12) should be satisfied. Based on parameters chosen to achieve maximum triple product, there are many approaches to nuclear fusion:

1. inertial confinement fusion (ICF)
2. inertial electrostatic fusion (IEF)
3. magnetized target fusion (MTF)
4. magnetic confinement fusion (MCF)

The typical triple product values of different approaches are given in the table 1.1. The inertial electrostatic fusion (IEF) is not considered here as they are small-scale experiments and are no way close to break-even conditions (Rider 1995). The main difference between ICF, MTF and MCF is how they balance the fusion triple products (T_e , n_e and τ_e) in order to satisfy Lawson criterion (equation 1.12). In ICF, high density plasmas are confined for very short time (in order of ns) whereas comparatively lower density plasma is confined for a longer time (in order of s) in MCF. In MTF, the

magnitude of the electron density is between ICF and MCF with a confinement time in order of few μs . In all cases, 100 million K is required to overcome Coulomb repulsion.

Approach	T_e [10^6]	n_e [m^{-3}]	τ_e [s]
ICF	100	10^{31} - 10^{33}	10^{-9}
MTF	100	10^{29} - 10^{30}	10^{-6}
MCF	100	10^{18} - 10^{22}	1

Table 1.1.: triple product values of ICF and MCF

1.3.1. Inertial confinement fusion (ICF)

In inertial confinement fusion (ICF) approach, the inertia of the fuel mass is used to confine the plasma (Lindl 1995). A capsule (called hohlraum) containing the fusion fuel (deuterium and tritium for instance) is compressed in an implosion process to very high density and temperature using high-energy beams. Normally laser lights are used as high-energy beams but beams of electrons and ions are also used. The National Ignition facility (NIF) (LLNL) and Laser Mégajoule (CEA) are examples of ICF experiments. In spite of significant progresses made in ICF, this approach is subjected to various major challenges for thermonuclear ignition (Betti 2016).

Sometimes, the laser pulse is combined with the magnetic pinch, which is called as magneto-inertial fusion or magnetized linear inertial fusion.

1.3.1.1. Z-pinch

Z-pinch (also called as zeta pinch) is an ICF device in which a magnetic field is generated by sending a strong current through the plasma in the z-direction. Through Lorentz force, the magnetic field compresses ("pinches") the plasma to fusion relevant conditions. In the Z-pinch, most of the motion of the particles is along the magnetic field line. Thus at the end of the machine, a lot of particles escape leading to a loss of plasma mass and energy. In addition, Z-pinch has stability problems, mainly kink instability. The circular pinch machine ZETA (Thonemann 1958) is one of the oldest fusion device. In August 1957, ZETA produced about a million neutrons per pulse with measurements suggesting the fuel reached between 1-5 million K.

1.3.2. Inertial electrostatic fusion (IEF)

In inertial electrostatic fusion (IEF) approach, the plasma is confined using electric fields. Deep electrostatic potential wells are created within plasma to accelerate ions to sufficient energies for fusion reaction to take place and confine them (Rider 1995). Fusor (Farnsworth 1968) is an example of IEF device that uses an electric field to heat ions to nuclear conditions. By inducing a voltage between two metal cages which are

kept inside a vacuum. Fusor is the simplest nuclear fusion machine to construct and many amateurs have managed to fuse atoms with fusor.

1.3.3. Magnetized target fusion (MTF)

In magnetized target fusion, inertia of the nuclear fuel is used to compress the plasma capsule and magnetic field is used to confine it. MTF consists of the hydrodynamic compression of magnetized deuterium-tritium (D-T) plasma to ignition conditions (Kirkpatrick 1995). LINUS project (Robson 1980) and General Fusion's MTF device (General Fusion) are some examples of MTF devices.

1.3.4. Magnetic confinement fusion (MCF)

In magnetic confinement fusion (MCF), the plasma is confined through magnetic fields produced by external coils. MCF is presently the most promising candidate for nuclear fusion energy. There are different MCF devices based on the magnetic configuration which confines the plasma.

1.3.4.1. Magnetic mirrors

The magnetic mirrors fusion device (also called pyrotron in US) is a MCF device in which the hot plasma is confined by the back and forth reflection using magnetic fields. It was developed by Richard Post and teams at LLNL (Post 1970) and is one of the earliest fusion devices.

1.3.4.2. Reversed field pinch (RFP)

Reversed-field pinch (RFP) is a MCF device in which the plasma is confined by a combination of a toroidal magnetic field and poloidal magnetic due to a toroidal plasma current (Bodin 1980). In RFP, both the poloidal and toroidal magnetic fields are of same magnitude. In addition, the toroidal field reverses on the outside of the plasma with respect to its value on the axis as shown in the figure 1.2.

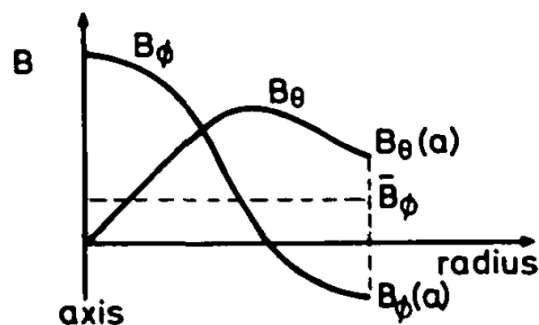


Figure 1.2.: radial distributions of magnetic field components B_θ and B_ϕ of RFP device across the minor radius (Bodin 1980)

1.3.4.3. Field reversed configuration (FRC)

Field reversed configuration (FRC) is an elongated prolate compact toroid which has no toroidal field (Tuszewski 1988). FRC is also called as field reversed θ -pinches as they were discovered accidentally during θ -pinch research (Kolb 1959).

1.3.4.4. Spheromaks

Spheromaks are MCF device in which no materials such as vacuum vessels and external magnetic field coils links the torus. The first wall has spherical topology and spheromaks have equal toroidal and poloidal field strengths (Jarboe 1994). The primary advantage of spheromaks is the engineering simplicity due to quasi-spherical first wall and that coils are circular. However, small and low-energy spheromaks seems to have limited performance. Spheromaks have also been used to inject plasma into a bigger MCF devices (Brown 1990).

1.3.4.5. Spherical tokamaks

Spherical tokamaks are a variation of the tokamak design (discussed in section 1.4) with a spherical torus. In the spherical tokamaks, the size of the hole in the center of a traditional tokamaks is reduced as much as possible which results in an almost "cored apple like" spherical shape. The difference between the traditional tokamaks and the spherical tokamaks is shown in the figure 1.3. The spherical plasma in the spherical tokamaks are shown for MAST in 1.4.

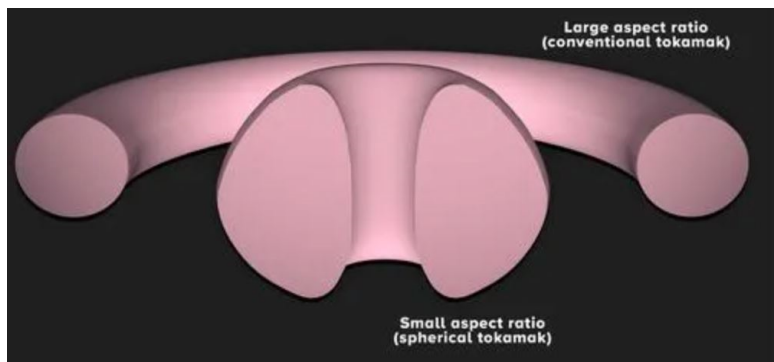


Figure 1.3.: illustration of the spherical tokamaks as compared to the traditional tokamaks (CCFE)

Spherical tokamaks are cheaper to construct than traditional tokamaks due to their relatively lower magnetic fields. Due to low aspect ratio, spherical tokamaks have more plasma stability as low aspect ratios were found to suppress MHD instabilities. Also, spherical tokamaks confine plasma more efficiently (Peng 1986). In spite of higher plasma beta, overall plasma pressure in a spherical tokamak is lower than conventional tokamaks. The disadvantage of spherical tokamaks is that they require more non-inductive current drive and therefore more additional power due to the

absence of central solenoid current drive. Spherical tokamaks rely on the so-called bootstrap current for economical operation.

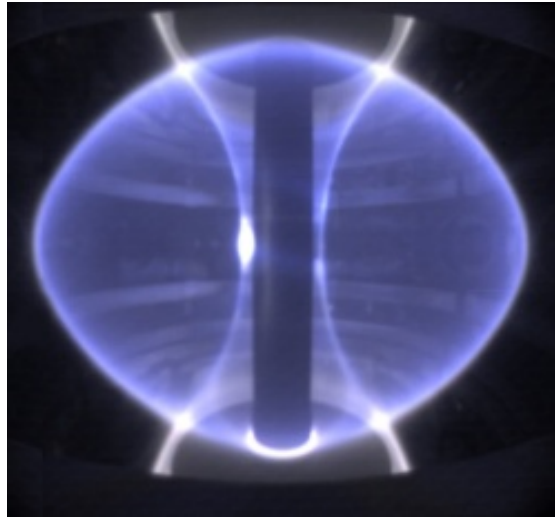


Figure 1.4.: Spherical plasma in MAST (CCFE)

1.3.4.6. Stellarators

The stellarator was developed by Lyman Spitzer (Spitzer 1958). It has a twisted plasma path created by external magnets as illustrated in the figure 1.5. In tokamaks, the particles on the inside edge of the tube would drift upwards (or downwards, based on the charge) as the field is stronger due to the change in the Larmor radius. In the outside edge, the particle would move down (or up, based on the charge). Thus, with the stellarator design, the drifts would be compensated enough to confine the plasma longer. Wendelstein 7-X (IPP-MPGb) is currently the world's largest stellarator situated in the North of Germany.

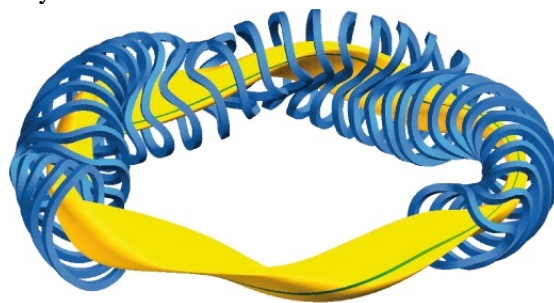


Figure 1.5.: illustration of the plasma confinement in the stellarator

The advantages of stellarators include steady state operation, stable operations with fewer instabilities, no plasma current and the absence of plasma disruptions. Moreover, the stellarator allows for higher electron plasma density (Xu 2016) and their larger aspect ratio enables less stress on the inner wall materials. However, the stellarator has a very complicated design and it is very expensive and very complicated

to construct. Stellarators have problems with the impurity build-up and particle transport losses. As a result, stellarators are far from ignition conditions and energy production and the stellarator power plant would be very large and expensive. As compared to the tokamaks, stellarators have much less operational experience. For these reasons, tokamak is considered as the ideal candidate for the fusion energy production.

1.3.4.7. Tokamaks

Tokamak, one of the MCF device is the most well studied approach to the nuclear fusion energy. Tokamaks have toroidal confinement region that gives it an overall shape similar to a donut, with a large hole in the middle. At present, the JET tokamak in the United Kingdom ([EUROfusion](#)) is currently the world's largest tokamak in operation (more information given in the section 1.3.4.7). The ITER tokamak ([ITERC](#)) in the South of France will soon be the world's largest tokamak and is now under construction. In the section 1.4, the magnetic field configuration and physics principles of the tokamak is discussed in detail.

1.4. Physics and engineering principles of tokamaks

The "tokamak" is the Russian abbreviation for "toroidal chamber with magnetic coils". In the tokamaks, magnetic fields are produced with the help of the external magnets. These magnetic fields are then used to confine the fusion plasma.

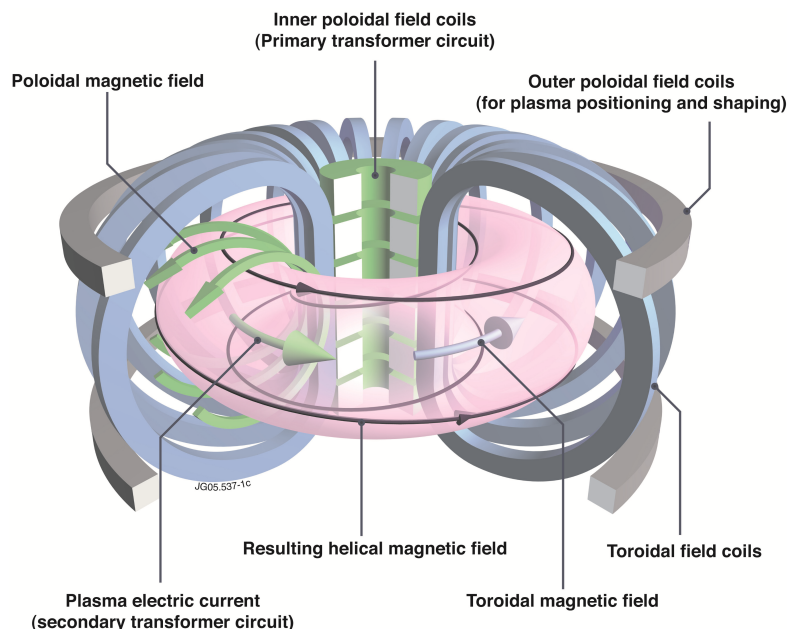


Figure 1.6.: illustration of the plasma confinement in the tokamak using magnetic fields ([EUROfusion](#))

As shown in the figure 1.6, the toroidal magnetic field is created in the tokamak using a series of toroidal field magnets in different toroidal positions. Poloidal field magnets are used to control the plasma shape and position. The central solenoid (primary transformer circuit) is used for current drive to induce the current in the plasma. The geometry of the tokamak is described using four parameters: major radius R , minor radius a , toroidal angle ϕ and the poloidal angle θ . In the poloidal cross-section, the poloidal magnetic field is peaked at the magnetic center. The direction of the toroidal magnetic field is shown in the figure 1.6.

1.4.1. Magnetic configuration of the tokamak

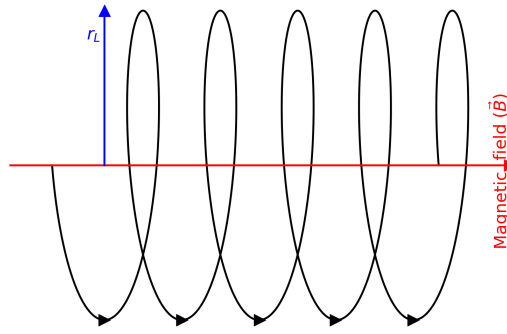


Figure 1.7.: illustration of particle gyration along the magnetic field \vec{B}

The fusion plasma comprises of the charged ions and free electrons in addition to some neutral atoms. According to Lorentz law, a charged particle in the plasma gyrates along the magnetic field \vec{B} which is illustrated in the figure 1.7. Thus, the Lorentz force experienced by the particle (ion/free electrons) can be given as,

$$m \frac{\partial \vec{v}}{\partial t} = q[\vec{v} \times \vec{B}] \quad (1.13)$$

where m , q and v are the mass, charge and velocity of the particle. Due to the cross product $\vec{v} \times \vec{B}$, only the velocity component perpendicular to the magnetic field is sensitive to the field whereas the parallel component is insensitive. The particles gyrate along the magnetic field line in a helical path with a radius called as Larmor radius r_L with the cyclotron frequency ω_c which are represented as,

$$r_L = \frac{mv_{\perp}}{q|B|} \quad (1.14)$$

$$\omega_c = \frac{q|B|}{m} \quad (1.15)$$

Thus, it can be deduced from the equations 1.14 and 1.15 that ions have larger Larmor radius whereas the gyration frequency is lower than the free electrons.

The magnetic field lines should be closed on themselves so that the particles do not escape at the end of the magnetic field line. This can be accomplished by bending the

magnetic field to a circular form to form a torus such that the magnetic field lines are closed and the plasma is confined. This is done precisely in the tokamak.

Since the magnetic field is curved, the particles experience an additional drift perpendicular to the magnetic field. The velocity corresponding to the drift is called as curvature drift velocity, which can be expressed as (Wesson 2004),

$$v_d = \frac{v_{\parallel}^2 + \frac{1}{2}v_{\perp}^2}{\omega_c} \frac{\vec{B} \times \nabla \vec{B}}{B^2} \quad (1.16)$$

The drift v_d also contains the $\nabla \vec{B}$ drift. This curvature drift tends to draw particles outside the guiding center of the plasma. Thus, by twisting the magnetic field lines, this curvature drift can be counteracted. This twisting strength is quantified using a quantity called "safety factor" q which indicates the number of toroidal turns the magnetic field line undergoes before completing a poloidal turn. Due to the induced plasma current, poloidal magnetic field is generated in the plasma itself due to Maxwell-Faraday's law. This generated poloidal field compensates the drift. Thus, a tokamak is a device in which electric current is induced in the plasma itself and confined through external magnetic fields.

1.4.2. Present tokamak parameters

In this section, configuration and parameters of the present tokamaks are reviewed.

1.4.2.1. The JET tokamak

The Joint European Torus (JET) (EUROfusiona) is the currently the largest operational tokamak (first plasma in 1983) located at Culham Center for Fusion Energy (CCFE) in Oxfordshire, United Kingdom. It is a joint European project maintained by EUROfusion (EUROfusionc).

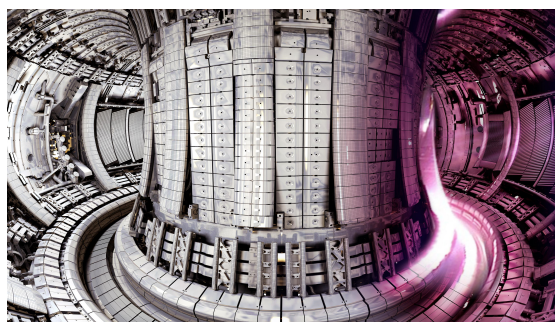


Figure 1.8.: interior view of the JET tokamak with ITER-like wall (EUROfusiona)

The interior view of the JET vessel is shown in the figure 1.8 and the tokamak parameters are tabulated in the table 1.2. In the JET tokamak, both limiter and single X point divertor discharges can be produced. Until 2011, JET tokamak had a carbon limiter. In 2011, the first wall made of tungsten and beryllium was installed with

tungsten divertor to reflect ITER's setup. The JET tokamak is tritium capable and this is a unique feature among the present tokamaks. JET has massive gas injection valves for disruption mitigation. Since 2019, Shattered pellet injection (SPI) systems is also used as disruption mitigation system (see section 2.5.3.3).

Parameter		Value
Major radius	R	2.96 m
Minor radius	$a_{horizontal}$	1.25 m
	$a_{vertical}$	2.1 m
Plasma current (max)	I_p	4.8 MA
Toroidal field	B_T	3.45 T
Heating	P_{NBI}	34 MW
	P_{ICRH}	10 MW
	P_{LHCD}	7 MW
Plasma volume	V_{plasma}	100 m ³
Duration	t	up to 60 s
Energy	$W_{thermal}$	10 MJ
	$W_{magnetic}$	10 MJ

Table 1.2.: parameters of the JET tokamak (EUROfusionb)

During the D-T fusion experiments in 1997, the JET tokamak produced a record output power (16.1 MW peak power and 4 MW quasi-steady state fusion power for 4 s) with a peak fusion gain ($Q = P_{out}/P_{in}$) of 0.62 (Keilhacker 1999).

1.4.2.2. The ITER tokamak

ITER (*the way* in Latin) is the world largest fusion project and is under construction in the Cadarache site in the South of France. It is an international collaboration of seven members : European Union, United States, India, China, South Korea, Japan and Russia. Upon completion, it will be the world's largest tokamak. The tokamak parameters are tabulated in the table 1.3 and the tokamak view is shown in the figure 1.9. The ITER magnet system will be the largest superconducting magnet system ever built with sophisticated component integration. The toroidal field magnets are cooled by liquid helium (4K) and produces a magnetic field of 11.8T in the coil. The ITER cryostat will be the largest stainless steel high-vacuum pressure chamber ever built with a volume of 16000 m³. Due to the low plasma contamination and low fuel retention, beryllium is used as the first wall in the blanket. ITER will be the first fusion device to have actively cooled blankets with water. ITER's first plasma is scheduled for 2025 with D-T plasma from 2035.

Parameter		Value
Major radius	R	6.2 m
Minor radius	$a_{horizontal}$	2 m
	$a_{vertical}$	3.4 m
Plasma current (max)	I_p	15 MA max
Toroidal field	B_T	5.3 T
Heating	P_{NBI}	33 MW
	P_{ICRH}	20 MW
	P_{ECRH}	24 MW
Plasma volume	V_{plasma}	840 m ³
Duration	t	up to 1000 s
Energy	$W_{thermal}$	353 MJ
	$W_{magnetic}$	395 MJ

Table 1.3.: parameters of the ITER tokamak (ITERc)

There are five main goals of the ITER tokamak which are as follows (ITERc):

1. Produce at least 500 MW of fusion power for pulses of 40s from 50 MW input power with $Q \geq 10$.
2. Deuterium-tritium fusion plasma in which the reaction is sustained through internal heating
3. Test tritium breeding capacities
4. Demonstrate the safe characteristics of a nuclear fusion reactor
5. Demonstrate the integrated operation of technologies for a future fusion power plant

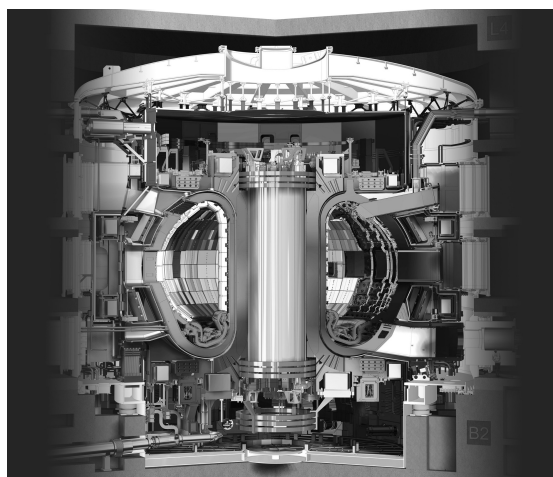


Figure 1.9.: inside design of the ITER tokamak (EUROfusiona)

1.4.3. Tokamak performance

Over the last few decades, progress has been made in the tokamak physics to reach the ignition conditions. The ignition criterion of the D-T plasma has been given by Lawson (equation 1.12) and states that triple products (T_e , n_e and τ_e) should be $\geq 5.1 \times 10^{21}$ keV m⁻³ s. In the figure 1.10, the triple product achieved by different tokamaks in the past few decades are plotted against the achieved electron temperature T_e .

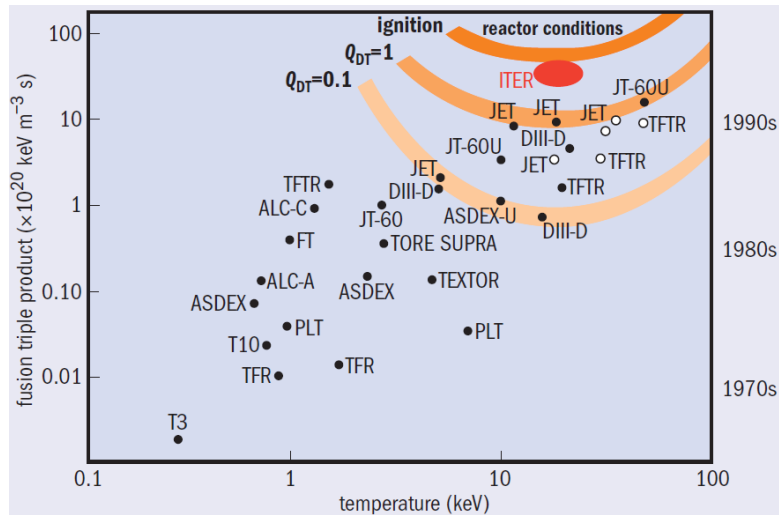


Figure 1.10.: fusion triple product and the plasma temperature achieved by the tokamaks in the recent decades (Pitts 2006)

Tokamak T3 is one of the earliest tokamaks to demonstrate plasma temperature of few 100 eV (Peacock 1969) and ever since, tokamak research has been developed substantially. Current tokamaks like ASDEX-U, DIII-D, JT-60U, JET can reach much hotter plasma temperatures, around 10 keV which is favorable for fusion conditions. Of the modern tokamaks, only JET reached a fusion gain of $Q = P_{out}/P_{in} = 0.62$ (EUROfusion) and other tokamaks were far from the required triple product.

Energy confinement time is one of the key ingredients in the triple product and it scales with the major radius of the tokamak. Thus, by constructing bigger tokamaks, higher energy confinement time will be achieved and the tokamaks will be close to ignition conditions. For this reason, ITER tokamak was designed with a major radius of 6.2 m with which $Q=10$ will be achieved. Even though the basic design of the ITER tokamak is already defined, the open challenges on the understanding some of the underlying physics can substantially shape the progress of tokamak performance.

2. Tokamak Disruptions and Runaway Electrons

In a tokamak plasma, instabilities can grow up to a point at which there is a rapid loss of thermal and magnetic energy stored in the plasma. This phenomenon of sudden plasma termination in tokamaks is called a disruption. In fusion devices such as stellarators, disruptions are nonexistent due to the fact that confinement does not depend on the plasma current. During tokamak disruptions, large heat and electromagnetic (EM) loads are deposited on the tokamak wall and structures in a very short timescale, in order of few milliseconds. These loads can cause severe damage to the plasma facing components (PFC) in proportion to the stored energy. Rapid loss of energy is particularly problematic in large future tokamaks, including ITER. The consequence of disruptions are discussed in the section 2.3. In addition, disruptions can also produce a beam of relativistic runaway electrons (RE) with few MeV of energy, which can cause a substantial damage to the in-vessel components. Thus, it is very important to mitigate the disruptions and weaken their consequences for the reliable operation of large and reactor scale tokamaks. The physics of disruptions and the runaway electrons is discussed in this chapter in section 2.4. Furthermore, this chapter also discusses the mitigation of disruptions and runaway electrons. The main subject of this PhD thesis will be discussed in the section 2.6 with some theoretical background.

2.1. Phases of Tokamak Disruptions

In tokamaks, plasmas are subjected to various kinds of instabilities. These instabilities grow and thereby perturbate the magnetic configuration. This results in the loss of confinement. Consequently, the energy stored in the plasma is lost and thus the plasma current drops to zero thereby marking the end of the discharge.

As illustrated in the figure 2.1, there are three main phases for a major disruption :

2.1.0.1. Pre-disruptive phase :

During the pre-disruptive phase, the conditions necessary for the plasma disruption develop from the onset of plasma instabilities. Various causes of the disruptions are discussed in the upcoming sections of this chapter. The time during which the instabilities grow is variable but is typically from 10 ms to 100 ms in medium sized tokamaks.

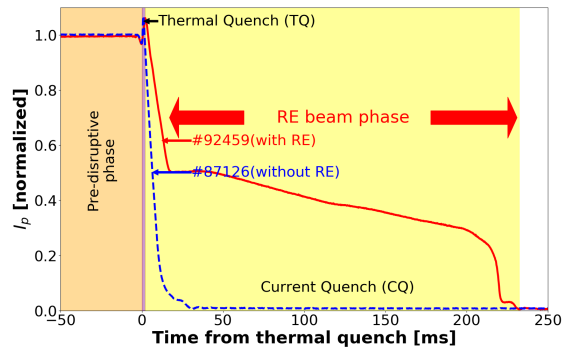


Figure 2.1.: Illustration of tokamak plasma disruption for the JET discharges #92459 (with RE, red solid) and #87126 (without RE, blue dashed). Plasma current I_p is normalized with the flat-top plasma current.

2.1.0.2. Thermal quench phase (TQ) :

The thermal quench is the beginning phase of the plasma disruption. During the thermal quench phase, the core plasma temperature drops from few keV to few eV with a timescale in order of microseconds depending on the tokamak size. The thermal energy loss during the thermal quench is predominately through impurity radiation and direct power conduction to the wall.

The current profile flattens (as internal inductance l_i decreases) and therefore the magnetic energy ($l_i I_p^2/2$) should decrease. But, magnetic energy dissipates more slowly as compared to the thermal energy dissipation. Therefore, the plasma current increases to balance the magnetic energy during the thermal quench phase (Wesson 2004). The duration of the thermal quench scales with the machine size (IPB 1999). It is in order of tens of microseconds in small tokamaks, hundreds of microseconds in medium-sized tokamaks. In the JET tokamak, thermal quench in order of few milliseconds are observed. Even within a tokamak, the thermal quench depends on the type of the disruption (section 2.2) and the growth rate of the instabilities in the pre-disruptive phase.

2.1.0.3. Current quench phase (CQ) :

The plasma resistivity increases with the drop in the electron temperature. Thus, the plasma current drops as the plasma can no longer conduct. The typical timescale for the current quench phase in order of few milliseconds to few hundreds of milliseconds.

During the current quench phase, the magnetic energy associated to the plasma current dissipates and the plasma shrinks in size. A part of the magnetic energy is dissipated through radiation by ohmic heating of the plasma. In addition, the magnetic energy is also converted into electromagnetic (EM) loads on the structures of the tokamak. Faster the current quench, higher are the EM loads on the structures. More information about the consequences of EM loads is discussed later in this section.

During the current quench phase, a toroidal electric field is induced which can accelerate free electrons and thus create a beam of so called relativistic runaway electrons (RE). In the following section, the physics of runaway electrons, their creation and loss are seen in detail.

2.2. Causes and Operational Limits of Tokamak Disruptions

Disruptions are caused due to the growing of plasma MHD instabilities. As explained in the section 2.1, instabilities develop during the pre-disruptive phase which may be few 100 milliseconds before the thermal quench. Detailed theoretical understanding of the disruptions in the pre-disruptive phase is not well known. However, it is possible to construct the operational limits of the tokamaks based on operational-based experiences.

2.2.1. Troyon beta limit

In a tokamak plasma, the plasma beta β is the ratio of the plasma pressure to the magnetic pressure,

$$\beta = \frac{\langle p_{plasma} \rangle}{p_{mag}} = \frac{n_e k_B T_e}{B^2 / 2\mu_0} \quad (2.1)$$

where k_B is the Boltzmann constant and T_e in K. Plasma beta normally represents the efficiency of plasma confinement and for a stable plasma, $\beta < 1$ otherwise the plasma would collapse. In a MCF device, β should be as high as possible with minimum magnetic force needed for confinement.

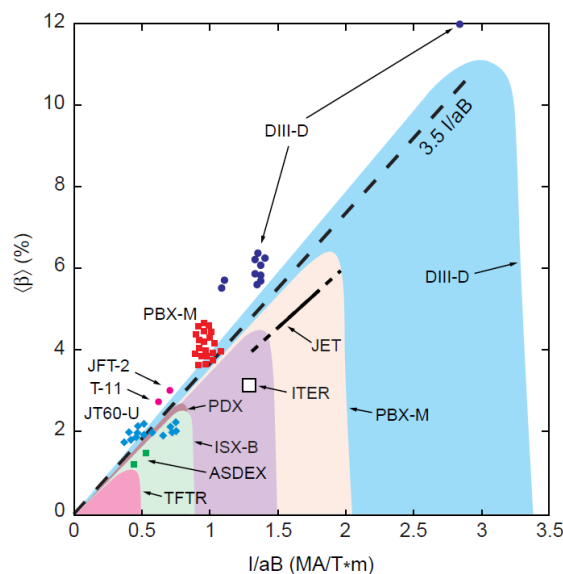


Figure 2.2.: Volume averaged β versus I_p / aB_ϕ for various tokamaks from (IPB 1999)

However, the present tokamak have low β due to plasma instabilities, around 2%-6%, as shown in the figure 2.2. The maximum achievable β is mainly limited due to the formation of high-n pressure-driven instabilities such as ballooning instabilities.

In 1984, F. Troyon studied MHD-limits to the confinement of plasma in (Troyon 1984). He found empirically that the limit set by onset of ideal MHD instability is reasonably well described by,

$$\beta_{max}[\%] \approx \frac{\beta_{N,max} I_p}{a B_\phi} \quad (2.2)$$

where I_p (in MA), a (in m) and B_ϕ (in T) are the plasma current, minor radius of the tokamak and toroidal magnetic field. The term β_N is the so-called "normalized beta". The value of $\beta_{N,max}$ has been determined numerically by Troyon as 2.8%. Empirical evaluation from the data of various tokamaks is $\beta_{N,max} = 3.5\%$.

The volume averaged β is plotted against $I_p / a B_\phi$ in the figure 2.2. The shaded regions show the range of β accomplished in the corresponding experiments. The upper bound on normalized beta achieved in many tokamaks with both circular and shaped plasmas is $3 \leq \beta_N \leq 4$ and this result is commonly referred to as the 'Troyon' limit.

2.2.2. Current limit (low- q limit) disruption

In a tokamak, the safety factor $q(r)$ is the ratio of toroidal to poloidal turns made by the magnetic field. The edge safety factor q_{edge} is given by the expression,

$$q_{edge} = \frac{a B_\phi}{R B_\theta} \quad (2.3)$$

where a and R are the major and minor radius of the tokamak. The terms B_ϕ and B_θ are the toroidal and poloidal magnetic field strength. When the edge safety factor q_{edge} drops below 1, the plasma becomes unstable due to external kink mode. This $q_{edge} \geq 1$ is the so-called Kruskal-Sharfanov (KS) limit (Kruskal 1958; Shafranov 1956). However for practical reasons, q_{edge} must be larger than 2 (Wesson 2004). Applying Biot-Savart law, the poloidal magnetic field strength and the plasma current can be related as,

$$B_\theta = \frac{\mu_0 I_p}{4\pi a} \quad (2.4)$$

Substituting the equation 2.4 in equation 2.3, edge safety factor can be expressed as,

$$q_{edge} = \frac{4\pi a^2 B_\phi}{\mu_0 R I_p} \quad (2.5)$$

Thus, the maximum value of the plasma current for a disruption-free tokamak operation can be represented as,

$$I_p(max) = \frac{2\pi a^2 B_\phi}{\mu_0 R} \quad \text{with} \quad q_{edge} \geq 2 \quad (2.6)$$

with $I_p(max)$ given in MA. For a given tokamak, the maximum current for the steady operation is limited by its aspect ratio (a/R) and the toroidal magnetic field strength B_ϕ . In practice, reaching $q_{edge} \sim 2$ with disruption free operation in present tokamaks is difficult. For the JET tokamak, $I_p(max)=4.3$ MA ($q_{edge}=2.7$) and for the ITER tokamak, $I_p(max)=14.9$ MA ($q_{edge}=2.3$).

2.2.3. Density or radiative limit disruption

A density limit disruption corresponds to the growth of instabilities in the plasma edge. As a result, the current profile is contracted and the disruption is triggered. One of the approaches to explain this density limit disruption is through impurity radiation. At higher densities, the impurity radiation is predominant in the edge of the plasma where the low Z impurities are not fully stripped. As a result, the resistivity increases due to the plasma cooling. This produces a contraction of the current profile which leads to increase of destabilizing current gradient inside the $q=2$ surface (Wesson 2004). As the current profile contracts, the value of q at the contracted edge of the plasma approaches an unstable value and thus the plasma becomes unstable (Wesson 2004). Eventually, the plasma disrupts due to the growing instabilities.

In another explanation, the density limit disruption involves transport and atomic processes (Greenwald 2002). Due to the increase in the transport at the edge of the plasma and scrape-off layer (SOL), "blobs" penetrate the separatrix and convect the plasma energy from the edge and thereby cool the plasma edge. Systematic degradation of the particle transport was observed at higher densities.

As the understanding of the physical mechanism behind the origin of the density limit is incomplete, a scaling law for the maximum achievable density without disruptions called the "Greenwald density limit" (Greenwald 2002) can be expressed as,

$$n_G = \frac{I_p}{\pi a^2} \quad (2.7)$$

where I_p is given in MA and n_G in 10^{20} m^{-3} . This limit is empirical based on observations of the tokamaks before 90s. Normally in tokamaks, exceeding this limit typically leads to disruptions. Unlike the current limit disruption, the Greenwald limit is not very strict and sometimes the limit can be crossed without deleterious effects. Stellarators can however be operated at higher densities than the tokamak with a different scaling.

The operational limits of the tokamak are sketched using Hugill's diagram as shown in the figure 2.3. The blue shaded region illustrates the stable operational limit of the tokamak. The current limit (equation 2.6) depends only on the tokamak parameters of aspect ratio and the toroidal magnetic field. Since the aspect ratio of a tokamak is usually fixed, only the toroidal field restricts the maximum achievable plasma current for stable tokamak operations. As shown in the equation 2.7, the density limit scales linearly with plasma current for a given tokamak as illustrated in the figure 2.3.

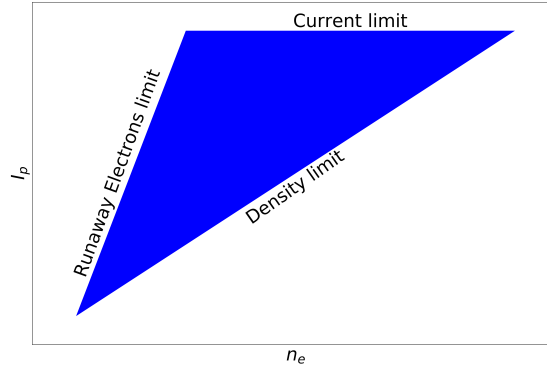


Figure 2.3.: illustration of various tokamak operational limit using Hugill's diagram

In low density plasmas, runaway electrons collide less with other electrons or ions and thus it is significantly accelerated. When the electric field E is much higher than the critical electric field E_c , runaway electrons are generated. As the critical field E_c depends on the electron density n_e , the possibility of generating runaway electrons is higher in low density regimes (Son 2016) (more information provided in the section 2.4). The density limit slope between n_e and I_p in the Hugill's diagram 2.3 is only a sketch and is often associated to the drift parameter $v_{drift}/v_{thermal}$ (Greenwald 2002).

2.3. Consequences of Tokamak Disruptions

During disruptions, a majority of the plasma energy is dissipated in a very short timescale. The plasma energy lost during the disruption is proportional to the size of the tokamak. As a result, they may cause unacceptable damages to the plasma facing components, especially for large future tokamaks, including ITER. There are three major consequence of the disruptions: thermal loads, electromagnetic (EM) loads and the runaway electrons.

2.3.1. Thermal loads

During the thermal quench phase of the plasma disruption, a majority of the plasma thermal energy is dumped to the tokamak wall in a very short timescale through conduction, convection and radiation. The thermal load impact on the wall due to conduction is normally localized. This localized energy dump may exceed the thermal limits of the wall material and may cause irreversible damage to them. Thus, disruption heat loads are a major threat to the reliable operation of the plasma facing components. To assess the impact of the heat load on the wall materials, a damage parameter ϕ_{damage} can be defined as,

$$\phi_{damage} = \frac{E}{\sqrt{\tau}} \quad \text{in MJ m}^{-2} \text{ s}^{-0.5} \quad (2.8)$$

where E is the energy deposited per unit surface of the wall (in MJm^{-2}) and τ is the thermal quench time. The $\sqrt{\tau}$ term in the denominator is due to heat diffusion. For the JET tokamak with thermal energy ~ 10 MJ, $E=0.892\text{MJm}^{-2}$ assuming divertor area of $\sim 1.6\text{m}^2$ and seven times scrape-off layer (SOL) expansion during the disruption-TQ (Hender 2007). Assuming thermal quench time $\tau=0.32$ ms (Hender 2007), the damage parameter is $\phi_{damage} = \sim 50$ in $\text{MJm}^{-2}\text{s}^{-0.5}$. For reference, the onset of melting for carbon or tungsten divertor is around $40\text{-}60\text{MJm}^{-2}\text{s}^{-0.5}$. For the ITER tokamak, $\phi_{damage} = \sim 530\text{MJm}^{-2}\text{s}^{-0.5}$. The above estimates are the worst case of disruption in which 100% of the initial thermal energy is dissipated to the divertor plates.

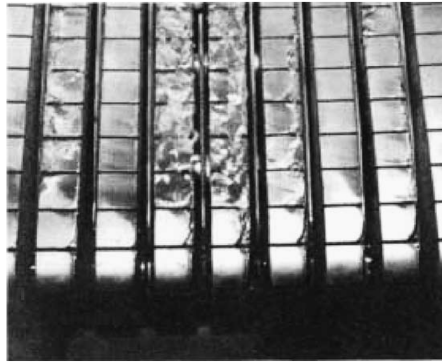


Figure 2.4.: photograph showing heavy melting of a section of the JET beryllium belt limiter following high power limiter experiments in the JET tokamak (Loarte 2005)

From the recent experiments in the JET tokamak (Arnoux 2009), it was observed that 50%-90% of the thermal energy is not flowing to the divertor plates even in the divertor configuration during the thermal quench. The majority of the thermal energy is dissipated as heat loads on the first wall. In addition to the energy dumped to the plasma facing components, some thermal energy is also dissipated through radiation. However, the radiated power is deposited more uniformly on the wall than the conducted power. Thus, the radiated power may be potentially less dangerous than the power conducted during the thermal quench. In the ITER tokamak, beryllium constitutes the tokamak first wall in which the onset of melting is around $15\text{MJm}^{-2}\text{s}^{-0.5}$ (Hender 2007). Thus, any localized impact of the heat loads on the wall may cause melting of the tokamak wall.

The JET beryllium belt limiters were designed to provide power flux density $\sim 3\text{MW/m}^2$ ($\phi_{damage}=0.29\text{MJm}^{-2}\text{s}^{-0.5}$ with $\tau=9.4$ ms (Hender 2007)) with peak power flux of $\sim 5\text{MW/m}^2$ ($\phi_{damage}=0.48\text{MJm}^{-2}\text{s}^{-0.5}$ with $\tau=9.4$ ms (Hender 2007)) (Deksnis 1997; Loarte 2005). During disruptions, the actual power handling capacities may be insufficient. Beryllium melting could be observed for even lower global energy deposition levels (Loarte 2005). This may be due to the local overheating of the tile edges with local power density $>100\text{MW/m}^2$ ($\phi_{damage} \sim \geq 9.7\text{MJm}^{-2}\text{s}^{-0.5}$ with $\tau=9.4$ ms (Hender 2007)) (Loarte 2005) may result in edge melting of the beryllium tiles as shown in the figure 2.4.

2.3.2. Electromagnetic loads

During the current quench phase of disruption, a major part of the magnetic energy is deposited as electromagnetic loads on the tokamak structures. There are three major classifications of this electromagnetic loads: induced eddy currents and halo currents.

2.3.2.1. Eddy currents

During the current quench, the decay of the plasma current and the plasma motion induces eddy currents in the tokamak structures including the first wall, vacuum vessel, divertors, coils, etc. The rate of plasma current decay influences the induced current.

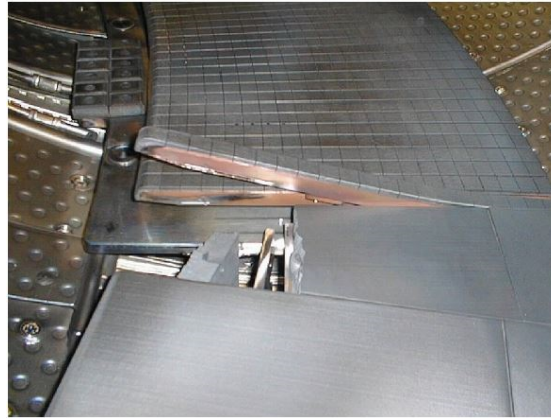


Figure 2.5.: photograph showing the damage to the limiter of the Tore Supra due to the eddy currents (Reux's PhD 2010)

Since the plasma is inductively coupled with the structures, the current flowing in the structure including plasma I_s can be estimated using the balance equation:

$$\mathbf{M} \cdot \frac{d}{dt} \mathbf{I}_s + \mathbf{R}_s \cdot \mathbf{I}_s = 0 \quad (2.9)$$

where \mathbf{I}_s is the matrix of currents flowing through the structure including the plasma and \mathbf{R}_s is the matrix of resistance of the structures including the plasma. The matrix \mathcal{M} is matrix of coefficients of mutual inductance of the structures including the plasma such that $\mathbf{M}_{s,s} = L_s$. The above balance equation 2.9 is an approximation in which the plasma motion is not considered. These induced currents may cause damage to the tokamak structures as they create Laplace forces as shown in the figure 2.5 for the Tore Supra tokamak.

2.3.2.2. Halo currents

For fusion performance, plasma shaping is one of the essential parameters. The energy confinement time τ_e increases with the elongation and thus increases the

fusion performance. However, the vertical instability is one of the main drawbacks of elongated plasmas.

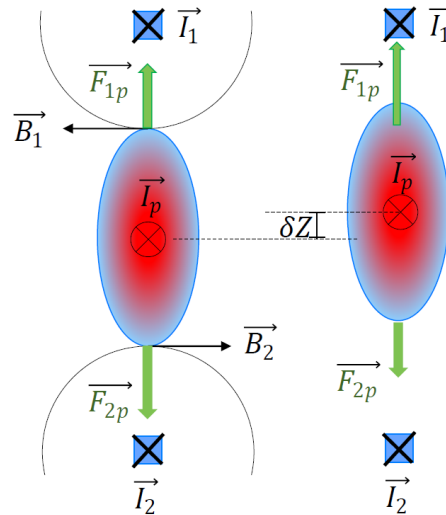


Figure 2.6.: illustration of the vertical plasma instability (Artola's PhD 2018)

The vertical instability of the plasma is illustrated in the figure 2.6. Using the poloidal field coils \vec{I}_1 and \vec{I}_2 , poloidal magnetic fields \vec{B}_1 and \vec{B}_2 are produced. As a result, the plasmas are elongated vertically using the forces \vec{F}_{1p} and \vec{F}_{2p} respectively as shown in the figure 2.6. For a plasma with vertical stationary position, the forces \vec{F}_{1p} and \vec{F}_{2p} balance each other.

The magnetic field is inversely proportional to the distance between the plasma and the coil. Thus, by giving a small vertical displacement δZ , the plasma is near to the coil \vec{I}_1 than the coil \vec{I}_2 and thus the force balance distorts as shown in the figure 2.6. As a result, the plasma is pulled closer to the coil \vec{I}_1 as the magnetic field gets stronger. This leads to exponential growth in the vertical position of the plasma. The loss of vertical position of the plasma in the tokamaks is called a Vertical Displacement Event (VDE).

Due to VDE, the loss of balance of the electromagnetic loads leads to a very fast vertical motion of the plasma. During VDE, currents are induced in the tokamak structures. This induced current in the structures oppose the VDE and thus stabilize on the resistive timescale of the structures. However, additional vertical control systems are normally used during the disruption experiments.

Nevertheless, the growth of this instability requires an initial vertical displacement δZ as shown in the figure 2.6. During disruptions, there can be two origins:

1. During the thermal quench phase of disruption, there is a fast drop in the beta β_p and internal inductance l_i which leads to a sudden inward shift of the current centroid. The field decay index (Yu 1994) n_{decay} at the center of the vessel cause the plasma to be more vertically unstable. As there is a rapid increase in κ , the plasma axis shifts to a region where n_{decay} is more negative than normal. The growth rate of $n=0$ mode is about an order of magnitude faster than the

penetration time for the horizontal magnetic field. Thus, the plasma continues to move upwards as observed in the Alcator C-Mod (Granetz 1996).

2. The vacuum chamber asymmetries may be responsible for the imbalance in the induced eddy current during current quench. As a result, plasma is attracted more in one direction than another. The presence of divertor may further enhance this asymmetry as seen in the ASDEX-Upgrade (Nakamura 2002).

In the context of a disruption, there are two kinds of VDE depending on whether they occur before or after the disruption. A VDE before disruption is called a "hot" VDE (i.e, when the plasma still has its thermal energy content). Failure of the control systems normally triggers the "hot" VDE, which in turn triggers disruption. A "cold" VDE occur after the thermal quench phase of the disruption and may deposit considerably less energy than a "hot" VDE.

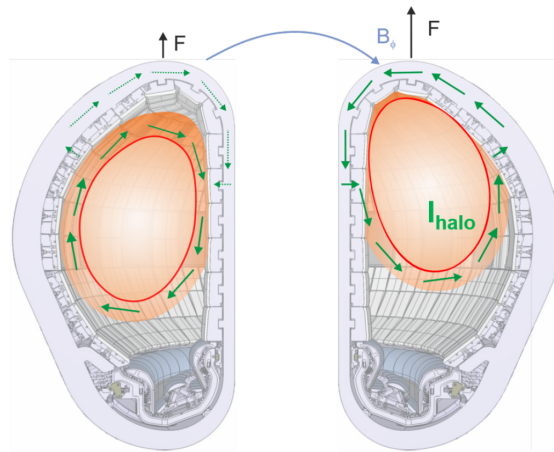


Figure 2.7.: illustration of the halo current in the tokamak (Artola's PhD 2018)

When the VDE is uncontrolled, the plasma moves vertically upwards to an extent that the plasma is in contact with the wall. Thus, plasma current flows through the wall and generates the so-called halo current as shown in the figure 2.7. Due to the halo current, a large Laplace force is produced on the vacuum vessel and in-vessel components. Thus, halo currents should be reduced and they may lead to the deformation of the vacuum vessel.

Due to the shrinkage of plasma during VDE, the edge safety factor can drop significantly and thus the plasma is subjected to additional MHD instability such as kink instability. This causes a 3D plasma deformation, toroidal localization of halo currents and the associated rotation of the toroidally asymmetric halo currents. The resonance between the rotation of the halo currents and the associated electromagnetic forces to the vessel with the mechanical Eigen modes of the machine are a particular area of concern (Schioler 2011). The physics of the 3D VDEs and the rotation during the VDE is not well established.

The system of Rogowski coils and shunts around the vacuum chamber can measure the halo currents. As they continue to follow the field lines, they have a toroidal and poloidal component. The halo current is characterized with the amount of current

entering the wall per toroidal radian and can be expressed as (Artola's PhD 2018),

$$I_{halo}(\phi) = \frac{1}{2} \int |J_n| dl \quad (2.10)$$

where J_n is the current density normal to the wall. The curvilinear integration in equation 2.10 is performed over poloidal wall length. A halo fraction is defined to characterize the amount of the halo current as (Artola's PhD 2018),

$$HF = \frac{\int I_{halo} d\phi}{I_p^{initial}} \quad (2.11)$$

where $I_p^{initial}$ is the initial value of the total toroidal plasma current. The toroidal peaking factor (TPF) is a characteristics of the amplitude of the toroidal asymmetry of the VDEs and can be defined as (Artola's PhD 2018),

$$TPF = \frac{\max(I_{halo})}{\int I_{halo} d\phi / 2\pi} \quad (2.12)$$

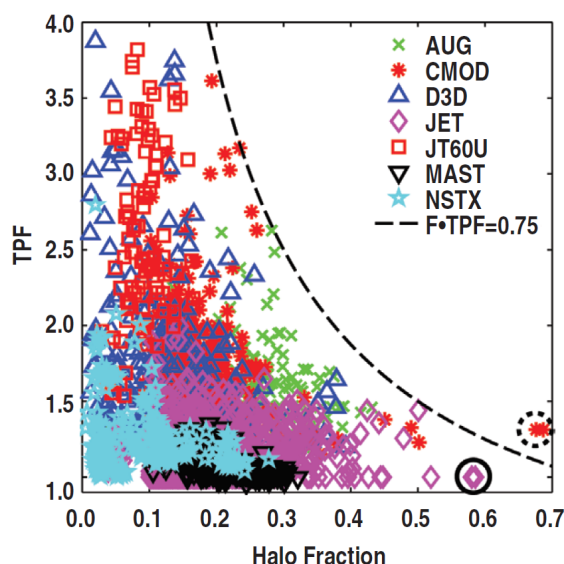


Figure 2.8.: TPF versus HF for different devices (Eidietis 2015)

The product of the halo current fraction and the toroidal peaking factor $HF_{\max} \times TPF$ indicates the maximum local poloidal halo current density as a function of the initial current $I_p^{initial}$. This factor is critical for the calculation of the maximum expected Laplace force in the in-vessel components. Thus, this factor is very important for engineering considerations of ITER as they determine the operational limit. The dependence of the toroidal peaking factor TPF with the halo current fraction HF is shown in the figure 2.8 from (Eidietis 2015) for different machines. The maximum $HF_{\max} \times TPF$ product is ~ 0.75 as shown in the figure 2.8. It was experimentally observed that the $HF_{\max} \times TPF$ decrease with the edge safety factor (Eidietis 2015).

2.4. Runaway Electrons

One of the main consequences of disruptions is the so-called Runaway Electron (RE) beam. A RE beam is a relativistic beam of energetic electrons with up to tens of MeV. The first postulation of RE was made by H.Dreicer in (Dreicer 1958). RE can cause severe damage to the PFCs when it is not controlled. In large tokamaks including ITER, the presence of high plasma current aggravate the RE formation, which concerns the robust and safe tokamak operation.



Figure 2.9.: melting of a beryllium tile in the JET tokamak due to runaway electrons.
Source:(EUROfusionc)

An instance of RE beam damage is the figure 2.9 in which melting of a beryllium tile in the JET tokamak is shown due to RE beam impact. In Tore Supra, the RE beam impact on the carbon limiter is shown in the figure 2.10.

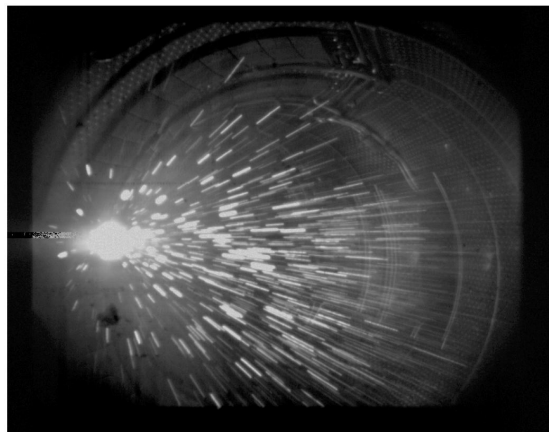


Figure 2.10.: impact of the RE beam on the carbon limiter in Tore Supra tokamak
(Reux's PhD 2010)

Due to vertical instability of the RE beam, the RE energy will be likely to be deposited on the upper or lower first-wall surface and divertor (Hender 2007). With a very small deposition area (estimated as 0.8m^{-2} (Hender 2007)), the energy flow is estimated between $15\text{-}65\text{MJ.m}^{-2}$ for a few milliseconds (Hender 2007). This is good enough to damage the PFCs. For instance, in the Tore Supra, RE interaction with the carbon tiles produced sparks as shown in the figure 2.10.



Figure 2.11.: damage to the signal cables down D-bottom port of the Alcator C-Mod tokamak due to RE beam (Granetz 2019)

The thermal loads during the thermal quench damages the surface of the PFCs. On the other hand, the RE beam can melt (or sublime if carbon) and penetrate the PFCs and deposit the energy to the whole volume of the materials. In the Alcator C-Mod tokamak, the RE beam damaged the signal cable below the bottom port as shown in the figure 2.11. In the WEST tokamak, high flux of the RE beam quenched one of the toroidal field coil as reported in (Torre 2019). Thus, it is very important to control and mitigate the RE beam.

In ITER, the RE beam may carry up to 70% of the plasma current (Hender 2007). Theoretical calculation predict that disruption of maximum plasma current ($I_p \sim 15$ MA) are likely to generate up to 10 MA of RE beam with relativistic energies of 10-20 MeV (Granetz 2014).

In this section, various physics processes that generate runaway electrons will be discussed.

2.4.1. Dreicer primary mechanism

In a tokamak, the toroidal electric field $E_{toroidal}$ accelerates the electrons and ions in the plasma. Due to their heavy mass, the acceleration of ions is very small as compared to the acceleration of the electrons. The Coulomb interaction of the electrons with other electrons and ions acts as a frictional drag force F_{drag} . When the force due to the electric field dominates the frictional force, the electrons are net accelerated. When the electrons are continuously accelerated, they no longer follow the Maxwellian velocity distribution of the thermal electrons. They runaway in phase-space and thus become runaway electrons.

The primary Dreicer mechanism is illustrated in the figure 2.12. The black solid line is the Chandrasekhar function corresponding to the drag force F_{drag} . The red horizontal line represents the corresponding accelerating field. The figure 2.12 is divided into three regions:

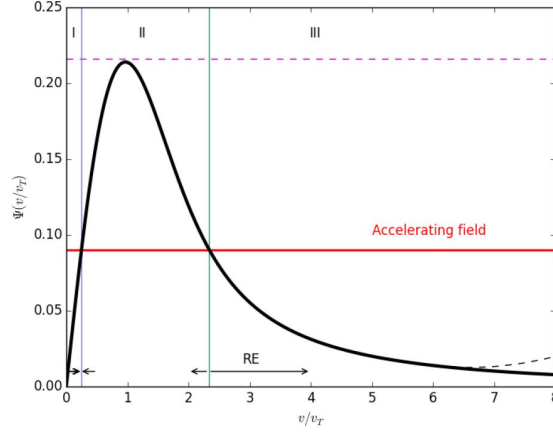


Figure 2.12.: illustration of the primary Dreicer mechanism using Chandrasekhar function $\Psi(v/v_T)$ (Ficker's Master 2015)

Region I : In this region, the accelerating electric field dominates the frictional drag force but the region is unstable.

Region II : In this region, the frictional drag force dominates over the accelerating electric field. Thus, the thermal electrons experience net deceleration in this region. The blue vertical line separating the regions I and II is a stable region at which the accelerating force balances the frictional drag force.

Region III : The accelerating field dominates the frictional drag force. As a result, the electrons are continuously accelerated and "runaway". The green vertical line separating the regions II and III is an unstable point at which the accelerating force balances the collisional drag force. The dashed raising tail of the function represents the increase in the drag force due to Synchrotron radiation. For a given electric field E , the accelerating electric force can be expressed as,

$$F_{acc} = -eE \quad (2.13)$$

whereas, the frictional drag force F_{drag} can be expressed as,

$$F_{drag} = -m_e \nu v_{coll}(v) \quad (2.14)$$

where m_e is the rest mass of an electron and v is the velocity of the electron. The term $\nu_{coll}(v)$ is the velocity dependent collisional frequency and can be expressed as,

$$\begin{aligned} \nu_{coll}(v) &= \frac{e^4 n_e \ln(\Lambda) (2 + Z_{eff})}{4\pi\epsilon_0^2 m_e^2 v^3} \\ \Rightarrow \nu_{coll}(v) &= \frac{3e^4 n_e \ln(\Lambda)}{4\pi\epsilon_0^2 m_e^2 v^3} \quad \text{assuming } Z_{eff}=1 \end{aligned} \quad (2.15)$$

where n_e is the electron density in the plasma, $\ln(\Lambda)$ is the Coulomb logarithm and Z_{eff} is the effective charge number of ions. Electron-electron collision is taken into consideration and hence the factor $(2 + Z_{eff})$. When the accelerating force balances the frictional drag force,

$$\begin{aligned}
F_{acc} &= F_{drag} \\
\Rightarrow -eE &= -\frac{3e^4 n_e \ln(\Lambda)}{4\pi\epsilon_0^2 m_e v^2}
\end{aligned} \tag{2.16}$$

Thus, the velocity at which $F_{acc} = F_{drag}$ is called as critical velocity v_c and it can be expressed as,

$$v_c = \sqrt{\frac{e^3 n_e \ln(\Lambda) (2 + Z_{eff})}{4\pi\epsilon_0^2 m_e E}} \tag{2.17}$$

For the electrons with $v \gg v_c$, the electric field acceleration dominates as shown in the region III of the figure 2.12. The horizontal dashed magenta line in the figure 2.12 shows the maximum of the Chandrasekhar function. The field corresponding to the maximum of the drag force is called Dreicer field, which can be expressed as,

$$E_D = \frac{n_e e^3 \ln(\Lambda)}{4\pi\epsilon_0^2 T_e} \tag{2.18}$$

Dreicer field is a very important quantity in the RE generation. It is taken as a benchmark to calculate whether an applied electric field can create RE for a given value of electron density. The most basic mechanism of RE generation is connected with the magnitude of Dreicer field. The rate of primary RE growth can be expressed as (Connor 1975),

$$\frac{dn_r^{primary}}{dt} \sim n_e v_{coll}(v) \epsilon^{\left(\frac{-3(1+Z_{eff})}{16}\right)} e^{\left(-\frac{1}{4\epsilon} - \sqrt{\frac{(1+Z_{eff})}{\epsilon}}\right)} \tag{2.19}$$

where $\epsilon = |E_{\parallel}|/E_D$. When $\epsilon \gtrsim 1$ with $v_c \gtrsim v_{Th}$, only the tail of the Maxwellian distribution runs away leading to exponentially small runaway production (Connor 1975). In (Connor 1975), the Fokker-Plank equation is solved including relativistic effects and ions with $Z \neq 1$. The critical electric field E_c for which electrons runaway is modified by relativistic effects and can be expressed as,

$$E_c = \frac{n_e e^3 \ln(\Lambda)}{4\pi\epsilon_0^2 m_e c^2} = \left(\frac{T_e}{m_e c^2}\right) E_D \tag{2.20}$$

A quasi-steady state RE distribution calculated using CODE (Collisional Distribution of Electrons) (Landreman 2014) is shown in the figure 2.13. Due to the temperature dependence of the Dreicer field in the equation 2.18, the primary RE growth rate depends on T_e , n_e and the field ratio $\epsilon = E/E_D$. Figure 2.13 shows the dependence of the primary RE growth rate with T_e and the field ratio E/E_c for $n_e = 5 \times 10^{19} \text{ m}^{-3}$ and $Z_{eff} = 1.5$ excluding the synchrotron radiation from the frictional drag force.

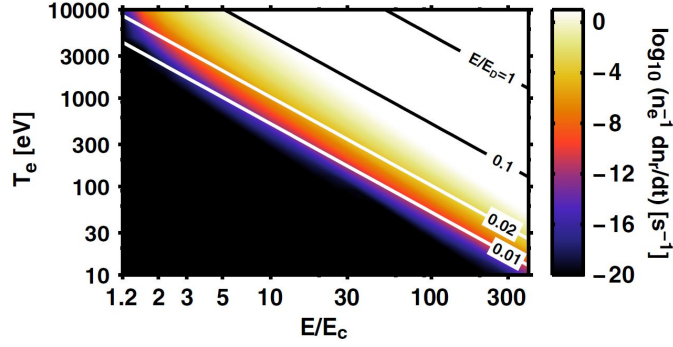


Figure 2.13.: primary RE growth given in equation 2.19 as a function of temperature and electric field without considering the effects of synchrotron. $n_e = 5 \times 10^{19} \text{ m}^{-3}$ and $Z_{eff} = 1.5$ were used. (Stahl 2015)

2.4.1.1. Effect of synchrotron radiation on E/E_c :

Synchrotron braking is important for the RE dynamics and is investigated in (Andersson 2001). The relative importance of the synchrotron effects is determined by the collisional frequency ν_{coll} (or collisional time $1/\nu_{coll}$) (Stahl 2015) and radiative time scale τ_r (Andersson 2001). For a given magnetic field B , the effect of synchrotron emission is given as,

$$\frac{1}{\nu_{coll}\tau_r} \sim \frac{T_e^{3/2} B^2}{n_e} \quad (2.21)$$

The synchrotron effect increases the frictional drag force F_{drag} force as shown in the figure 2.13 as dashed lines at higher ν/ν_c . Thus, synchrotron emission limit the maximum possible energy of RE beam and the primary RE growth rate is affected by it.

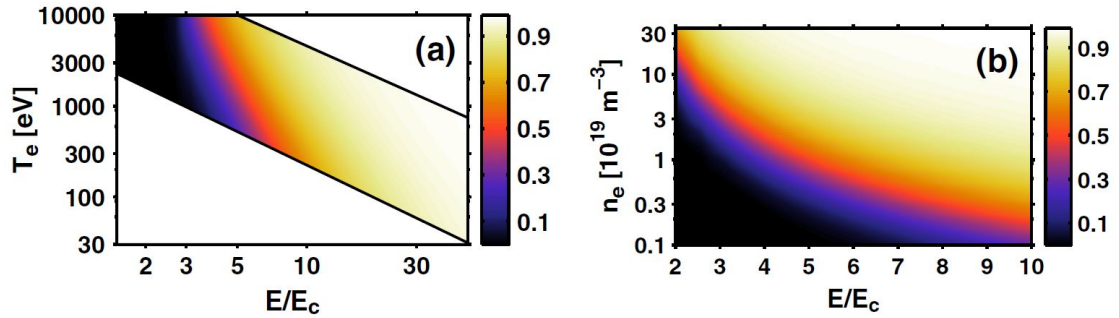


Figure 2.14.: contour plots showing the dependence of the primary RE growth rate with temperature (a) and density (b) in CODE. The Z-axis is the ratio of the primary RE growth rate with and without synchrotron effects included. The parameters used are $B = 4 \text{ T}$, $Z_{eff} = 1.5$, and (a) $n_e = 1 \times 10^{19} \text{ m}^{-3}$, (b) $T_e = 2 \text{ keV}$ (Stahl 2015)

Using CODE, the temperature and density dependence of the primary RE growth rate is shown in the figure 2.14. It is to be noted that the Z-axis in the figure is $d_t n_r^R = d_t n_r^{withsyn} / d_t n_r^{withoutsyn}$. From the figure 2.14, it can be seen that the synchrotron

effect during post-disruption tokamak plasma is negligible due to low T_e and high n_e . However, the synchrotron effects can be substantial when RE beam is formed during the ramp-up and flattop phase of the plasma current (Stahl 2015).

2.4.2. Hot-tail primary mechanism

The primary hot-tail mechanism of RE generation is different from Dreicer mechanism and is connected mainly with plasma disruptions. Primary RE generation due to hot-tail mechanism is caused by incomplete thermalization of the velocity distribution during rapid plasma cooling.

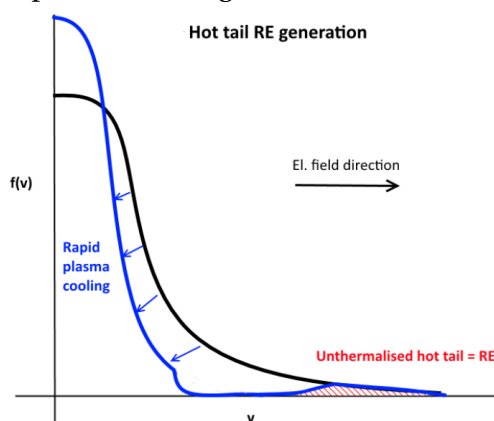


Figure 2.15.: illustration of the hot-tail mechanism (Ficker's Master 2015).

During the flattop phase, the electrons in the tokamak plasma are considered to be in Maxwellian velocity distribution as shown as the black line in the figure 2.15. During the thermal quench phase of disruption, the thermal plasma is rapidly cooled which is represented as the blue line. From the equation 2.15, it can be observed that $v_{coll} \propto v^{-3}$. As a result, the energetic particles in the tail of the initial Maxwellian need longer time to cool down than the low energy part. If the thermal quench rate is rapid as compared to the collisional frequency v_{coll} , the energetic part of the Maxwellian is unthermalised as shown in the figure 2.15. The unthermalised electrons are accelerated by the increasing toroidal electric field during the current quench. Thus, the unthermalised part of the Maxwellian are accelerated and generated as primary RE.

Since Dreicer field is inversely proportional to electron temperature $E_D \propto T_e^{-1}$ from equation 2.18, hot tail mechanism is the dominant mechanism. The number of RE generated due to hot-tail mechanism is estimated in (Smith 2008) by solving the kinetic equation for electrons without including the electric field,

$$\frac{\partial f}{\partial t} = \mathcal{C}(f) + S \quad (2.22)$$

where $\mathcal{C}(f)$ is the Fokker-Plank collision operator for electrons colliding with Maxwellian electrons and with population of new electrons originating from the

ionized impurity. The term S is an energy sink and particles source. In this estimation, a simplified model is assumed in which the temperature decrease exponentially during the thermal quench (Smith 2008),

$$T(t) = T_{final} + (T_{initial} - T_{final})e^{(-t/t_{initial})} \quad (2.23)$$

where $T_{initial}$ and T_{final} are the temperature before and after the thermal quench. The accumulated RE density due to hot-tail mechanism can be estimated from an approximate temperature decay (equation 2.23) using velocity moments of the kinetic equation (equation 2.22) as (Smith 2008),

$$n_r^{hot-tail} = \int_{v_c}^{\infty} f 4\pi(v^2 - v_c^2) dv \quad (2.24)$$

with $f = \frac{n_e}{\pi^3/2v_{Th}^3} \exp\left[-\left(\frac{v^3}{v_{Th}^3} + 3\tau\right)^{2/3}\right]$

Thus, RE density due to hot-tail mechanism can be expressed as (Smith 2008),

$$n_r^{hot-tail} = \frac{4n_e}{\sqrt{\pi}} \int_{u_c}^{\infty} \left[1 - \frac{(u_c^3 - 3\tau)^{2/3}}{(u^3 - 3\tau)^{2/3}}\right] e^{-u^2} u^2 du \quad (2.25)$$

where $u^3 = v^3/v_{Th}^3 + 3\tau$ and $u_c^3 = v_c^3/v_{Th}^3 + 3\tau$. $\tau(t)$ can be calculated by solving a first order ODE, which gives approximate result, $\tau(t) \approx (t - t_{exp})v_{coll}c^3/v_{Te}^3$.

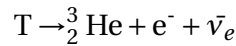
Different parameters are important for the efficiency of Dreicer and hot-tail mechanisms. For the JET tokamak, disruptions simulations in (Smith 2008) show that Dreicer mechanism dominates the primary RE generation for slower thermal quenches ($t_{TQ} \gtrsim 0.3$ ms) whereas for faster thermal quenches ($t_{TQ} \lesssim 0.3$ ms), hot-tail mechanism dominates. It was also observed that hot-tail mechanism has a much weaker dependence on T_{final} than the Dreicer mechanism. An increased post thermal quench density n_{final} reduces the efficiency of both Dreicer and hot-tail mechanisms, however, hot-tail generation dominated the Dreicer generation.

2.4.3. Other seeding mechanisms

In addition to Dreicer and hot-tail mechanisms, other mechanisms can contribute to RE seed although in smaller quantities:

2.4.3.1. Tritium β -decay:

Tritium has a half-life period of ~ 12 years (4500 ± 8 days). Tritium decays into helium-3 by β -decay process:



where $\bar{\nu}_e$ is the electron antineutrino. Thus, the product rate of β -electrons can be written as (Martin-Solis 2017),

$$\left[\frac{dn_\beta}{dt} \right]_T = \lambda_T n_T = \ln 2 \frac{n_T}{\tau_T} \quad (2.26)$$

where n_T is the tritium density and $\ln 2/\tau_T$ is the tritium disintegration rate constant. Only the β -electrons in the β -decay energy spectrum with an energy larger than RE critical energy E_c (corresponding to velocity v_c) will contribute to runaway seed. Thus, primary RE growth rate due to tritium β -decay can be estimated as (Martin-Solis 2017),

$$\left[\frac{dn_r}{dt} \right]_T = \ln 2 \frac{n_T}{\tau_T} F_\beta(E_c) \quad (2.27)$$

where $F_\beta(E_c)$ is the fraction of β -spectrum that would become runaway and can be represented as,

$$F_\beta(E_c) = \int_{E_c}^{E_{max}} f_\beta(E) dE \quad (2.28)$$

with $f_\beta(E)$ is the β -energy spectrum normalized to one. E_{max} for the β -electrons is ~ 18.6 keV which is comparable to T_e in tokamaks like ITER. Thus, RE seeding from tritium β -decay may significant for longer tokamak operations.

2.4.3.2. Compton scattering of γ -rays:

Other RE seeding mechanism could be the Compton scattering of the γ -rays. During the DT fusion reaction, almost 80% of the energy is carried by the neutrons. As neutrons cannot be confined by the magnetic field, they bombard the tokamak wall and thus activate it. In addition, uncontrolled RE beams may also contribute to the wall activation. As a result, γ -rays are emitted from the tokamak walls. The RE seeding rate associated with the Compton scattering of γ -rays can be expressed as (Martin-Solis 2017),

$$\left[\frac{dn_r}{dt} \right]_{compton} \approx n_e \int \Gamma_\gamma(E_\gamma) \sigma(E_\gamma) dE_\gamma \quad (2.29)$$

where $\Gamma_\gamma(E_\gamma)$ is the γ -energy flux spectrum, $\sigma(E_\gamma)$ is the Compton cross-section of photons of energy E_γ . In ITER, the total γ -flux for an H-mode discharge at 15 MA and 500 MW fusion power is evaluated to be $10^{18} \text{ m}^{-2} \text{ s}^{-1}$ (Martin-Solis 2017). Assuming $n_e^0 = 10^{20} \text{ m}^{-3}$, the RE seeding rate due to Compton scattering $\left[\frac{dn_r}{dt} \right]_{compton} \approx 10^{10} \text{ m}^{-3} \text{ s}^{-1}$ (Iida 2005). This population is significantly less as compared to other RE generation mechanisms.

2.4.4. Secondary avalanche mechanism

The seed of RE generated by the primary mechanism can be multiplied by the secondary mechanism called "avalanche" mechanism. In big tokamaks like ITER, it is one of the most important way of RE production. This mechanism was first discovered by Sokolov (Sokolov 1979). In (Rosenbluth 1997), the secondary mechanism of RE generation is explained in detail.

Seed runaway electrons on collision with thermal electrons can produce supra-thermal electrons (with $v \gg v_{th}$) and another runaway electron (with $v \gg v_c$). Similar to the primary generation mechanism, the seed runaway electron produces supra-thermal electrons and nascent runaway electrons are accelerated by the electric field. As a result, there is an exponential growth of RE population. This cascading effect of RE growth is called the "avalanche" mechanism. This mechanism is called a secondary generation because it requires RE seed to amplify them.

In (Jayakumar 1993), massive RE formations were predicted due to secondary mechanism (amplification factor e^{50}). This is because the avalanche phenomenon was dealt with a non-relativistic framework without the effect of pitch angle scattering. In addition, no threshold for the electric field was considered in (Jayakumar 1993).

In (Rosenbluth 1997), the growth rate due to the secondary mechanism is obtained from the analytical solution of Fokker-Plank gyro kinetic relativistic equation averaged over a particle bounce period as,

$$\left[\frac{dn_r}{dt} \right]_{sec} = \frac{n_r}{\tau \ln(\Lambda)} \sqrt{\frac{\pi \Gamma}{3(Z_{eff} + 5)}} \left(\frac{E}{E_c} - 1 \right) \times \left(1 - \frac{E_c}{E} + \frac{4\pi(Z_{eff} + 1)^2}{3\Gamma(Z_{eff} + 5)(E^2/E_c^2 + 4/\Gamma^2 - 1)} \right)^{-1/2} \quad (2.30)$$

where $\Gamma = [1 - 1.46\sqrt{a/R} + 1.72(a/R)]^{-1}$ with a and R being the minor and major radius of the tokamak with $\tau = m_e c / e E_c$. The equation 2.30 is the "worst case" scenario in which no loss of RE is considered and the energy is not limited.

For $E \gg E_c$, the number of e-folding of the runaway current I_{RE} due to avalanche mechanism, N , is proportional to the initial plasma current I_p , $N \approx 2.5 \times I_p$ (IPB 1999). In small and medium sized tokamaks, avalanche multiplication of the runaway electrons may not be significant. However, in tokamaks like ITER with high plasma current (up to 15 MA), secondary avalanche mechanism is very important and they are a point for concern.

2.5. Disruption Mitigation Systems

The damages made by disruptions are seen in the section 2.3. Thus, mitigation of disruptions and their consequences are vital for reliable tokamak operations. A disruption mitigation system (DMS) has to fulfill three main aims: mitigation of heat loads during thermal quench, mitigation of electromagnetic loads like eddy and halo currents and the mitigation of the runaway electron (RE) beam.

In addition to the efforts taken to avoid the disruption, one of the most successful approaches to mitigate an unavoidable disruption is by massive material injection (MMI) of high-Z species. The injected materials influence the evolution of the disruption since it increases the density and cools the plasma down by dilution and radiation before the thermal quench occurs. It is important to note that MMI trig-

gers disruptions. However, these "controlled" disruptions are less violent than the unintended disruptions. There are two main techniques tested in tokamak to inject the massive materials: massive gas injection (MGI) and shattered pellet injection (SPI). Usually noble gases such as helium, neon and argon are used due to their low chemical reactivity with the fusion fuel and the wall materials.

2.5.1. Massive gas injection (MGI)

In the initial stages of DMS, standard valves were used to deliver high Z gases. Faster valves were then developed to deliver high-Z gases to the plasma, at approximately the sound of speed. MGI is one of the most explored technique for the MMI so far. It is implemented in many tokamaks around the world: Alcator C-mod ([Whyte 2007](#)), DIII-D ([Hollmann 2008](#)), ASDEX-U ([Pautasso 2009](#)), Tore Supra ([Reux 2010](#)), JET ([Kruezi 2009](#)), JT60-U ([Bakhtiari 2005b](#)), MAST ([Thornton 2011](#)) and TEXTOR ([Bozhenkov 2008](#)).

2.5.2. Shattered pellet injection (SPI)

Historically, disruption mitigation experiments were performed using a frozen pellet of high-Z gases. However, the idea was not feasible due to the low assimilation of the materials in the plasma. To overcome this drawback, a new concept called Shattered Pellet Injection (SPI) was developed ([Baylor 2019](#)).

In the SPI system, the cryogenic pellet is shot from a pipe gun. Just before the pellet reaches the plasma, it is shattered into numerous small fragments using two metal plate targets or a bent tube. Shattering the pellet increases the pellet surface area and generates a gas/liquid spray to increase the ablation rate. As a result, shattering the pellet increases the assimilation efficiency of the materials in the plasma. As compared to MGI, SPI systems deposit the materials deeper into plasma. Thus, SPI are theoretically more efficient in dissipating the RE beam.

DIII-D is the first tokamak to achieve fast plasma shutdowns using SPI system ([Commaux 2010](#)). In JET tokamak, SPI system was commissioned ([ITERa](#)). The JET SPI experiments will be discussed in detail later in this thesis. In addition to DIII-D and JET, K-STAR ([Park 2020](#)) and J-TEXT ([Li 2018](#)) tokamaks have SPI system capabilities. For the ITER tokamak, SPI is the disruption mitigation system ([Baylor 2010](#)).

2.5.3. DMS systems of the various tokamaks

2.5.3.1. ASDEX-Upgrade

The parameters of the ASDEX Upgrade tokamak is given in the table [2.1](#). The position of the EM valves and the in-vessel valve is shown in the figure [2.16](#). In the ASDEX Upgrade tokamak there are two types of fast valves to deliver MGI ([Pautasso 2009](#)):

1. Two electromagnetic (EM) valves located 1.5 m from the plasma in the outside of the vessel. It is in operation since 2004.
2. One piezo-released valve installed in 2007 without iron parts in the torus 10 cm from the plasma. This is called in-vessel valve.

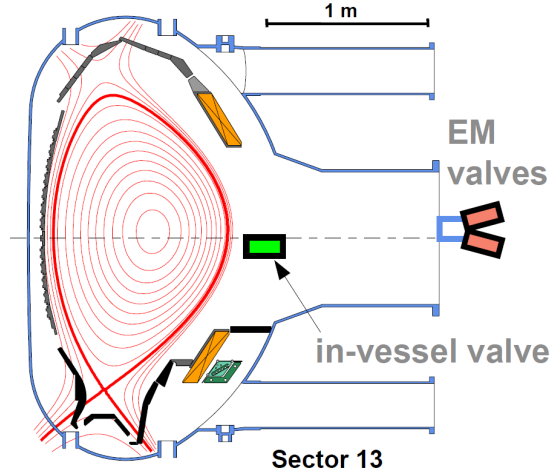


Figure 2.16.: illustration of poloidal position of the MGI valves in the ASDEX-Upgrade tokamak (Pautasso 2008)

Both valves open within 1 ms. The two EM valves have reservoir volume of 0.032l (32 cm³). For the in-vessel valve, the reservoir volume is 0.08l (80 cm³). For the in-vessel valve, the reservoir volume has been operated at 0.04l (40 cm³) for some experiments. For the mitigation of thermal loads and electromagnetic forces, one EM valve is routinely used with a gas pressure of 10 bar. With the in-vessel valve, up to 3.3 bar.l of helium, neon, argon and mixtures neon and argon with deuterium are used.

Parameter		Value
Major radius	R	1.6 m
Minor radius	$a_{horizontal}$	0.5 m
	$a_{vertical}$	0.8 m
Plasma current (max)	I_p	2 MA
Toroidal field	B_T	3.9 T
Heating	P_{NBI}	20 MW
	P_{HF}	6 MW
	$P_{microwave}$	8 MW
Plasma volume	V_{plasma}	13 m ³
Duration	t	up to 10 s

Table 2.1.: parameters of the ASDEX-Upgrade tokamak (IPP-MPGa)

A disruption mitigation experiment in ASDEX-Upgrade tokamak is shown in the figure 2.17 where the discharge is disrupted using 0.73 bar.l of helium. For the in-vessel valve, the flight time of the helium gas can be considered negligibly small due to the proximity of the valve to the plasma. It can be seen that after the introduction of the helium gas, the density increase followed by the thermal and current quench. As a result, the plasma is disrupted within a few ms.

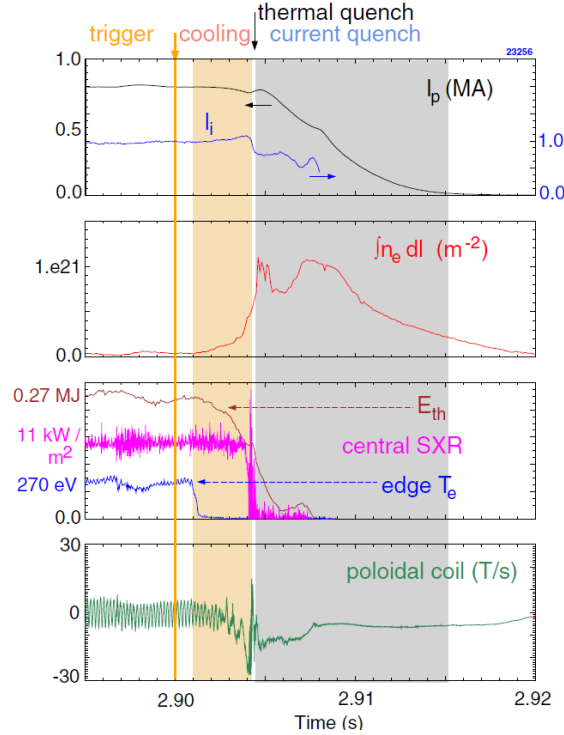


Figure 2.17.: Cooling, thermal and current quench phases after the injection of 0.73 bar.l of helium with in-vessel valve in the ASDEX-Upgrade tokamak (Pautasso 2009). Time traces of the following plasma parameters are shown: plasma current (I_p), internal inductance (l_i), line integrated density from the CO₂ interferometer ($\int n_e dl$), thermal energy from equilibrium reconstruction (E_{th}), central SXR channel from a vertical array, edge electron temperature (T_e) from Electron Cyclotron Emission (ECE), time derivative of the poloidal flux measured by a Mirnov coil (Pautasso 2009).

Through thermographic measurements of the divertor load plates, it was observed that the plasma thermal is not conducted along the SOL to the divertor plates, as in the case of natural disruptions. Through the foil bolometry, it was measured that a total radiated power between 60% and more than 100% of the total (thermal plus magnetic) plasma energy. Through AXUV diagnostics at different toroidal positions, toroidal asymmetry in the radiated power was observed. However, the radiated energy has lower degree (0%-30%) of toroidal asymmetry than the radiated power (Pautasso 2009).

The mitigation of heat loads and EM forces was found to be effective even for moderate injection of 2×10^{22} particles. Higher amount injections did not lead to any significant reduction of the divertor heat loads and were usually aimed at the suppression of REs.

In the ASDEX-Upgrade tokamak, neon was found to have advantage over other noble gases in the mitigation of disruptions. The ratio between the effective electron density and the critical electron density to suppress the RE beam, $n_{e,eff}/n_c \sim 24\%$ by injecting $330 \text{ Pa}\cdot\text{m}^3$ of Ne (Pautasso 2009). The divertor heat loads and the vertical forces seems to decrease more than 50% with respect to unmitigated disruptions by a tolerable amount of neon ($18 \text{ Pa}\cdot\text{m}^3$), which raised the line integrated electron density of $\Delta n_e \sim 10^{20} \text{ m}^{-3}$. The forces were found to be reduced further for density higher than $n_e \sim 5 \times 10^{20} \text{ m}^{-3}$.

ASDEX Upgrade RE mitigation experiments: For the RE mitigation experiments, the toroidal field is kept at $B_T=2.5 \text{ T}$ and the plasma current is $I_p=800 \text{ kA}$. Circular, ohmic, inner-wall limited and L-mode discharges are used. 2-2.5 MW of electron cyclotron resonant heating (ECRH) heating was applied for 100 ms before the first injection (Papp 2016). From the in-vessel valve, 0.05-0.2 bar.l (corresponding to $1.2\text{-}4.8 \times 10^{21}$ particles, $\sim 14.5 \times$ the plasma inventory) of argon gas is injected from the low field side (LFS). The trigger is pre-set 1 s after the start of the discharge, at the end of the ramp-up. The argon MGI produces the controlled disruption with thermal quench time $t_{TQ} < 1 \text{ ms}$. 100-400 kA of initial RE current I_{RE} are generated.

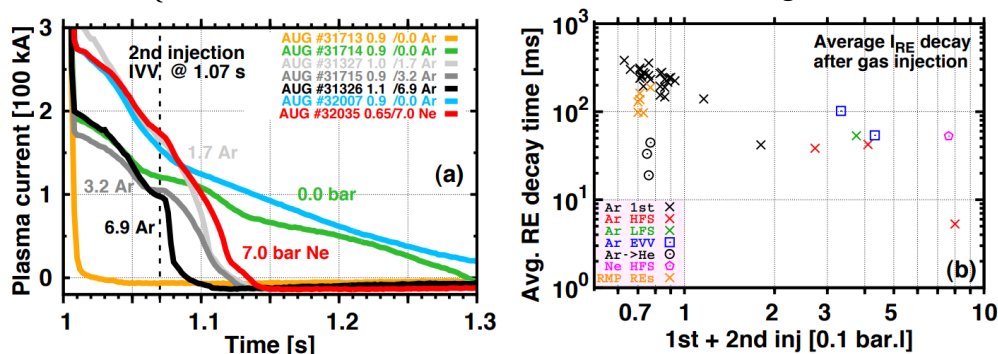


Figure 2.18.: (a) Runaway current evolution following argon or neon killer MGI (at 1.07 s) into an already formed RE beam. (b) Average RE decay time as a function of injected gas quantity (Papp 2016).

As shown in the figure 2.18(a), a second MGI was injected with various amounts of argon or neon from different geometrical positions, 70 ms after the first injection at $t=1.07 \text{ s}$. When 0.17 bar.l of argon or 0.7 bar.l are injected as the second injection from the in-vessel valve, suppression of the REs was achieved as shown in the figure 2.18(a). The geometrical position of the valves are insignificant to the results as the argon injection from low and high field sides (LFS and HFS) lead to similar results. RE suppression was also possible using the EM valves, but almost twice the amount of gas is required to do so as compared to the in-vessel valves.

In the figure 2.18(b), average decay time of the RE beam is plotted against the total injection amount. It can be seen that with only one argon injection and no killer injection to mitigate the RE beam (black crosses), RE beam is sustained for several 100ms. By injecting the second killer argon injection from in-vessel valve in the HFS/LFS, the RE beam duration was considerably reduced to few ms as shown as the red/green crosses in the figure 2.18(b). When argon is injected in to the helium plasma (circles), RE beam duration is reduced significantly for the similar quantity of the argon. As compared to argon, neon require more gas injection amount to suppress RE beam.

2.5.3.2. DIII-D

The parameters of the DIII-D tokamak is given in the table 2.2. The MGI system in DIII-D (Hollmann 2008) is a 'medusa' valve configuration (2007) in which six valves fire simultaneously. This configuration deliver about $133 \text{ Pa}\cdot\text{m}^3$ of argon gas ($\sim 3 \times 10^{22}$ particles) in about 3 ms. The drift tube is about 1.3 m. The distance between the tube end and the plasma edge is of order 20 cm.

Parameter		Value
Major radius	R	1.66 m
Minor radius	a	0.67 m
Plasma current (max)	I_p	2 MA
Toroidal field	B_T	2.2 T
Heating	P_{NBI}	16 MW
	P_{ICRH}	6 MW
	P_{ECRH}	4 MW
Plasma volume	V_{plasma}	$\sim 15 \text{ m}^3$

Table 2.2.: parameters of the DIII-D tokamak (Luxon 2002)

DIII-D is the first tokamak to employ SPI systems to mitigate the disruption loads and the RE beam (Commaux 2010). For the deuterium SPI, pellets are injected with a speed range $500\text{-}600 \text{ ms}^{-1}$. The pellet mass range is $1.6\text{-}2.6 \times 10^{23}$ atoms for deuterium as measured with a microwave cavity at the barrel exit. In another set of experiments, a small argon pellet (with diameter $D=2.7 \text{ mm}$, 7 Torr^{-1} corresponding to 2.3×10^{20} argon atoms) with $v \approx 5500 \text{ ms}^{-1}$ are used for the disruption and RE mitigation (Hollmann 2013). The toroidal and poloidal location of the MGI valve and SPI pellet are shown in the figure 2.19.

The evolution of the RE beam following different MMI : 100% deuterium SPI, 100% deuterium MGI, 92% neon + 8% deuterium SPI and 100% neon MGI are shown in the figure 2.20. Following the neon SPI and MGI, the RE current dissipates as shown

in the figure 2.20. The loop voltage and density increases rapidly. MGI and SPI are comparable as the pellets were ablated at the edge. In the DIII-tokamak tokamak, RE dissipation was achieved through argon and neon MGI and SPI (Shiraki 2018).

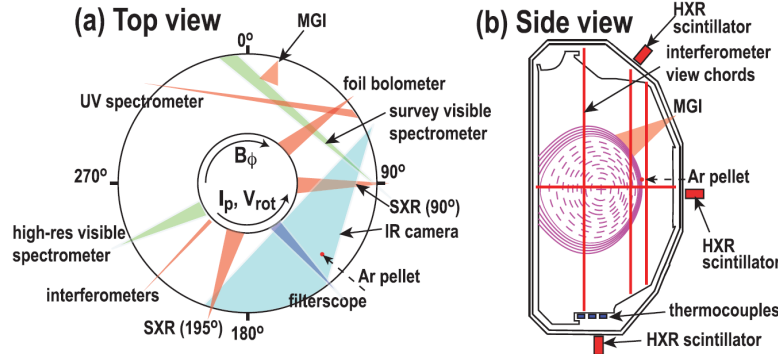


Figure 2.19.: Top (a) and side (b) view of MGI and SPI systems and other essential diagnostics in the DIII-D tokamak (Hollmann 2020)

One curious case in the figure 2.20 is the injection of the deuterium MGI and SPI into the plasma. Following the deuterium MMI, the plasma current increases whereas the electron density drops to very low values. The loop voltage and the hard X-ray (HXR) signals drops suggesting that RE generation and losses are lowered post deuterium injections. This case was also observed in the JET tokamak and will be discussed in chapter 5.

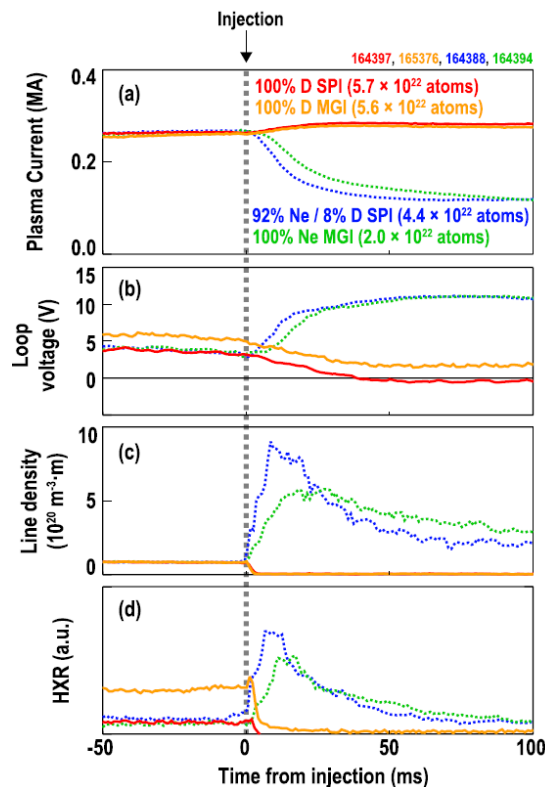


Figure 2.20.: evolution of RE beam following deuterium SPI and MGI, neon MGI and 92%neon+8%deuterium SPI (Shiraki 2018)

2.5.3.3. JET

In the JET tokamak, massive gas injection (MGI) are injected using three Disruption Mitigation Valve (DMVs). The toroidal locations of the DMV and their characteristics are shown in the figure 2.21 and table 2.3 respectively. More information about the valves can be found in the reference (Kruezi 2009) and (Kruezi 2014). Due to the short tube length and largest valve opening, DMV3 is the fastest valve to inject gases. High Z-gases such as helium, neon, argon, krypton and xenon are used. In addition, pure deuterium and mixture of deuterium with other gases can also be injected through DMVs.

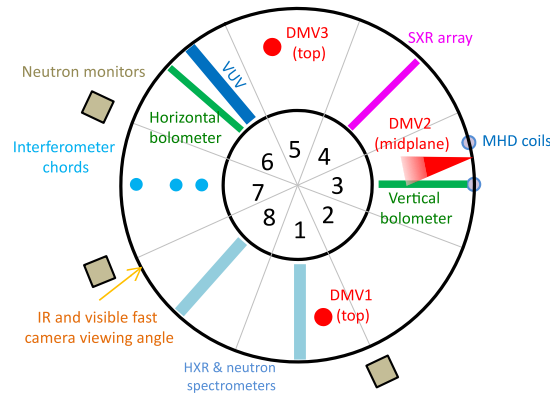


Figure 2.21.: Top view of the various diagnostics and DMV ports in the JET tokamak (Sridhar 2020)

DMV	Volume	Max. D ₂ amount	Tube length
1	0.65l	1 kPa.m ³	4.06 m (slow)
2	0.975l	5 kPa.m ³	2.36 m (fast)
3	0.35l	1.7 kPa.m ³	1.9 m (fastest)

Table 2.3.: Characteristics of DMVs in the JET tokamak from (Kruezi 2009) and (Kruezi 2014)

During 2018, the commissioning of Shattered Pellet Injection (SPI) commenced in the JET tokamak replacing DMV1. SPI for JET is based on the design for DIII-D tokamak. In the JET SPI system, there are three barrels (A, B and C) which produce three pellets of different sizes. The size information of the pellets are given in the table 2.4. SPI system in JET can deliver frozen pellets of argon, neon and deuterium of different quantities (table 2.5) in addition to pellets mixed with D₂. Using a mechanical punch, pellet speed is $\sim 100\text{-}250\text{ ms}^{-1}$ (Baylor 2017). The pellets can be fired independently with flight time $\sim 20\text{-}50\text{ ms}$ (Baylor 2017). Using a microwave cavity diagnostics, the pellet mass, velocity and the pellet integrity can be estimated. The end of the injection tube is bent 20 degree to shatter the pellet. The tube geometry has good collimation

and the shattered fragments are too small to damage PFCs but large enough for good penetration.

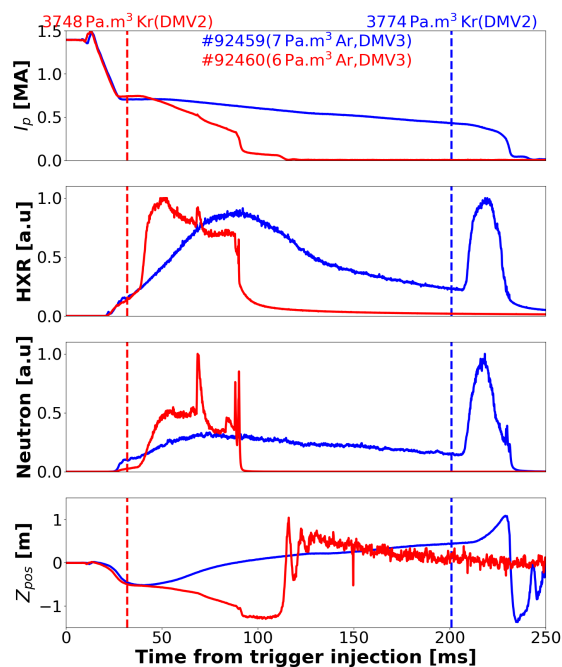


Figure 2.22.: Time traces of plasma current I_p , hard x-rays (HXR) and neutron monitors of the discharges #92459 and #92460 showing successful mitigation of the RE beam using 3774 Pa.m^3 and 3748 Pa.m^3 krypton injections from DMV2 respectively. The RE beam is triggered using $6\text{-}7 \text{ Pa.m}^3$ of argon from DMV3 in both the discharges.

Barrel	Pellet		Shell	
	D [mm]	V [mm ³]	Thickness [mm]	V [mm ³]
SPI A	12.5	2209	0.5	489
SPI B	8.1	626	0.5	204
SPI C	4.57	97.5	0.3	33.5

Table 2.4.: Size and volume of different SPI pellet sizes in the JET tokamak

RE mitigation experiments in the JET tokamak using massive gas injection (MGI) is extensively reported in (Reux 2017) and (Reux 2015). An example of RE mitigation experiments in the JET tokamak are shown in the figure 2.22 for the JET-ILW discharges #92459 and #92460. Using $\sim 6\text{-}7 \text{ Pa.m}^3$ argon from DMV3, disruption and thus the RE beams are triggered. RE beam is usually monitored using the hard X-ray (HXR) and neutron diagnostics. HXR and neutrons are produced due to the interaction of the RE beam with the high-Z gases and the wall materials. In both discharges #92459 and #92460, the dynamics of the RE beam was altered using $\sim 3774 \text{ Pa.m}^3$ of krypton

from DMV2 at different times. After the entry of the krypton killer injection, HXR and neutron rises rapidly thereby suggesting interaction of the killer injection with the RE beam. As a result, the RE beams are terminated which is given by the decay of plasma current.

Barrel	Pellet Content [$\times 10^{22}$ atoms]			Shell Content [$\times 10^{22}$ atoms]
	Ar	Ne	D ₂	D ₂
SPI A	5.4	9.49	13.3	2.94
SPI B	1.53	2.69	3.77	1.23
SPI C	0.238	0.419	0.587	0.202

Table 2.5.: Material contents different SPI pellet sizes in the JET tokamak as designed

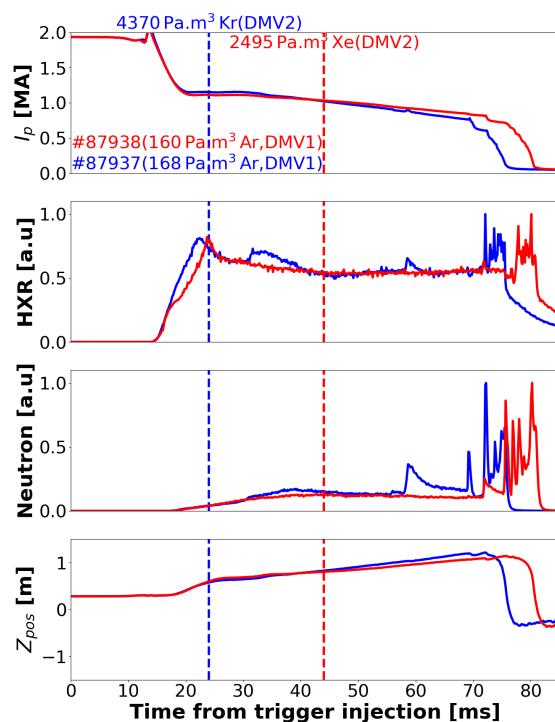


Figure 2.23.: Time traces of plasma current I_p , hard x-rays (HXR) and neutron monitors of the discharges #87937 and #87938 showing unsuccessful mitigation of the RE beam. The RE beam is triggered using $\sim 160 \text{ Pa.m}^3$ of argon from DMV1 in both the discharges.

Unlike ASDEX-Upgrade (section 2.5.3.1) and DIII-D (section 2.5.3.2) tokamaks, no apparent effect of the second killer injection on the RE beam was observed in some circumstances in the JET-ILW experiments (Reux 2017). An example of such unsuccessful RE mitigation is shown in the figure 2.23 for the JET-ILW discharges #87937 and #87938. In spite of injecting high-Z gases like krypton and xenon, there is

no effect of the killer injection on the RE beam as seen from the HXR and neutron data. The final termination of the beam in those discharges are mainly due to the upward movement (Z_{pos}) of the RE beam.

Initially, geometry effect of the gas plumes were considered as one of the hypothesis for this unsuccessful mitigation. It was observed in (Reux 2017) no effect of killer injection from DMV2 and DMV3 on HXR and neutrons and no soft landing of the RE beam. Thus, gas plume geometry was not responsible for the poor efficiency of the killer injections.

With respect to ASDEX-Upgrade and DIII-D, RE beams of JET tokamak have higher RE currents. On reducing the RE current by reducing the pre-disruptive plasma current, RE population seems to have lower energies but no easier penetration of the killer gas was observed (Reux 2017). Thus, efficiency of the killer injections were found to be not related to the current and energy of the RE beam.

It was also observed in (Reux 2017) that after the thermal quench phase of disruption, the impurities of the trigger injection (like argon) forms a **cold dense background plasma** which co-exists with the RE beam. The presence of cold background plasma was speculated to shield the penetration of the killer injection neutrals in to the RE beam and thus reducing its mitigation efficiency.

In 2019, RE mitigation experiments were performed in the JET experiments using SPI. In this PhD thesis, the experiments will be analyzed quantitatively.

2.5.3.4. ITER

For the ITER tokamak, SPI is is the technology that will be used for the ITER DMS. The strategy for the DMS is as follows :

1. Mitigation of thermal loads and EM forces using a SPI injection. Avoidance of RE beam generation.
2. If RE generation cannot be avoided, mitigation of the developed RE beam using a second SPI.

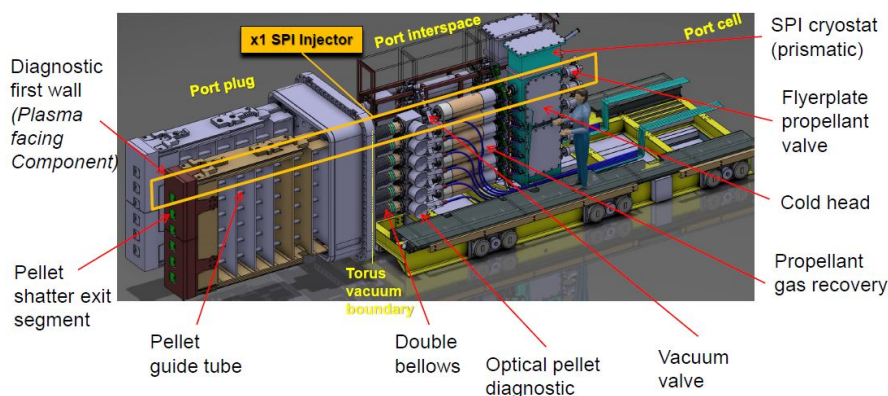


Figure 2.24.: Schematics of the ITER SPI injector DMS (Lehnen 2019 ITPA)

The schematics of a SPI DMS system is shown in the figure 2.24. There are 3 flight

tubes in three upper ports and 24 flight tubes in three equatorial ports as shown in the figure 2.25 for the SPI. Each pellet is around 28.5 mm in diameter and length 57 mm. Each flight tube has a diameter of 60 mm with a shatter bend at the end.

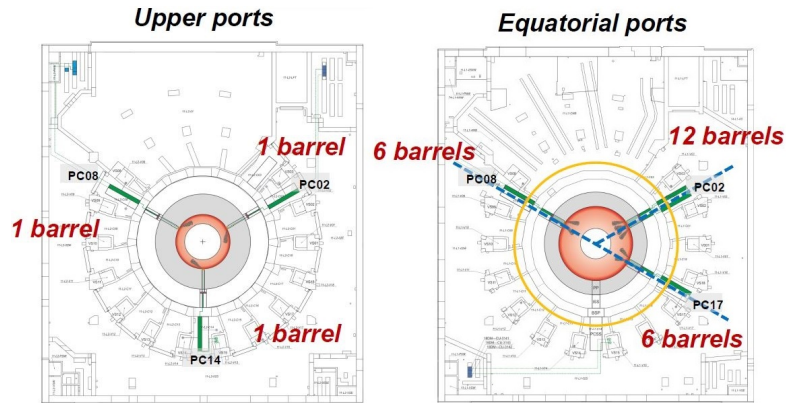


Figure 2.25.: Upper and Equatorial ports of the Shattered Pellet Injection (SPI) systems in ITER (Lehnen 2019 ITPA)

Quantity	Species	Purpose	# of pellets
6×10^{24}	D	RE avoidance	3
$\sim 10^{25}$	Ar	RE energy dissipation	3
5×10^{21}	Ne	EM loads	Mixed into D pellets
		CQ heat loads	
4×10^{22}		TQ heat loads	

Table 2.6.: SPI requirements for disruption mitigation in ITER based on present knowledge (Lehnen 2019 ITPA). 100% assimilation of the pellets assumed.

Based on the present knowledge, required assimilated quantities is tabulated in the table 2.6, assuming a 100% assimilation. For the RE avoidance, a minimum of three pellets would be required. RE energy dissipation could be achieved with at least three argon pellets. For the thermal and EM loads, neon pellets could be used by mixing into deuterium pellets. It is to be noted the data in the table 2.6 are estimates based on the present knowledge and the design may subject to change.

	Mass m (g)	Velocity v ms^{-1}	flight time Δt_{flight} (ms)
argon	60	~ 200	32
deuterium	7	~ 600	11
hydrogen	3.5	~ 800	8

Table 2.7.: flight times for different pellets (Lehnen 2019 ITPA)

The flight time Δt_{flight} of the pellets differ based on the pellet materials used are shown in the table 2.7. Since the precursors of disruption appear very close to the thermal quench (see section 2.2), it is important to deliver the SPI as quickly as possible to the plasma after the trigger. Mechanical punches have been used with the SPI system in the JET tokamak (Baylor 2017) to deliver high-Z species such as Ar. According to the current design, similar mechanical punches will be used in ITER DMS.

For a successful DMS in ITER, there are many open questions to be answered. The effect of multiple SPI injections will be tested in the DIII-D tokamak and the KSTAR tokamak (Park 2020). In ASDEX Upgrade tokamak, SPI system is in preparation to support DMS research for ITER tokamak (Lehnen 2019 ITPA). Since JET provides the closest extrapolation for ITER DMS, the size and energy scaling of the SPI could be studied using different pellet sizes. Thus, JET experiments is of particular interest as it may substantially change the design of ITER DMS. In this PhD thesis, a preliminary analysis on the first set of JET SPI experiments is addressed.

2.6. Scope of this thesis

Among the consequence of the disruptions, runaway electrons are very difficult to deal with. For the future large and reactor-scale devices, including ITER, higher plasma current are needed to increase the confinement and reach the performances compatible with energy production. Since the amplification of the runaway seed population grows exponentially with the plasma current, the RE beam may cause severe damage to in-vessel components, posing a major threat to robust operation. The control and mitigation of the runaway electron is still a field of development.

The present strategy for RE mitigation is to first mitigate the heat and EM loads using a massive material injection (MMI) and possibly avoid RE generation. If the RE generation cannot be avoided, a second MMI will be used to mitigate the RE beam. In ITER DMS, shattered pellet injection (SPI) is chosen over massive gas injection (MGI) as the MMI technology to mitigate disruption heat loads and runaway electrons.

In small tokamaks such as DIII-D, both MGI and SPI was found to be successful in mitigating the runaway electrons unconditionally. Additionally, no significant difference between SPI and MGI was observed as SPI tends to ablate in the edge of the plasma. In ASDEX-Upgrade, MGI of high-Z impurities was successful in mitigating the RE beam.

However, in JET, no apparent effect of the mitigation injection on the RE beam was observed for some discharges. The presence of cold background plasma of high-Z impurities may be reason for inefficiency of the mitigation injection for some discharges. Since JET is currently the world's biggest tokamak and provides the closest extrapolation towards future tokamaks including ITER, conditional mitigation of the RE beam is a wake-up call to understand the physics of RE mitigation, particularly in large tokamaks. For a reliable RE mitigation system, it is important to understand the

physics behind the interaction of killer injection with the RE beam in the presence of cold background plasma.

The physics of interaction between the mitigation injection, RE beam and the cold background plasma may depend significantly on the characteristics of the cold background plasma. However, the characterisation of the background plasma is non-trivial as T_e measurement are out of range for conventional diagnostics during the RE beam after disruptions. Thus, a method to estimate the temperature of the background plasmas is developed during this PhD thesis. In the chapter 3, the methodology of temperature and the background plasmas of JET discharges are analyzed. In addition, the VUV spectra and the background plasmas of the MGI and SPI discharges are studied both qualitatively and quantitatively.

Using the characterization of the background plasma, a 0D/1D power balance of the systems of the post-disruption plasmas (RE beam and background plasma) is proposed and are discussed in great detail in the chapter 4.

Chapter 5 deals with the modeling of the background plasma using a 1D diffusion transport model. After performing a sensitivity analysis of the model, the background plasmas are simulated using this model. The results are discussed extensively.

Chapter 5 is dedicated to summarize the results and give perspectives and hint to what could be further developed using the analysis performed in this PhD thesis.

3. Characterization of the Cold Background Plasma

As discussed in the chapter 2, RE beams should be mitigated for the reliable and safe operation of the tokamak, especially for the plasma facing components (PFCs). The present RE mitigation strategy is to first mitigate heat and EM loads and possibly avoid RE beam generation using a massive material injection (MMI). The impurities from MMI form a cold dense background plasma. The efficiency of the second MMI to mitigate the RE beam may be affected by the characteristics of cold background plasma.

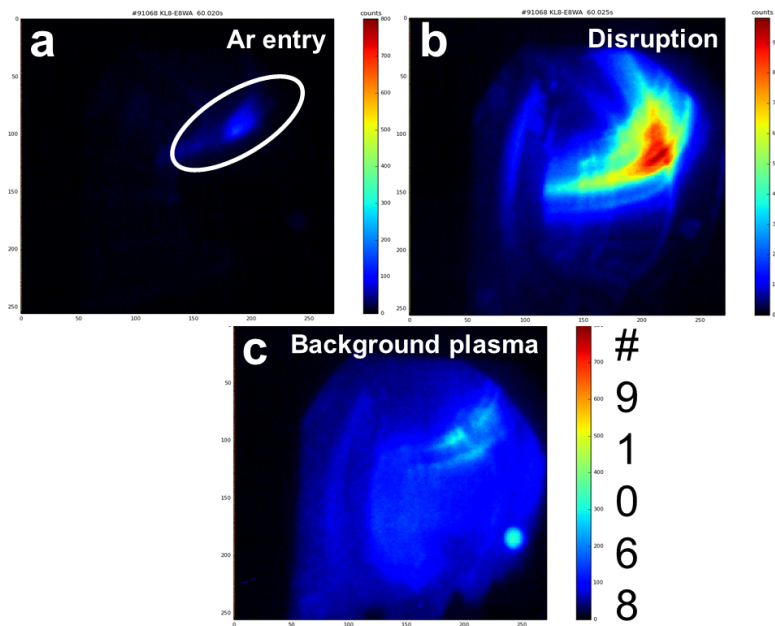


Figure 3.1.: Fast visible camera images in the JET tokamak discharge #91068 : (a) entry of argon MGI, (b) disruption, (c) argon background plasma

In the JET tokamak, mixed argon MGIs (usually 10%Ar+90%D₂) are used to trigger controlled disruptions in order to mitigate localized heat and EM loads. The entry of such argon MGI in the JET tokamak is seen in the figure 3.1(a) using a wide-angle fast visible camera (location of various diagnostics in the JET tokamak shown in the figure 2.21). The disruption is triggered thereafter which can be seen in the figure 3.1(b). In this phase, a cold dense background plasma is formed containing high-Z impurities from the 'trigger' MMI. Such a background plasma is shown in the figure 3.1(c). In addition to visible cameras, background plasma is also evident through

electron density measurements (see section 3.1 for more information).

It was observed in the JET tokamak (Reux 2017) (Reux 2015) that this dense background plasma seem to have a deteriorating effect of the killer MMI to mitigate the RE beam. In order to understand the interaction of killer injection with the RE beam in presence of the background plasma, the characterization of the background plasma is very important. In the JET tokamak, the density of the background plasma is estimated using interferometry system. For the electron temperature measurements of the background plasma, a method based on the VUV spectroscopy is used.

3.1. Electron density of background plasmas

Electron density is an important characteristics of the background plasma. One of the reliable way to measure electron density of the tokamak plasmas is using interferometry. Interferometry techniques are based on the interference of electromagnetic waves. When an electromagnetic wave with frequency ω propagates in a collision-less magnetized plasma with its electric field parallel to the magnetic field, the refractive index μ of the electromagnetic waves depends on the free electron density n_e of the plasma and can be given as (Wesson 2004),

$$\mu = [1 - (\omega_p/\omega)^2] \quad \text{with} \quad \omega_p = \sqrt{\frac{n_e e^2}{m_e \epsilon_0}} \quad (3.1)$$

The term ω_p is called the plasma frequency (in rad/s) which is a function of electron density n_e .

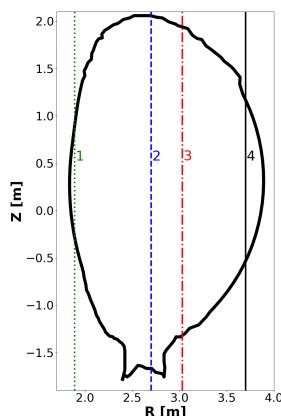


Figure 3.2.: Line of sight for the four vertical chords of the interferometry system

At $\omega \gg \omega_p$, there is a change in the phase of the beam of coherent radiation passing through a plasma as compared to that of a reference beam due to the change in refractive index. This change of phase $\Delta\phi$ is proportional to the electron density n_e and can be represented as (Wesson 2004),

$$\Delta\phi = \frac{\lambda e^2}{4\pi\epsilon_0 m_e c^2} \int n_e dl \quad (3.2)$$

where λ is the wavelength of the radiation. An interferometer usually measures the phase difference between the probing beam and the reference beam. Using this phase difference, the the line-integrated electron density is calculated.

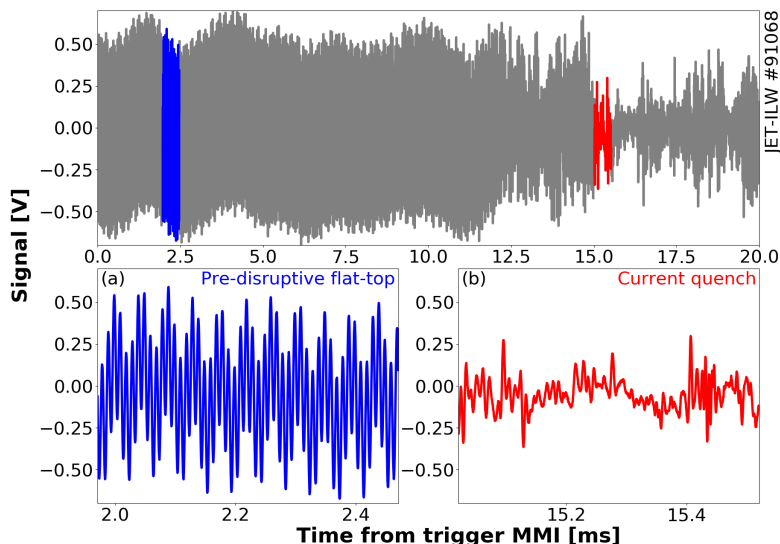


Figure 3.3.: Signals by the interferometer chord 4 during (a) pre-disruptive flat-top and (b) current quench, for the JET-ILW discharge #91068

In the JET tokamak, electron density of the background plasma is estimated using far infrared (FIR) interferometry system. It uses a 120 mW methanol laser optically pumped by a 40W CO₂ and operating at $\lambda=118.8 \mu\text{m}$. This system has 4 vertical chords whose positions are shown in the figure 3.2. The chord 1 is close to the inner wall and so is not of interest in this PhD thesis. The chords 2 usually passes through the plasma confined region. Depending on the plasma radial position and size, chord 3 may pass through the confined region or scrape-off layer (SOL) region. The chord 4 views the far SOL plasma. More information on the interferometry is given in (Boboc 2012).

The interference fringes are measured by interferometry as sinusoidal signals. The figure 3.3(a) gives the sinusoidal signals measured by the interferometry chord 4 during the flat-top phase of the JET discharge #91068. Pulse trains are obtained from zero-crossing detection of the sinusoidal signals. Using the pulse trains, the phase is calculated by time delay counting using a 25 MHz clock (Boboc 2012). From the phase calculation, line-integrated densities are estimated.

However, during the disruption events, there may be a drop in laser intensity and the signal from the interferometer is erratic and perturbed as shown in the figure 3.3(b). This may be due to strong plasma density gradients or fast density changes during disruptions and impurity injections. Strong plasma refraction of the electromagnetic waves and too slow frequency modulation may be a reason for the drop in laser intensity (Murari 2006). During disruption, $\omega_p > \omega$ because of high n_e increase during MMI, therefore plasma maybe opaque to electromagnetic waves (Wesson 2004). As a consequence, the counting of the fringes can be affected (so called "fringe jumps").

The measured phase difference gives a relative evolution of the line-integrated

electron density measurements. Absolute density measurement is iterative for which appropriate phase reference is needed.

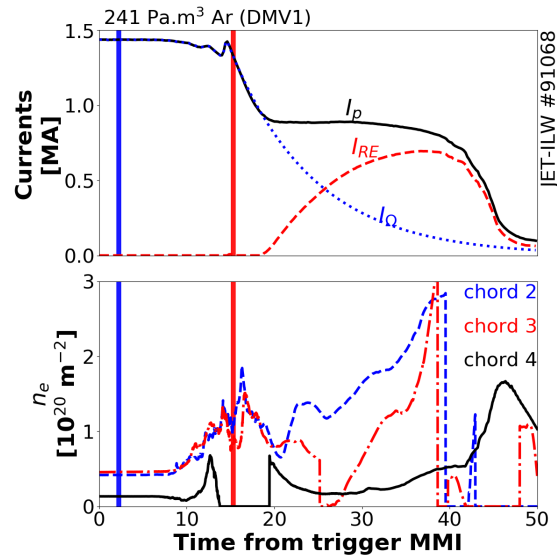


Figure 3.4.: Density of the background plasma measured using interferometry system for the JET-ILW discharge #91068

As seen in the figure 3.4, fringes are lost during the thermal and current quench phases of disruptions for the discharge #91068 in the interferometry chord 4 (viewing far SOL, figure 3.2). This is due to erratic signals shown in the figure 3.3(b) where signals are no longer sinusoidal with no zero-crossing. During this phase, the line-integrated electron density measurement is invalid. After the fringes are recovered (from 20 ms in the figure 3.4), the interferometer measures only relative density evolution (dn_e/dt) because the absolute reference is lost. Since the electron density goes to zero at the end of discharge, the actual value of the line-integrated density value can be recovered backwards as shown in the figure 3.4 for the chord 4.

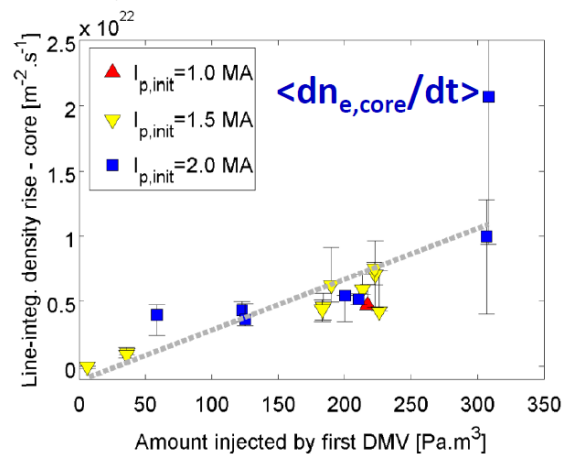


Figure 3.5.: Dependence of (relative) core density on the argon MGI amount used to trigger disruptions (Reux 2017)

If fringes are lost for two different time intervals, only the relative evolution of the density can be measured between the two times. By fixing the offset to zero (as negative densities are not possible), the lower bound of the line-integrated electron density measurements can be estimated. For the MMI triggered disruption experiments in the JET tokamak, in most of the cases, chord 2 and 3 only gives a lower bound on the line-integrated electron density measurements. In the chord 4, absolute density measurements are possible for many discharges.

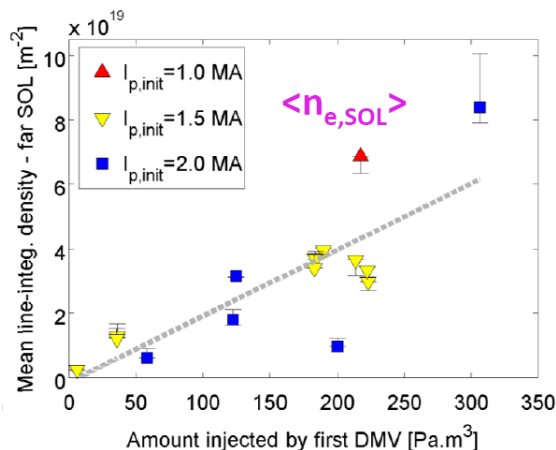


Figure 3.6.: Dependence of SOL density on the argon MGI amount used to trigger disruptions (Reux 2017)

From the figure 3.5, the time averaged line integrated density rise of the background plasma in the core $\langle dn_{e,core}/dt \rangle$ was found to increase with the amount of argon MGI (Massive Gas Injection) used to trigger disruptions. In the far-SOL, the time averaged line-integrated electron density $\langle n_{e,SOL} \rangle$ was also found to increase with argon MGI amount. Another important observation was that no effect of pre-disruption flat-top plasma current $I_{p,init}$ on the density of the background plasma was observed. In (Reux 2017), decrease in efficiency of the killer injection with increase in trigger MMI content was speculated to be due to the rising electron density with the trigger MMI content.

However, in tokamaks like DIII-D (Hollmann 2013) and ASDEX-Upgrade (Papp 2016), MGI killer injection was successful in mitigating the RE beam for the comparable densities of the background plasma unlike on the JET tokamak. This may suggest that more than the density of the background plasma, the temperature may also play an important role in explaining the inefficient of the killer injection.

3.2. Electron temperature of background plasmas

In addition to the electron density, electron temperature of the background plasma is also an important characteristic. During the normal tokamak operations in the JET tokamak, there are two principal diagnostics for the electron temperature measurement:

Thomson Scattering (TS) system: The high resolution Thomson scattering (HRTS) system in the JET tokamak measures electron density and temperature. In HRTS system, a 20 ns laser light beam with wavelength 1064 nm interacts with the free electrons in the plasma via Thomson scattering. The laser's electric field oscillates the electrons and the electrons emit a photon of same wavelength as that of the incident light. Due to the thermal motion of the electrons, the laser spectrum is broadened due to Doppler effect. The width of the Thomson scattered spectra due to Doppler broadening gives the electron temperature T_e . The total amount of the scattered light is proportional to the number of electrons and thus the intensity of the spectrum gives the electron density n_e .

HRTS uses optical filters to chop the spectrum band of interest from the received spectrum. The default HRTS filter is designed to estimate density and temperature measurements for normal plasma operations with temperatures in the keV range, with threshold of 100 eV. In order to view lower temperatures suitable for post-disruption background plasma, the optical filter should be changed. In the JET tokamak, change of optical filter is time consuming. Thus, the cold background plasma is out of HRTS measurement range.

Electron Cyclotron Emission (ECE): The electrons when gyrating around the magnetic field lines emit electromagnetic radiation. This electromagnetic radiation is the so-called cyclotron emission. This radiation occurs at discrete angular frequencies (Wesson 2004),

$$\omega = n\omega_{ce} \quad (3.3)$$

where $\omega_{ce} = eB/m_e$ is the cyclotron frequency of electrons and n is the harmonic number. The intensity of the emission I_n is related to the electron temperature T_e as,

$$I_n(\omega) = \frac{\omega^2 T_e(R)}{8\pi^3 c^2} \quad (3.4)$$

where ω is the frequency of the emitted radiation and can be represented as,

$$\omega(R) = \frac{neB_0R_0}{m_eR} \quad (3.5)$$

where B_0 and R_0 are the values of B_ϕ and R at the plasma center. In contrast to the Thomson scattering system, the measurement of electron cyclotron emission (ECE) is passive. One main issue with ECE diagnostic during disruption is that RE beam totally dominates the intensity (Liu 2018).

Thus, estimation of T_e of the background plasma using ECE require subtracting the non-thermal radiation due to RE beam which is non-trivial. Neglecting the RE beam contribution to ECE may produce high uncertainty in the T_e measurement. For this reason, ECE diagnostics was not considered for the electron temperature T_e estimation of the background plasma.

Both Thomson scattering system and ECE diagnostics are not suitable to measure electron temperature of the background plasma. Thus, a method based on the VUV

spectroscopy has been developed to estimate the temperature T_e of the background plasma. For this, a synthetic spectrum is constructed using atomic data. In the following section, this method will be extensively discussed.

3.2.1. VUV spectroscopy in the JET tokamak

The Vacuum Ultra-Violet (VUV) spectrometer in the JET tokamak views the plasma along the horizontal mid-plane as shown in the figure 3.7. The size of the slit viewing the plasma is 165.5 mm high and 8 mm wide. It is a grazing incidence McPherson model 251 SPRED spectrometer (Fonck 1982) with a Microchannel plate/phosphorous detectors coupled to 2048 pixel diode arrays. It records the line brightness between 10-110 nm with a spectral resolution of 0.4 nm. The fastest acquisition mode of the spectrometer has a time resolution of 11 ms.

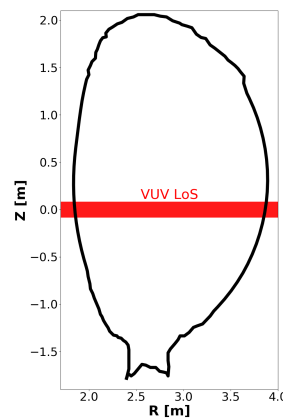


Figure 3.7.: Line of sight of VUV spectrometer (KT2) in the JET tokamak

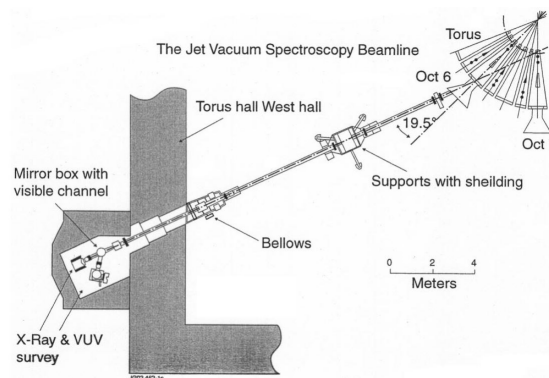


Figure 3.8.: VUV spectrometer kept in a shielded bunker outside the JET torus hall shared with with soft X-ray and visible spectrometers (Barnsley 2003).

The VUV spectrometer is kept in a shielded bunker outside the JET torus hall as shown in the figure 3.8. There is no window at the torus and the entire beamline vacuum system is included in the JET tritium circuit. In the mirror chamber shown

in the figure 3.9, the available aperture is shared between the X-ray, visible and VUV spectrometers. The VUV channel is reflected horizontally by a 15° grazing incidence spherical gold mirror.

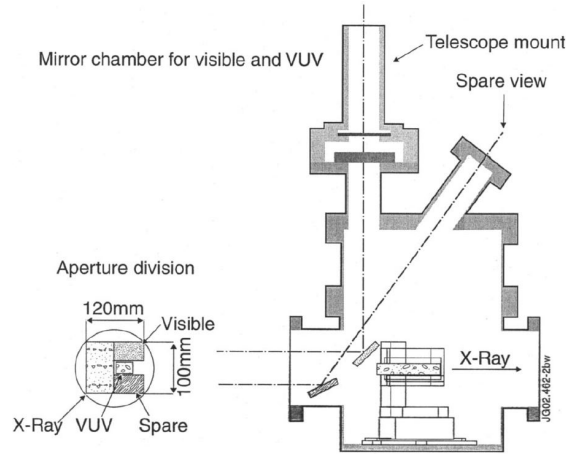


Figure 3.9.: Mirror chamber of the visible and VUV spectrometers dividing the aperture between the instruments (Barnsley 2003). The visible channels are reflected in the vertical plane and the VUV channel is reflected horizontally using a spherical gold mirror with 15deg grazing incidence.

The correction due to detector's solid angle is processed automatically and the data are stored as line brightness (or intensity, in counts/s) for wavelengths between 10-110 nm (through 2048 pixel diodes).

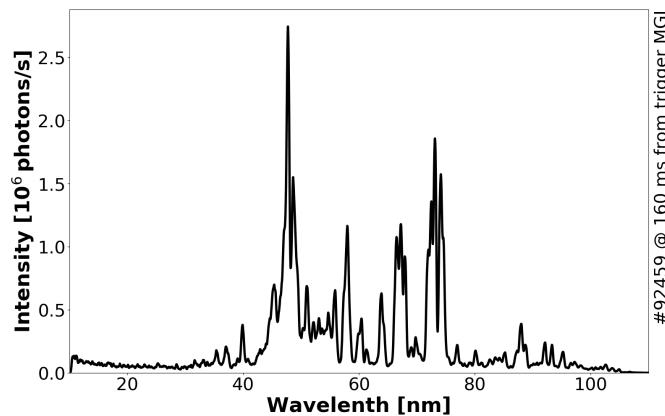


Figure 3.10.: typical VUV spectrum of the JET discharges during argon background plasma

3.2.2. VUV spectrum processing

The raw VUV spectrum shown in the figure 3.10 is due to overlapping of different argon lines. In order to estimate the electron temperature from the VUV spectrum, line intensities should be clearly known. Therefore, the VUV spectrum is processed in three stages as shown in the figure 3.11.

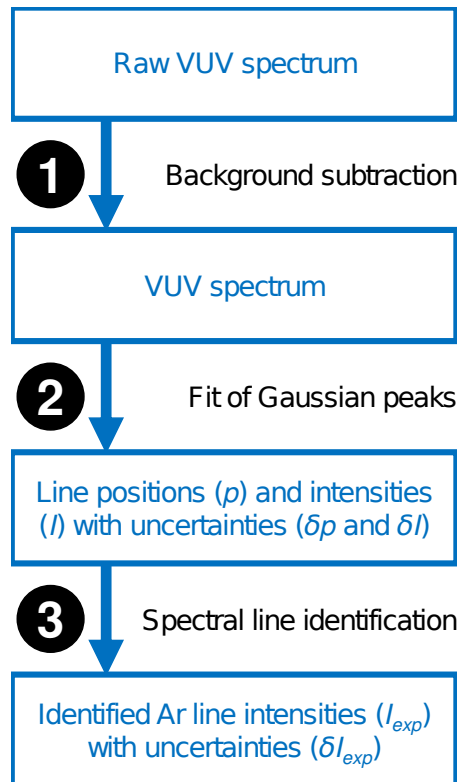


Figure 3.11.: Flowchart of the VUV spectrum processing

3.2.2.1. VUV background subtraction

As shown in the figures 3.10 and 3.12, there is a continuum in the argon VUV spectra between 10-30 nm. In order to remove it, a constant linear background is assumed for a VUV spectrum as shown as the red region in the figure 3.12.

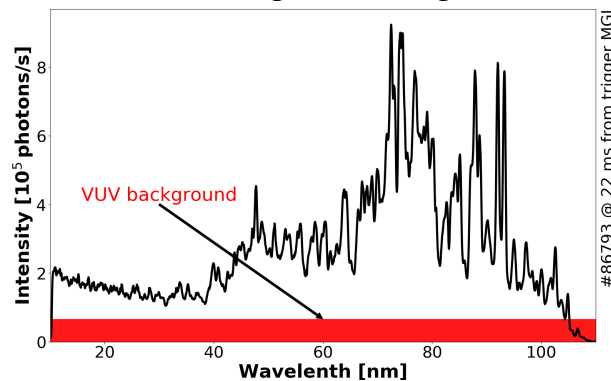


Figure 3.12.: Background subtraction of the VUV spectrum

3.2.2.2. Fit of multiple Gaussian peaks

After removing the background of the VUV spectrum, the overlapping of the line intensities are resolved through multiple fitting of the peaks. For simplicity, a Gaussian

distribution is assumed as the instrumental function of the VUV spectroscopy of the form,

$$I(\lambda) = I_{peak} \cdot \exp\left(-\frac{(\lambda - \lambda_{peak})^2}{2w^2}\right) \quad (3.6)$$

where I_{peaks} and λ_{peaks} are the intensity and central wavelength of the peaks. The term w is the Gaussian width of the instrumental function. For the determination of the instrumental width w , the experimental VUV fit is performed for different widths w for discharges #92459 and #92454. As shown in the figure 3.13, the VUV fit is better (higher R^2 , coefficient of determination) for $w=0.25$ nm. Therefore, the Gaussian instrumental width is set as $w=0.25$ nm for the VUV spectra.

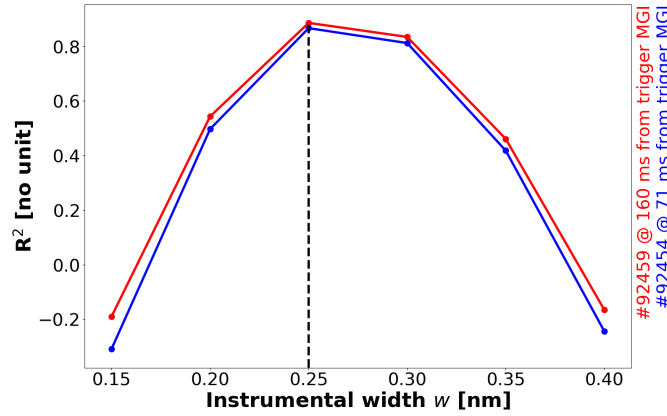


Figure 3.13.: Coefficient of determination (R^2) of the fit of multiple Gaussian peaks for different instrumental widths w of the Gaussian peaks for the JET discharges #92459 and #92454.

Let n be the number of peaks in the spectrum with central wavelengths $\lambda_{peak,j}$ and central intensities $I_{peak,j}$. The total intensity for a given wavelength λ_i due to the Gaussian peaks can be expressed as,

$$y_{fit}(\lambda_i; \lambda_{peak,j=1:n}, I_{peak,j=1:n}) = \sum_{j=1}^n I_{peak,j} \cdot \exp\left(\frac{-(\lambda_i - \lambda_{peak,j})}{2w^2}\right) \quad (3.7)$$

For a given peak, the unknowns are the peak central wavelength λ_{peak} and intensity I_{peak} as the Gaussian instrumental width w is fixed. Thus for n number of peaks, there are $2n$ number of unknowns. For the estimation of unknowns, an error function χ^2 is constructed of the form,

$$\chi^2(\lambda_{peak,j=1:n}, I_{peak,j=1:n}) = \sum_i \left(\frac{y_{exp}(\lambda_i) - y_{fit}(\lambda_i; \lambda_{peak,j=1:n}, I_{peak,j=1:n})}{y_{exp}(\lambda_i)} \right)^2 \quad (3.8)$$

where $y_{exp}(\lambda_i)$ is the line intensity from VUV spectrum for the wavelength λ_i . By minimizing the error functions χ^2 , the central wavelengths $\lambda_{peak,j=1:n}$ and intensities $I_{peak,j=1:n}$ of the peaks are estimated. Nelder-Mead algorithm (Nelder 1965) is used for the minimization of the error function.

Nelder-Mead method is also called as downhill simplex and amoeba method. The algorithm needs only function evaluations and not derivatives. This, it is usually applied to non-linear optimizations for which derivatives are unknown. For the multi-dimensional minimization of N -unknowns, initial guess of the N -independent variables are given to the algorithm. The algorithm now takes steps called "reflections" moving the point of the simplex where the function is largest (called as "highest points") through the opposite faces of the simplex to a lowest point. As a result, the algorithm computes the optimized solution. More information can be found in (Nelder 1965) and (Press 1992). Nelder-Mead algorithm is a heuristic search method and it may converge to a non-stationary local minima instead of absolute minima and is very sensitive to the initial guess.

The central wavelength λ_{peak} at which the peaks are expected and the corresponding intensities I_{peak} are selected as the initial guess of the parameters for the optimization. In the optimization, the central wavelength λ_{peak} are allowed to change ± 0.05 nm from the initial guess of the peak central wavelength. The intensities are bound between 0 and the experimental line intensities $I_{peaks}(exp)$ from the VUV spectrum for the given wavelength (λ_i). The rate of convergence is highly sensitive to the number of unknown, viz, number of peaks in the fit. Thus, the VUV spectrum is split into small isolated regions and the optimizations are performed for each regions separately for faster convergence. The central wavelength λ_{peak} and intensities I_{peak} are selected manually. For consistency, same VUV lines are selected for given discharge.

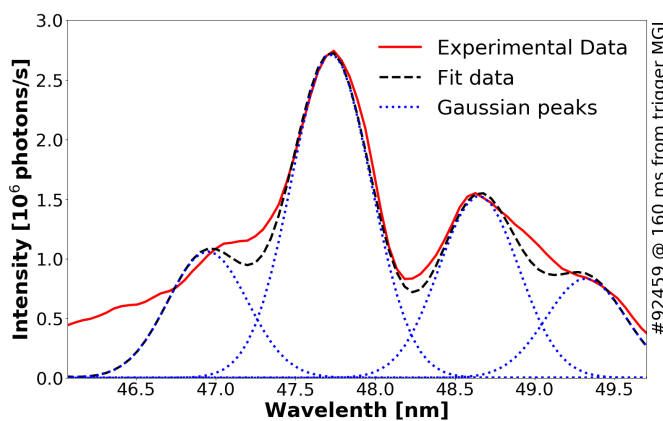


Figure 3.14.: An example of multiple Gaussian fitting of the VUV spectrum for the discharge #92459, 160 ms from trigger MGI.

An example of the multiple Gaussian fitting of the VUV spectrum is shown in figure 3.14 for the discharge #92459. Based on the difference between the experimental spectrum (y_{exp}) and the fit spectrum based on the multiple Gaussian peak fitting (y_{fit} from equation 3.7), the uncertainties in the intensities ($\delta I_{peak,j=1:n}$) are estimated. The uncertainties in the wavelengths ($\delta \lambda_{peak,j=1:n}$) are determined as the difference between the fit and manual selection of the peak wavelengths. Using the line wavelengths and their uncertainties, the spectral lines are identified.

3.2.2.3. Spectral line identification

A given VUV line is characterized by the central wavelength λ_{peak} and intensity I_{peak} . Due to the Gaussian fitting, there is an uncertainty in the central wavelength $\delta\lambda_{peak}$ and intensity δI_{peak} . In addition to the uncertainty in the central wavelength due to Gaussian distribution $\delta\lambda_{peak}$, the spectral resolution of the VUV spectrometer $\Delta\lambda=0.4\text{ nm}$ also contributes to the uncertainty in the central wavelength $\delta\lambda_{peak}$. Thus, for a given VUV line, the total uncertainty in the central wavelength is $\delta\lambda_{peak}^{total}=\delta\lambda_{peak}+\Delta\lambda$.

As a first stage of spectral line identification, the possible argon lines are selected with $\lambda_{peak} - \delta\lambda_{peak}^{total} \leq \lambda \leq \lambda_{peak} + \delta\lambda_{peak}^{total}$. The argon lines are taken from the NIST database (Kramida 2018).

From the set of possible argon lines, the most probable argon line is identified by constructing a normalized score (0-3) based on :

1. relative intensity (scored 0-1 ; 0=least bright line & 1=brightest line)
2. transition probability (scored 0-1 ; 0=least probable & 1=most probable)
3. energy of the lower transition level (scored 0-1 ; 1=lower energy level is the ground state of the ion)

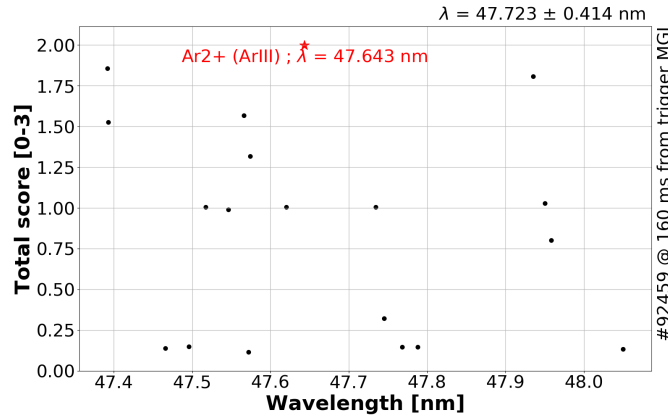


Figure 3.15.: Selection of VUV line by selecting the most probable line from NIST database (Kramida 2018) using normalized score method for the most intense peak of #92459

The normalized score is constructed for all the possible argon lines and the line with maximum score is identified as the spectral line. The information used in the construction of the normalized scores are taken from the NIST database.

One such example of VUV line selection is shown in the figure 3.15 for the most intense line ($\lambda_{peak}=47.723\text{ nm}$ of the discharge #92459). The probable argon lines within the wavelength ranges and their normalized scores are selected using the NIST database as shown as black circles in the figure 3.15. It can be seen that for the ArIII line (in spectroscopic notation ArIII line corresponds to Ar2+) with wavelength $\lambda=47.643\text{ nm}$, the score is the highest. Thus, this ArIII is selected as the argon line for the VUV line of $\lambda_{peak}=47.723\text{ nm}$.

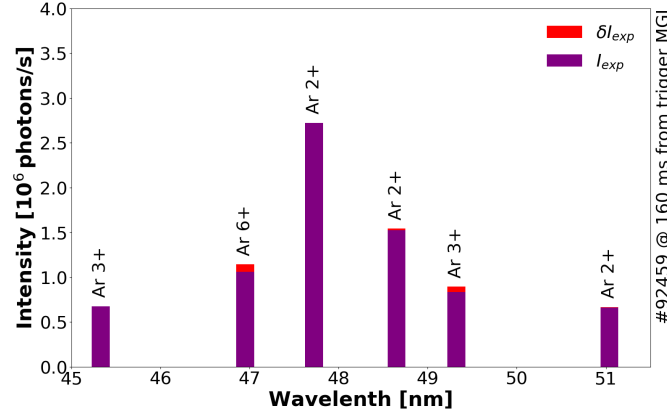


Figure 3.16.: Processed VUV spectrum of #92459 at 160 ms from the trigger injection

An example of a processed VUV spectrum is shown in the figure 3.16 for the discharge #92459. After subtracting the VUV background from the VUV spectrum, the spectrum is fit with multiple Gaussian and the lines are identified using the NIST database. The red region in the figure 3.16 is the error in the intensities due to the fitting of multiple Gaussian peaks.

In the estimation of the electron temperature of the background plasma using the VUV spectroscopy, the ratios of the experimental line intensities (denoted by \mathcal{I}_{exp}) are taken into account rather than the absolute line intensities. This is because by taking the line ratios, the possible error in the calibration factor of the spectrum can be avoided.

It was observed in the figure 3.1 that for some discharges, only relative evolution of the electron density can be estimated rather than the absolute value. The intensity amplitude of the VUV lines depend directly on the electron density. By talking the ratio of line intensities, the uncertainties of the line intensities due to uncertainty in the electron density can also be omitted.

Propagation of the error in line intensities Let us consider two lines with intensities $I_{exp,1}$ and $I_{exp,2}$. The error in the line intensities due to the fitting of Gaussian peaks are $\delta I_{exp,1}$ and $\delta I_{exp,2}$. The error in the ratio of the two lines $\mathcal{I}_{exp,12} = I_{exp,1}/I_{exp,2}$ can be propagated as,

$$\frac{\delta \mathcal{I}_{exp,12}}{\mathcal{I}_{exp,12}} = \sqrt{\left(\frac{\delta I_{exp,1}}{I_{exp,1}}\right)^2 + \left(\frac{\delta I_{exp,2}}{I_{exp,2}}\right)^2} \quad (3.9)$$

The error in the experimental line intensities δI_{exp} due to the fitting of the multiple Gaussian peaks are propagated to the error in the experimental line ratios $\delta \mathcal{I}_{exp}$ as given in the equation 3.9. For a number n of VUV lines, there are $n \cdot (n - 1)/2$ number of experimental ratios (\mathcal{I}_{exp}). The uncertainty in the ratios $\delta \mathcal{I}_{exp}$ are propagated to the temperature profile estimation.

3.2.3. Synthetic line ratios

For the electron temperature estimation of the background plasma, synthetic line ratios depend on the temperature profile. By fitting the synthetic line ratios to the experimental line ratios, the temperature profile of the background plasma is estimated.

3.2.3.1. Temperature profile

In the DIII-D tokamak, a peaked temperature profile was estimated in (Hollmann 2013), around 1.5-2 eV in plasma core and ~ 1 eV outside the confined region. In the JET tokamak, a similar peaked profile of the background plasma is considered of the form,

$$T_e(\rho) = (T_e^0 - T_e^{LCFS}) \cdot (1 - \rho^\alpha)^\beta + T_e^{LCFS} \quad (3.10)$$

where ρ is the normalized radius and α and β are shaping parameters. T_e^0 is the electron temperature of the background plasma at the center of the plasma at $\rho=0$. In the open field line region with $\rho \geq 1$, the temperature is assumed to be a constant with value T_e^{LCFS} . An example of a temperature profile is shown in the figure 3.17.

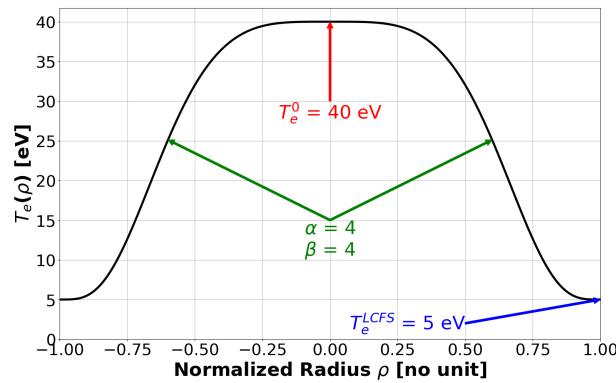


Figure 3.17.: Temperature profile of the background plasma with parameters $T_e^0=40$, $T_e^{LCFS}=5$, $\alpha=4$ and $\beta=4$

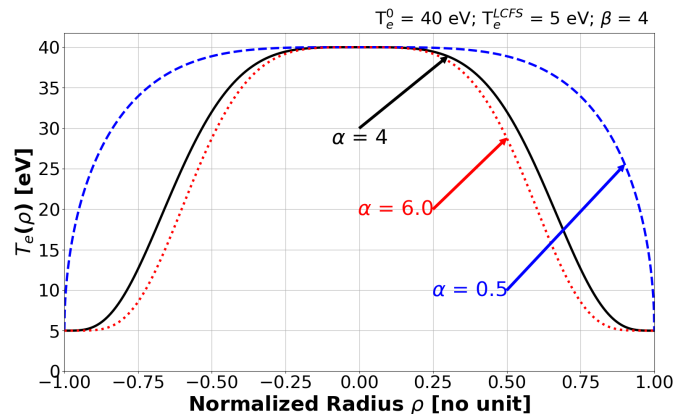


Figure 3.18.: Dependence of the T_e -profile on the shaping parameter α . Other parameters are set at $T_e^0=40$, $T_e^{LCFS}=5$ and $\beta=4$

As given in the equation 3.10, the parameters α and β define the shape of the T_e -profile. From the figure 3.18, it was observed that for increasing α , the T_e -profile is peaked due to the $T_e(\rho) \propto (1 - \rho)^\alpha$ dependence from the equation 3.10.

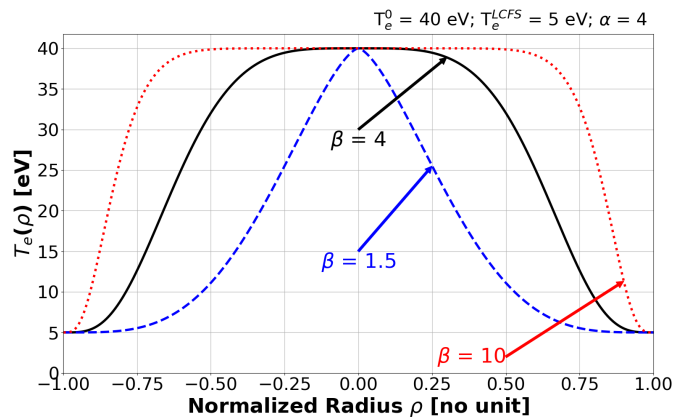


Figure 3.19.: Dependence of the T_e -profile on the shaping parameter β . Other parameters are set at $T_e^0=40$, $T_e^{LCFS}=5$ and $\alpha=4$

Another parameter which determines the peakness of the T_e -profile is β as expressed in the equation 3.10. Lower the β , more peaked is the T_e -profile as shown in the figure 3.19.

For the temperature estimation, the bounds for T_e^0 are fixed between 5-100 eV and 1-20 eV for T_e^{LCFS} . The shaping parameter α is bound between 0.5-6 whereas β is bound between 1.5-10.

3.2.3.2. Discretization of background plasma regions

The spectrum measured by the VUV spectrometer is integrated throughout the line of sight. This implies that the spectrum measured by the VUV spectrometer is the integrated measurement of the spectra emitted by regions of different temperatures. Thus, the background plasma is divided into \mathcal{N} isothermal regions concentric to the plasma centroid. One such example is shown in the figure 3.20 where the discharge \$92459 is split into 5 regions where the T_e and n_e are constant throughout the region. The line intensity I_i measured by the spectrometer for the wavelength λ_i integrated throughout the line of sight can then be expressed as,

$$I_i = \sum_{j=1}^{\mathcal{N}} I_j \quad (3.11)$$

where I_j is the line intensity of the wavelength λ_i from discrete region j with temperature T_e^j . The area A_j of the region j seen by the VUV spectrometer extending from y_1 to y_2 can be expressed as,

$$A_j(a_{j-1}, b_{j-1}, a_j, b_j, y_1, y_2) = \mathcal{A}_{ellipse}(a_j, b_j, y_1, y_2) - \mathcal{A}_{ellipse}(a_{j-1}, b_{j-1}, y_1, y_2) \quad (3.12)$$

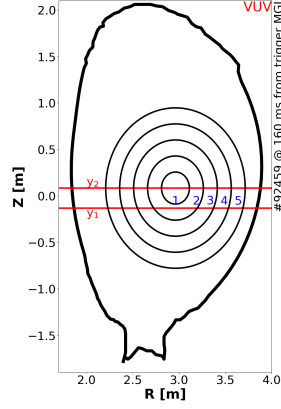


Figure 3.20.: Illustration of discretization of background plasma regions for discharge #92459, 160 ms from the trigger injection.

where (a_{j-1}, b_{j-1}) and (a_j, b_j) describes the ellipses enclosing the area A_j . y_1 and y_2 are the spectrometer line of sight as shown as red horizontal lines in the figure 3.20. The term $\mathcal{A}(a, b, y_1, y_2)$ is the area subtended by the ellipse and the VUV spectrometer LoS, viz, area of the ellipse with (a, b) seen by the VUV spectrometer line of sight and can be expressed as,

$$\mathcal{A}(a, b, y_1, y_2) = \frac{a}{b} \left[y_2 \sqrt{b^2 - y_2^2} + y_1 \sqrt{b^2 - y_1^2} + b^2 \arcsin\left(\frac{y_2}{b}\right) - b^2 \arcsin\left(\frac{y_1}{b}\right) \right] \quad (3.13)$$

For the temperature estimation, the background plasma in the confined region is split into $\mathcal{N}=40$ regions. The background plasma in the open field-line region (or the scrape-off layer SOL) outside the confined region is assumed to have a uniform temperature T_e^{LCFS} and the corresponding area of the region is given by,

$$A_{SOL} = A_{total} - \sum_{j=1}^{\mathcal{N}} A_j \quad (3.14)$$

where A_{total} is the total area seen by the VUV spectrometer. It is calculated as,

$$A_{total} = \int_{y_1}^{y_2} l_{chord}(y) \cdot dy \quad (3.15)$$

where $l_{chord}(y)$ is the length of the plasma vessel seen by the VUV spectrometer at $Z = y$. This is estimated by the intersection of a line $z = y$ at wall coordinates given as thick black line in the figure 3.20 defining the first wall.

3.2.3.3. Photon Emissivity Coefficient (PEC)

In the initial part of this PhD thesis, an unsuccessful effort has been made to compute the synthetic spectrum based on the collisional radiative modeling (CRM). In the temperature estimation, instead of building the entire spectrum manually, the Photon-Emissivity Coefficient (PEC) from the ADAS database (Summers 2004) is used in the construction of synthetic line ratios. PEC is a function of electron temperature T_e and density n_e . Using the PEC data, the emission in a spectrum line from $i \rightarrow j$ (i and j are the ground state and the excited state of the emission) corresponding to wavelength λ ϵ_λ is given by (Summers 2004),

$$\epsilon_\lambda = n_e n_z \text{PEC}_\lambda(T_e, n_e) \quad (3.16)$$

where n_e and n_z are the electron density and the density of ion with ionization state z given in m^{-3} . The PEC data is in photons $\text{m}^{-3} \text{s}^{-1}$ with line emission ϵ_λ given in photons $\text{m}^{-3} \text{s}^{-1}$. PEC is a function of electron temperature T_e and density n_e .

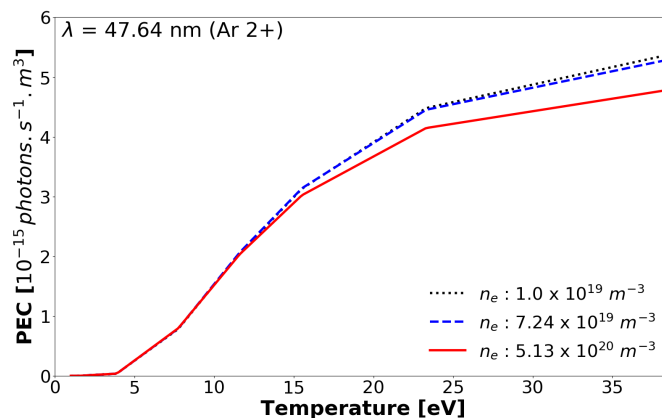


Figure 3.21.: Electron temperature dependence of the PEC data for different electron densities for the Ar2+ line with $\lambda=47.64$ nm

As shown in the figure 3.21, PEC is weakly correlated with the density and is a strong function of the temperature for most of the spectral lines used in the analysis. In the PEC data generation from the ADAS database, it is assumed that the argon lines excited only by the thermal bulk electron. Excitation due to the runaway electron beam is not considered.

3.2.3.4. Fractional abundance of argon

Ion densities n_z are one of the most important parameter in the synthetic line ratios and it depends on the electron temperature T_e and density n_e . For a given argon ionization state z , the ion density n_z can be expressed as,

$$n_z(T_e, n_e) = n_{total} \cdot f_z(T_e, n_e) \quad (3.17)$$

where n_{total} is the total argon density in the plasma per unit volume, assuming the argon impurities are spread homogeneously in the plasma. The term $f_z(T_e, n_e)$ is the argon fractional abundance which defines the distribution of various argon states for a given T_e and n_e . The temperature dependence of the argon fractional abundance is shown in the figure 3.22. The fractional abundance data used in the estimation are taken from the NIST database (LLNL) which is based on time-independent collisional radiative modeling.

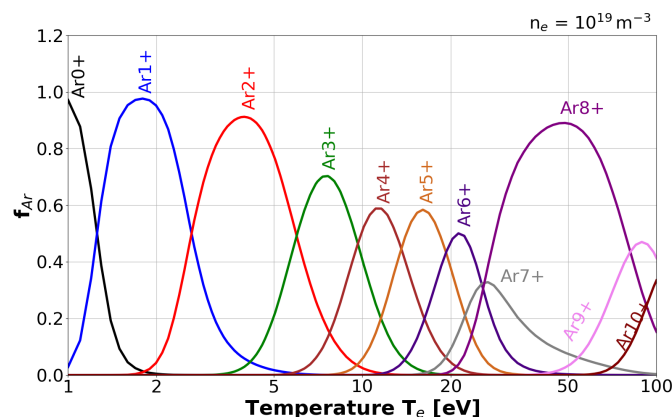


Figure 3.22.: Fractional abundance of argon at $n_e=10^{19} \text{ m}^{-3}$ from the NIST database (Kramida 2018)

3.2.3.5. Synthetic line ratios construction

Using the PEC data (section 3.2.3.3), the synthetic line ratio $\mathcal{J}_{syn}^{1,2}$ of two spectral lines of wavelengths λ_1 and λ_2 for a T_e -profile ($T_e^0, T_e^{LCFS}, \alpha$ and β) can be constructed as,

$$\mathcal{J}_{syn}^{1,2}(T_e^0, T_e^{LCFS}, \alpha, \beta) = \frac{\sum_{j=1}^{\mathcal{N}} n_{z,1} \cdot \text{PEC}_{\lambda_1}(T_{e,j}, n_e) \cdot A_j}{\sum_{j=1}^{\mathcal{N}} n_{z,2} \cdot \text{PEC}_{\lambda_2}(T_{e,j}, n_e) \cdot A_j} \quad (3.18)$$

where $n_{z,i}$ is the ion density corresponding to the ionization of the line λ_i estimated from the argon fractional abundance (discussed in section 3.2.3.4). A_j is the estimated area of the plasma region seen by the VUV spectrometer with temperature $T_{e,j}$ from the equation 3.12. A pure argon plasma is assumed with flat density profile in the construction of the synthetic line ratios. In this estimation, the argon neutral density is considered to be negligible (Reux 2015; Reux 2017).

As discussed in the section 3.2.2.3, the VUV lines are identified using NIST database whereas PEC data are from ADAS database. The PEC data are assigned for NIST lines by matching the wavelength and configuration of transition states of the lines. Most of the intense VUV lines have corresponding PEC data. Only the VUV spectral lines with available PEC data are considered in the temperature estimation.

3.2.4. T_e -profile estimation

The temperature profile of the background plasma in the confined region is estimated by fitting the synthetic line ratios \mathcal{J}_{syn} with the experimental line ratios \mathcal{J}_{exp} . For the fitting, an error function χ^2 is construction based on the weighted least-squared (Press 1992) as,

$$\chi^2(T_e^0, T_e^{LCFS}, \alpha, \beta) = \sum_{i=1}^{\#ratios} \left(\frac{\mathcal{J}_{exp}^i - \mathcal{J}_{syn}^i(T_e^0, T_e^{LCFS}, \alpha, \beta)}{\delta \mathcal{J}_{exp}^i} \right)^2 \quad (3.19)$$

The T_e -profile parameters ($T_e^0, T_e^{LCFS}, \alpha$ & β) are estimated by optimizing the error function (equation 3.19) using the Nelder-Mead algorithm (already discussed in section 3.2.2.2). The optimization is sensitive to the initial guesses of the parameters. Therefore, the initial guesses are swept and optimizations are performed for each value of the initial guess.

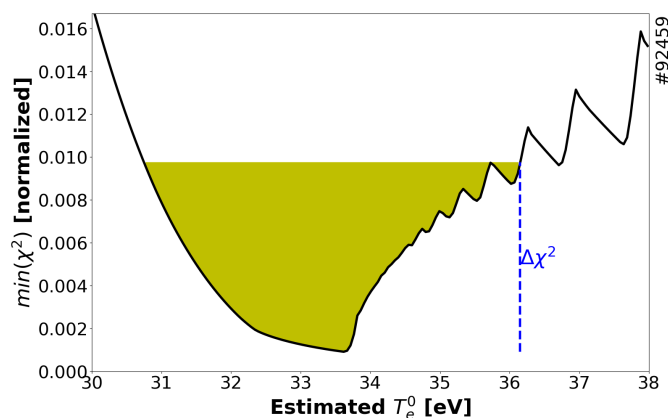


Figure 3.23.: An example of optimizations sweeping initial guesses and the confidence bound

An example of the optimizations for different values of the initial guess of the central temperature T_e^0 and the corresponding estimated T_e^0 value is shown in the figure 3.23. A confidence region ($\Delta\chi^2$) is constructed on the residuals with 68% confidence. This means that 68% of the residual values lies between $\min(residuals)$ and $\min(residuals) + \Delta\chi^2$ as denoted by the shaded region in the figure 3.23. The temperature at the LCFS (T_e^{LCFS}) and the profile shaping parameters (α & β) are fixed in the figure 3.23 for better visualization of this illustration of the model. In actual optimizations, all the four parameters are varied simultaneously.

For a given VUV spectrum, the initial guesses of the parameters ($T_e^0, T_e^{LCFS}, \alpha$ & β) are swept and optimizations are performed for every initial guess. One such example is given in the figure 3.24 for the discharge #92459, 160 ms from the trigger injection. It was already seen that Nelder-Mead is an heuristic algorithm and thus it may not converge if the initial guesses are far from the solution. For instance, out of 300 optimizations, only 69 optimizations managed to converge in the case of 3.24. Each optimization has a solution for the parameters and a residual $\min(\chi^2)$ value.

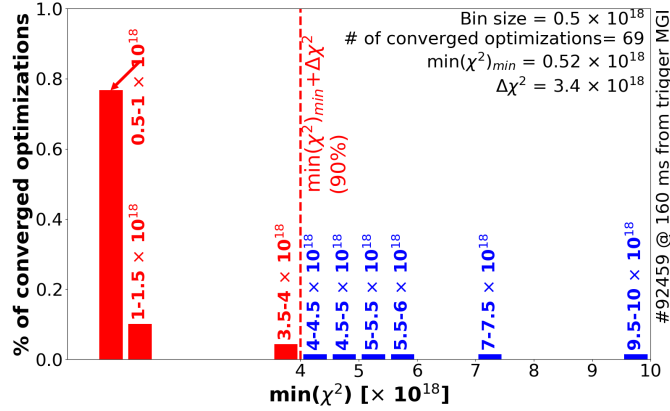


Figure 3.24.: Selecting 90% (confidence bound) of optimizations with lowest residuals $\min(\chi^2)$ for the discharge #92459, 160 ms from the trigger injection. Red and black represents the selected and rejected optimizations respectively.

The converged optimizations are selected based on their residual value. Assuming a confidence bound, for instance, 90% like in case of figure 3.24, a residual bound $\Delta\chi^2$ is constructed such that 90% of the converged optimizations have the residual value $\min(\chi^2)$ between $\min(\chi^2)_{\min}$ and $\min(\chi^2)_{\min} + \Delta\chi^2$. The selections corresponds to the red data in the figure 3.24.

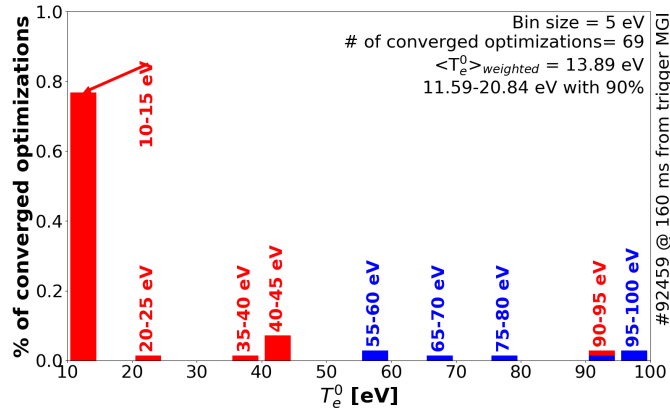


Figure 3.25.: T_e^0 of the selected optimizations (corresponding to the figure 3.24) for the discharge #92459, 160 ms from the trigger injection. Red and black represents the selected and rejected optimizations respectively.

For the selected optimizations, the corresponding solutions to the parameters are also selected. One example is provided in the figure 3.25 where the solutions of the core temperature T_e^0 corresponding to the selected optimizations are displayed in red and the black data corresponds to the discarded optimizations with $\min(\chi^2)$ greater than $\min(\chi^2)_{\min} + \Delta\chi^2$. For the selected solutions, a mean is taken using the residual values as weights. For instance, the weighted mean of the core temperature T_e^0 can be taken as,

$$\langle T_e^0 \rangle_{weighted} = \frac{\sum_{j=1}^{n_s} T_{e,j}^0 \cdot W_j}{\sum_{j=1}^{n_s} W_j} \quad \text{with} \quad W = \frac{1}{\min(\chi^2)} \quad (3.20)$$

Weighted mean gives more weightage to optimizations with lower residuals. For instance, the weighted mean of the core temperature T_e^0 in the figure 3.25 is ~ 13.89 eV. The boundaries of the selected parameters gives the natural confidence boundary of the estimated parameters as explained in (Press 1992). For instance, the selected T_e^0 extends from 11.59 eV to 99.95 eV which is the natural confidence boundary. However, it can be seen from the 3.25 that most of the values lies between 10-15 eV and only few optimizations corresponds to 90-95 eV. Therefore, considering the natural boundary may not be a fair treatment to the profile estimation. To solve this problem, a confidence interval (Press 1992) of the selected parameters are taken. For instance, 90% of the selected T_e^0 lies between 11.59-20.84 eV with weighted mean value 13.89 eV as shown in the figure 3.25. This confidence interval provides the uncertainty of the estimated parameters ($\delta T_e^0, \delta T_e^{LCFS}, \delta \alpha$ & $\delta \beta$). These uncertainties are propagated to the construction of the T_e -profile.

For a function $f(x, y)$ with two independent variables x and y , the propagation of uncertainties δx and δy can be expressed as,

$$\delta f = \sqrt{\left(\frac{\partial f}{\partial x}\right)^2 (\delta x)^2 + \left(\frac{\partial f}{\partial y}\right)^2 (\delta y)^2} \quad (3.21)$$

The equation 3.21 can be applied to the T_e -profile as,

$$\delta T_e = \sqrt{\left(\frac{\partial T_e}{\partial T_e^0}\right)^2 (\delta T_e^0)^2 + \left(\frac{\partial T_e}{\partial \alpha}\right)^2 (\delta \alpha)^2 + \left(\frac{\partial T_e}{\partial \beta}\right)^2 (\delta \beta)^2 + \left(\frac{\partial T_e}{\partial T_e^{LCFS}}\right)^2 (\delta T_e^{LCFS})^2} \quad (3.22)$$

The uncertainties in the estimated T_e -profile parameters can be asymmetric. Thus, the uncertainties are divided into two, the lower part and the higher part. For instance, the uncertainties in the T_e^0 shown in the figure 3.25 are $\delta T_{e,1}^0 = 13.89 - 11.59 = 2.3$ eV (lower) and $\delta T_{e,2}^0 = 20.84 - 13.89 = 6.95$ eV (higher). The same can be said for other parameters, T_e^{LCFS} , α and β .

Thus, the uncertainty in the profile parameters, $\delta T_{e,i}^0$, $\delta \alpha_i$, $\delta \beta_i$ and $\delta T_{e,i}^{LCFS}$ ($i = 1$ for lower error and $i = 2$ for higher error) can be propagated to the T_e -profile as,

$$\delta T_{e,i} = \sqrt{(\partial T_{e,i})_{\delta T_{e,i}^0}^2 + (\partial T_{e,i})_{\delta \alpha_i}^2 + (\partial T_{e,i})_{\delta \beta_i}^2 + (\partial T_{e,i})_{\delta T_{e,i}^{LCFS}}^2} \quad (3.23)$$

where, $(\partial T_{e,i})_{\delta \mathcal{A}_i}$ is the change in the T_e -profile due to $\delta \mathcal{A}_i$, with $\mathcal{A} \rightarrow T_e^0, \alpha, \beta$ and T_e^{LCFS} .

An example of the estimated T_e -profile is shown as the black line in the figure 3.26 for the discharge #92459, 160, s from the trigger injection. The shaded region of the figure 3.26 represents the uncertainty of the T_e -profile propagated from the uncertainties of profile parameters as given in the equation 3.23. The asymmetric

uncertainties of the T_e -profile in the figure 3.26 is due to the asymmetric uncertainties of the T_e -profile parameters.

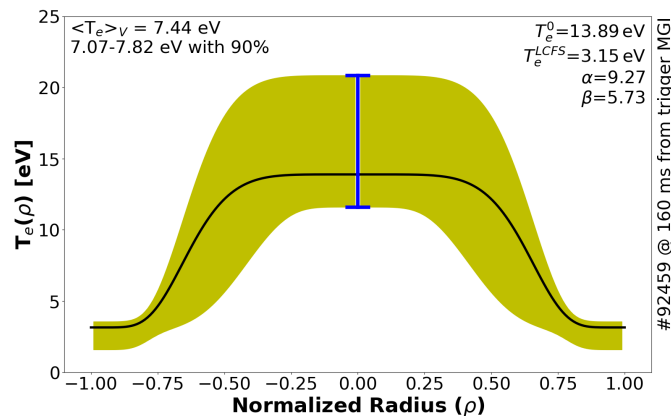


Figure 3.26.: Estimated T_e -profile of the discharge #92459, 160ms from the trigger injection

In the figure 3.26, the term $\langle T_e \rangle_V$ is the volume averaged T_e -profile which can be expressed as,

$$\langle T_e \rangle_V = \frac{\sum_{\rho} T_e(\rho) \cdot V_i(\rho)}{\sum_{\rho} V_i(\rho)} \quad \text{with} \quad V_i(\rho) = \pi(a_i b_i - a_{i-1} b_{i-1}) \quad (3.24)$$

where $V_i(\rho)$ is the ring volume of the region i enclosed between two ellipse (a_i, b_i) and (a_{i-1}, b_{i-1}). a and b are the minor and major axis of the ellipse.

3.3. Database analysis of background plasmas

The estimation of the temperature profile from the VUV spectroscopy was discussed in the section 3.2. Using this method, the background plasmas of the discharges in the database are characterized and are analyzed. Three kinds of experiments are considered in the database analysis of background plasmas performed in the JET tokamak with ITER-like wall (ILW) configuration:

1. Experiments in which background plasmas are created using argon MGI and RE mitigation attempt using killer MGI (mostly krypton, argon and neon also used)
2. Experiments in which background plasmas are triggered using argon SPI
3. Experiments in which background plasmas are triggered using argon MGI and RE mitigation attempt using argon SPI

3.3.0.1. Argon MGI trigger and mitigation with MGI

The experiments consists of 24 limiter discharges with toroidal magnetic field $B_T=3T$ in which different amount of argon massive gas injection is used to trigger the disruption. Attempts to mitigate the generated RE beams are performed using high-Z

MGI such as Kr, Xe and Ar. The ranges of different parameters of the experiments are tabulated in the table 3.1. The temperature profiles of the argon background plasma are estimated from the start of current quench (CQ) until the entry of killer injection in the plasma. 3.2. The characterisation of the background plasmas for these experiments were reported in (Sridhar 2020).

Parameters		Range	
Argon gas amount	(Pa.m ³)	5-530	(57% between 190-255)
RE beam plateau current	(MA)	0.4-1.15	(73% between 0.6-1)
RE beam duration	(ms)	30-210	(87% between 30-95)
Vertical plasma movement	(m.s ⁻¹)	2-39	(61% between 5.8-21)
Electron density in the far-SOL	(m ⁻²)	10 ¹⁸ – 9 × 10 ¹⁹ (74% between 7 × 10 ¹⁸ – 4.3 × 10 ¹⁹)	
Plasma current	(MA)	66% with $I_p^{initial}=1.5$ MA 34% with $I_p^{initial}=2$ MA	
Configuration		Limiter	

Table 3.1.: Ranges of the parameters of the experiments with trigger MGI and killer MGI

3.3.0.2. Argon SPI as trigger injection

These experiments consists of 9 discharges in which background plasmas are triggered using argon SPI from barrel B ~60 Pa.m³ of argon quantity. Of the discharges, three discharges are ohmic with no additional heating. Additional power in the form of Ion-Cyclotron Radio-frequency Heating (ICRH or RF in short) is used in six discharges. In addition to RF heating, Neutral Beam Injection (NBI) additional power is used in two discharges. All the discharges have initial plasma current of 2MA. In eight out of the nine discharges, toroidal magnetic field was kept at 3 T whereas for one ohmic discharge, the field was kept at 2.4 T. The RE beam is very short, between 6-26 ms. In five of the discharges, the argon pellets are broken before reaching the shattering target. This was measured using the microwave diagnostics in the SPI system.

In this section, the VUV spectrum is first studied qualitatively for different experiments. Then, the estimated temperature profiles are then studied against the parameters of the background plasma and the runaway electron beam.

3.3.0.3. Argon MGI trigger and mitigation with argon MMI

These experiments consists of 5 discharges in which background plasmas are triggered using ~3 Pa.m³ of argon from DMV3. In two discharges, the RE beam are mitigated using argon SPI from barrel A with ~240 Pa.m³ Ar content. In two discharges, RE

mitigation is by argon SPI from barrel B with $\sim 60 \text{ Pa}\cdot\text{m}^3$. In one discharge, $\sim 280 \text{ Pa}\cdot\text{m}^3$ of argon MGI from DMV2 is used to mitigate the RE beam. All the discharges have initial plasma current of 1.5 MA with 3 T toroidal magnetic field in the limiter configuration. The RE current plateau is around 0.65 MA for all the discharges. An improved runaway electron specific vertical control system algorithm was in place and as a result, vertical plasma movement is between $0.03\text{-}0.25 \text{ ms}^{-1}$ which is very low compared to the MGI experiments (from table 3.1). Due to the vertically controlled plasma, the mitigated RE beam duration is about half a second (unmitigated RE beam went on for more than 1 s).

3.3.1. Analysis of Ar MGI as trigger injections

Before analyzing the estimated temperature of the background plasmas of the database, VUV spectra of the discharges in different experiments are first analyzed qualitatively in this section. In this analysis, Ar MGI is used as trigger injection.

3.3.1.1. Qualitative VUV analysis: Ar MGI as trigger injection

In the first analysis, Ar MGI is used to trigger disruptions. Typical argon VUV spectra for the JET-ILW discharges in which background plasma is triggered using different amounts of Ar MGI are shown in the figure 3.27.

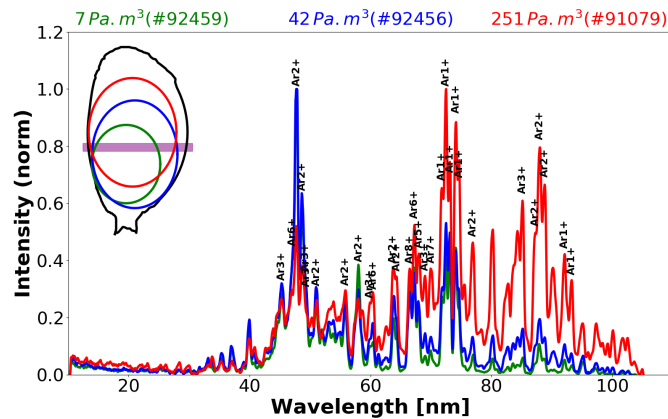
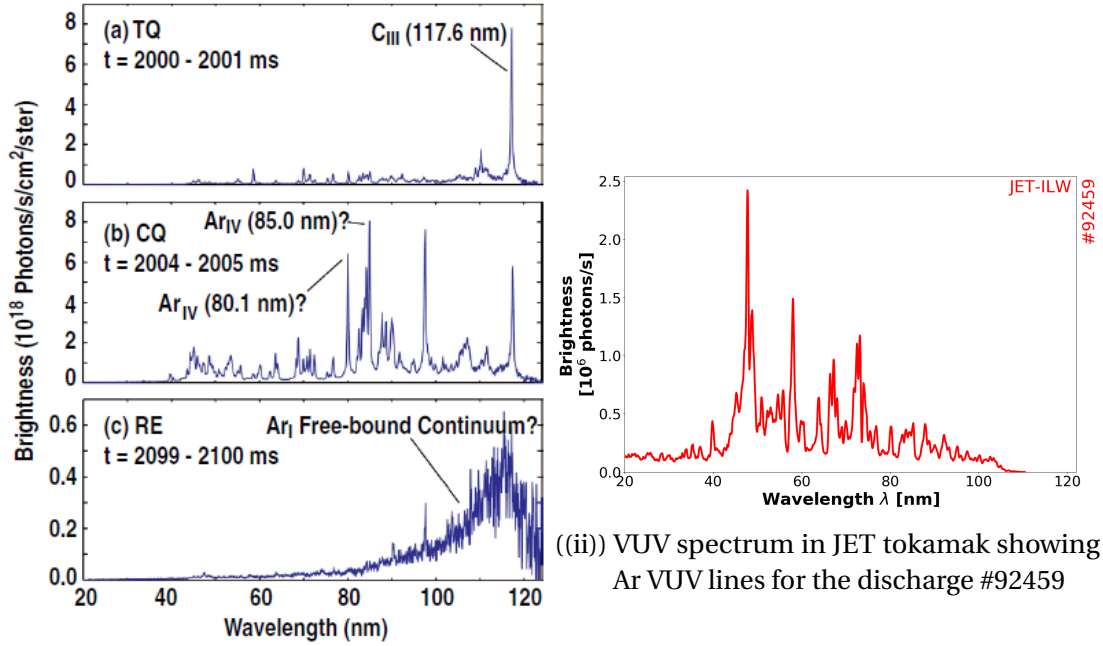


Figure 3.27.: VUV spectra of discharges with different trigger Ar MGI amounts. VUV line of sight is looking into the RE beam/confined background plasma. In all the three discharges, the pre-disruption plasma current $I_p^{initial} = 1.5 \text{ MA}$ and the toroidal field is 3 T.

Most of the bright lines of the VUV spectra corresponds to Ar1+ and Ar2+ ionization states. In addition, higher ionization states up to Ar8+ can be observed. The argon neutral line, which is usually around 100 nm is faint as compared to other ionization lines. This may be because background plasmas of the JET discharges have very low argon neutral content. Low argon neutrals in the background plasma of the JET tokamak was also inferred in the (Reux 2015) using ESTAR (Berger 1992) calculations.

For all the VUV spectra, the same lines are observed independent of argon MGI amounts used to trigger the background plasmas as shown in the figure 3.27. An interesting observation is that with the increase in the amount of the argon trigger injection, the brightest lines are shifted to higher wavelengths. For instance, the JET discharge #91079 in which the background plasma is triggered using 251 Pa.m³, the most intense line is around 70-80 nm as compared to other discharges inspite of having comparable line brightness of lines between 40-60 nm.



(i) VUV spectrum in DIII-D showing Ar recombination continuum (Hollmann 2011)

Figure 3.28.: Comparison of VUV spectra in (a) DIII-D and (b) JET during RE beam with argon background plasma.

The distinct lines of the VUV spectra is in contrast with the VUV spectra of the DIII-D tokamak as shown in the figure 3.28(ii) (DIII-D VUV spectra shown in figure 3.28(i) is taken from (Hollmann 2011)). In the DIII-D tokamak, no argon lines are found; a continuum of argon neutral is observed instead. This is attributed to a cold background plasma, $T_e \sim 1-2$ eV from (Hollmann 2011). Presence of distinct argon lines may suggest that JET background plasmas are much hotter than DIII-D background plasmas. Assuming a collisional-radiative modeling, Ar²⁺ and Ar³⁺ lines are expected for background plasma temperatures between 5-10 eV from the fractional abundance (figure 3.22).

The VUV spectra of discharges with different argon trigger MGI is shown in the figure 3.29 when the VUV spectrometer is viewing the far-SOL region, far away from the confined region. The brightest line is between 80-100 nm and its predominantly Ar₁₊ and Ar₂₊. The RE beam is expected to follow the magnetic field lines and thus its safe to assume that the RE beam direct impact on the background plasma in the

far-SOL is negligible. No clear dependency of the line intensities on the injected argon gas amount is seen as shown in the figure 3.29. The presence of Ar1+ and Ar2+ in the spectra may suggest a significant background plasma temperature of 1-5 eV in the far-SOL.

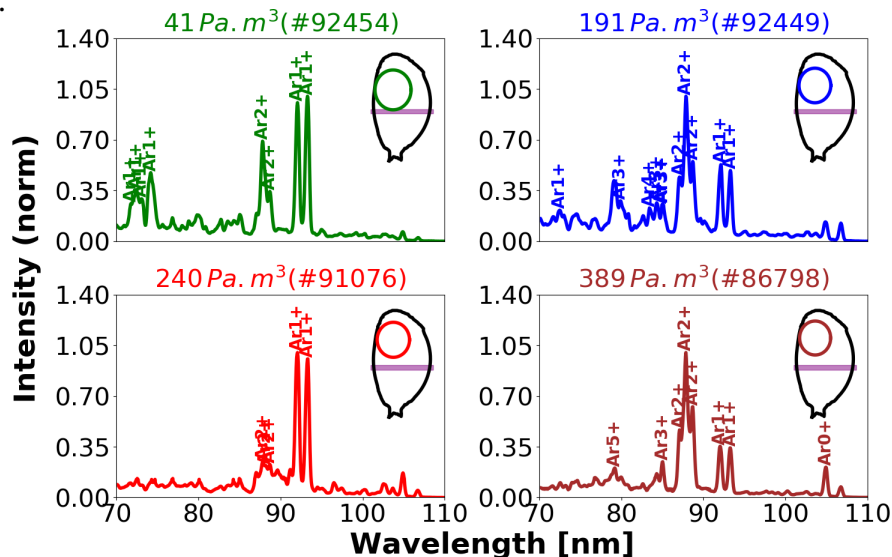


Figure 3.29.: VUV spectra with line of sight outside the RE beam/confined background plasma, looking into the far-SOL region for different trigger gas amounts. VUV spectra are normalized to its most intense peak.

From the figures 3.27 and 3.29, it can be said that background plasmas may be hotter in the core ($T_e \sim 1-100$ eV due to Ar1+-Ar8+ ionization states) than in the far-SOL region ($T_e \sim 1-5$ eV due to Ar1+ and Ar2+ ionization states). This may justify the consideration of peaked T_e -profile in the section 3.2.3.1.

3.3.2. Quantitative analysis of Ar MMI as trigger injections

Following the qualitative analysis of the VUV spectra, the temperatures of the background plasmas are estimated using the synthetic line ratio method discussed in the section 3.2. As discussed in the section 3.2.3.1, a peaked temperature profile is assumed using four parameters : core temperature T_e^0 , temperature on the separatrix T_e^{LCFS} and two shaping parameters α and β . In this section, the background plasma temperatures are analyzed quantitatively for the database of discharges in which background plasma is triggered using Ar MGI or Ar SPI.

The evolution of the temperatures of the background plasmas are shown in the figure 3.30. During the initial phases of the RE beam, the plasma cools down as observed in the figures 3.30(a), 3.30(b) and 3.30(c). During the RE beam plateau phase, no significant evolution in the VUV spectra are observed. As a result, the temperatures of the background plasma are more or less constant during RE plateau phase as shown in the figure 3.30. During the end of the beam, the temperature rise is correlated with the radiated power measurements (using bolometer).

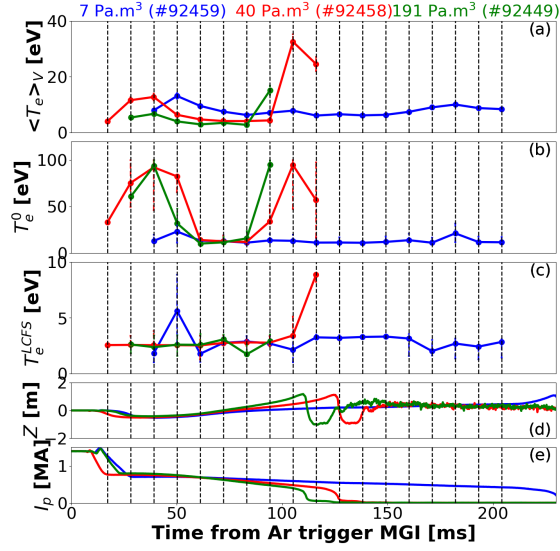


Figure 3.30.: Time evolution of (a) volume averaged temperature profile $\langle T_e \rangle_V$, (b) core temperature T_e^0 , (c) temperature at separatrix T_e^{LCFS} , (d) plasma vertical position Z and (e) plasma current I_p . Background plasmas are triggered by various amount of Ar MGI.

The volume averaged temperatures $\langle T_e \rangle_V$ are time and volume averaged along the RE beam when $I_{RE} \geq 20\%I_p$, $\langle \langle T_e \rangle_V \rangle_t$. The current carried by the RE beam I_{RE} is estimated by assuming exponential decay of the ohmic current I_Ω following current quench.

When background plasma is triggered using argon SPI from barrel B with $\sim 60 \text{ Pa.m}^3$, the RE beams are short and thus only one VUV spectrum can be recorded for a discharge. Thus, the evolution of background plasma temperatures are not possible for SPI discharges.

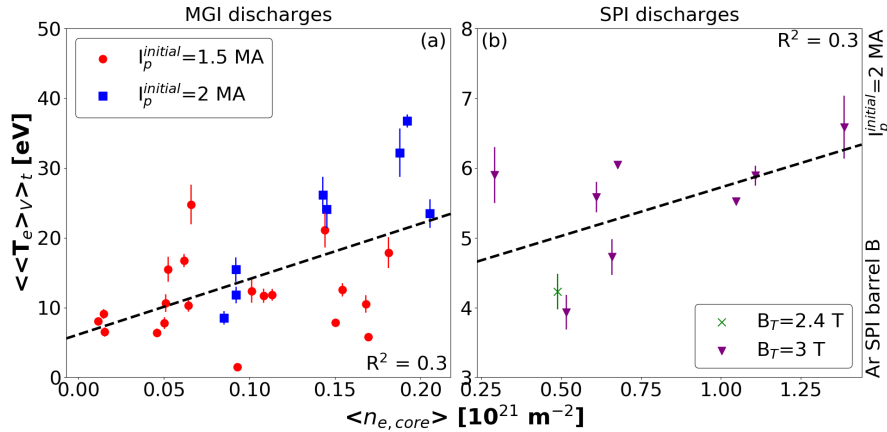


Figure 3.31.: Dependence of the time and volume averaged background plasma temperature $\langle \langle T_e \rangle_V \rangle_t$ on the averaged core electron density $\langle n_{e,core} \rangle$ for (a) MGI and (b) SPI discharges

For the MGI discharges, the time and volume averaged temperature of the back-

ground plasmas tend to reach higher value with increase in electron density in the core $\langle n_{e,core} \rangle$ as shown in the figure 3.31(a). For the SPI discharges, the time and volume averaged temperature of the background plasmas reach lower value with an increase in electron density in the core $\langle n_{e,core} \rangle$ as shown in the figure 3.31(b). However, the dependency of the background plasma temperature on the background plasma electron density is unclear. It can also be observed from the figure 3.31(a) that the background plasma temperature is independent of the pre-disruption plasma current $I_p^{initial}$. Linear regression of the quantities and the dependence parameters are made and shown as black dashed lines in the figures.

It is to be noted that the time and volume averaged core electron density measurements $\langle n_{e,core} \rangle$ measured using interferometry for the MGI discharges are the lowest possible value and not the absolute value (more information in section 3.1). For the SPI discharges, the core electron densities are measured using the far infrared polarimeter systems and the average values are absolute.

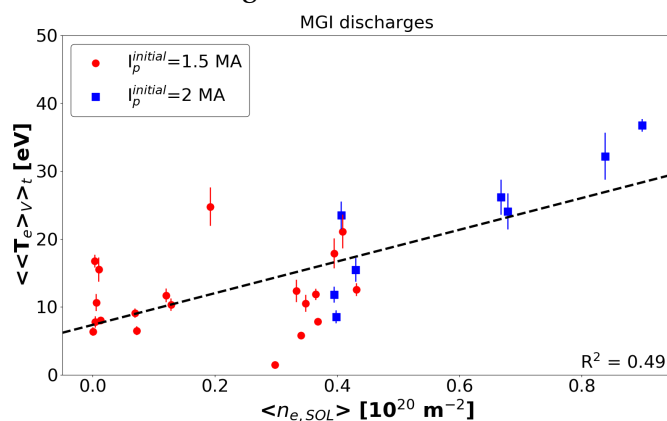


Figure 3.32.: Dependence of the time and volume averaged background plasma temperature $\langle\langle T_e \rangle_V \rangle_t$ on the averaged core electron density $\langle n_{e,core} \rangle$ for the MGI discharges.

The time and volume averaged temperature $\langle\langle T_e \rangle_V \rangle_t$ of the MGI discharges increase with the electron density in the far-SOL as shown in the figure 3.32.

It can be observed from the figure 3.33 that that time and volume averaged electron temperature $\langle\langle T_e \rangle_V \rangle_t$ increase with the argon MMI amount. For SPI discharges shown in the figure 3.33, the trend is not clear as the range of Ar MMI amounts are rather narrow as disruptions are triggered using Ar SPI from barrel B ($\sim 60-70 \text{ Pa}\cdot\text{m}^3$). It is to be noted that the MGI amounts are estimated based on difference in initial to final pressure of the reservoir. For the SPI discharges, amounts are taken from the logbook of the SPI operator in the JET tokamak. From the figure 3.33, it can also be observed that background plasma is hotter for MGI discharges than SPI discharges.

The background plasma temperatures $\langle\langle T_e \rangle_V \rangle_t$ show no clear correlation with the runaway current I_{RE} . For the MGI discharges, the background plasma temperature $\langle\langle T_e \rangle_V \rangle_t$ increases with input power density of the RE beam $\langle I_{RE} \times V_{loop} / V_{plasma} \rangle$ as shown in the figure 3.34(a). For the SPI discharges, the background plasma tempera-

ture $\langle\langle T_e \rangle_V \rangle_t$ decreases with input power density of the RE beam $\langle I_{RE} \times V_{loop} / V_{plasma} \rangle$ as shown in the figure 3.34(b).

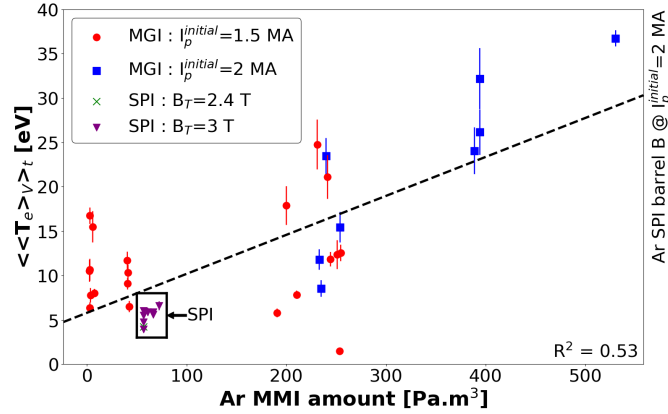


Figure 3.33.: Dependence of the time and volume averaged background plasma temperature $\langle\langle T_e \rangle_V \rangle_t$ on the amount of Ar MMI used to trigger the background plasma for MGI and SPI discharges.

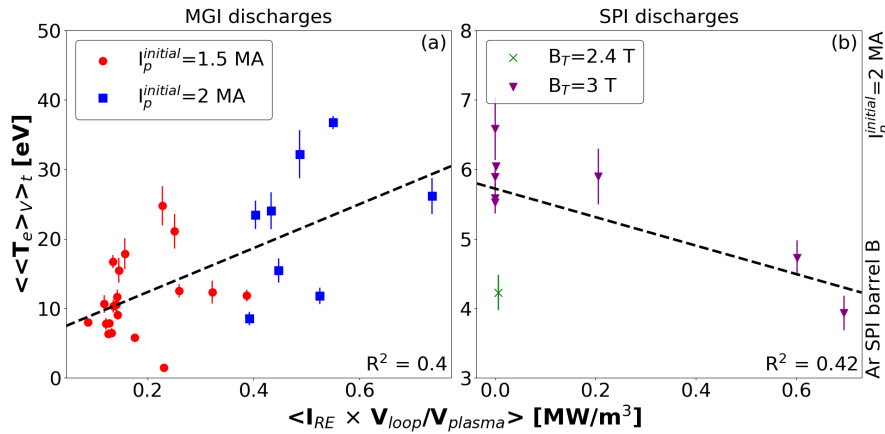


Figure 3.34.: Dependence of the time and volume averaged background plasma temperature $\langle\langle T_e \rangle_V \rangle_t$ on the input power $\langle I_{RE} \times V_{loop} / V_{plasma} \rangle$ for (a) MGI and (b) SPI discharges. V_{loop} is the loop voltage measured by magnetics and V_{plasma} is the volume of the RE beam.

Similar to time and volume averaged background plasma temperature $\langle\langle T_e \rangle_V \rangle_t$, the time and volume averaged core temperature of the background plasma $\langle T_e^0 \rangle_t$ shows no clear dependence on the core density $\langle n_{e,core} \rangle$ for the MGI discharges as shown in the figure 3.35(a). However for the SPI discharges, the core electron temperature increases with the core electron density as shown in the figure 3.35(b). It is reminded that core density measurement for the MGI discharges are only the lower bounds whereas for the SPI discharges, calculated core density measurements are absolute.

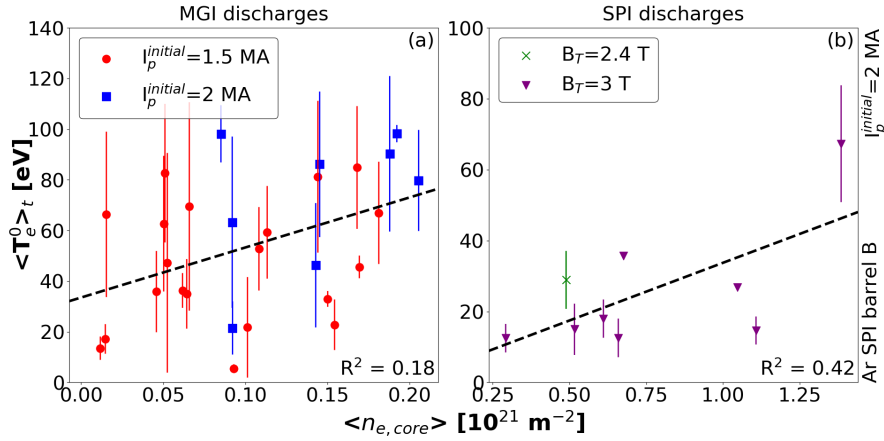


Figure 3.35.: Dependence of the time-averaged core background plasma temperature $\langle T_e^0 \rangle_t$ on the core electron density $\langle n_{e,core} \rangle$ for (a) MGI and (b) SPI discharges.

The core temperature of the background plasma $\langle T_e^0 \rangle_t$ show no clear dependency on the input power density of the RE beam $\langle I_{RE} \times V_{loop} / V_{plasma} \rangle$ as shown in the figures 3.36(a) and 3.36(b).

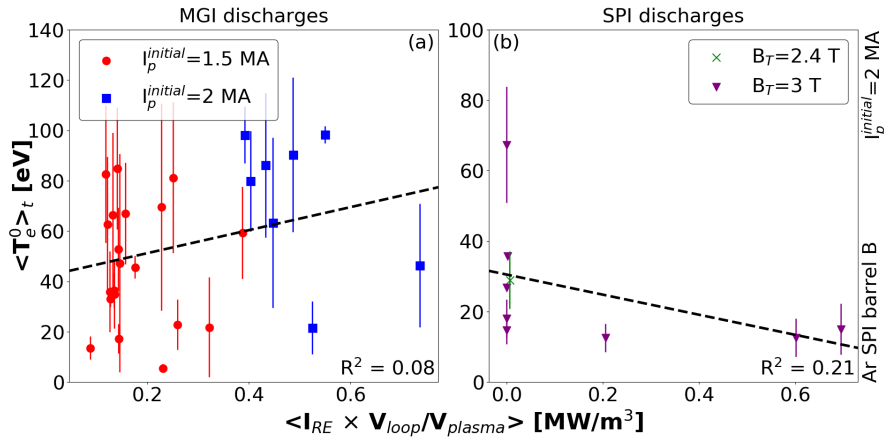


Figure 3.36.: Dependence of the time-averaged core background plasma temperature $\langle T_e^0 \rangle_t$ on the input power $\langle I_{RE} \times V_{loop} / V_{plasma} \rangle$ for (a) MGI and (b) SPI discharges. V_{loop} is the loop voltage measured by magnetics and V_{plasma} is the volume of the RE beam.

No correlation between time and volume averaged separatrix temperature $\langle T_e^{LCFS} \rangle_t$ and the averaged electron density on the SOL $\langle n_{e,SOL} \rangle$ was observed for the MGI discharges as shown in the figure 3.37.

From the table 3.2, it can be seen that MGI discharges tend to have hotter background plasmas than SPI discharges. It is important to mention here that MGI discharges were performed with limiter configuration whereas SPI discharges were performed with divertor configuration. In the core of the plasma, MGI discharges are much hotter than the SPI discharges. In the open field line region (SOL), temperatures

of MGI and SPI discharges are comparable. The estimated background plasma temperature is consistent with previous estimates of 5-15 eV using the identified lines of the VUV spectra (Reux 2017).

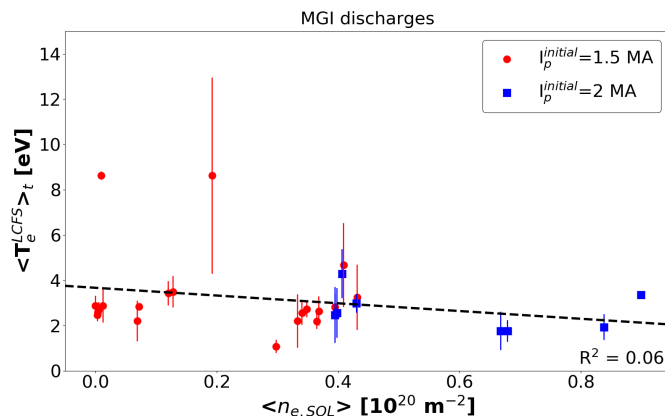


Figure 3.37.: Dependence of the time-averaged background plasma temperature in the separatrix $\langle T_e^{LCFS} \rangle_t$ on the core electron density $\langle n_{e,core} \rangle$ for MGI discharges.

Quantity	Values	
	MGI	SPI
$\langle \langle T_e \rangle_V \rangle_t$	1.5-36.7 eV 71% between 5.8-17.9 eV	3.9-6.6 eV 78% between 4.2-6 eV
$\langle T_e^0 \rangle_t$	5.5-98.2 eV 71% between 22.8-86.1 eV	12.5-67.3 eV 78% between 12.5-28.9 eV
$\langle T_e^{LCFS} \rangle_t$	1.1-8.6 eV 71% between 2.2-3.5 eV	2.7-5.4 eV 78% between 2.7-4.6 eV

Table 3.2.: Range of background plasma temperatures for MGI and SPI discharges

Background plasmas of the JET tokamak trigger using Ar MGI (5.8-17.9 eV for 71% of discharges) are much hotter than DIII-D background plasmas (1-2 eV from (Hollmann 2011)). This is consistent with the qualitative VUV spectra comparison between JET-ILW discharges and DIII-D discharges (figures 3.28(i) and 3.28(ii)).

The agreement between the linear regression and the data are determined using the coefficient of determination R^2 (Press 1992). The R^2 for different temperature profile quantities and the dependence parameters are tabulated in the table 3.3.

Strong correlation from the analysis are summarized : the time and averaged temperature of the background plasma $\langle \langle T_e \rangle_V \rangle_t$ increases with density in the far-SOL $\langle n_{e,SOL} \rangle$, amount of Ar MMI used to trigger the background plasma and the input power $\langle I_{RE} \times V_{loop} / V_{plasma} \rangle$.

Quantity	R^2 of dependency parameters							
	MMI Amount		$\langle n_{e,core} \rangle$		$\langle n_{e,SOL} \rangle$		$\langle I_{RE} \times V_{loop}/V_{plasma} \rangle$	
	MGI	SPI	MGI	SPI	MGI	SPI	MGI	SPI
$\langle \langle T_e \rangle_V \rangle_t$	0.46	0.44	0.3	0.3	0.49	-	0.4	0.42
$\langle T_e^0 \rangle_t$	0.1	0.25	0.18	0.42	0.19	-	0.08	0.21
$\langle T_e^{LCFS} \rangle_t$	0.04	0.06	0.03	0.14	0.07	-	0.04	0.06

Table 3.3.: The coefficient of determination R^2 of temperature profiles with dependent plasma quantities for the database. $R^2=0$ and 1 indicates worst and best agreement of the linear regression with the data.

3.3.3. Analysis of Ar SPI as trigger injection

In this section, discharges in which disruptions are triggered using Ar SPI are analyzed.

3.3.3.1. Qualitative VUV analysis: Ar SPI as trigger injection

During the thermal and current quench, the VUV spectrometers are saturated for few tens of ms. This is a problem for SPI discharges as RE beam durations are very short, between 6-26ms in the database. Thus, the gain of the VUV spectrometer was lowered so that useful information on the background plasmas triggered by Ar SPI can be obtained.

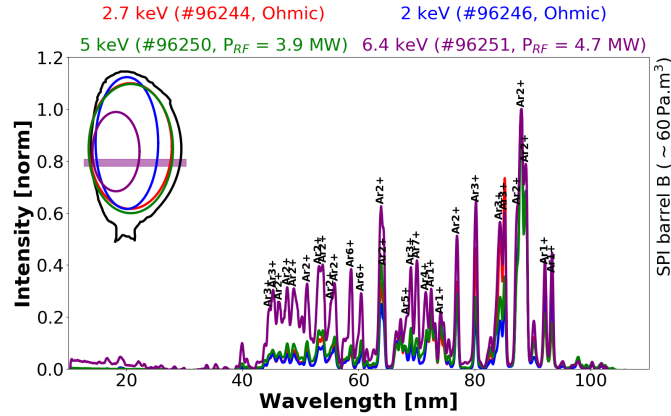


Figure 3.38.: Comparison of VUV spectra of discharges with different pre-disruption initial T_e in which background plasma is triggered using Ar SPI from barrel B (with $\sim 60 \text{ Pa.m}^3$). Different RF powers are used to increase the temperature value. NBI heatings are absent in the discharges. Electron density before disruption is less than $5 \times 10^{19} \text{ m}^{-2}$.

From the VUV spectra of argon background plasmas triggered using SPI shown in the figure 3.38, it can be observed that most intense lines are between 85-100 nm.

In addition, the lines are much different than the MGI discharges (figure 3.27 for instance). However, it should be noted that MGI discharges are in limiter configuration whereas the SPI discharges are in divertor configuration. Thus, it is not clear whether the difference is solely due to MGI and SPI or there is an effect of plasma configuration on the VUV spectra.

The impact of initial electron temperature before disruption on the VUV spectra of the background plasmas are studied using the figure 3.38. Using the RF additional heating, the pre-disruption temperature $T_e^{initial}$ of the plasmas are increased and background plasmas are triggered using Ar SPI from barrel B. It can be seen from the figure 3.38 that no significant change in the VUV spectra are observed for different pre-disruption temperatures. Thus, the background plasmas seems to be independent of the pre-disruption electron temperature.

It is to be noted that in the discharge #96251, the most brightest line intensities (around 85-100 nm) are a magnitude lower than other discharges. However, line intensities between 40-60 nm are in the same order of magnitudes. Thus, the relative line intensities between 40-60 nm look brighter in discharge #96251 than other discharges. The decrease in the line intensity is due to the fact that VUV spectrum in discharge #96251 is taken later during the RE beam than other discharges.

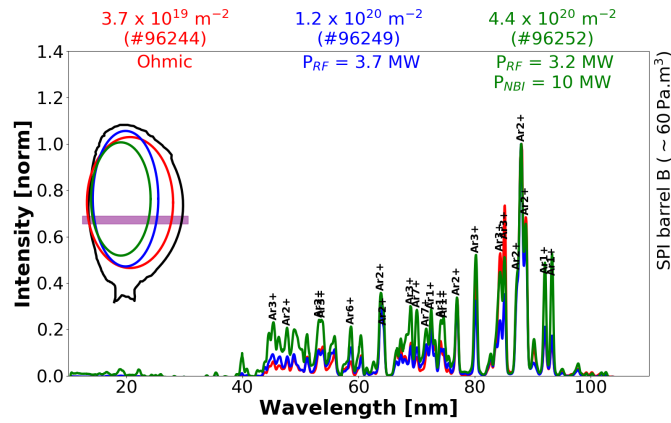


Figure 3.39.: Comparison of VUV spectra of discharges with different pre-disruption initial n_e in which background plasma is triggered using Ar SPI from barrel B (with $\sim 60 \text{ Pa}\cdot\text{m}^3$). Different RF and NBI heating powers are used. $T_e^{initial} \sim 3 \text{ keV}$ before disruption for all discharges.

Using the RF and NBI additional heating, the electron temperature and densities are increased during the flat-top phase. Argon background plasmas are generated using Ar SPI from barrel B. On looking at the shape of the VUV spectra, no significant difference can be observed as shown in the figures 3.39 and 3.40, although absolute line intensities are different for different discharges due to change in the electron density values. In the figure 3.39, $T_e^{initial} \sim 3 \text{ keV}$ whereas in figure 3.40, $T_e^{initial} \sim 6 \text{ keV}$.

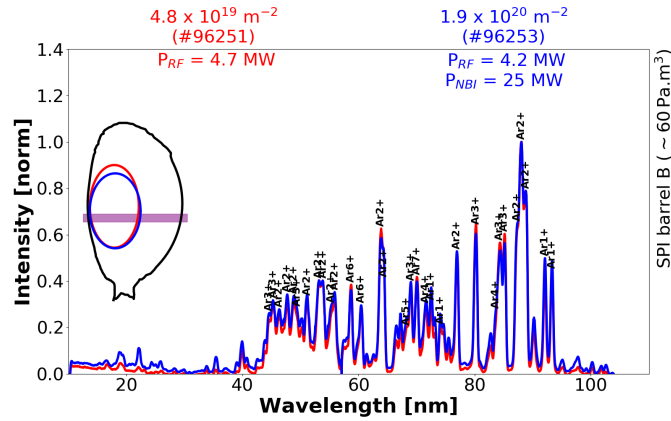


Figure 3.40.: Comparison of VUV spectra of discharges with different pre-disruption initial n_e in which background plasma is triggered using Ar SPI from barrel B (with $\sim 60 \text{ Pa.m}^3$). Different RF and NBI heating powers are used. $T_e^{initial} \sim 6 \text{ keV}$ before disruption for all discharges.

In some of the discharges, pellets are broken before reaching the shattering cone. The microwave cavity diagnostics of the SPI system is used to check the integrity of the pellets. The VUV spectra of the argon background plasmas with different pellet integrity is shown in the figure 3.41. On looking at the VUV spectra, no significant change was observed due to the pellet integrity. The three pellets have different values of initial electron density and the pre-disruption temperature is $T_e^{initial} \sim 3 \text{ keV}$.

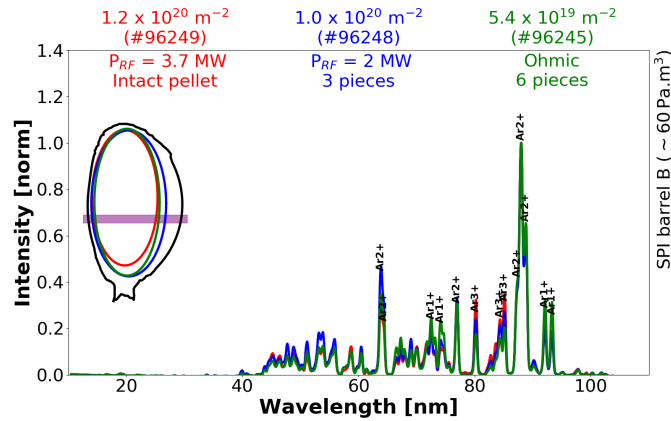


Figure 3.41.: Comparison of VUV spectra of discharges with different pellet integrity. The background plasma is triggered using Ar SPI from barrel B (with $\sim 60 \text{ Pa.m}^3$). Different RF powers are used and NBI additional heating is absent. $T_e^{initial} \sim 3 \text{ keV}$ before disruption for all discharges.

3.3.3.2. Quantitative analysis of discharges with Ar SPI as trigger injection

When disruptions are triggered using Ar SPI, in addition to Ar SPI amount and electron density of the background plasma, there are four other parameters which could change the background plasma temperature : pre-disruption temperature $T_e^{initial}$,

pre-disruption density $n_e^{density}$, additional heating using RF and NBI heating and integrity of the pellets before reaching the shattering bent tube. The pre-disruption temperature and density are consequences of additional heating. Therefore in the analysis, the integrity of the pellet is shown in the scatter ("solid" points implies intact pellets and "hollow" points indicate broken pellets) whereas the other defining parameter (usually $n_e^{initial}$ or $T_e^{initial}$) is reflected in the size of the markers. It is to be noted that RE beams are shorter when triggered by Ar SPI. Thus, the current carried by the thermal plasma may be significant in these discharges as compared to longer RE beams.

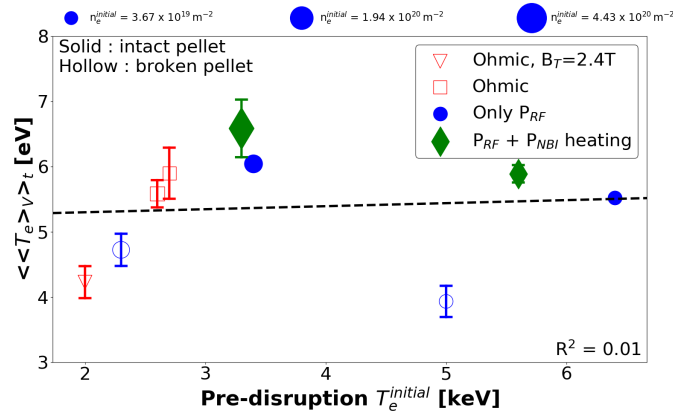


Figure 3.42.: Dependence of the temperature of the background plasma $\langle\langle T_e \rangle\rangle_t$ on the pre-disruption plasma temperature $T_e^{initial}$. Background plasmas are triggered using $\sim 60 \text{ Pa.m}^3$ Ar using SPI from barrel B. Scatter sizes corresponds to the value of pre-disruption electron density $n_e^{initial}$. Solid points indicates an intact pellet and hollow points indicate broken pellets.

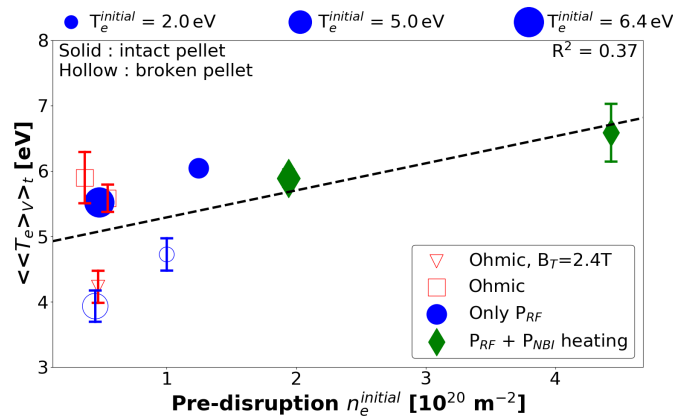


Figure 3.43.: Dependence of the temperature of the background plasma $\langle\langle T_e \rangle\rangle_t$ on the pre-disruption plasma current $n_e^{initial}$. Background plasmas are triggered using $\sim 60 \text{ Pa.m}^3$ Ar using SPI from barrel B. Marker sizes corresponds to the value of pre-disruption electron temperature $T_e^{initial}$. Solid points indicates an intact pellet and hollow points indicate broken pellets.

The electron temperature of the background plasma $\langle\langle T_e \rangle_V \rangle_t$ triggered by Ar SPI from barrel B shows no dependence on the pre-disruption electron temperature $T_e^{initial}$ as shown in the figure 3.42. This is consistent with the qualitative analysis of the VUV spectra shown in the figure 3.38.

The electron temperature of the background plasma $\langle\langle T_e \rangle_V \rangle_t$ triggered by Ar SPI from barrel B increases with the pre-disruption electron density $n_e^{initial}$ as shown in the figure 3.43. In these discharges, electron densities are increased using additional RF and NBI heating. Higher pre-disruption density $n_e^{initial}$ shows a small correlation with higher core electron density $n_{e,core}$.

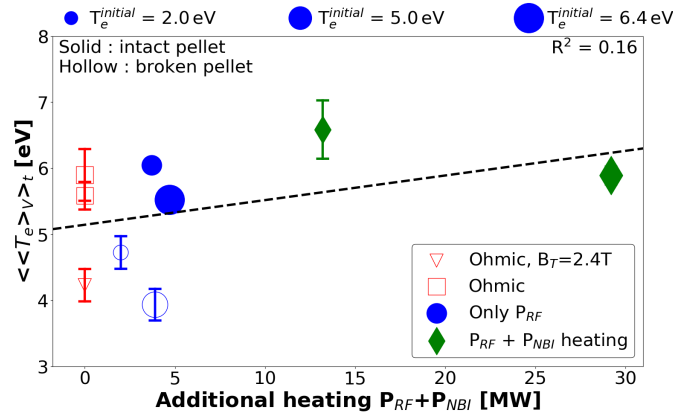


Figure 3.44.: Dependence of the temperature of the background plasma $\langle\langle T_e \rangle_V \rangle_t$ on the total additional power $P_{RF} + P_{NBI}$. Background plasmas are triggered using $\sim 60 \text{ Pa.m}^3$ Ar using SPI from barrel B. Scatter sizes corresponds to the value of pre-disruption electron temperature $T_e^{initial}$. Solid points indicates an intact pellet and hollow points indicate broken pellets.

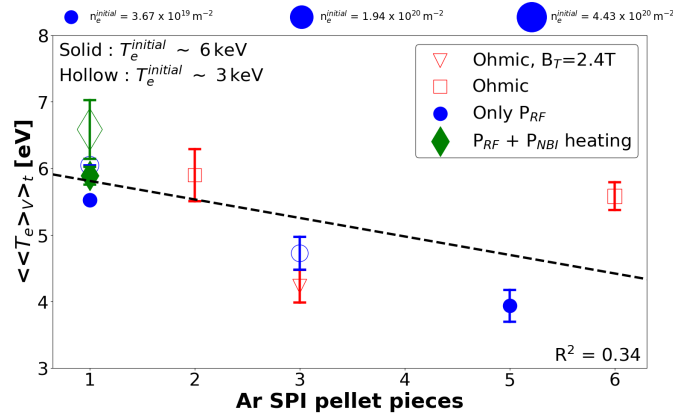


Figure 3.45.: Dependence of the temperature of the background plasma $\langle\langle T_e \rangle_V \rangle_t$ on the pellet integrity. Background plasmas are triggered using $\sim 60 \text{ Pa.m}^3$ Ar using SPI from barrel B. Scatter sizes corresponds to the value of pre-disruption electron density $n_e^{initial}$. Solid points indicates an intact pellet and hollow points indicate broken pellets.

Increasing the additional heating increases the pre-disruption temperature $T_e^{initial}$. The pre-disruption density $n_e^{initial}$ is also increased by NBI heating. From the figure 3.44, it can be seen that increasing the additional heating increases the temperature of the background plasma but the dependence is very weak.

It can be observed that intact pellet seems to have hotter background plasmas as compared to the pellets broken inside the SPI flight tube before reaching the shattering bent tube as shown in the figure 3.45.

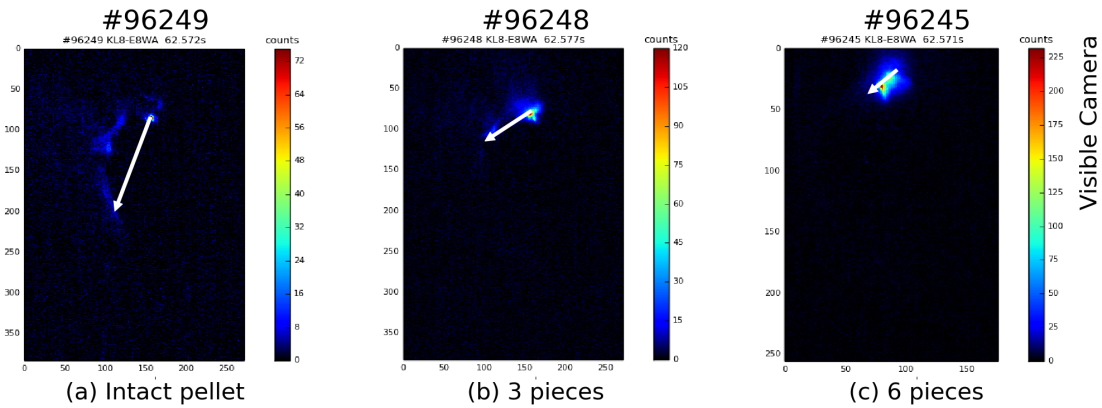


Figure 3.46.: Penetration of Ar SPI pellets seen through visible camera without filters, for (a) #96249, intact pellet (b) #96248, pellet broken into 3 pieces and (c) #96245, pellet broken in to 6 pieces. The white arrow shows the penetration dept of the pellet.

From the figure 3.46(a), the intact pellet seems to penetrate deeper into the plasma as compared to pellets broken into multiple pieces, figure 3.46(b) and 3.46(c). Thus, higher temperatures may be due to the deeper penetration of the Ar SPI pellets.

It is to be noted that the intact pellets coincidentally have higher electron density before disruptions. Even though intact pellets seems to have a better penetration, hotter electron temperature of the background plasma may just be due to higher density.

3.3.4. Analysis of discharges with Ar MMI as killer injection

In the third set of experiments, argon background plasma is triggered using $\sim 3 \text{ Pa.m}^3$ of Ar MGI in the JET tokamak. Mitigation the RE beam is attempted using Ar MMI into the background plasma.

3.3.4.1. Qualitative comparison of MGI and SPI

In the figure 3.47, the VUV spectra $\sim 45 \text{ ms}$ after the triggering of the Ar MMI are compared for different killer MMIs : Ar SPI from barrel B with 64 Pa.m^3 (blue), Ar SPI from barrel A with 244 Pa.m^3 (red) and Ar MGI from DMV2 with 283 Pa.m^3 (green). The VUV spectrometer views identical plasma regions for all the three discharges.

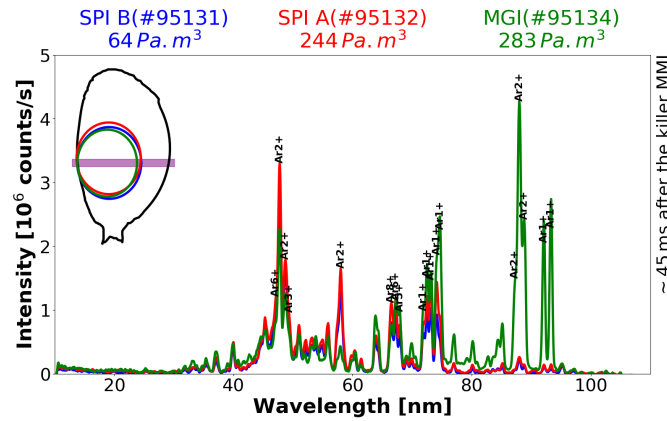


Figure 3.47.: Comparison of VUV spectra of discharges with MGI and SPI as killer injection. Argon background plasma is triggered using $\sim 3 \text{ Pa.m}^3$ Ar MGI. The VUV spectra are taken $\sim 45 \text{ ms}$ after the killer injection.

At lower wavelengths (40-60 nm), the VUV spectra due to different SPI pellets and MGI are identical. In the mid wavelengths (60-80 nm), the VUV line intensities are roughly the same although the MGI line intensities are marginally higher than SPI pellets. At higher wavelengths (85-100 nm), there is a significant difference between the MGI and SPI VUV spectra. The line intensities of the MGI discharge at higher wavelength is much higher than SPI discharges. This may indicate that the temperatures of background plasmas due to killer MGI and SPI pellets is different.

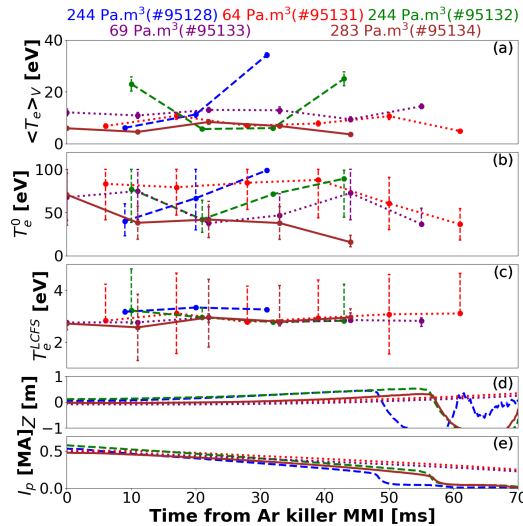


Figure 3.48.: Time evolution of (a) volume averaged temperature profile $\langle T_e \rangle_V$, (b) core temperature T_e^0 , (c) temperature at separatrix T_e^{LCFS} , (d) plasma vertical position Z and (e) plasma current I_p . Background plasmas are triggered by $\sim 3 \text{ Pa.m}^3$ Ar MGI. Killer MMIs are SPI pellet from barrel A (dashed), SPI pellet from barrel B (dotted) and MGI (solid).

No clear trend in the evolution of the argon background plasma following the killer

MMI is observed from the figure 3.48. In these experiments, Ar SPI from barrel A ($\sim 240 \text{ Pa.m}^3$), Ar SPI from barrel B ($\sim 70 \text{ Pa.m}^3$) and Ar MGI are used as killer injections. In these discharges, $\sim 3 \text{ Pa.m}^3$ of Ar MGI are used to trigger disruptions. On analyzing the time and volume averaged temperature $\langle \langle T_e \rangle_V \rangle_t$ of the background plasma, it can be seen from the figure 3.49 that the background plasma due to Ar SPI from barrel A have higher temperature ($\sim 14\text{-}18 \text{ eV}$) than Ar SPI from barrel B ($\sim 8\text{-}12 \text{ eV}$) and Ar MGI ($\sim 6 \text{ eV}$). It is to be noted that when Ar SPI is used as trigger injection, background plasma is colder than Ar MGI as shown in the figure 3.33. It can be observed that Ar SPI from barrel A shut down the RE beam faster than SPI from barrel B and MGI killer injections as shown in the figure 3.50.

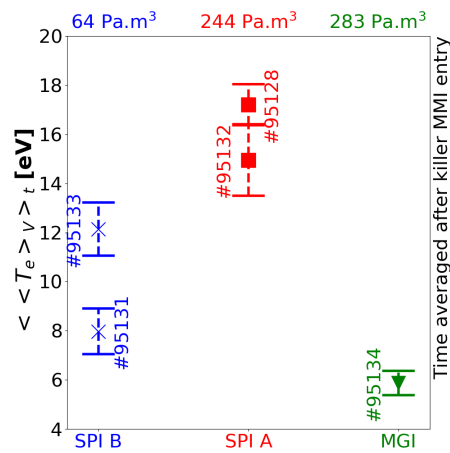


Figure 3.49.: time and volume averaged temperatures of background plasmas $\langle \langle T_e \rangle_V \rangle_t$ following the killer MMI into the argon background plasma. Temperature profiles averaged after killer MMI entry until the beam termination.

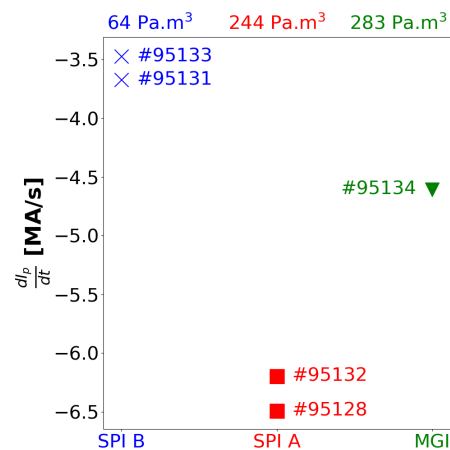


Figure 3.50.: Rate at which the plasma current decays $\frac{dI_p}{dt}$ following the killer MMI until the final collapse.

It should be noted that during the JET-SPI experiments, Ar SPI as a killer injection

was tested only in the low density background plasma (triggered using $\sim 3 \text{ Pa}\cdot\text{m}^3$ of Ar MGI) with low background plasma temperature. MGI killer injections were also successful in RE beam mitigation under similar conditions. The mitigation efficiency of Ar SPI as a killer injection may be different at higher electron density and temperature of the background plasmas and it should be tested experimentally.

The characterization of the background plasmas is the first stage in understanding how the RE beam reacts with the killer injection in the presence of the cold background plasma. The chapter 4 is dedicated to the development of a simple 0D/1D power balance to understand the RE beam interaction with the background plasma and assess the credibility of the temperature measurements using VUV spectroscopy.

3.3.5. Conclusions

- JET background plasma hotter ($T_e \sim 6\text{-}18 \text{ eV}$ for Ar MGI discharges and $T_e \sim 4\text{-}6 \text{ eV}$ for Ar SPI discharges) than on other tokamaks (DIII-D, $T_e \sim 1\text{-}2 \text{ eV}$ ([Hollmann 2011](#)))
- Background plasma temperature increases with gas amount used to trigger disruption and electron density.
- If disruptions are triggered using Ar SPI, background plasma temperatures are higher for intact pellets and are weakly correlated with the pre-disruption electron density.

4. 0D/1D Power balance

For a reliable MMI to mitigate the RE beam, it is important to understand the interaction between the RE beam and the background plasma. In this section, the interactions are studied by using a 0D/1D power balance of the post-disruption systems (RE beam and the background plasma).

During the post-disruption plasma phase, the RE beam coexists with the cold background plasma created by the initial injection. The background plasma is not limited to the confined region defined by the last closed flux surface (LCFS). It is also present in the open field line region.

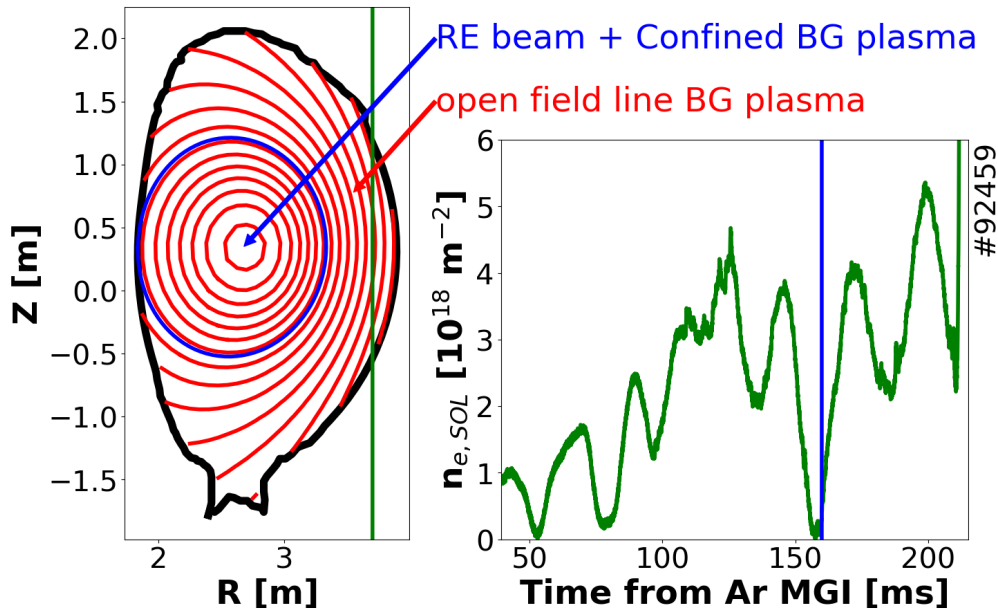


Figure 4.1.: Illustration of post-disruption systems

Even in the far-SOL, the background plasma is present with significant electron density ($\sim 10^{18} \text{ m}^{-2}$ in interferometry chord4) as shown in the figure 4.1. Thus, the background plasma can be present both in the confined region defined by the separatrix and also in the open field line region.

The background plasma in the open field line region has high line-integrated electron density ($10^{18} - 10^{19} \text{ m}^{-2}$) and significant plasma temperature ($T_e \sim 1-9 \text{ eV}$, from VUV spectroscopy). Thus, it is important to consider the background plasma in the open field line region for the power balance. Before making a more detailed 1D power balance, first a simple 0D power balance is performed in the section 4.2. The total radiated power measured by the bolometry in JET is discussed in the section 4.1.

4.1. Bolometer system in JET

The free electrons of the tokamak plasma loses power through line radiation. This line radiated power loss is a very important quantity of the background plasma. Using a device called bolometer, the power lost by the background plasma through line radiation is measured.

In a bolometer, a thin layer of absorptive materials is connected to a thermal reservoir through a thermal contact. The radiation impinging on the absorptive material raises the temperature. The raise in temperature is directly related to the power of the impinging radiation. Thus, by measuring the raise in temperature through electrical circuits, the power of the incident radiation is measured.

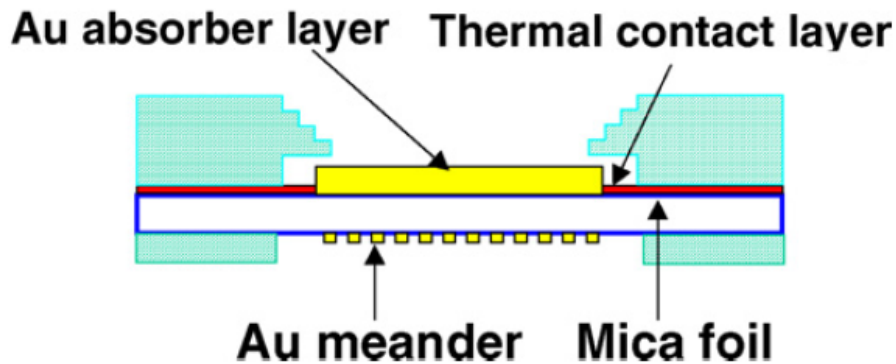


Figure 4.2.: Schematic representation of the bolometer detector head used in JET (Huber 2007)

A schematic representation of a bolometer head used in JET is shown in the figure 4.2 taken from (Huber 2007). The bolometer head consists of $8\ \mu\text{m}$ -thick gold absorber layer connected to $20\ \mu\text{m}$ -thick mica substrate through thermal contact layer. On the other side of the mica substrate, interwoven gold meanders with a typical resistance of $1.2\ \text{k}\Omega$ are connected as shown in the figure 4.2.

The power absorbed by the mica foil is monitored by its temperature and the consequent rise in resistance of the gold meanders. A second reference bolometer is employed which is optically shielded from the plasma to compensate for temperature drifts and electromagnetic disturbances. The reference and measurement meanders are connected to the Wheatstone bridge such that the output voltage $\Delta U(t)$ corresponds to the temperature excursion of the gold absorber. The power incident on the bolometer $P(t)$ according to the bolometer equation (Murari 1995) can be given by,

$$P(t) = \frac{\tau_c}{S_{bolo}} \left(\frac{d\Delta U(t)}{dt} + \frac{\Delta U(t)}{\tau_c} \right) \quad (4.1)$$

where $\Delta U(t)$ is the output voltage. S_{bolo} (in V/W) is the sensitivity and τ_c is the cooling time constant of the mica foil which are determined by calibration of the bolometers. The gold absorptive layer is sensitive in the spectral range from 0.1-480 nm which corresponds to the photon energy of $\sim 10\ \text{keV}$ to $2.5\ \text{eV}$.

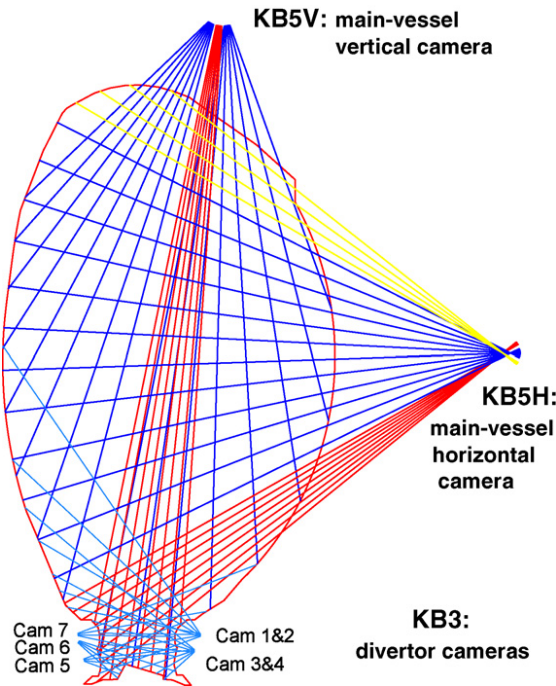


Figure 4.3.: Lines of sight of the bolometer system in JET (Huber 2007)

As shown in the figure 4.3, there are two main-vessel bolometric cameras: vertical camera (KB5V) and horizontal camera (KB5H). Both the camera collects radiation along 24 chords. The toroidal location of the cameras are shown in the figure 2.21. More information on the bolometer system in JET is given in (McCormick 2005) and (Huber 2007).

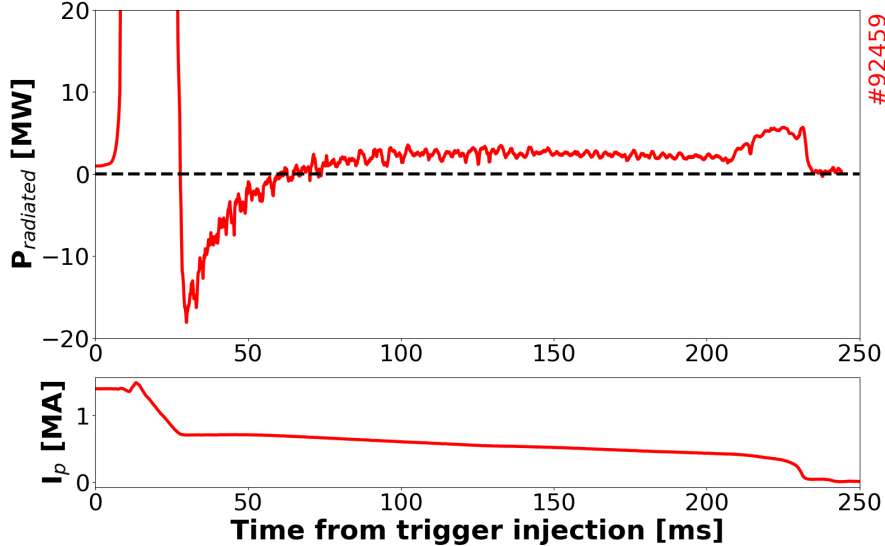


Figure 4.4.: Illustration of negative bolometer reading during high-Z gas injections in JET

During RE mitigation experiments in JET where disruptions are triggered using Massive Gas Injection (MGI), the bolometer reaches negative values after the radiation

peak as shown in the figure 4.4 for the JET discharge #92459 where disruptions are triggered using Ar MGI from DMV2 (see section 2.5.3.3).

As shown in the figure 2.21, both vertical bolometer camera and DMV2 are located close to each other. The massive materials from DMV2 may cool down the gold foil to temperatures lower than the thermal reservoir. This may be a possible reason for negative bolometer measurements.

It can also be observed from the figure 4.4 that after few ms, the negative bolometer measurements recover. It is to be noted that at the end of the discharge, the bolometer measurements reaches zero. Thus, it can be assumed that after bolometer recovery, the measurements are absolute with no offset due to negative measurement.

4.2. Simple 0D model

As a first step to understand the RE beam interaction with the background plasma, a simple 0D model of the power balance is proposed : the input power of the runaway electron beam ($I_{RE} \times V_{loop}$) is transferred to the background plasma. $I_{RE} \times V_{loop}$ is roughly the power gained by the runaway electron beam due to parallel electric field. It is the simplified form of E-field accelerated power given in the equation 4.3. The power is lost by the background plasma through radiation and conduction. Assuming that power conducted from the background plasma is negligible as compared to the radiated power, the input power of the RE beam balances the radiated power from the background plasma.

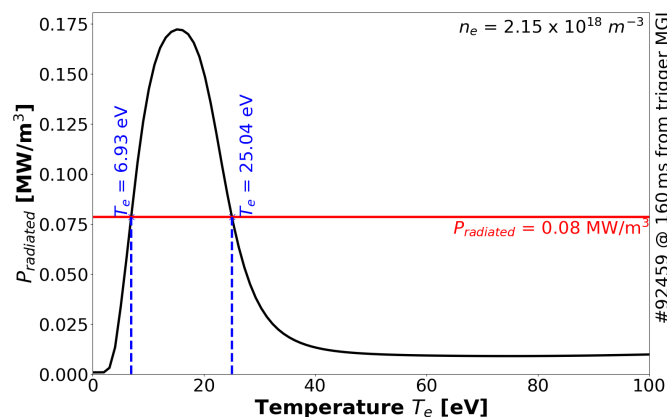


Figure 4.5.: 0D estimation of the electron temperature for the JET discharge #92459 at 160ms from the trigger gas MGI. Line-integrated density is measured from interferometry chord 4 (green vertical line). Blue vertical line shows the time which equilibrium is reconstructed (red data lines) by EFIT.

The radiated power of the background plasma is a non-monotonous function of the electron temperature as shown in the figure 4.5 (more information in the section 4.4). Considering a homogeneous background plasma, two temperature values can be estimated by matching the value of the radiated power (measured by the bolometry). For instance, for the JET discharge #92459 with radiated power 2.6 MW

($P_{radiated} = 0.08 \text{ MW/m}^3$), the 0D estimates of the electron temperatures are 6.93 eV or 25.04 eV as shown in the figure 4.5. This is consistent with the volume average electron temperature of the background plasma was estimated at 7.44 eV (14 eV in the center and 3 eV in the separatrix) using VUV spectroscopy for the discharge #92459 as shown in the figure 3.26.

In the section 3.3, heterogeneity in the background plasma was observed through VUV spectra. Thus, it may be possible that both the temperatures estimated by the 0D model maybe present in the background plasma but different regions. Thus, a profile in the electron temperature should be considered instead of a 0D estimate. Using a profile in the electron temperature, a more advanced model of the power balance is proposed in the following section including all possible interactions between the systems.

4.3. 1D power balance : Interactions overview

As seen in the introductory part of this chapter, the RE beam co-exists with the background plasma during the post-disruption phase. It was also seen that the background plasma is not limited to the confined region described by the separatrix. Thus, for the 1D power balance, three systems are considered :

1. Runaway electron (RE) beam
2. Background plasma in the confined region defined by the last closed flux surface (LCFS, also called separatrix)
3. Background plasma in the open field line region (SOL)

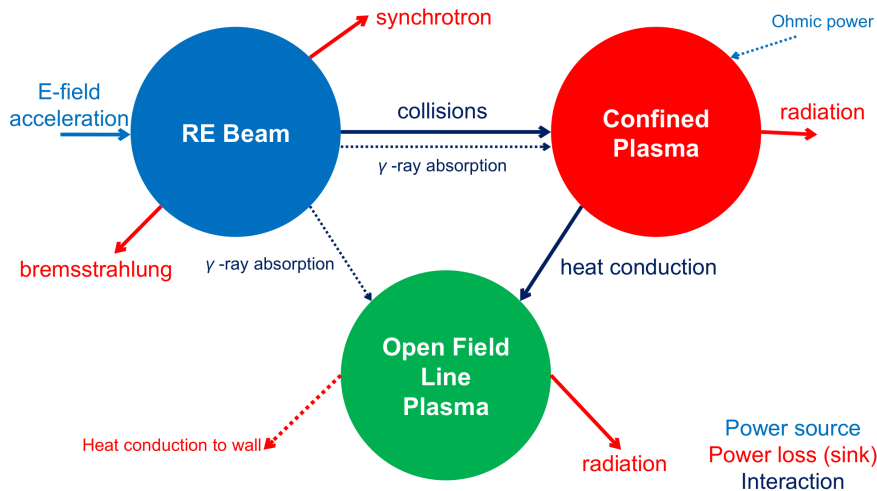


Figure 4.6.: Illustration of post-disruption systems

These three systems interact with each other which is of interest in the 1D power balance. An overview of how the post-disruption plasma systems interact with each other is illustrated in figure 4.6. Runaway electrons are accelerated by the electric field

and lose part of their power through synchrotron radiation and bremsstrahlung. In addition, runaway electrons transfer the majority of their power through collisions to the background plasma in the confined region. These collisions act as a power source for the background plasma in the confined region. In addition to the collisional power transfer, ohmic power also feeds the background plasma in the confined region. Significant power is lost from the background plasma due to radiation. Power loss can also be in the form of conduction to the open field line region from the background plasma in the confined region. This power conduction may be the reason for the sustainment of the background plasma in the open field line region. The background plasma in the open field line region loses its power through radiation and heat conduction to the wall.

A steady-state system is considered during the power balance of the RE beam and the background plasma. The background plasma evolves very slowly during the RE plateau phase (see figure 3.30 for reference). For the RE beam, RE current and hard x-ray signal are constant during RE plateau phase and thus steady-state system could be assumed for simplicity. In addition, no significant wall impact of the RE beam is seen by the camera during the RE plateau phase. The power terms are computed using analytical formulae.

4.4. Estimation of power terms

The mechanisms by which the RE beam and the background plasma interact are shown in the figure 4.6. Using analytical formulae, the interaction power terms are estimated which is the subject of this section. For this section, the plasma parameters (I_{RE} , $E_{||}^{RE}$, V_{RE} , B_T , n_e , T_e , q_{edge}) used in the example figures given below are taken from discharge #92459.

4.4.1. Power terms of the RE beam

For the estimation of power terms of the RE beam, the energy distribution of RE beam should be defined. For simplicity, a normally distributed runaway electron energy distribution function f_{RE} is assumed of the form,

$$f_{RE}(E_{RE}) = a_{REdist} \cdot \exp\left(\frac{-(E_{RE} - E_{RE}^0)^2}{2\sigma_{REdist}^2}\right) \quad (4.2)$$

where E_{RE}^0 is the central energy of the runaway electron distribution. a_{REdist} is the amplitude term computed such that $\int f_{RE} \cdot dE_{RE} = n_{RE}$. The spread of the distribution σ_{REdist} is estimate by from the FWHM(Full Width at Half Maximum, FWHM=2 MeV is assumed) of the runaway electron beam.

An example of runaway electron energy distribution function is shown in figure 4.7. Central energy of $E_{RE}^0 = 10$ MeV and FWHM= 2 MeV is assumed in figure 4.7 with runaway electron density $n_r = 10^{16} \text{ m}^{-3}$. The runaway distribution function f_{RE} given

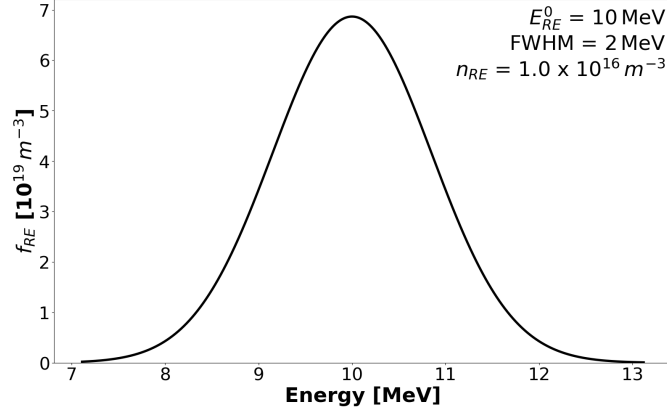


Figure 4.7.: An example of RE distribution function for a RE beam with $E_{RE}^0=10$ MeV in the equation 4.2 is used in the estimation of the power terms using n_{RE} estimation from plasma current.

4.4.1.1. E-field acceleration of the RE beam

Runaway electrons are accelerated by the electric field and are the primary power source of runaway electron beam. The power due to the electric field acceleration is given by,

$$P_{E\text{-field acceleration}} = e \cdot E_{\parallel}^{RE} \cdot V_{RE} \int_{v_1}^{v_2} v_{RE} \cdot f_{RE}(v) \cdot dv \quad (4.3)$$

where E_{\parallel}^{RE} is the parallel electric field action on the runaway electron beam and v_{RE} is the velocity. f_{RE} is the runaway electron distribution function given in equation 4.3. e is the electron charge and V_{RE} is the volume of the runaway electron beam. The electric field E_{\parallel}^{RE} is estimated from the loop voltage measurements. v_1 and v_2 are the velocity bounds of the RE distribution function. From the equation 4.3, it can be observed that electric field acceleration of the RE beam depends mainly on the electric field E_{\parallel}^{RE} and the runaway density n_{RE} . It has a very weak dependence on the energy of the RE beam as shown in the figure 4.8.

4.4.1.2. Synchrotron radiation loss of the RE beam

The relativistic runaway electrons in the presence of the magnetic field loses its power due to synchrotron emission. The power radiated by a single relativistic electron due to synchrotron radiation in the presence of magnetic field B can be expressed from (Stahl 2017) as,

$$P_{synchrotron}^{e^-} = \frac{e^4 B^2 \sin^2(\mu) v_{RE}^2 \gamma^2 (v_{RE})}{6\pi\epsilon_0 m_e^2 c^3} \quad (4.4)$$

where μ is the pitch angle of the synchrotron emission and v_{RE} is the velocity of the runaway electron. Considering the runaway electron energy distribution function

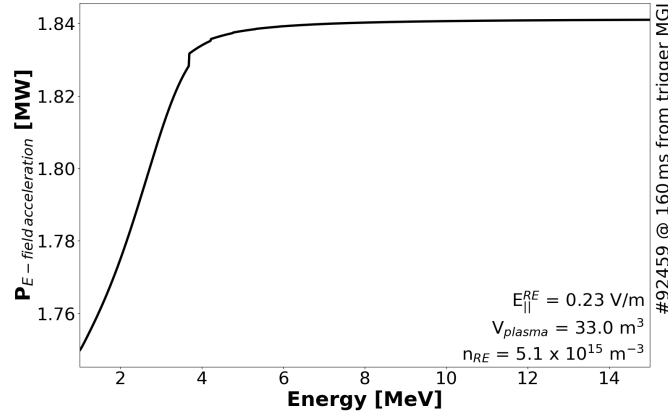


Figure 4.8.: Dependence of the E-field acceleration of the RE beam on the central energy E_{RE}^0

$f_{RE}(v)$, the power loss of the runaway electron beam due to synchrotron radiation is expressed from equation 4.4 as,

$$P_{synchrotron} = \frac{e^4 B^2 \sin^2(\mu) V_{RE}}{6\pi\epsilon_0 m_e^2 c^3} \cdot \int_{v_1}^{v_2} v_{RE}^2 \cdot f_{RE}(v_{RE}) \cdot \gamma^2(v_{RE}) \cdot dv_{RE} \quad (4.5)$$

where $\gamma(v_{RE})$ is the Lorentz gamma factor for relativistic velocity of runaway electrons v_{RE} . v_1 and v_2 are the velocity bounds of the RE distribution function. The synchrotron power loss depends on the square of the magnetic field B .

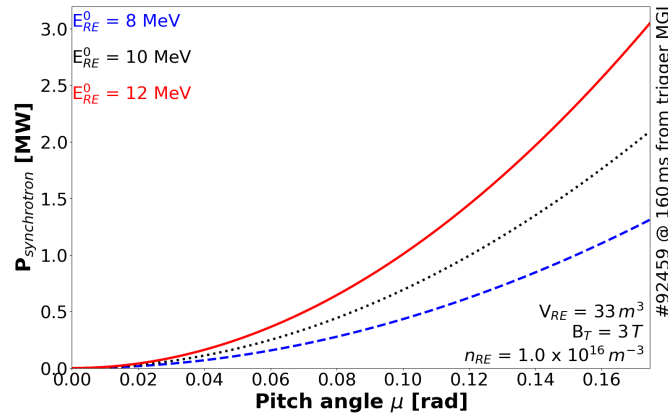


Figure 4.9.: Pitch angle μ dependence of the power lost by the RE beam due to synchrotron radiation

The dependence of the power loss of the runaway electron beam due to synchrotron radiation on the pitch angle of synchrotron emission μ is shown in figure 4.9. The synchrotron radiated power is proportional to the square of the sine of the pitch angle ($P_{synchrotron} \propto \sin^2(\mu)$). From equation 4.5, it can be seen that the synchrotron radiated power also depends on the square of the runaway electron velocity and thus the runaway electron energy distribution function. This dependency is shown in

figure 4.10. When the energy of the runaway electron increases, the power lost by the runaway electron beam due to the synchrotron radiation increases.

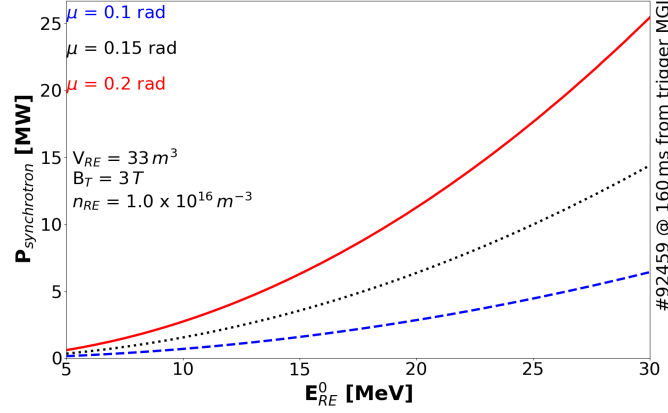


Figure 4.10.: Dependence of the power lost by the RE beam due to synchrotron radiation on the central energy E_{RE}^0 of the RE distribution function

When the RE beam gains higher energies, it also emits higher synchrotron radiated power. As a result, the synchrotron radiation limits the energy of the runaway electron beam (Andersson 2001). In the database of JET discharges considered (section 3.3), the synchrotron radiation is in the order of few MW. Pitch angle μ of 0.1 rad is assumed for the database estimations (Jaspers 2001; Gill 2000).

4.4.1.3. Bremsstrahlung radiation loss of the RE beam

When the runaway electrons are strongly deflected by the nuclei of the background plasma impurities, the RE beam lose energy in the form of bremsstrahlung radiation. In addition to the synchrotron radiation, bremsstrahlung radiation can also limit the energy of the runaway electrons in tokamaks (Bakhtiari 2005a). The drag force on a single runaway electron is given by (Jackson 2007),

$$F_{BR}^{e-} = \frac{4}{137} n_e (Z_{eff} + 1) r_e^2 m_e c^2 \gamma \left[\ln(\gamma) - \frac{1}{3} \right] \quad (4.6)$$

where $r_e = \frac{e^2}{4\pi\epsilon_0 m_e c^2}$ is the classical electron radius. Using this drag force, the power lost from a mono-energetic RE beam due to bremsstrahlung radiation can be defined as,

$$\begin{aligned} P_{bremsstrahlung} &= F_{BR}^{e-} v_{RE} n_{RE} V_{RE} \\ &= \frac{4}{137} n_e (Z_{eff} + 1) r_e^2 m_e c^2 \gamma v_{RE} n_{RE} V_{RE} \left[\ln(\gamma) - \frac{1}{3} \right] \end{aligned} \quad (4.7)$$

where n_{RE} , V_{RE} and v_{RE} are the density, volume and average velocity of the RE beam. Considering the runaway electron energy distribution function $f_{RE}(v)$, the power loss of the runaway electron beam due to bremsstrahlung radiation can be expressed using the equation 4.7 as,

$$P_{\text{bremsstrahlung}} = \frac{4}{137} n_e (Z_{\text{eff}} + 1) r_e^2 m_e c^2 V_{RE} \times \int_0^\infty \gamma(v_{RE}) f_{RE}(v_{RE}) \left[\ln(\gamma) - \frac{1}{3} \right] dv_{RE} \quad (4.8)$$

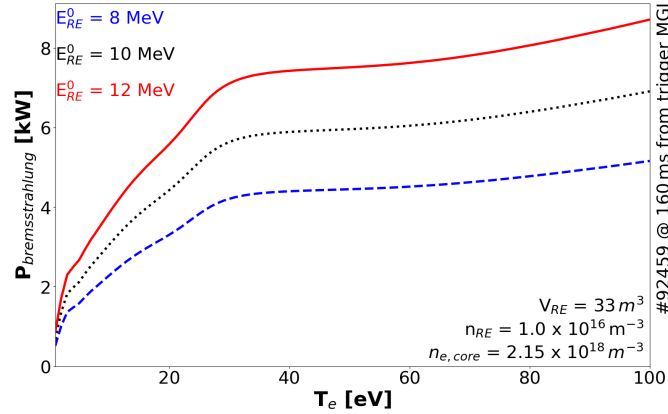


Figure 4.11.: Dependency of the power lost by the RE beam due to bremsstrahlung radiation on the temperature T_e of the background plasma.

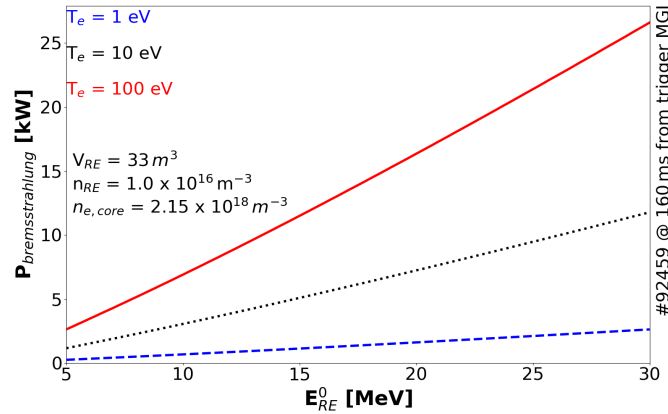


Figure 4.12.: Dependency of the power lost by the RE beam due to bremsstrahlung radiation on the central energy E_{RE}^0 of the RE distribution function

Unlike synchrotron radiation (equation 4.5), bremsstrahlung radiation is independent of the toroidal magnetic field. Bremsstrahlung power losses increase linearly with the energy of the RE beam as shown in the figure 4.12. Bremsstrahlung radiation loss also increases with the electron temperature of the background plasma as shown in the figure 4.11. The background plasma temperature dependence of the bremsstrahlung power given in the equation 4.8 stems from the temperature dependence of the Z_{eff} estimation. As given in the equation 4.8, the presence of high-Z impurity also enhances the bremsstrahlung radiation. Thus, in the mitigation of the RE beam with high-Z impurities, bremsstrahlung radiation may play a major role in limiting the runaway energies.

4.4.1.4. Collisional loss of the RE beam

The runaway beam interacts through collisions with the background plasma in the confined region defined by the separatrix. As a result, power is lost by the runaway electron beam. These collisions act as a source of power for the background plasma in the confined region. This power transfer maybe responsible for the sustainment of the background plasma at higher temperature. The power transfer due to collisions can be estimated by using a relativistic collisional operator as,

$$P_{collision} = m_e v_{RE}^0 \int C(f_{RE}, T_e, n_e) dv_{RE} \quad \text{in W/m}^3 \quad (4.9)$$

where v_{RE}^0 is the velocity of the runaway electron beam corresponding to the central energy E_{RE}^0 in the distribution function f_{RE} . The volume of the RE beam is multiplied to the equation 4.9 to get the power in W. The term $C(f_{RE}, T_e, n_e)$ is the relativistic collisional operator. The collisional operator is expressed from (Sandquist 2006) as,

$$C(f_{RE}) = \frac{1}{p^2} \frac{\partial}{\partial p} p^2 \left(A(p) \frac{\partial f_{RE}}{\partial p} + F(p) f_{RE} \right) + \frac{2B(p)}{p^2} \mathcal{L}(f_{RE}) \quad (4.10)$$

where $p = \gamma m_e c v$ is the momentum. The velocity v is normalized to the speed of light c . The term $A(p)$ in the equation 4.10 is given as (Sandquist 2006),

$$A(p) = \frac{\Gamma v_t^2}{c v^3} \quad (4.11)$$

where $v_t^2 = T_e e / m_e c^2$ and $\Gamma = n_e e^4 \ln \Lambda / 4 \pi \epsilon_0^2$. T_e is given in eV and n_e in m^{-3} . The terms $B(p)$ and $F(p)$ in equation 4.10 are (Sandquist 2006),

$$B(p) = \frac{\Gamma}{2c v} \left(1 + v_t^2 \frac{v^4 - 1}{v^2} \right) \quad (4.12)$$

$$F(p) = \frac{c v}{T_e e} A(p) = \frac{\Gamma v_t^2}{T_e e v^2} \quad (4.13)$$

After gyro-averaging, the pitch angle operator $\mathcal{L}(f_{RE})$ is expressed as,

$$L(f_{RE}) = \frac{1}{2} \frac{\partial}{\partial \mu} (1 - \mu^2) \frac{\partial f_{RE}}{\partial \mu} \quad (4.14)$$

The assumed normally distributed runaway electron energy distribution given in equation 4.2 is taken to be independent of the pitch angle μ . Thus, the pitch angle operator term $\mathcal{L}(f_{RE}) = 0$. From the above equation, it can be seen that the collisional operator $C(f_{RE}) \propto v_t^2 \propto T_e$ and $C(f_{RE}) \propto \Gamma \propto n_e$. Thus, the collisional operator not only depends on the runaway electron distribution function but also on the characteristics (T_e & n_e) of the background plasma in the confined region.

The collisional power increases linearly with the increase in the electron temperature of the background plasma as shown in figure 4.13. It can also be observed that for higher values of the central energy E_{RE}^0 of the RE distribution function, the collisional

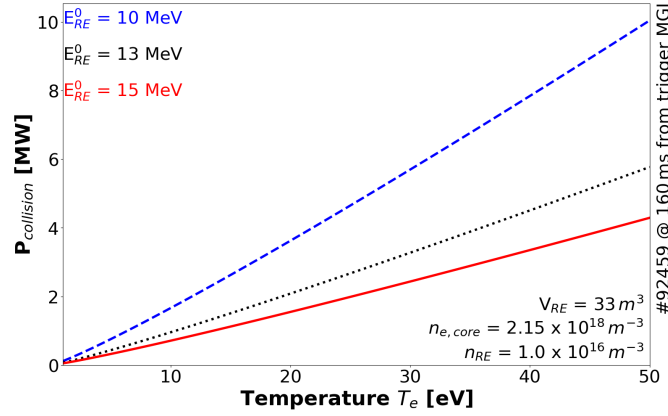


Figure 4.13.: Dependence of the power lost by the RE beam due to collisional power transfer on the electron temperature of the background plasma

power is lower as shown in the figure 4.14. This is due to the fact that the scattering cross-section decreases exponentially with increase in energy.

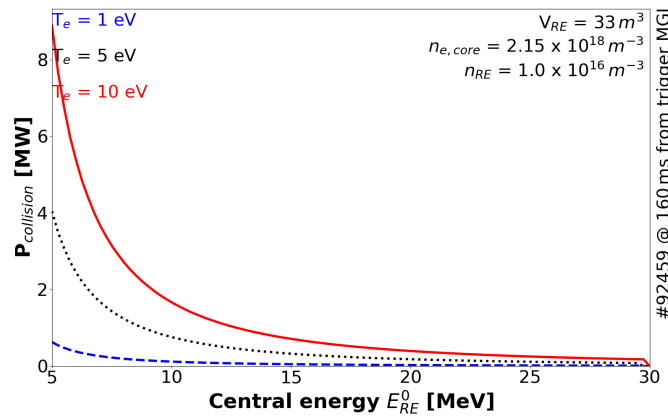


Figure 4.14.: Dependency of the power lost by the RE beam due to collisional power transfer on the central energy E_{RE}^0 of the RE distribution f_{RE}

Assuming a runaway electron beam with central energy of the distribution at 10 MeV, the collisional power transfer can be as low as few hundreds of kW and for higher temperature and pressure, it can be as high as few GW. In the database of the discharges, the collisional power values are in the range of few MW. In the figure 4.15, a 0D electron density n_e and temperature T_e is considered.

As shown in the figure 4.13, the collisional power transfer increases linearly with the electron temperature of the background plasma. Using the estimated temperature profile (figure 3.26 for instance), a profile in the collisional power transfer is constructed as shown in the figure 4.16. The uncertainty in the collisional power profile (shaded regions in the figure 4.16) is constructed by estimating the collisional power losses corresponding to lower and higher bounds of the temperature profile (shaded regions in the figure 3.26). A less energetic runaway electron beam loses its power predominantly through collisions with the background plasma. In more energetic

runaway electron beams, power loss is predominantly due to synchrotron radiation.

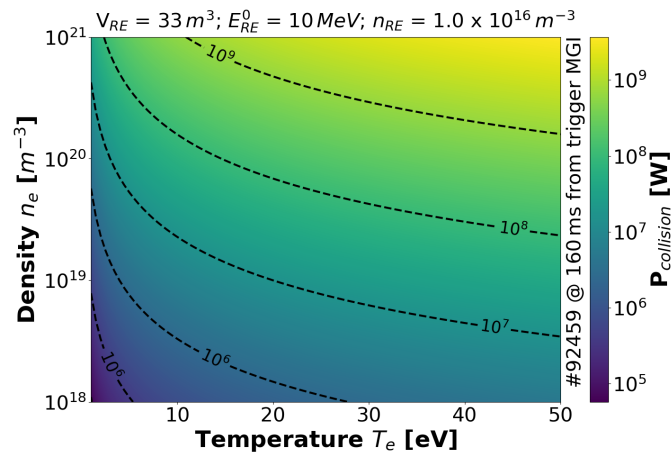


Figure 4.15.: Dependency of the power lost by the RE beam due to collisional power transfer on the electron temperature and density of the background plasma

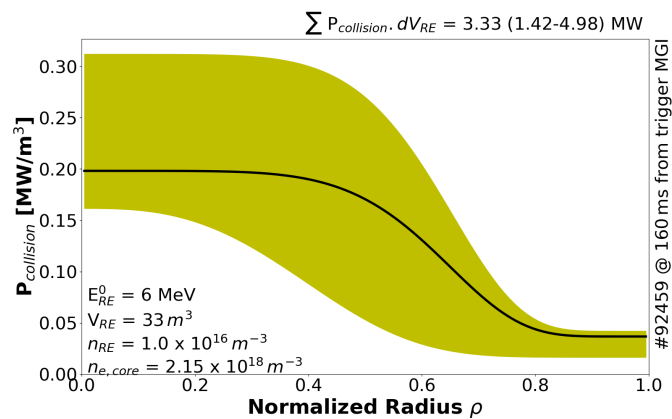


Figure 4.16.: Profile of the collisional power transfer between RE beam and the confined background plasma for #92459 at ~ 160 ms from the trigger MGI (corresponding to T_e -profile from the figure 3.26). The shaded region indicates the uncertainty due to uncertainty in the T_e -profile.

Collisional power transfer vs Collisional stopping power:

Due to the interaction with the argon neutrals, RE beam loses energy due to collisions and radiation. Energy lost by the RE beam per unit length dE/dX (the so called stopping power) are calculated using ESTAR code (Berger 1992) and are shown in the figure 4.17. At lower energies of RE beam, energy lost by the RE beam is predominantly through collisions whereas radiative stopping power is dominant at higher energies.

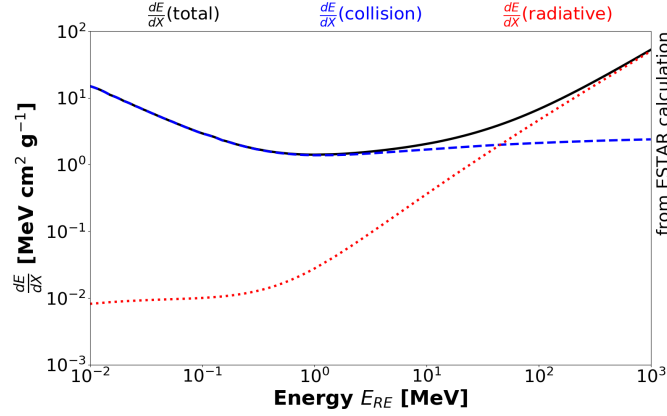


Figure 4.17.: Stopping power of the RE beam for argon gas calculated from ESTAR calculations (Berger 1992)

It can be also observed that collisional stopping power per mass density (given as blue dashed line in the figure 4.17) has the lowest value around 1 MeV and it increases slightly above 1 MeV. This gradual increase of stopping power is much different than the asymptotic decay of the collisional power loss $P_{collision}$ shown in the figure 4.14 with the energy of the RE beam.

Using the stopping power per mass density dE/dX (in $\text{MeV cm}^2 \text{g}^{-1}$) from the ESTAR code (Berger 1992) is related to the collisional stopping power of a runaway electron $P_{collision,RE}^{ESTAR}$ as,

$$P_{collision,RE}^{ESTAR} = \frac{dE}{dX} c d_n \quad (4.15)$$

where c is the light speed and d_n is the argon particle density in g cm^{-3} . Assuming a mono-energetic RE beam of energy E , the collisional stopping power of the RE beam with RE density n_{RE} and plasma volume V_{RE} can be calculated as,

$$P_{collision}^{ESTAR} = P_{collision,RE}^{ESTAR} \cdot n_{RE} \cdot V_{RE} \quad (4.16)$$

The energy dependence of the ratio of collisional power loss of the RE beam $P_{collision}$ (equation 4.9) to the collisional stopping power $P_{collision}^{ESTAR}$ (equation 4.16) in the figure 4.18. It can be seen from the figure 4.18 that with increase in the RE beam energies, the ratio of the powers decrease. It may be due to the fact that the collisional stopping power increases with RE beam energies (figure 4.18) whereas the collisional power loss decreases with RE beam energies (figure 4.14). Furthermore, it can be observed that collisional stopping power and the collisional power loss are magnitudes different to each other.

As shown in the figure 4.19, it can be observed that at lower temperatures, collisional power loss $P_{collision}$ is magnitudes lower than that of the collisional stopping power $P_{collision}^{ESTAR}$. At higher temperatures, the collisional power loss is magnitudes higher than collisional stopping power. This may be due to the fact that collisional stopping power is based on the argon neutral amount of the first order. This means that at

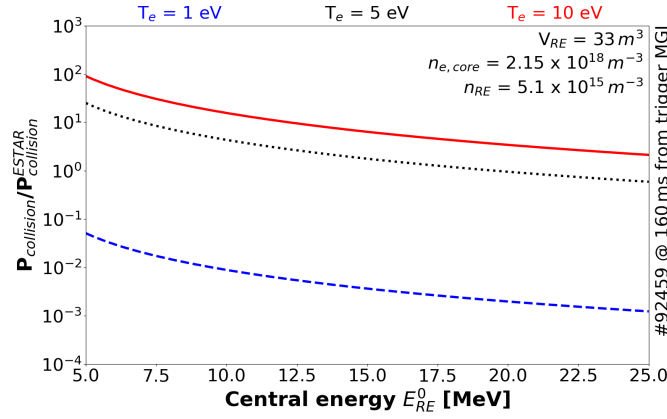


Figure 4.18.: Energy dependence of the ratio between collisional power transfer (equation 4.9) and collisional stopping power (equation 4.16) for the discharge #92459, 160 ms from trigger injection. The background plasma temperatures are assumed as $T_e=1$ eV, $T_e=5$ eV and $T_e=10$ eV.

higher temperatures of the background plasma, very low argon neutral contents are expected and thus the collisional stopping power is magnitudes lower than collisional power loss.

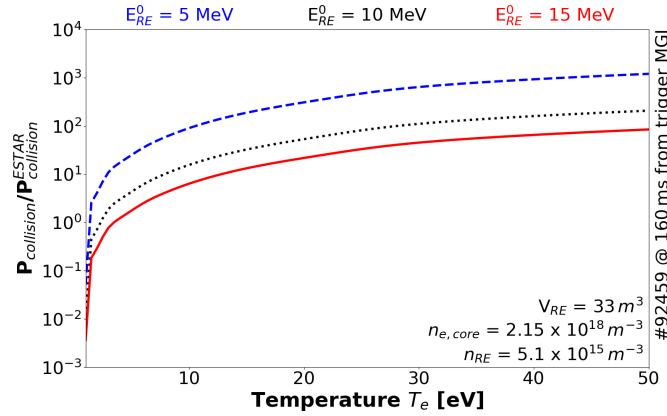


Figure 4.19.: Background plasma temperature dependence of the ratio between collisional power transfer (equation 4.9) and collisional stopping power (equation 4.16) for the discharge #92459, 160 ms from trigger injection. The RE beam energies are taken as $E_{RE}^0=5$ MeV, $E_{RE}^0=10$ MeV and $E_{RE}^0=15$ MeV.

It is to be noted that for the collisional stopping power calculations, the background plasma temperature and free electron density are used only during argon density estimations. On the other hand, the collisional power loss increases linearly with temperature and density of the background plasma as shown in the figure 4.15.

4.4.1.5. Comparison of RE beam power loss terms

The power lost by the RE beam through collisions with the background plasma is the most significant mechanism as shown in the figure 4.20. On the other hand, synchrotron radiation loss is roughly a magnitude less than the collisional power loss and is independent of the background plasma temperature. Bremsstrahlung radiation losses of the RE beam are magnitudes lower than the synchrotron radiation loss and collisional power loss of the RE beam as shown in the figure 4.20. It is to be noted that a 0D T_e value is used in the figure 4.20 rather than the T_e -profile.

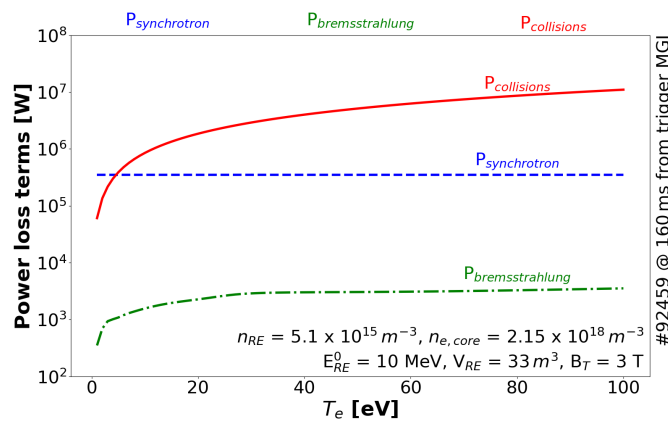


Figure 4.20.: Comparison of power loss terms of the RE beam (synchrotron, bremsstrahlung and collisional power transfer) as a function of the electron temperature of the background plasma. A constant central energy of the RE energy distribution E_{RE}^0 is assumed.

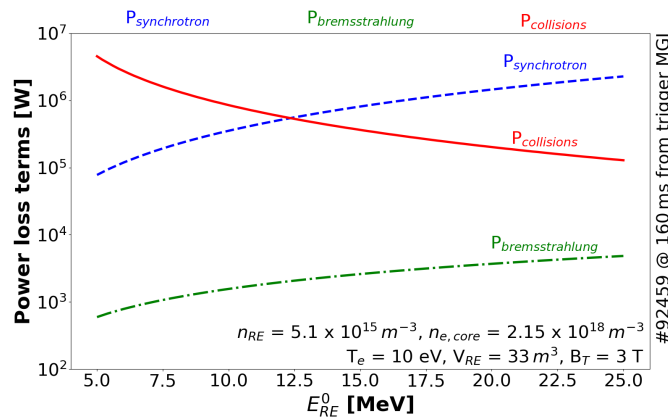


Figure 4.21.: Comparison of power loss terms of the RE beam (synchrotron, bremsstrahlung and collisional power transfer) as a function of the central energy E_{RE}^0 of the RE distribution f_{RE} . Background plasma temperature of $T_e=10$ eV is assumed.

As shown in the figure 4.21, the collisional power loss of the RE beam dominates the synchrotron radiation loss for lower energies. With the increase of RE energies,

the collisional power loss decreases whereas the synchrotron radiation loss increases. An increase in the synchrotron power further decreases the maximum achievable energy of the RE beam (Entrop 2000; Andersson 2001). It can also be observed that bremsstrahlung power indeed increases with the RE beam energy but they are still magnitudes less than other loss channels. It is to be noted that similar to figure 4.20, a constant T_e value is assumed in the calculation rather than 1D T_e -profile.

For the RE beam, RE energy distribution function f_{RE} (mainly the central energy of the RE energy distribution E_{RE}^0) is a free parameter. Assuming that power source due to electric field acceleration $P_{E-field\ acceleration}$ balances the RE power losses in the form of synchrotron radiation, bremsstrahlung radiation and collisional power transfer to the background plasma, the central energy of the RE distribution E_{RE}^0 can be estimated.

4.4.2. Power terms of the confined background plasma

4.4.2.1. Ohmic power of the confined background plasma

In addition to the power transfer from the runaway electron beam the ohmic power can also act as power source of background plasma in the confined region. The ohmic power of background plasma can be expressed as,

$$P_{ohmic} = \sigma_{neo} \cdot E_{\Omega}^2 \quad (4.17)$$

where E_{Ω} is the electric field due to the ohmic part of the background plasma. Neo-classical conductivity σ_{neo} (Hirshman 1977) is used which can be expressed as,

$$\sigma_{neo} = \sigma_{Spitzer} \cdot G_c \quad (4.18)$$

where the Spitzer conductivity $\sigma_{Spitzer}$ can be expressed as,

$$\sigma_{Spitzer} = \frac{(4\pi\epsilon_0)^2 (T_e e)^{3/2}}{\pi Z_{eff} e^2 \sqrt{m_e} \ln \Lambda} \quad (4.19)$$

T_e is in eV and $\ln \Lambda$ is the Coulomb logarithm. G_c is the geometric correction term (Hirshman 1977) due to the aspect ratio of the tokamak and can be expressed as,

$$G_c = \Lambda_E(\bar{Z}) \left(1 - \frac{f_T}{1 + \xi v_{*e}}\right) \left(1 - \frac{C_R(\bar{Z}) f_T}{1 + \xi v_{*e}}\right)$$

with,

$$\Lambda_E(\bar{Z}) = \frac{3.4}{\bar{Z}} \left(\frac{1.13 + \bar{Z}}{2.67 + \bar{Z}} \right) \quad (4.20)$$

$$f_T = 1 - (1 - \delta)^2 (1 - \delta^2)^{-1/2} (1 + 1.46\delta^{1/2})^{-1}$$

$$\xi = 0.58 + 0.2\bar{Z}$$

where \bar{Z} is the effective charge and $\delta = a/R$ is the aspect ratio. The term v_{*e} is the electron collisionality parameter. For JET-ILW discharges, $G_c \sim 0.6$.

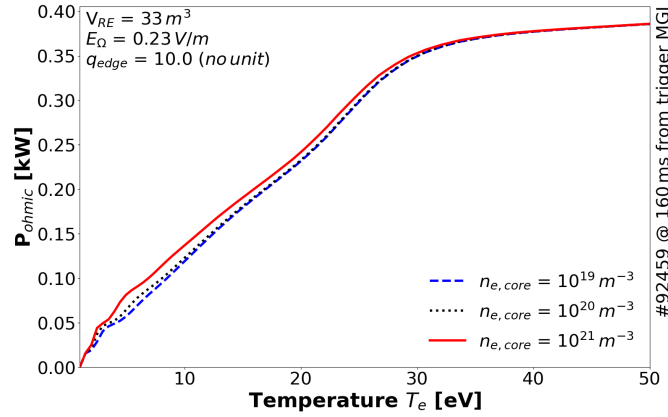


Figure 4.22.: Electron temperature dependency of the ohmic power of the background plasma for the discharge #92459 at 160 ms from the trigger MGI.

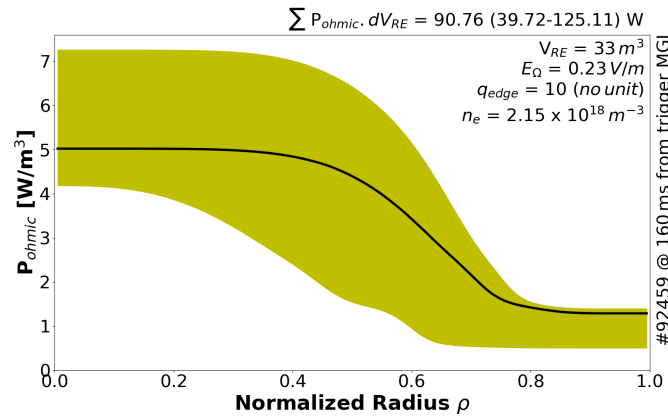


Figure 4.23.: Ohmic power profile of the confined background plasma for the discharge #92459 at ~ 160 ms from the trigger MGI (corresponding to T_e -profile from the figure 3.26). The shaded region indicates the uncertainty due to uncertainty in the T_e -profile.

From the figure 4.22, it can be seen that the ohmic power increases with temperature for lower temperatures (around 30 eV in figure 4.22) and the ohmic power attains saturation for higher temperature. It can also be noted that the ohmic power is less sensitive to the electron density of the background plasma ($\ln \Lambda$ depends on the electron density n_e).

The ohmic power profile with the uncertainty due to uncertainty in the temperature profile is shown in figure 4.23. In the database, the ohmic power is in order of few kW. The ohmic power source of the confined background is negligible as compared to the collisional power transfer source from the RE beam. Thus, collisional power transfer is the primary source of power for the background plasma in the confined region.

4.4.2.2. γ -ray absorption of the confined background plasma

The γ -rays are the energetic bremsstrahlung radiation of the runaway electron beam (energies from few 100 keV to few MeV) and they may be absorbed by the background plasma. The amount of energy, ϵ , absorbed by the background plasma per unit time in a volume of interest ΔV from the γ -rays due to the runaway electron beam can be given by the formula from (Hubbell 1969) as,

$$\epsilon = \int_{\Delta V} (dr)^3 \rho(r) \int_{E_{min}}^{E_{max}} dE \cdot \phi(E, r) \cdot E \cdot \frac{\mu_{en}}{\rho}(E) \quad [MeV s^{-1}] \quad (4.21)$$

where E is the γ -ray energy in MeV and ϕ is the γ -ray flux in $MeV^{-1}cm^{-2}s^{-1}$. The term $\frac{\mu_{en}}{\rho}(E)$ is the mass energy-absorption coefficient in $cm^2 \cdot g^{-1}$. The mass energy-absorption coefficients are taken from the NIST database (Kramida 2018). The term $\int_{\Delta V} (dr)^3 \rho(r)$ is the mass density term of the plasma impurities. Assuming uniform density of argon atoms in the plasma, the term can be minimized to $M_{Ar}(tot)$ which is the total mass of the argon impurities in the plasma given in g.

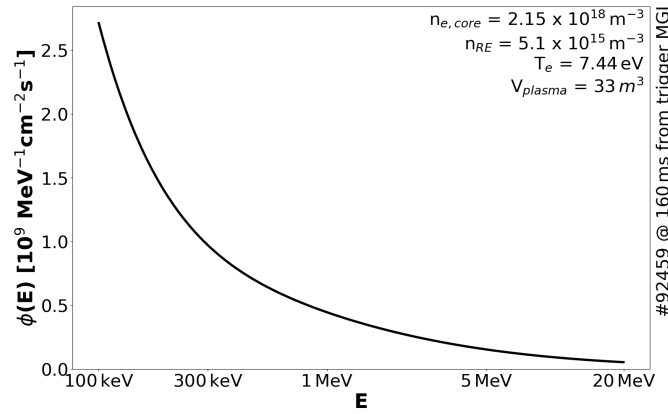


Figure 4.24.: Energy dependence of the gamma ray flux $\phi(E)$ from bremsstrahlung radiated power $P_{bremsstrahlung}$ of the RE beam.

The γ -ray flux $\phi(E)$ in the equation 4.21 is estimated using the bremsstrahlung power loss of the RE beam given in the equation 4.7 as,

$$\phi(E) = \frac{P_{bremsstrahlung}}{E^2 e A} \quad [MeV^{-1}cm^{-2}s^{-1}] \quad (4.22)$$

where E is the energy of the γ -ray photon (in MeV). The term $A_{surface}$ is the surface area of the plasma. An example of the γ -ray flux $\phi(E)$ is shown in the figure 4.24 for the discharge #92459 at 160ms from the trigger injection. It is to be noted that flat T_e -profile is assumed in the figure 4.24 for simplicity.

The energy dependence of the mass-energy absorption coefficient for argon is shown in the figure 4.25. It can be observed that with increase of energy, the absorption coefficient decreases. However for very high energies ($E > 1$ MeV), the absorption coefficient is almost saturated.

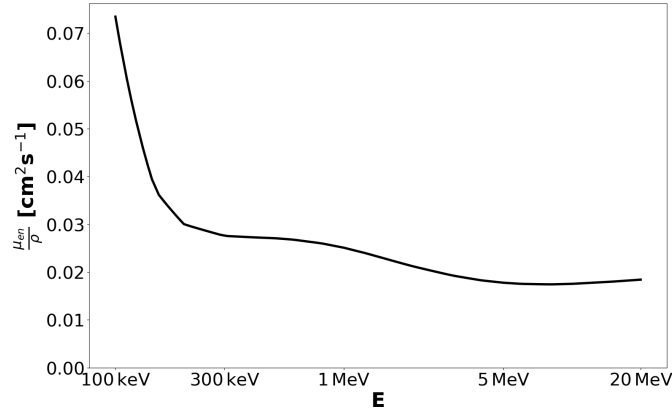


Figure 4.25.: Variation of the mass-energy absorption coefficient μ_{en}/ρ on the energy E . Values are taken from the NIST database (Kramida 2018).

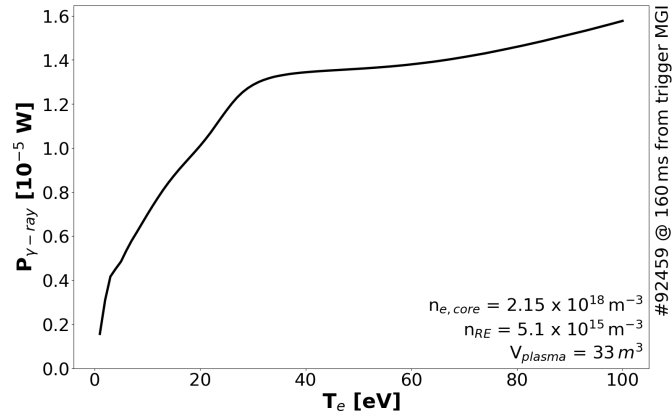


Figure 4.26.: Temperature dependence of the power source due to γ -ray absorption for the discharge #92459 at 160 ms from the trigger MGI.

The power source due to γ -ray absorption ϵ depends on the electron temperature of the background plasma. The absorbed power increases with temperature of the background plasma as shown in the figure 4.26. However, the power is on order of 10^{-5} W which is magnitudes less than other power terms. Thus, γ -ray absorption term is not significant in the power balance.

4.4.2.3. Radiated power of the confined and open field line background plasma

Using information about the characteristics of the background plasma, the radiated power can be estimated with the help of cooling rate coefficients $L_{coolingrate}$ from the ADAS database (Summers 2004).

For argon, the cooling rate is maximum around $T_e \sim 18$ eV as shown in the figure 4.27. Using the cooling rates, the radiated power can be estimated as,

$$P_{radiated} = n_e \cdot n_{total}(T_e, n_e) \cdot L_{coolingrate} \cdot V_{confined} \quad (4.23)$$

where $V_{confined}$ is the volume of the background plasma in the confined region. $n_{total}(T_e, n_e)$ is the total argon impurity density estimated using the fractional abundance information. In the estimation of n_{tot} , the neutral ion density is assumed to be negligible as compared to the ion density of higher ionization states.

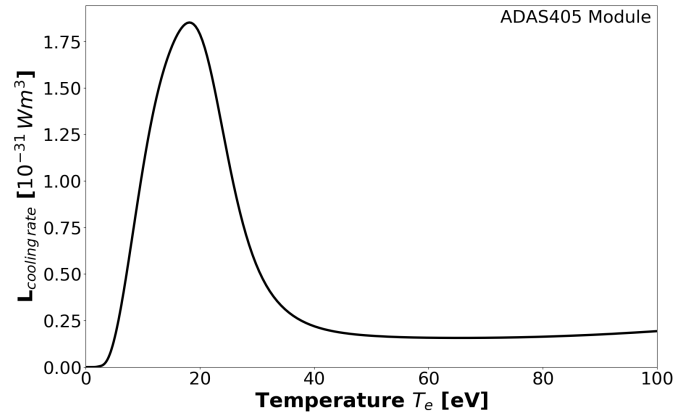


Figure 4.27.: Argon cooling rate coefficients generated using ADAS405 module from the ADAS database (Summers 2004)

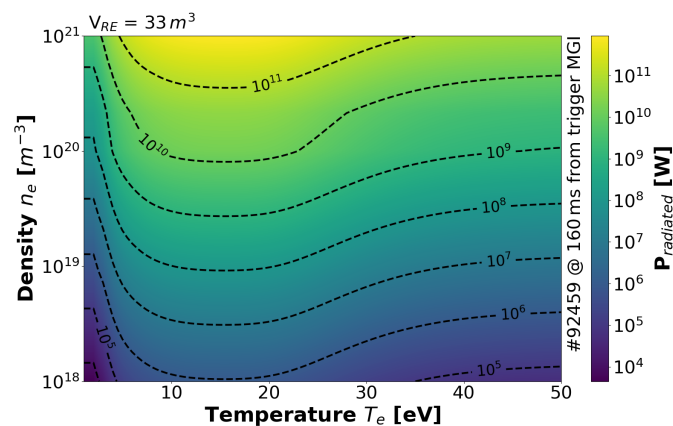


Figure 4.28.: Variation of the radiated power for different electron temperature and density of the background plasma

The power radiated by the background plasma depends on the electron density and temperature profile of the background plasma as shown in the figure 4.28. Depending on the temperature and density of the background plasma, the radiated power can vary between few kW to few TW. In our database, the power radiated by the background plasma in the runaway electron beam phase is in order of few MW. In the figure 4.28, 0D values of electron temperature and density are considered.

Considering the estimated temperature profile, a profile in the radiated power can be constructed as shown in the figure 4.29. The shaded region denotes the uncertainty in the radiated profile due to the uncertainty in the temperature profile. In figure 4.29, the total power radiated by the background plasma in the confined region is comparable with the total radiated power measured by the bolometry (see table 4.2).

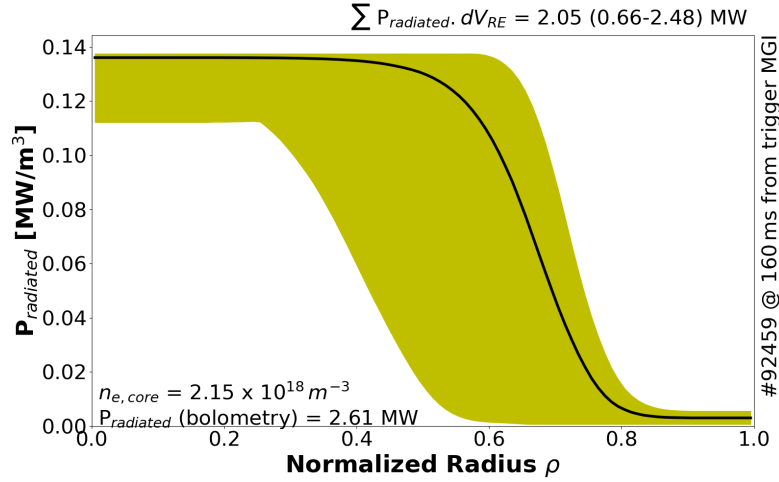


Figure 4.29.: Radiated power profile of the background plasma in the confined region for the discharge #92459 at 160 ms from the trigger MGI. Flat density profile is considered in the figure.

4.4.3. Heat conduction from the background plasma of the open field line region to the wall

In addition to radiation, the background plasma in the open field line region also loses part of its power by heat conduction to the wall. The power lost by the open field line background plasma to the wall due to heat conduction can be estimated using an analytical formula from (Stangeby 2000) as,

$$P_{conduction} = q_{||} \cdot \frac{B_{\theta}}{B_T} \cdot \lambda_q \cdot 2\pi R \cdot 2 \quad (4.24)$$

where $q_{||}$ is the parallel heat flux. λ_q is the scrape-off layer width corresponding to the parallel heat flux. B_{θ} is the poloidal magnetic field and R is the plasma major radius. The estimation of these terms is discussed in this section.

4.4.3.1. Parallel heat flux $q_{||}$

There are two regimes in which the parallel heat flux can be estimated :

Conduction-limited regime (CLR) : In conduction-limited regime, the energy losses are limited by the collisional properties of the plasma and it deals with high collisionality ($\nu^* \geq 10$; high n_e and low T_e). The parallel heat flux due to the conduction-limited regime can be expressed as (Stangeby 2000),

$$q_{||}^{CLR} = k_0 \cdot T_e^{7/2} \cdot L_c^{-1} \quad (4.25)$$

where $k_0 = 2000 \text{ Wm}^{-1}(\text{eV})^{-7/2}$ is the classical electron parallel heat conductivity coefficient and $L_c = \pi q_{cyl} R$ is the connection length.

Sheath-limited regime (SLR) : In sheath-limited regime, the energy losses are limited by the heat transmission properties of the sheath and it deals with low collisionality ($v^* < 10$; low n_e and high T_e). the parallel heat flux due to the sheath-limited regime can be expressed as (Stangeby 2000),

$$q_{\parallel}^{SLR} = \gamma_{sheath} \cdot n_{e,SOL} \cdot c_s \cdot T_e \quad (4.26)$$

where γ_{sheath} is the sheath-heat transmission factor ($\gamma_{sheath} \sim 8-9$ for argon with $T_i = T_e$ using analytical formulae from (Stangeby 2000)). $n_{e,SOL}$ is the electron density at the scrape-off layer and c_s is the sound speed in the plasma.

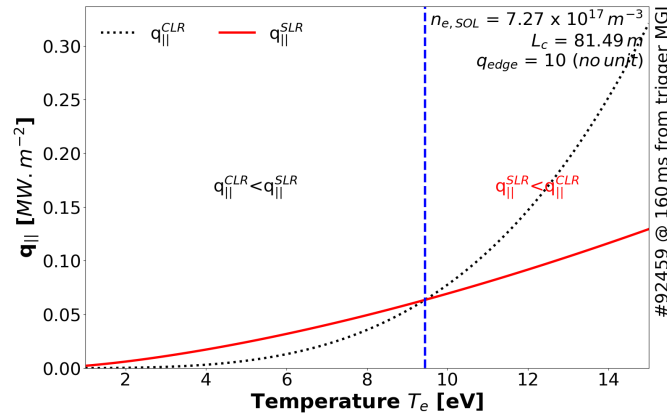


Figure 4.30.: Comparison of the temperature dependence of the parallel heat fluxes estimated using conduction-limited and sheath-limited regimes

In the figure 4.30, for lower temperatures, the parallel heat flux estimated with the conduction-limited regime is much lower than the parallel heat flux estimated with the sheath-limited regime. In lower temperatures, the conduction-limited regimes are more accurate. On the other hand, sheath-limited accurately calculates parallel heat flux at higher temperature. The transition temperature depends on the electron density in the scrape-off layer and the connection length. The minimum of the parallel heat flux values between the two regimes are considered in the rest of the analysis to eliminate the risk of the parallel heat flux overestimation. The recycling of the argon particles near the wall is hidden during the estimation of parallel heat flux q_{\parallel} .

4.4.3.2. Scrape-off layer width λ_q

Using the spectral filament model of turbulent plasma, the characteristic decay length of the electron density in the scrape-off layer λ_n is given from (Fedorczak 2019),

$$\lambda_n = 10 \cdot q^{6/11} \cdot R^{3/11} \cdot B^{-8/11} \left(\frac{A}{Z} \right)^{4/11} \cdot T_e^{4/11} \cdot \left(1 + \frac{T_i}{Z T_e} \right)^{4/11} \quad [R \text{ in m and } \lambda_n \text{ in mm}] \quad (4.27)$$

where $q = \frac{a}{R} \cdot \frac{B_T}{B_\theta}$ is the cylindrical edge safety factor, R is the tokamak major radius and B is the toroidal magnetic field. A and Z are the atomic and mass number

of the background plasma species (argon in this study). The scrape-off layer width corresponding to the heat flux λ_q is assumed to be half of λ_n ($\lambda_q = \lambda_n/2$).

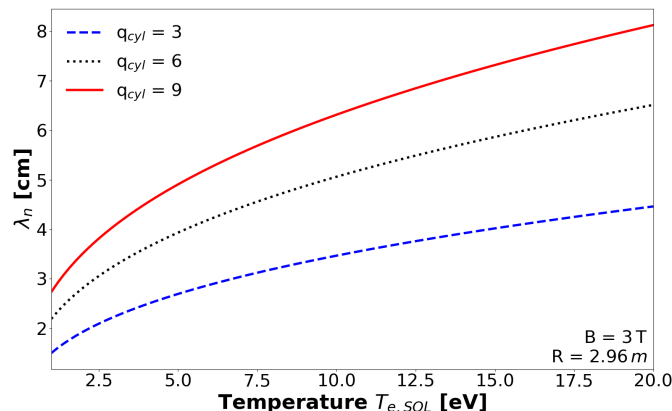


Figure 4.31.: Temperature dependence of the density SOL width λ_n . Magnetic field of $B_T=3\text{ T}$ is taken for the JET tokamak with major radius $R=2.96\text{ m}$

The width of the scrape-off layer increases with increase in the electron temperature and the order of magnitude is a few cm as shown in the figure 4.31. The width also increases with the increase of the safety factor.

4.4.3.3. Magnetic field ratio $\frac{B_\theta}{B_T}$

The safety factor q at edge is related to the ratio of the poloidal to the toroidal magnetic fields. Assuming large aspect-ratio approximation, the field ratio can be calculated from the safety factor value as,

$$\frac{B_\theta}{B_T} = \frac{a}{q \cdot R} \quad \text{since} \quad q = \frac{a}{R} \cdot \frac{B_T}{B_\theta} \quad (4.28)$$

where a and R are the minor and major radius of the plasma.

4.4.3.4. Calculation of power conducted from the background plasma

Using the estimates of the parallel heat flux, scrape-off layer width and the magnetic fields ratio, the power conducted to the wall is estimated using the equation 4.24.

From the figure 4.32, it can be observed that the power conducted to the wall from the background plasma in the open field line region is highly sensitive to electron temperature. The electron density in the scrape-off layer only decides the regime at which the parallel heat flux is estimated through its dependence of the parallel heat flux in the sheath-limited regime as shown in the equation 4.26. The conducted power can be as low as few W and it can be as large as tens of kW as shown in the figure 4.32. For the discharges in the database, the conducted power is in order of tens of W.

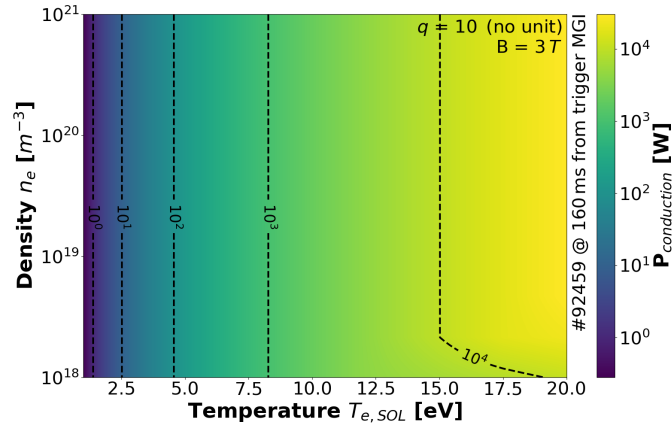


Figure 4.32.: Power conducted from the background plasma in the open field line region to the wall for the discharge #92459 at 160 ms from the trigger MGI.

In the upcoming section 4.5, the analytical formulae to estimate different power terms are applied to experimental data and a power balance is performed.

4.5. 1D Power balance of JET-ILW and DIII-D discharges

The analytical formulae to estimate the various power terms of the RE beam and background plasma were discussed in the section 4.4. In the present section, the experimental values are used to estimate different power terms of the RE beam and background plasma system. Using the power estimates, the power balance of the systems is performed in this section.

It was observed in the section 3.3 that background plasmas of the JET discharges were much hotter than the background plasmas of the DIII-D tokamak. Using the 1D power balance, the differences between the JET and DIII discharges are studied to understand the difference in background plasma temperature. For this study, JET discharges #92454 and #92459 are used. For the DIII-D tokamak, discharge parameters are assumed based on the figures and values from (Hollmann 2011; Hollmann 2013).

Two JET-ILW discharges are considered in the comparison of the estimated power: a discharge with low density background plasma (#92459) and a discharge with high density background plasma (#92454) with lower temperature of the background plasma. The parameters of the discharges are tabulated in the table 4.1. The T_e -profiles of the discharges #92459 and #92454 are shown in the figure 4.33. The power balance estimations are performed during the full conversion of plasma current to the runaway current. The discharges are compared with a DIII-D discharge in which the parameters are assumed based on the references. It is to be noted that the core electron density ($n_{e,core}$) in the JET-ILW discharges are the lowest possible values and are subjected to higher uncertainties. However, the electron density in the far scrape off

layer is expected to be lower than the core electron density. In JET-ILW discharges, the confined plasma volume (and hence the runaway beam volume) is ~ 12 times more than the DIII-D discharge. Thus, the JET-ILW discharges have higher number of runaway electrons than the DIII-D discharge.

Parameters		JET-ILW		DIII-D
		#92459	#92454	
Trigger gas amount	(Pa.m ³)	7	41	-
Toroidal magnetic field	B_T (T)	3	3	2
Electric field	$E_{ }^{RE}$ (V/m)	0.23	0.36	1.91
Runaway current	I_{RE} (MA)	0.5	0.67	0.3
Runaway density	n_{RE} (m ⁻³)	5.1×10^{15}	5.46×10^{15}	2.27×10^{16}
Central RE energy (calculated)	E_{RE}^0 (MeV)	6.41	8.51	6.1
T_e -profile	$\langle T_e \rangle_V$ (eV)	7.44 ± 0.37	3.21 ± 0.12	2
	T_e^0 (eV)	13.9	13.64	
	T_e^{LCFS} (eV)	3.15	2.68	
Confined density	$n_{e,core}$ (m ⁻³)	2.15×10^{18}	1.94×10^{19}	10^{20}
Open field line density	$n_{e,SOL}$ (m ⁻³)	7.27×10^{17}	7.39×10^{18}	10^{19}
Confined plasma volume	$V_{confined}$ (m ³)	33.3	42.8	2.88
Edge safety factor	q_{edge} (no unit)	10	9.01	5
Radiated power (bolometry)	$P_{radiated}$ (MW)	2.61	10.61	~ 1

Table 4.1.: Parameters of the JET-ILW discharges and assumed DIII-D discharge used in the comparison study.

Assuming a steady state of the runaway electron beam, the central energies of the runaway electron energy distributions for the JET-ILW discharges are calculated by balancing the electric field acceleration with the synchrotron radiation, collisional power loss and the bremsstrahlung radiation. The calculated RE distribution function for the discharges by the balance of the RE beam is shown in the figure 4.34.

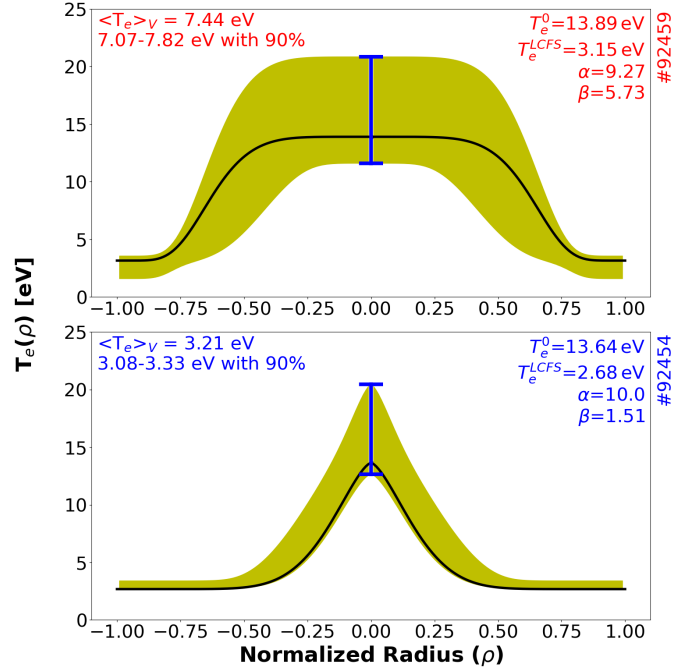


Figure 4.33.: T_e -profile of the discharges #92459 (top) and #92454 (bottom). Shaded regions represent the uncertainty in the T_e -profile.

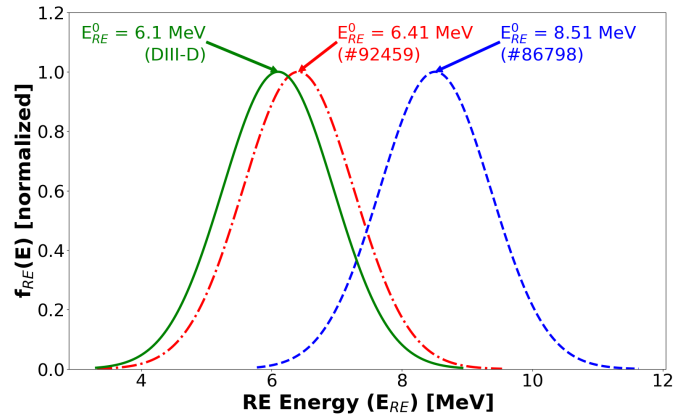


Figure 4.34.: RE distribution functions of the discharges #92459, #92454 and DIII-D discharge. FWHM of 2 MeV is considered for the distributions.

For DIII-D, the estimated central energy of the runaway beam is within the range observed in figure 5(e) of (Paz-Soldan 2017). For DIII-D, the loop voltage measurement of figure 1(g) of (Hollmann 2011) was taken ($V_{loop} \sim 20$ V). The synchrotron pitch angle value of 0.1 rad is assumed for the synchrotron power estimates (Jaspers 2001).

4.5.1. RE beam power terms

Using the estimated RE distribution function from the power balance of the RE beam, the power terms of the RE beam are estimated and tabulated in table 4.2. The

electric field of the JET-ILW discharge #92454 is higher than that of #92459 and thus the discharge #92454 has higher E-field acceleration as compared to the discharge #92459. The power source of the RE beam due to the electric field acceleration and the collisional power transfer to the background plasma estimated given in the table 4.2 are comparable with the simple input power of the runaway beam previously derived ($I_{RE} \times V_{loop}$; 2.14 MW for #92459, 4.49 MW for #92459 and 6 MW for DIII-D discharge).

RE beam powers (MW)	#92459	#92454	DIII-D
(+) $P_{E-field\ acceleration}$	1.839	4.074	5.994
(-) $P_{synchrotron}$	0.137	0.346	0.021
(-) $P_{bremsstrahlung}$	0.001	0.010	0.007
(-) $P_{collision}$	1.7 (0.72-2.54)	3.72 (3.67-6.87)	5.97

Table 4.2.: Power terms estimations for runaway electron beams for JET-ILW discharges and assumed DIII-D discharge (bracket terms indicate error bar due to T_e -profile uncertainties).

Significant power is lost by the RE beam due to the synchrotron emission, however, power lost by the RE beams are predominantly due to the collisional power transfer with the BG plasma. As compared to the synchrotron radiation loss and the collisional power loss, the power loss due to bremsstrahlung radiation is negligible for the discharges as shown in the table 4.2.

4.5.2. Confined background plasma power terms

The power terms of the confined background plasma are estimated using the estimated temperature profiles as shown in the table 4.3. The ohmic power source of the background plasma is magnitudes lower than the collisional power source from the RE beam. Thus, the collisional power transfer is the primary source of power for the background plasma in the confined region. The power conducted from the confined background plasma $P_{conducted}$ is to be determined.

Despite having lower volume-averaged temperature, the collisional power of #92454 is almost two times higher than the discharge #92459 due to the higher electron density. On the other hand, discharge #92454 has ~ 9 times more free electrons ($N_{e,core}, n_{e,core} \times V_{confined}$) in the background plasma as compared to the discharge #92459 as shown in the table 4.4. Thus, discharge #92459 transfers ~ 5 times more power per free electron ($P_{collision}/(N_{e,core})$) than the discharge #92454. This higher power transfer per free electron of the background may be the possible explanation of hotter background plasma in the discharge #92459 as compared to #92454.

In the table 4.3, it can be observed that the collisional power transfer is comparable to the radiated power measured by the bolometer for the discharge #92459 whereas for the discharge #92454, the collisional power transfer is much less than the radi-

Background plasma powers in Confined region (MW)		#92459	#92454	DIII-D
(+)	$P_{collision}$	1.7 (0.72-2.54)	3.72 (3.67-6.87)	5.99
(+)	$P_{ohmic} (\times 10^{-3})$	0.09 (0.04-0.13)	0.16 (0.16-0.27)	0.47
(-)	$P_{radiated}$	2.05 (0.68-2.31)	44.45 (42.45-160.73)	6.45
	$P_{radiated}$ (bolometer)	2.61	10.61	~1
(-)	$P_{conduction}$	TBD	TBD	TBD

Table 4.3.: Power balance of the confined background plasmas for JET-ILW discharges and assumed DIII-D discharge (bracket terms indicate error bar due to T_e -profile uncertainties).

		#92459	#92454	DIII-D
$\langle T_e \rangle_V$	[eV]	7.44 ± 0.37	3.21 ± 0.12	2
$P_{collision}$	[MW]	1.7 (0.72-2.54)	3.72 (3.67-6.87)	5.97
$N_{e,core}$	$[\times 10^{19}]$	7.16	83	28.8
$\frac{P_{collision}}{N_{e,core}}$	$[\times 10^{-14} \text{ W/e}^-]$	2.37 (1-3.55)	0.45 (0.44-0.83)	2.07

Table 4.4.: Collisional power transferred per free electron of the background plasma for JET-ILW discharges and assumed DIII-D discharge (bracket terms indicate error bar due to T_e -profile uncertainties).

ated power. It is to be noted that a stationary RE beam is assumed in the RE energy estimation which may introduce additional uncertainties to the estimation of collisional power transfer. Moreover, collisional power transfer increases with background plasma temperature as shown in the figure 4.13. Which means that the background plasma temperature may be higher than estimated T_e -profile for the discharge #92454 in order to match the collisional power transfer and the radiated power.

In the discharge #92459, the estimated radiated power loss of the background plasma is comparable to the collisional power transfer and is in good agreement of the radiated power measured by the bolometry. The radiated power measured in #92454 is higher than #92459 and this trend is observed qualitatively by the power balance model. However, the calculated radiated power is overestimated by a factor 4 for the discharge #92454 as shown in the table 4.3. It is to be noted that in the estimation of the radiated power, flat electron density profile is considered which may be subject to higher uncertainty in the estimation. The power terms are qualitatively comparable, although not exactly balanced due to the simplicity of the model and the assumptions made in the calculations.

4.5.3. Open field line background plasma power terms

Background plasma powers in Open field line region		#92459	#92454	DIII-D
(+)	$P_{conduction}$ (W)	TBD	TBD	TBD
(-)	$P_{conduction\ to\ wall}$ (W)	23.78 (1.63-37.39)	16.04 (15.68-40.3)	4.48
(-)	$P_{radiated, SOL}$ (MW)	0.01 (0.01-0.08)	0.49 (1.13-3.18)	0.22

Table 4.5.: Power balance of the open field line background plasmas for JET-ILW discharges and assumed DIII-D discharge (bracket terms indicate error bar due to T_e^{LCFS} uncertainties)

In the estimation of power terms for the background plasma in the open field line region given in table 4.5, the conducted power from the confined to the open line plasma is not estimated and is left for future work. The power conducted from the confined background plasma is the source of power for the background plasma in the open field line region. This term is yet to be estimated. The power lost by the background plasma in the open field line region due to heat conduction to the wall is in order of few W and are negligible compared to other power terms. Thus, the radiated power of the background plasma in the open field line region is the main power loss channel of the background plasma even though it is only a fraction of the total radiated power of the background plasma. The estimations in the table 4.5 considers constant temperature of the background plasma in the open field line region and is the same as the electron temperature at the separatrix (T_e^{LCFS}). Thus, high uncertainty in the estimations can be expected associated to this assumption.

4.5.4. Conclusions

- For the RE beam, bremsstrahlung radiation is negligible as compared to synchrotron radiation and collisional power loss.
- The collisional power transfer due to the interaction of the RE beam is the dominant primary source term to heat the background plasma in the confined region.
- Higher collisional power transfer per free electron of the background plasma may be the possible explanation for hotter background plasma.
- Power conducted to the wall from the background plasma is negligible as compared to the radiated power.
- Good qualitative agreement between the background plasma temperature from the 1D power balance and the measurement from VUV spectroscopy.

It is to be noted that during this power balance estimations, the energies of the RE beam and the background plasmas are considered constant with net power of

the systems being zero. By assuming gain or loss in energies of the RE beam and the background plasma, this power balance can be further improved.

Simulations of the background plasma with the RE beam will be particularly useful not just for the validation of the experimental background plasma characterization but also can help in understanding better the interaction of the RE beam with the background plasma. For this purpose, the background plasma is simulated using a 1D diffusion model in the [chapter 5](#).

5. 1D Diffusion model

In chapter 4, a time-independent 1D power balance of the post-disruption systems showed that the collisional power transfer between the RE beam and the background plasma is the primary heating term of the background plasma in the JET tokamak. However, in this power balance, transport within the plasma is not considered and the time evolution of the background plasma is not addressed. Thus, in the chapter, the background plasma will be simulated using the 1D diffusion model from (Hollmann 2019). This model was originally developed for the DIII-D tokamak and the code was adapted to the JET tokamak. In the section 5.1 of this chapter, the diffusion model is explained. An analysis of sensitive parameters of the model are discussed in the section 5.2. The CRETIN and ADAS atomic data used in the diffusion model are compared in the section 5.2.8. Using the simulation results of the JET discharges from the diffusion model, a database analysis is performed in the section 5.3. The simulation results are then compared with experimental data analysis performed in the section 3.3. In the section 5.5, the simulation of a D₂ SPI into an argon runaway background plasma for the JET discharges are discussed.

5.1. Description of the 1D diffusion model

The description of the 1D diffusion model which follows can be found in detail in (Hollmann 2019).

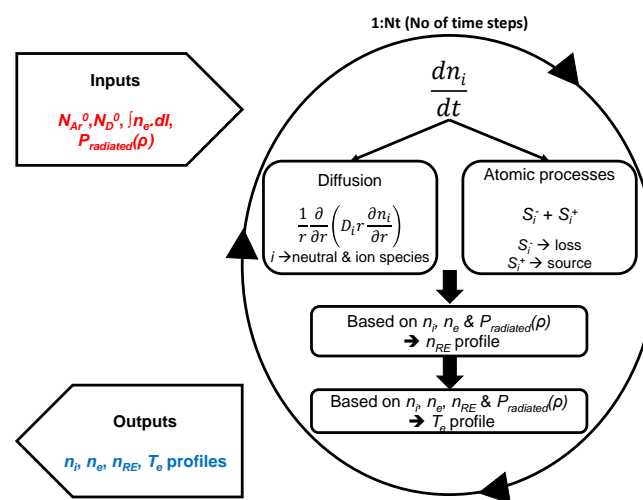


Figure 5.1.: Workflow of the 1D diffusion model

The workflow of the diffusion model is illustrated in the figure 5.1. The line-integrated electron density $\int n_e \cdot dl$, the total argon atoms N_{Ar}^0 , the total deuterium atoms N_D^0 and radial profile of total radiated power $P_{radiated}(\rho)$ are the inputs of the code. The model is iterated for N_t number of time steps. The profiles of species densities, free electron density, RE density and the T_e -profile of the background plasma are the outputs of this diffusion model.

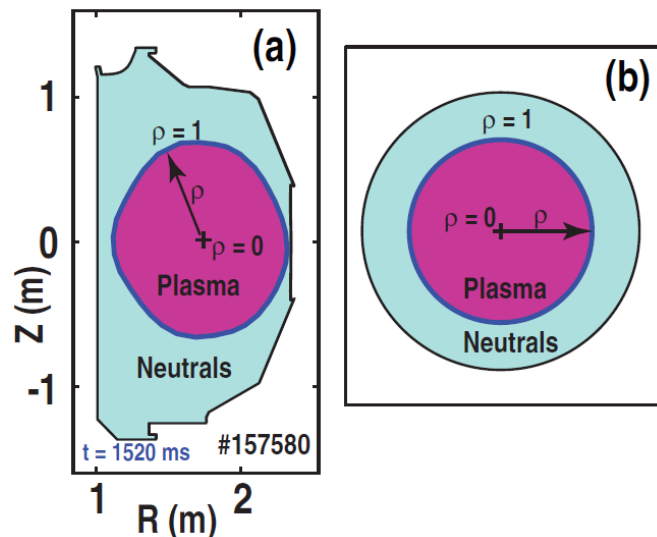


Figure 5.2.: Schematics of 1D diffusion model geometry showing (a) actual experimental geometry and (b) computational domain used in 1D model from (Hollmann 2019)

A 1D radial grid is used to approximate the 3D geometry as shown in the figure 5.2. There are two boundary conditions used in the 1D cylindrical geometry (figure 5.2(b)): RE beam boundary at $\rho=1$ (at last closed flux surface (LCFS)) and a computational outer radius R_w (also called wall radius) for the wall boundary at which ions and neutrals recycle. The radii r_a (corresponding to $\rho=1$) and R_w are chosen to approximately give the correct plasma and vacuum vessel volumes. For instance, $R_w=1.11$ m for the DIII-D tokamak (Hollmann 2019) and for the JET tokamak, the wall radius is taken as $R_w=1.92$ m. The code solves the continuity equation, for this reason, iterations are performed.

The species considered in this 1D diffusion model are D_2 , D , D^+ , D_2^+ , D_3^+ , Ar^{+n} (with $n=0-4$ in the original model, for the JET tokamak, it is extended to $n=0-9$) and ArD^+ . For each species i , the continuity equation used is,

$$\frac{dn_i}{dt} = \left(\frac{\partial n_i}{\partial t}\right)_{recycle} + \left(\frac{\partial n_i}{\partial t}\right)_{puff} - \underbrace{\frac{1}{r} \frac{\partial}{\partial r} \left(D_i r \frac{\partial n_i}{\partial r} \right)}_{diffusion} + \overbrace{(S_i^+ - S_i^-)}^{atomic\ processes} \quad (5.1)$$

The term $\left(\frac{\partial n_i}{\partial t}\right)_{recycle}$ in the equation 5.1 refers to the recycling at the computational

outer wall R_w . In the model, unity recycling is assumed with no wall pumping. It is also assumed that only D_2 and Ar are released from the wall. Ion and D atom reflection is ignored in the model. The ions in contact with the wall recombine as neutrals.

The term $\left(\frac{\partial n_i}{\partial t}\right)_{puff}$ in the equation 5.1 refers to the external gas puffing. In addition to the initial argon and deuterium atoms N_{Ar}^0 and N_D^0 , the external gas puffing term is used to introduce additional atoms on top of the initial number atoms due to the triggering of the injection. Additional injected atoms are introduced at the computational wall radius R_w . This is a way to simulate a secondary killer injection made once the beam is already formed.

The last two terms in the continuity equation 5.1 are the terms due to diffusion and atomic processes.

5.1.1. Diffusion of species

In the continuity equation 5.1, the term $\frac{1}{r} \frac{\partial}{\partial r} \left(D_i r \frac{\partial n_i}{\partial r} \right)$ refers to the diffusion of the species. The term D_i is the diffusion coefficient of the species i . A single diffusion coefficient is assumed for all ions and is left as a free parameter. The ion diffusion coefficient is typically tuned automatically by the code such that it best matches the measured central line density. For ions, D_i values are in order of $D_i \approx 1-10 \text{ m}^2 \text{ s}^{-1}$. For neutrals, the diffusion coefficient D_N can be expressed as,

$$D_N = \frac{\bar{v}_i^2}{\nu_{i,tot}} \quad \text{with} \quad \bar{v}_i = \sqrt{\frac{kT_i}{m_i}} \quad (5.2)$$

The term \bar{v}_i is the thermal velocity of the neutral with neutral temperature T_i .

5.1.1.1. Total neutral collision rate $\nu_{i,tot}$

The term $\nu_{i,tot}$ in the equation 5.2 is the total neutral collision rate including momentum scattering and ionization/dissociation and can be expressed as (Chapman 1970; Pigarov 2012),

$$\nu_{i,tot} = \sum_{\text{neutrals } j} \nu_{ij}^{NN} + \sum_{\text{ion } k} \nu_{ik}^{iN} + \sum_{\text{ions } k} \nu_{ik}^{CX} + \sum_{\text{processes } m} n_m S_{im}^- \quad (5.3)$$

The term $\sum_{\text{neutrals } j} \nu_{ij}^{NN}$ is the sum over neutral-neutral collisions. Using the elastic neutral-neutral scattering rate in the hard sphere approximation, the term ν_{ij}^{NN} can be expressed as (Poline 2004; Marrero 1972),

$$\nu_{ij}^{NN} = \frac{2}{3} \sqrt{\pi} n_j v_{ij} \left(\frac{m_j}{m_i + m_j} \right) r_{ij}^2 \quad (5.4)$$

where $v_{ij} = \sqrt{2T_{ij}/\mu_{ij}}$ is the reduced velocity, $T_{ij} = (m_j T_i + m_i T_j)/(m_i + m_j)$ is the reduced temperature, $\mu_{ij} = (m_i m_j)/(m_i + m_j)$ is the reduced mass and $r_{ij} = (r_i + r_j)/2$

is the effective radius for momentum scattering.

The term $\sum_{\text{ions } k} v_{ik}^{iN}$ is the sum over ion-neutral collisions. Using the neutral momentum scattering rate off ions assuming Langevin collisions between ions and polarizable neutrals can be expressed as (Osterbrock 1961),

$$v_{ij}^{iN} = \frac{2.41\pi(\alpha_i\mu_{ij})^{1/2}n_jZ_je}{m_i} \quad (5.5)$$

where α_i is the polarizability of the neutral and Z_j is the charge of the target ion. Energy-resolved elastic scattering cross section data for D+D⁺ elastic scattering collisions is available (Thomas 1997). In this case, an improved ion-neutral scattering rate is used from the Ω -integral formulation from classical gas dynamics as (Bachmann 1995),

$$v_{ij}^{iN} = \frac{4}{3\sqrt{\pi}}n_jv_{ij}\left(\frac{m_j}{m_i+m_j}\right)\int_0^\infty d\xi e^{-\xi^2}\xi^2\sigma_M(T_{ij}\xi^2) \quad (5.6)$$

where σ_M is the momentum scattering cross section versus center of mass collision energy.

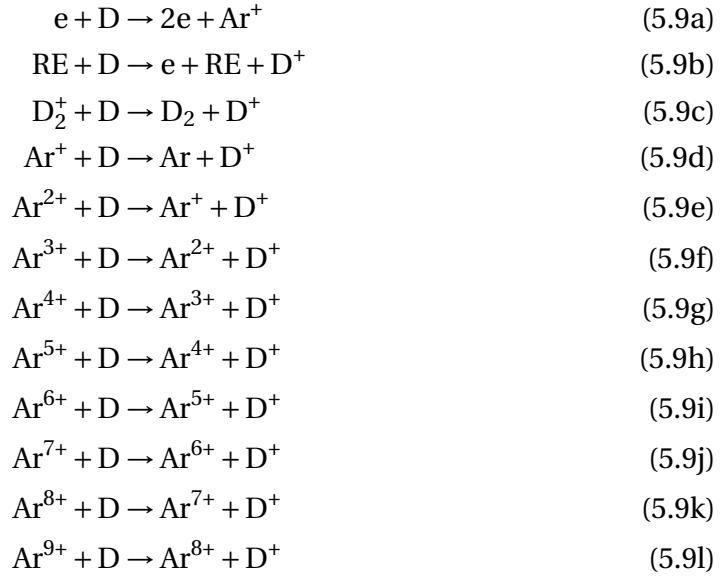
All symmetric (resonant) charge exchange collisions are included for the term $\sum_{\text{ions } k} v_{ik}^{CX}$ resulting in a fast neutral with random velocity vector. For the rate of symmetric charge exchange collisions, a Ω -integral is used without the mass ratio as,

$$v_{ij}^{CX} = \frac{4}{\sqrt{\pi}}n_jv_{ij}\int_0^\infty d\xi e^{-\xi^2}\xi^2\sigma_{CX}(T_{ij}\xi^2) \quad (5.7)$$

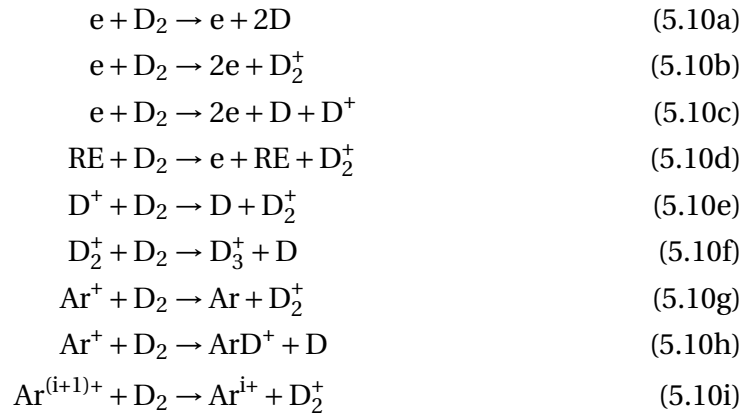
The following charge exchange reactions are considered in the term $\sum_{\text{ions } k} v_{ik}^{CX}$ are as follows :



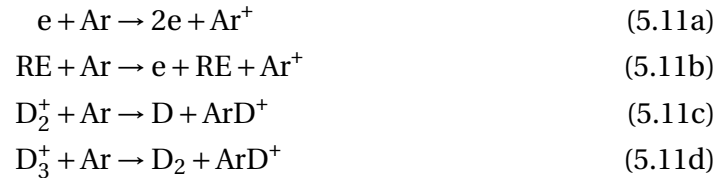
The term $\sum_{\text{processes } m} n_m S_{im}^-$ is a sum over all collision processes which destroy neutrals. This is included to capture the effect of the shortening of the mean free path of neutrals during the neutral diffusion processes due to ionization, dissociation, etc. The following D destruction reactions are included in this term (Phelps 1992; Pigarov 1996; Anicich 1993; Can 1985):



In the equations 5.9, e refers to the thermal electrons of the background plasma and RE refers to the runaway electrons. The following D_2 destruction reactions are included (Phelps 1992; Pigarov 1996; Anicich 1993; Can 1985; Reiter 2004):



with i from 1-8 in equation 5.10i. Ar destruction reactions included are (Anicich 1993; Scott 2001):



Using the above equations, the total neutral collision rate $\nu_{i,tot}$ is estimated. The next unknown in the neutral diffusion coefficient is the neutral temperature T_i

5.1.1.2. Neutral temperature T_i

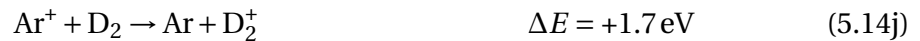
In the equation 5.2, neutral temperatures T_i is estimated with the rate equation,

$$\frac{dT_i}{dt} = \sum_j v_{ij}^T (T_j - T_i) + \sum_{\text{exotherm } m} v_{mi}^+ (T_{mi} - T_i) + v_i^{\text{diff}} (T_{\text{wall}} - T_i) \quad (5.12)$$

In the equation 5.12, the term $\sum_j v_{ij}^T (T_j - T_i)$ is sum over all species j (excluding electrons) and reflects heating by different species. The term v_{ij}^T is the thermalization rate and can be expressed as,

$$v_{ij}^T = \left(\frac{2m_i m_j}{(m_i + m_j)^2} \right) v_{ij}^{NN} \quad (5.13)$$

where v_{ij}^{NN} is the neutral-neutral scattering date given in the equation 5.4. In the equation 5.12, the term $\sum_{\text{exotherm } m} v_{mi}^+ (T_{mi} - T_i)$ is sum over all exothermic reactions which are given below :



The term v_{mi}^+ is the rate at which neutral species i is formed due to reaction m . The term $T_{mi} = \left(\frac{M-m_i}{M} \right) \Delta E_m$ is the reaction product energy where M is the total mass of reaction products and ΔE_m is the total energy released by reaction m . The term $v_i^{\text{diff}} (T_{\text{wall}} - T_i)$ is a rough estimation of the cooling rate of neutrals i due to heat diffusion to the wall. It is assumed that the thermal and neutral diffusivity are similar in size (modulo factors of order unity) (Pigarov 2009). Using the neutral temperature T_i , the neutral diffusion coefficient given in the equation 5.2 is estimated.

5.1.1.3. Diffusion flux

The neutral diffusion coefficient D_N is estimated using the equation 5.2. In this system, neutral diffusion coefficients can be quite large ($D_N \approx 50 \text{ m}^2 \text{ s}^{-1}$) and thus diffusive treatment is not completely valid (Hollmann 2019). Thus, a flux limit is imposed on the neutrals to avoid nonphysically large neutral diffusion at certain radii. Thus, the effective diffusion coefficient $D_{L,i}$ can be expressed as,

$$D_{L,i} = \frac{D_i}{1 + \Gamma_i/\Gamma_L} \quad (5.15)$$

where $\Gamma_i = D_i \nabla n_i$ is the initial (unlimited) radial flux and $\Gamma_L = n_i \bar{v}_i$ is the maximum flux.

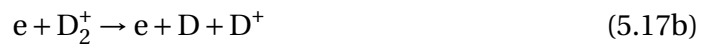
5.1.2. Atomic processes

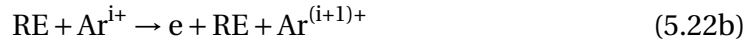
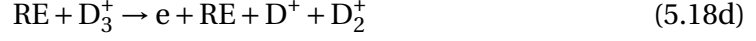
The reactions which destroy neutrals, given in the equations 5.8, 5.9, 5.10 and 5.11, are used in diffusion of species. In addition to the reactions which destroy neutrals, reactions which destroy ions are also included. The population of ions are destroyed by atomic processes such as ionization, recombination and charge exchange. These reactions are used in the source/sink terms S_i^- and S_i^+ in the continuity equation 5.1 are as follows (Pigarov 1996; Reiter 2004; Scott 2001):



For the D reactions given in the equations 5.9(a) and 5.16, CRAMD collisional radiative code (Pigarov 1996) is used with D UV (Lyman) transitions opaque. For cold D temperatures ($\sim 1 \text{ eV}$) and long path lengths ($\sim 1 \text{ m}$), this may be true. For the charge transfer reaction given in equation 5.9(d), the rate coefficient for D_2 is used but scaled to the smaller D radius.

For the reactions involving molecular D neutrals or ions, most recent experimental data or calculations are used for rate coefficients, but the CRAMD code is used to estimate the enhancement due to vibrational excitation of the molecules. A rough scaling for D_2 vibrational temperature as a function of electron density is used (Hollmann 2006). In the CRAMD code, enhancement of D_3^+ rates due to vibrational excitation are not explicitly treated but are assumed to be similar to D_2^+ . The vibrational temperatures of D_2^+ and D_3^+ are assumed to be half as large as D_2 vibrational temperature. The reactions which destroy ions are given below :





with $i=3-8$ for the equation 5.22. For the electron impact ionization of the argon neutral, equation 5.11(a), rates from CRETIN code (Scott 2001) is used to approximate the ionization of UV-thick argon with a cylindrical escape factor. For the Ar^+ ionization given in the equation 5.20(b), experimental data of (Muller 1985) is used but scaled with the estimated collisional-radiative electron density dependence from CRETIN.

For the electron impact disassociation of ArD^+ , reactions 5.19(b) and 5.19(c) are assumed equal probability. For the argon recombination, 3-body, radiative and dielectronic contributions are considered. Dielectronic recombination was found to be dominant (Hollmann 2019).

In the original code, electron-impact ionization for states higher than Ar^{2+} is ignored. This is because of the fact that for colder background plasmas with $T_e < 2.5$ eV which is observed in the DIII-D tokamak, ionization is predominantly through RE impact ionization. However for the JET tokamak, higher temperatures of the background plasmas are observed (discussed in the section 3.3). Thus, electron-impact ionization for higher ionization states of argon are enabled in the current code.

5.1.2.1. RE impact ionization

RE beam have the potential to ionize the neutrals and ions to high ionization states. Using the Bethe formula for the stopping power of bound electrons on impacting relativistic electrons, the ionization rate due to the RE beam impact on neutrals and

ions can be estimated as (Rohrlich 1954),

$$\begin{aligned} \frac{dE}{dx} = \frac{2\pi e^4 n_{e,b}}{m_e v^2} & \left[\log\left(\left(\frac{\gamma+1}{2}\right)\left(\frac{K}{I_i^*}\right)^2\right) + \frac{1}{\gamma^2} \right. \\ & \left. + \frac{1}{8}\left(\frac{\gamma-1}{\gamma}\right)^2 - \left(\frac{2\gamma-1}{\gamma^2}\right)\log 2 \right] \end{aligned} \quad (5.23)$$

where K is the kinetic energy of the RE beam with Lorentz factor γ , $n_{e,b}$ is the bound electron density and I_i^* is the effective ionization energy taken from (Sauer 2015). The deposited energy goes into both direct ionization and excitation. The RE impact excitation can then result in ionization through Auger processes. The total direct ionization cross section σ_i^* can be expressed as,

$$\sigma_i^* = \sum_{n,l} \sigma_{n,l}^* \quad (5.24)$$

The sublevel ionization cross-section $\sigma_{n,l}^*$ is related to the sublevel energy $E_{n,l}^*$ as $\sigma_{n,l}^* \sim 1/E_{n,l}^*$ (Llovet 2014). With the stopping power dE/dx , total ionization σ_i^* is related as (Peterson 1968),

$$\frac{dE}{dx} \sim \sigma_i^* E_i^* n_{e,b} \quad (5.25)$$

where E_i^* is the ionization energy of the uppermost shell of charge state i . By combining the equations 5.23 and 5.25, the ionization cross section σ_i^* for an arbitrary charge state i can be obtained. For Ar ions, a small ($\sim 10\%$) correction for Auger excitation for lower argon charge states is added using the enhancement factor from (Salop 1974). For D₂ molecule, RE ionization rates are taken from (Rieke 1972).

5.1.3. Estimation of species and free electron density profiles

In this 1D diffusion model, the density profile of species are solved iteratively with time step dt using the continuity equation 5.1. Correspondingly, the thermal electron density profile is determined by charge neutrality as,

$$n_e(r) = \sum_{species} n_i(r) \cdot Z_i \quad (5.26)$$

where Z_i is the charge state of the species i . The term r represents the radial vector of the profile. Due to the iterative nature of the code, an initial guess of the density profiles of the species and free electron density is taken. It can also be seen that electron and ion temperatures are needed in the estimation of both diffusion and atomic reactions. Hence, an initial guess of the temperature profile must also be provided. More information about the sensitivity of different initial guesses will be seen in the section 5.2. It is to be noted that in this 1D diffusion model, ion tempera-

tures are assumed to be equal to the electron temperature. This was justified because ion-electron thermalization timescales are usually much shorter compared to the problem timescales.

5.1.4. Estimation of RE density profile

In this 1D diffusion model, RE density n_{RE} is estimated from the thermal electron heat balance equation. Thermal electron temperature T_e of the background plasma is assumed to evolve rapidly (sub-ms timescales) relative to the transport timescales (several ms). Thus, it is assumed that $dT_e/dt=0$ and so T_e is always in equilibrium during the impurity profile evolution. At higher thermal temperatures, typically $T_e > 1.5$ eV, the RE impact is balanced by the line radiation as observed in (Hollmann 2015). This was also observed in the section 4.2 of the chapter 4 where the collisional power loss of the RE beam was in the same order of magnitude as the radiated power measured by the bolometry. Thus, an approximate rate equation can be constructed as,

$$\frac{d}{dt} \left(\frac{3}{2} n_e T_e \right) = 0 = n_{RE} \sum_j n_j S_j^{RE} - \sum_k n_k n_e S_k^{rad}(n_e, T_e) - v_{D_2}^{diff} n_{D_2} (T_e - T_{wall}) \quad (5.27)$$

where T_{wall} is the temperature of the wall. In the diffusion model, T_{wall} is taken as 300K. In the original model proposed in (Hollmann 2019), the energy of the RE beam K is taken as 1 MeV for the DIII-D tokamak. However, higher RE energies are seen in the JET tokamak from the hard x-ray (HXR) spectra. It is to be noted that higher RE energies are estimated from the 1D power balance of the RE beam (table 4.2). Thus, for the JET tokamak, RE energy was taken as $K=10$ MeV (Reux 2015). The accuracy of the ionization rate is not significantly affected by mono-energetic approximation. This may be due to the fact that stopping power (and thus the ionization rate) doesn't change significantly for kinetic energies higher than ionization energy.

The term S_j^{RE} in the equation 5.27 is the fast electron stopping power on species j and can be expressed as,

$$S_j^{RE} = \frac{v_{RE}}{n_j} \left(\frac{dE}{dx} \right)_j \quad (5.28)$$

where v_{RE} is the relativistic velocity of the RE beam corresponding to energy K . dE/dx is the Bethe stopping power from equation 5.23. The term S_k^{rad} is the radiation rate coefficient for species k . Radiation rate coefficients are calculated with CRETIN code (Scott 2001). For D₂ molecule, radiation cooling rate is taken from EIRENE code (Reiter 2004). The solution of the RE density n_{RE} can be constrained by using experimental radiated emissivity ϵ_{rad} which is represented as,

$$\epsilon_{rad} = \sum_k n_k n_e S_k^{rad}(n_e, T_e) \quad (5.29)$$

The above equation 5.29 is similar to the equation 4.23. The only difference is that in the equation 4.23, cooling rate is taken from ADAS database (Summers 2004) whereas in the diffusion model, the equation 5.29 uses cooling rate coefficients from CRETIN (Scott 2001).

In the equation 5.27, the term $v_{D_2}^{diff} n_{D_2} (T_e - T_{wall})$ express the D_2 lost to the wall. Here, $v_{D_2}^{diff} = D_{D_2} / \Delta R_w^2$, where $\Delta R_w = R_w - R_a$. Since the equilibration timescale between the vibrational temperature of D_2 T_{vib} and electron temperature T_e is very low ($\sim 10 \mu s$ from (Hollmann 2008)), $T_e = T_{vib}$ is assumed.

By substituting equation 5.29 in equation 5.28, the rate equation can be rewritten as,

$$n_{RE} \sum_j n_j S_j^{RE} = \epsilon_{rad} + v_{D_2}^{diff} n_{D_2} (T_e - T_{wall})$$

$$n_{RE} = \frac{\epsilon_{rad} + v_{D_2}^{diff} n_{D_2} (T_e - T_{wall})}{\sum_j n_j S_j^{RE}} \quad (5.30)$$

In the 1D diffusion model, the RE density n_{RE} is updated for every few iterations using the latest information of species densities, electron density profile and the T_e -profile. Similar to species density profiles and T_e -profile, initial guess of the RE density n_{RE} is required before iterations. Initial guess of the n_{RE} profile is estimated using the radiated power profile and initial guesses of T_e and species density profiles. Thus, experimental radiated power profile is a critical input of the code as RE density and electron temperatures depend on it.

5.1.5. Estimation of T_e profile

In the 1D diffusion model, experimental total radiated emissivity ϵ_{rad} is given as an input. This is usually from the tomographic inversion of bolometer data. If no tomographic inversion is available, the total radiated power is given as input to the code. From the total experimental radiated power value, a Gaussian emissivity profile ϵ_{rad} of width w (usually 0.3m, but can be changed in the code).

From the equation 5.29, it can be observed that emissivity ϵ_{rad} is a function of species densities n_j , free electron density n_e and electron temperature T_e . Thus, the electron temperature T_e of the background plasma is determined by matching the theoretical emissivity from equation 5.29 (from cooling rate coefficients from CRETIN (Scott 2001)) with the experimental emissivity profile ϵ_{rad} .

In the 1D diffusion model, the T_e -profile is updated for every few iterations using the information of species density profiles, free electron density profile and the RE density profile. This updated T_e -profile is then used as the input for the next iteration for the calculation of diffusion and atomic processes.

5.1.6. Conservation of Ar and D atoms

At the end of each iteration, the total number of Ar and D atoms are recalculated as,

$$N_{Ar/D}^{tot} = \sum_{\rho} \left(dV(\rho) \sum_i n_i^{Ar/D}(\rho) \right) \quad (5.31)$$

where $dV(\rho)$ is the grid volume corresponding to the normalized radius ρ . n_i^{Ar} comprises of argon species for N_{Ar}^{tot} and deuterium species n_i^D corresponds to N_D^{tot} . The total Ar and D atoms from the model $N_{Ar/D}^{tot}$ can be either higher or lower than the initial input atoms, N_{Ar}^0 and N_D^0 . When the model predicts fewer atoms, $N_{Ar/D}^{tot} < N_{Ar/D}^0$, neutrals are added near the tokamak wall. When the model predicts higher atoms, $N_{Ar/D}^{tot} > N_{Ar/D}^0$, the species density profiles $n_i^{Ar/D}$ are scaled as,

$$\begin{aligned} n_i^{Ar} &= A_{Ar} \cdot n_i^{Ar} \quad \text{for Ar species with} \quad A_{Ar} = \frac{N_{Ar}^0}{N_{Ar}^{total}} \\ n_i^D &= A_D \cdot n_i^D \quad \text{for D species} \quad A_D = \frac{N_D^0}{N_D^{total}} \end{aligned} \quad (5.32)$$

5.2. Sensitivity analysis of the 1D diffusion model

In the section 5.1, the working of the 1D diffusion model was explained. Before eventually simulating the background plasma in this chapter, the sensitivity of the parameters in the model should be analyzed. The following are the parameters upon which the results of the simulation from the diffusion model can be sensitive :

1. initial guesses of the parameters
2. inclusion of higher ionization states
3. inclusion of electron impact ionization
4. impact of RE direct ionization
5. conservation of Ar and D atoms
6. change of wall radius R_w
7. iteration time step
8. rate calculations from atomic model

In the 1D diffusion code, experimental emissivity profile ϵ is an important input parameter. For the simulations, experimental emissivity profile ϵ is constructed using total radiated power from bolometer, assuming a Gaussian radius of 30cm. In the 1D diffusion code, the emissivity profile is fixed during the simulation and no evolution is considered.

5.2.1. Initial guesses of the parameters

As discussed in the section 5.1, the 1D diffusion model simulates the background plasma iteratively. This means that before the iteration, the initial guesses of the parameters : electron density profile, electron temperature profile, species density profiles and RE density profile, should be given. For simplicity, the initial guesses of the electron density and temperature profile assumes a flat profile in the confined region $\rho \leq 1$. From $\rho=1$ until the wall, the electron density and temperature decreases linearly as shown in the figures 5.3 and 5.4. At the confined region, initial value of the background plasma temperature is taken as T_e^0 and at the wall, $T_{wall}=300$ K or 0.026 eV.

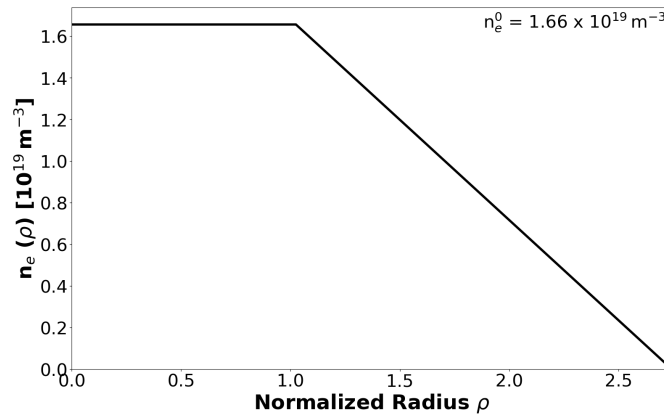


Figure 5.3.: Shape of the electron density profile $n_e(\rho)$ with $n_e^0=1.66 \times 10^{19} \text{ m}^{-3}$

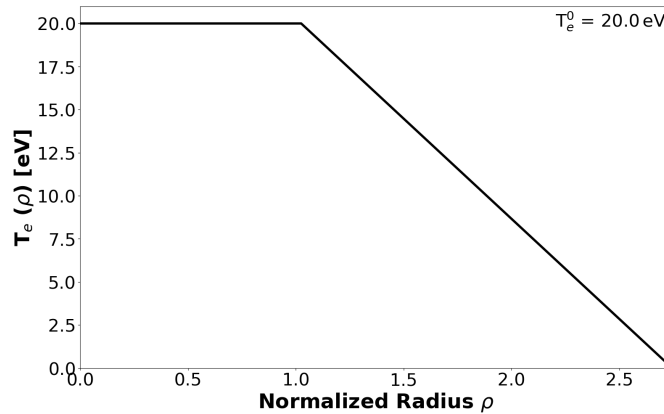


Figure 5.4.: Shape of the electron temperature profile $T_e(\rho)$ with $T_e^0=20 \text{ eV}$

5.2.1.1. Initial guesses of electron density n_e^0

Three initial guess of the core electron density n_e^0 is swept as shown in the figure 5.3 : the red dotted line ($n_e^0=1.66 \times 10^{19} \text{ m}^{-3}$) corresponds to an actual line-integrated density measurement ($\int n_e \cdot dl=4.4 \times 10^{19} \text{ m}^{-3}$) from interferometry for the discharge #95125, blue dashed line with $n_e^0=10^{20} \text{ m}^{-3}$ and green solid line with $n_e^0=2 \times 10^{20} \text{ m}^{-3}$.

The core electron temperature value for the initial guess is $T_e^0=20$ eV and RE density is from the radiated power profile (as discussed in section 5.1). Species density is assumed such that half of the electron density comes from Ar^{1+} and other half from D^{1+} . The other species are set to zero initially.

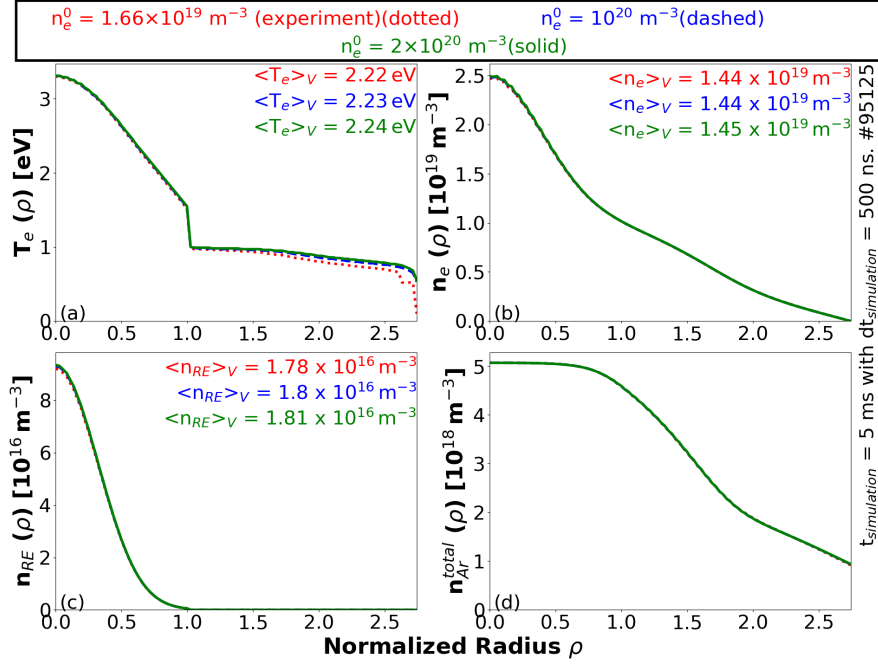


Figure 5.5.: Profile of (a) Temperature T_e , (b) electron density n_e , (c) RE density n_{RE} and (d) total argon density n_{Ar} , after 5 ms simulation with $dt=500$ ns. Initial guess of the core electron density n_e^0 is swept.

It can be seen from the figure 5.3 that for a magnitude change in the initial guess of the electron density, no significant change is observed in the electron density, RE density and the total argon density of the simulation. In the temperature profile, no change is observed in the confined region. Near the wall, temperature seems to be slightly higher for a magnitude change in the initial density guess. This change in the temperature may be due to the fact that the cooling rate coefficients used in the temperature estimation are selected from the initial guess of the electron density profile. As discussed in the section 4.4, the dependence of the cooling rate coefficients on the electron density is very weak and the simulation should not be affected significantly due to the initial guess of the electron density profiles.

5.2.1.2. Initial guesses of electron temperature T_e^0

Now, the initial guess of the electron density is fixed at $n_e^0=1.66 \times 10^{19} \text{ m}^{-3}$. The initial guess of the temperature profile T_e^0 is swept in the figure 5.4. It can be observed from the figure 5.6 that initial guess of the T_e -profile has no effect on the simulation results.

It is to be noted that by changing the initial guess of the temperature profile, the initial energy of the system is changed. However, the 1D diffusion code efficiently

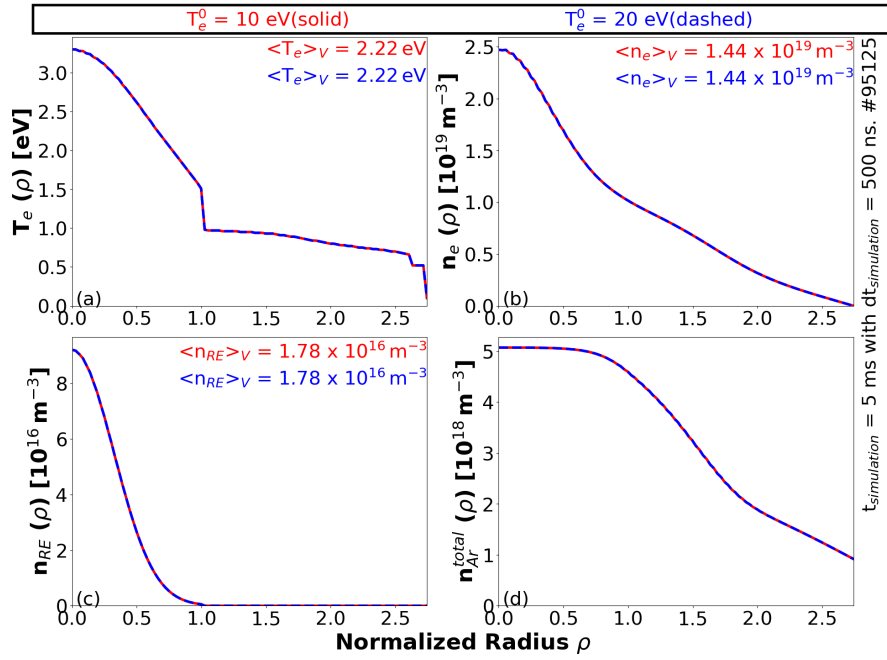


Figure 5.6.: Profile of (a) Temperature T_e , (b) electron density n_e , (c) RE density n_{RE} and (d) total argon density n_{Ar} , after 5 ms simulation with $dt=500$ ns. Initial guess of the core electron temperature T_e^0 is swept.

converges as shown in the figure 5.7. Thus, it can be said that the code is insensitive to the initial guess of the temperature profile.

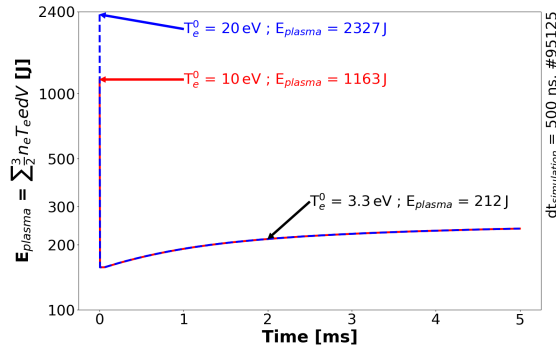


Figure 5.7.: Time evolution of the plasma energy E_{plasma} of the background plasma in the confined region for the discharge #95125. The simulation is performed for 5 ms simulation with iteration time step is $dt=500$ ns.

The initial guess of the temperature is used to estimate the diffusion coefficients of the neutrals D_N for the first iteration. But since neutral diffusion coefficient is flux limited (equation 5.15), the effect of initial guess of the T_e -profile is considerably reduced.

5.2.1.3. Initial guesses of species density profiles

The next parameter to analyze is the initial guesses of the species density profiles. The initial guess of the electron density and temperatures are fixed at $n_e^0 = 1.66 \times 10^{19} \text{ m}^{-3}$ and $T_e^0 = 20 \text{ eV}$ respectively in the figure 5.8. It is assumed that half of the free electron comes from Ar^{1+} , Ar^{2+} , Ar^{3+} or Ar^{4+} ionization states corresponding to the red (dotted), blue (dashed), green (dashed dotted) and purple (solid) of the figure 5.8. The other half of the free electrons comes from D^{1+} in all the cases. Other ionization states are assumed to be absent before the simulation.

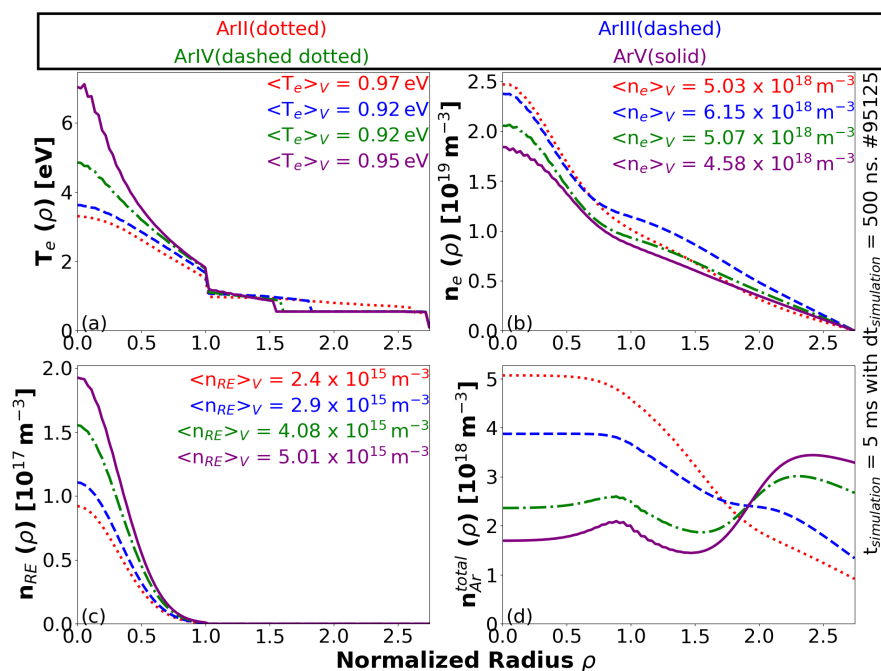


Figure 5.8.: Profile of (a) Temperature T_e , (b) electron density n_e , (c) RE density n_{RE} and (d) total argon density n_{Ar} , after 5 ms simulation with $dt=500 \text{ ns}$. Initial guess of the species densities are swept.

It can be observed in the figure 5.8 that increase in the initial predominant species (Ar^{1+} - Ar^{4+}), the central temperature T_e^0 and core RE density n_{RE}^0 increases whereas the core electron density n_e^0 slightly decreases. It can also be observed in the figure 5.8(a) that higher the predominant ionization states, lower is the electron temperature outside the confined region. On looking at the total argon density profile shown in the figure 5.8(d), it can be seen that most of the argon impurities is near the wall as neutral due to lower temperatures. In the confined region, argon ions of higher ionization states are present which contributes to the higher temperature.

An energy profile can be constructed for different initial guesses of the species density profiles as shown in the figure 5.9 and it can be observed that higher the ionization states in the assumption of the initial guesses, the stored energy increases in the confined region. Thus, by assuming higher ionization states as the initial guess of the parameters, higher initial potential energy of the system may be assumed which

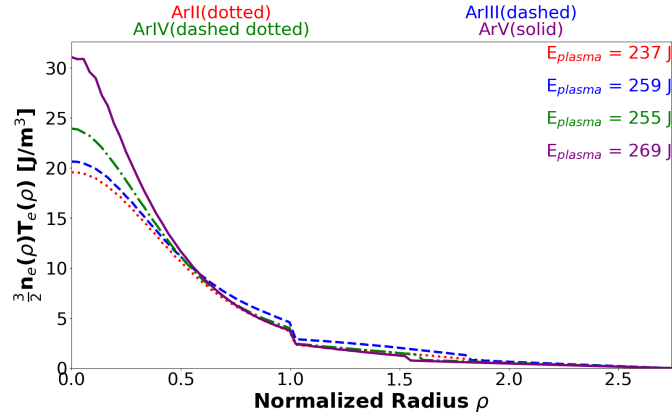


Figure 5.9.: Plasma energy profile constructed using T_e and n_e profiles from the 1D diffusion code for the discharge #95125, for various initial guesses of the species densities. Background plasma is simulated for 5 ms with iteration time step $dt_{simulation}=500$ ns.

results in the higher electron temperature of the background plasma. Thus, the initial guesses of the species density should be carefully dealt with.

5.2.1.4. Initial guesses of RE density

As discussed in the section 5.1, RE density is calculated from the radiated power profile. In the figure 5.10, the red (solid) data has RE density profile from the experimental emissivity profile (with total radiated power $P_{rad}=2$ MW and Gaussian radius 30 cm, for the discharge #95125). In the blue (dashed) data of the figure 5.10, the initial guess of the RE density n_{RE} is increased by a factor 10. The initial guess of the electron density and temperatures are fixed at $n_e^0=1.66 \times 10^{19} \text{ m}^{-3}$ and $T_e^0=20$ eV respectively. It is assumed that one half of the free electrons are from Ar^{1+} and other half is from D^{1+} . From the figure 5.10, no change in the simulation results are observed by changing the initial guess of the RE density profile.

On analyzing the sensitivity of various initial guesses of the parameters, the initial guesses of the species densities was found to be the most sensitive which can significantly change the simulation results. The initial guess of the electron density are a bit sensitive as the cooling rate coefficients are selected based on the magnitude of the initial electron density profile. On the other hand, the initial guesses of the electron temperature profile and the RE density profiles were found not to alter the simulation results.

By default, the initial guess of the electron density profile is taken from interferometry (for instance, $n_e^0=1.66 \times 10^{19} \text{ m}^{-3}$ for #95125) for all the simulations of 1D diffusion code. The initial guess of the electron temperature profile is fixed as $T_e^0=20$ eV and it is assumed that one half of the free electrons are from Ar^{1+} and other half from D^{1+} . The RE density is taken from the radiated power profile by default.

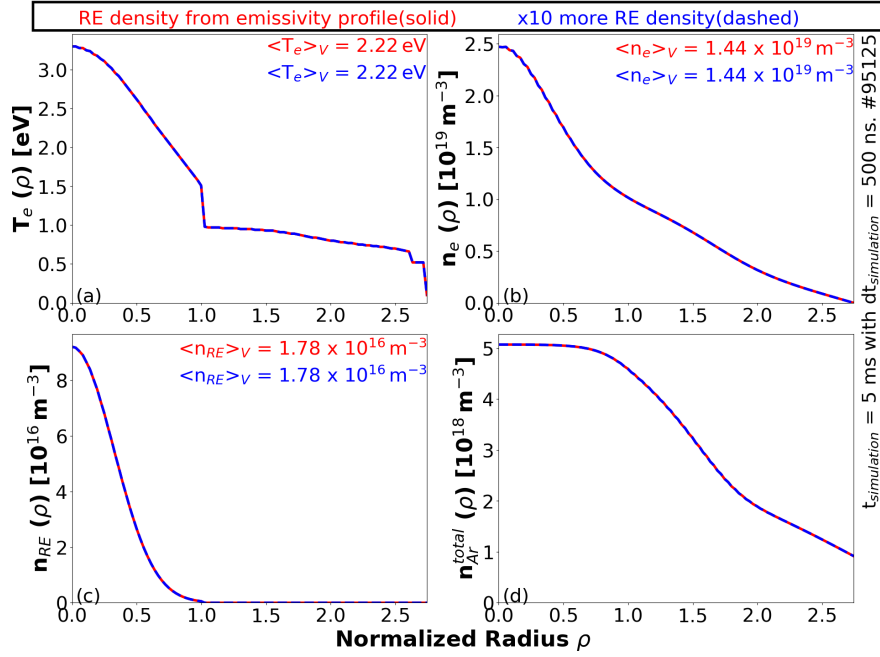


Figure 5.10.: Profile of (a) Temperature T_e , (b) electron density n_e , (c) RE density n_{RE} and (d) total argon density n_{Ar} , after 5 ms simulation with $dt=500$ ns. Initial guess of the RE density n_{RE} is swept.

5.2.2. Inclusion of higher ionization states

In the original 1D diffusion model (Hollmann 2019), only argon species up to Ar^{4+} (ArV) are considered. From the VUV spectroscopy of the JET tokamak, higher ionization states such as Ar^{8+} and Ar^{9+} are observed (figure 3.27). Thus, in the 1D diffusion model, the atomic reactions and diffusion of higher ionization states up to Ar^{10+} are added to simulate the background plasmas in the JET tokamak.

The profile of various parameters after 5 ms simulations with and without the inclusion of higher ionization states are shown in the figure 5.11. It can be observed that by including higher ionization states, the electron temperature and density profiles are slightly higher than by excluding higher ionization states. No significant change in the RE density can be observed though from figure 5.11(c). On looking at the total argon density profile shown in the figure 5.11(d), it can be observed that near the wall, fewer argon atoms are found when higher ionization states are included. As argon atoms near the wall are neutrals due to low temperature, fewer argon neutrals are observed with inclusion of higher ionization states than the original model. This is qualitatively consistent with the low argon neutral brightness in the VUV spectra in the far-SOL region (figure 3.29).

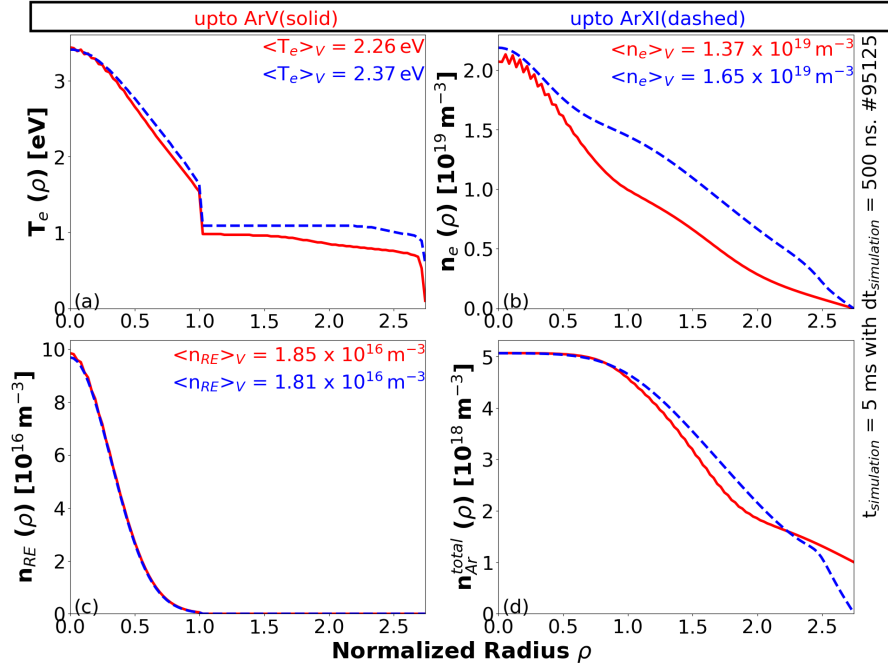


Figure 5.11.: Profile of (a) Temperature T_e , (b) electron density n_e , (c) RE density n_{RE} and (d) total argon density n_{Ar} , after 5 ms simulation with $dt=500$ ns. Inclusion of higher ionization states are compared.

5.2.3. Inclusion of electron impact ionization

In the original 1D diffusion model (Hollmann 2019), electron-impact ionization of higher ionization states starting from Ar^{2+} is neglected. This is due to the fact that direct ionization due to the RE beam may be much stronger than the electron-impact ionization. However, in the original model, RE energy of $E_{RE}=1$ MeV was considered for the DIII-D tokamak (Hollmann 2019). For the JET tokamak, we assume $E_{RE}=10$ MeV (Reux 2015) and RE impact ionization may be much lower for the JET tokamak as compared to the DIII-D tokamak. This is because the cross section of RE impact ionization decreases with RE energy. Thus, the effect of including the electron-impact ionization in the 1D diffusion model is studied.

From the figure 5.12, it can be seen that by including the thermal electron impact ionization, there is no significant change in the simulation results of the diffusion model. From the figure 5.13, it can be observed that ionization of Ar^{0+} (argon neutral) is predominantly through thermal electron impact ionization. For Ar^{1+} and Ar^{2+} , electron-impact ionization is important for very high T_e . For ionization states beyond Ar^{2+} , ionization is predominantly through RE ionization rather than thermal electrons. Thus, excluding the electron-impact ionization can be a good approximation. However, for completeness, electron impact ionization for higher ionization states are performed in the 1D diffusion model for the JET tokamak.

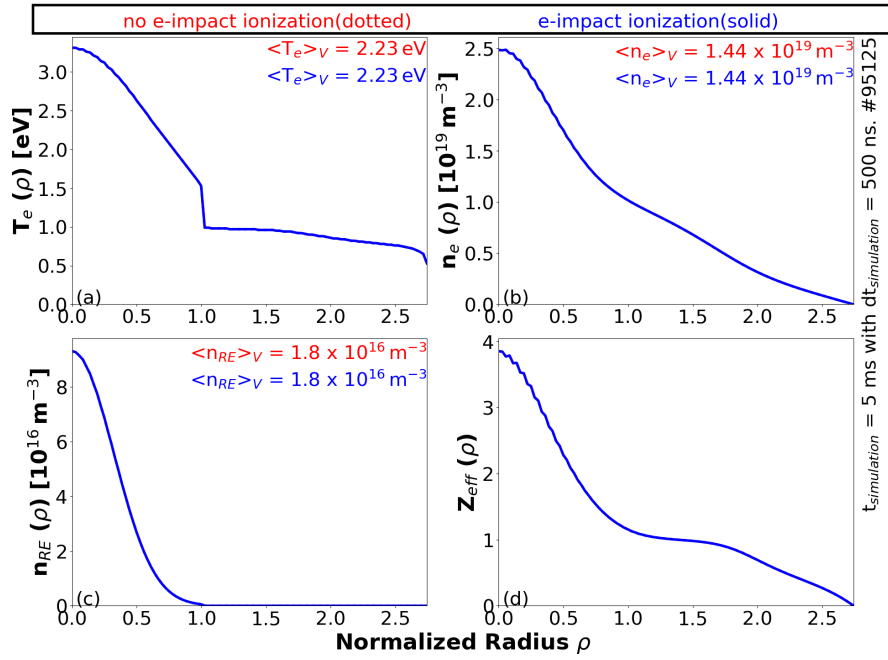


Figure 5.12.: Profile of (a) Temperature T_e , (b) electron density n_e , (c) RE density n_{RE} and (d) Effective ion charge state Z_{eff} , after 5 ms simulation with $dt=500$ ns. Inclusion of electron-impact ionization for higher ionization states.

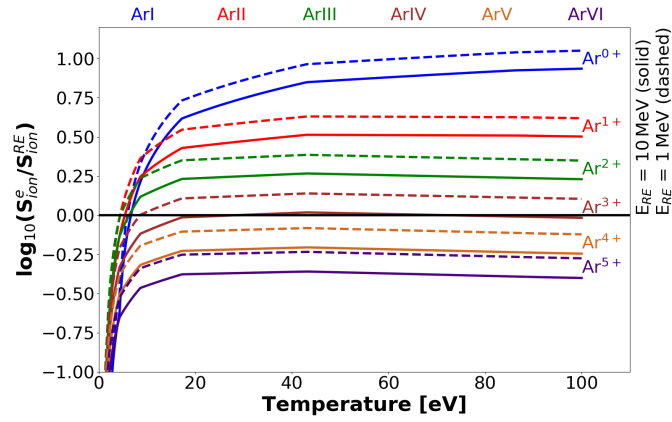


Figure 5.13.: Ratio of the ionization rates due to thermal electron-impact ionization and RE direct ionization for $E_{RE}=10$ MeV (solid) and $E_{RE}=1$ MeV (dashed)

5.2.4. Impact of RE direct ionization

In the cold background plasma, argon particles can be ionized through two mechanisms : ionization by thermal electrons and RE impact direct ionization. From the VUV spectroscopy of the JET tokamak, it was observed that for argon background plasma, Ar^{1+} and Ar^{2+} are the most predominant charge states. In addition, higher ionization states such as Ar^{8+} can also be observed in the confined background plasma, probably due to the direct impact of RE beam. It can be seen from the figure 5.13 that hotter background plasma may result in Ar^{1+} and Ar^{2+} even without RE impact ionization, however, higher ionization states may be due to RE beam. Thus, the effect of including RE impact ionization on the simulation results are checked.

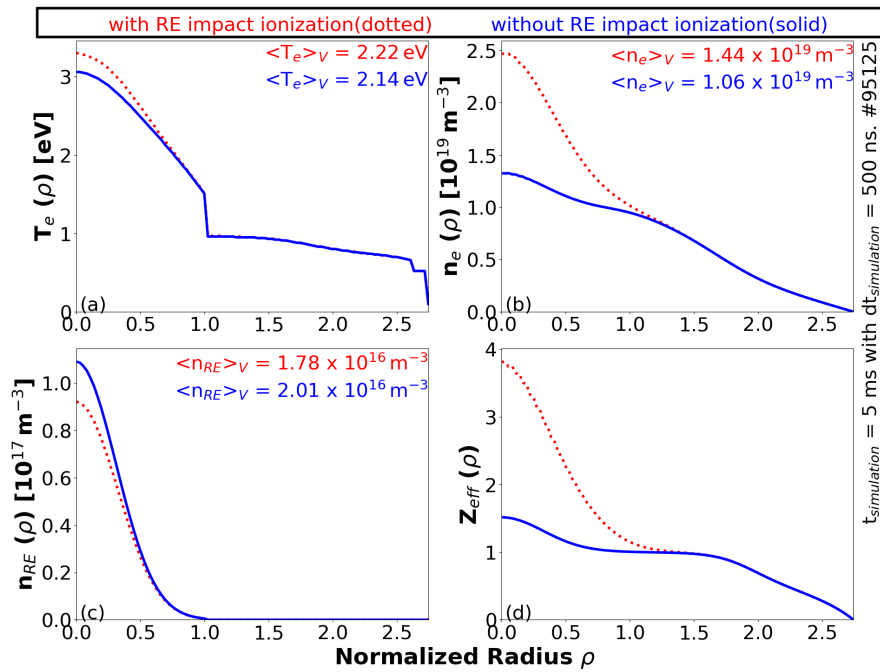


Figure 5.14.: Profile of (a) Temperature T_e , (b) electron density n_e , (c) RE density n_{RE} and (d) Effective ion charge state Z_{eff} , after 5 ms simulation with $dt=500$ ns. Inclusion and exclusion of RE impact direct ionization.

From the figure 5.14, the RE beam enhances the direct ionization and as a result, the electron density increases (figure 5.14(b)) and effective ion charge state (figure 5.14(d)). There is an increase in the electron temperature in the confined region as shown in the figure 5.14(a).

From the figure 5.14(a), it can also be observed that the increase in the confined electron temperature is only ~ 0.5 eV. As discussed in section 3.2, the line intensities depend primarily on the electron temperature (see figure 3.21 for instance) Thus, it can be said that RE beam contributes mainly by direct impact ionization of the background plasma and RE beam excitation is rather very small. From the figure 5.15, it can be seen that for $E_{RE}=10$ MeV, the ratio between the excitation to ionization rate coefficients due to the direct impact of the RE beam is as small as $\sim 3\%$. The data are

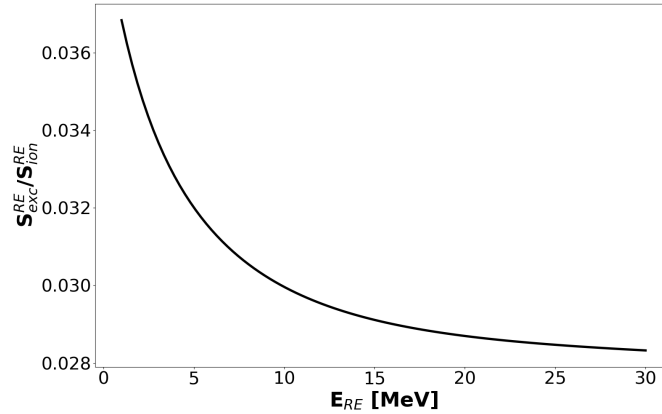


Figure 5.15.: Ratio of the excitation to ionization rates due to RE direct impact. Data taken from (Bretagne 1986).

taken from (Bretagne 1986). Thus, the RE direct excitation can be neglected as they are much smaller. It is to be noted that during the T_e -estimation from VUV spectroscopy (discussed in the section 3.2), RE impact direct excitation is neglected.

5.2.5. Conservation of Ar and D atoms

As discussed in the section 5.1, by the end of each iteration, the total number of the argon and deuterium atoms are counted and the species densities are resealed such that number of atoms are conserved by the end of each iteration. The dependency of the simulation results on the conservation of the argon and deuterium atoms are now studied. In the 1D diffusion code, the argon and/or deuterium atoms conservation is switched off and the simulated results are compared as shown in the figure 5.16. For these simulations, the same default values of the initial guesses are used.

It can be observed from the figure 5.16(a) that electron temperatures are higher in the confined region when argon atoms are conserved (red dotted and green dashed dotted). The effect of deuterium atoms conservation on temperature T_e and total argon density n_{Ar}^{total} is clear seen only near the wall. RE density is higher when argon conservation is in place as shown in the figure 5.16(b) and no clear effect of the deuterium conservation on the RE density profile is seen. For the case of both argon and deuterium atoms conservation (red dotted and green dashed dotted), the electron density is the lowest as shown in the figure 5.16(b).

Usually in the 1D diffusion code, free electron and species densities are usually overestimated. The conservation mechanism in the code scales down the profiles such that the total argon and deuterium atoms are conserved. Thus, when argon and deuterium atoms are not conserved, the density profiles are high as shown in the figure 5.16. By turning off the conservation, the argon and deuterium atoms continues to increase in the 1D diffusion code which is non-physical. Thus, the conservation mechanisms are always turned on in the code.

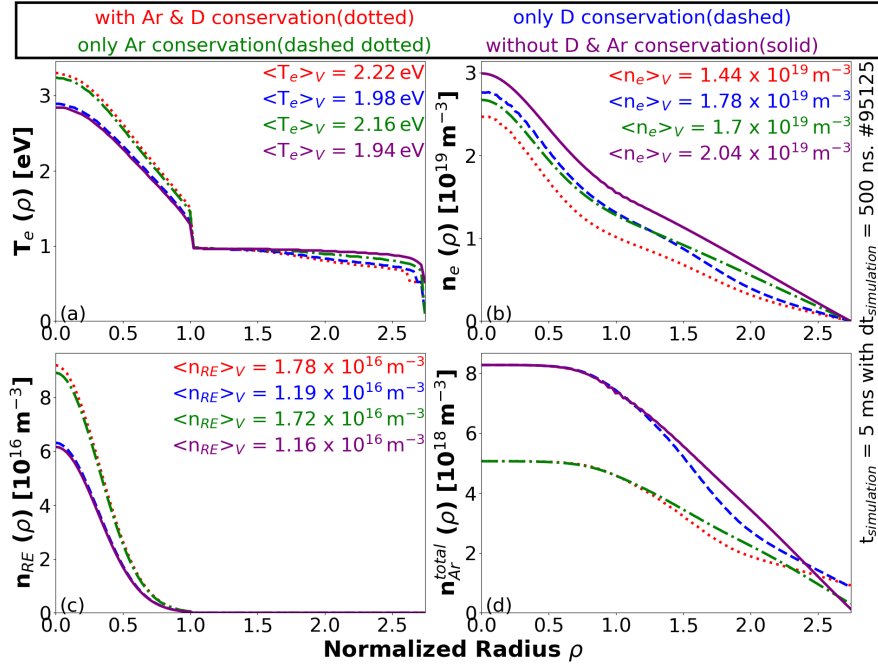


Figure 5.16.: Profile of (a) Temperature T_e , (b) electron density n_e , (c) RE density n_{RE} and (d) total argon density n_{Ar} , after 5 ms simulation with $dt=500 \text{ ns}$. Conservation of the Ar and D atoms are switched on and/or off.

5.2.6. Change of wall radius R_w

As shown in the figure 5.2, an outer (wall) radius of the model R_w is chosen to give the correct vacuum vessel volume. For instance, $R_w=1.92 \text{ m}$ is chosen such that the total plasma volume in the model is 190 m^3 . However, this 190 m^3 is the total volume of the vacuum vessel including recessed volumes behind the plasma facing components which are less well connected to the main part of the vessel. Using the wall coordinates (see the thick black data line in the figure 3.2 for instance) and the plasma radial position, R_w can be estimated as 1.3-1.4 m in the JET tokamak. The question is how sensitive is this wall radius to the 1D diffusion model. To study this, the wall radius is swept from 1 m to 2.5 m as shown in the figure 5.17. For reference, for DIII-D, R_w is taken as 1.1 m and for previous sensitivity studies, $R_w=1.92 \text{ m}$.

As seen from the figures 5.17(a) and 5.18(a), the electron temperature T_e in the confined region increases with the increase in the wall radius R_w .

As explained in the section 5.1, RE density is calculated based on the profiles of radiated power emissivity, electron temperature and density. Thus, RE density n_{RE} increases with wall radius R_w as shown in the figures 5.17(c) and 5.18(c). It is also observed that the total RE current ($I_{RE} = (ec/2\pi R) \int_{\rho} n_{RE}(\rho) dV(\rho)$) also increases with the wall radius R_w .

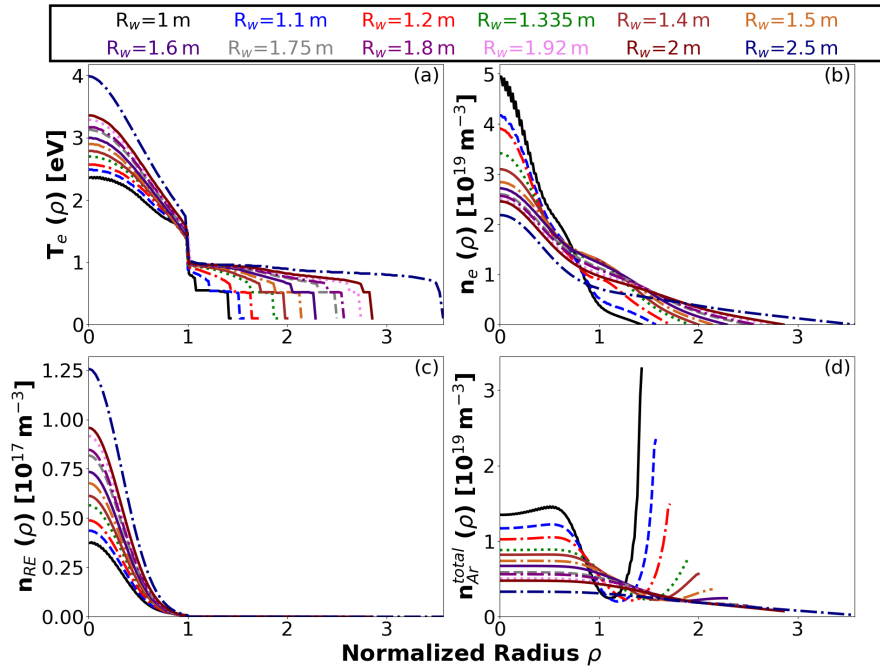


Figure 5.17.: Profile of (a) Temperature T_e , (b) electron density n_e , (c) RE density n_{RE} and (d) total argon density n_{Ar} , after 5 ms simulation with $dt=250$ ns. Sweep of the wall radius R_w .

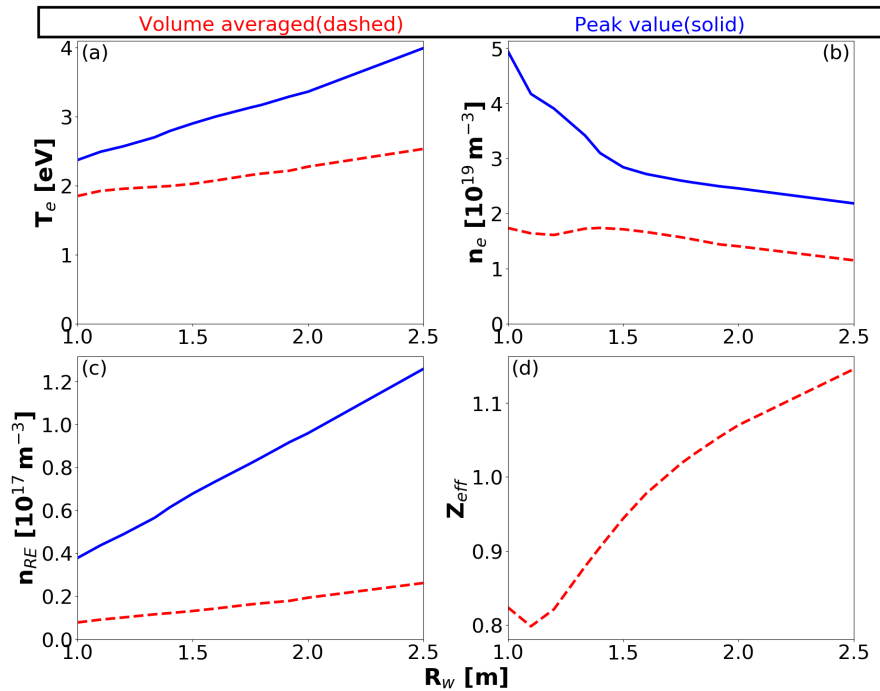


Figure 5.18.: Dependence of the (a) temperature T_e , (b) electron density n_e , (c) RE density n_{RE} and (d) effective ion charge state Z_{eff} on the wall radius R_w , after 5 ms simulation with $dt=250$ ns.

On the other hand, the electron density decrease with the wall radius R_w . However, the total number of free electrons ($\sum_{\rho} n_e(\rho) \cdot dV(\rho)$) increases with the wall radius R_w . Therefore, for N_{Ar}^0 argon atoms for all the simulation, the average ion charge state Z_{eff} increases with the wall radius R_w as shown in the figure 5.18(d). From the figure 5.17(d), it can be seen that lower the wall radius, higher is the total argon density n_{Ar}^{total} near the wall which is predominantly argon neutrals. Thus, it can be observed that argon neutral content decreases with increase in the wall radius.

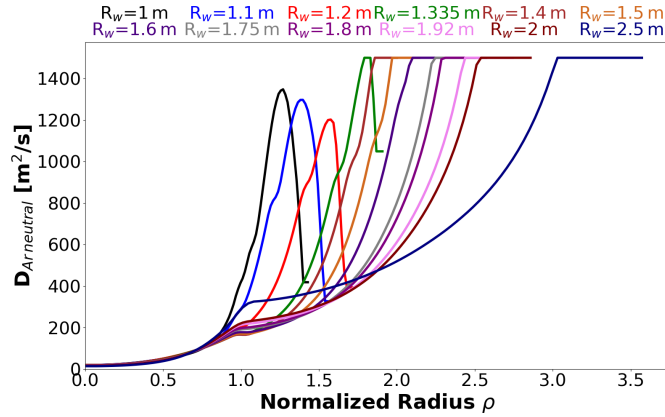


Figure 5.19.: Diffusion coefficient profiles of Ar neutrals for different wall radii R_w , after 5 ms simulation with $dt=250$ ns. In the code, the maximum value of the diffusion coefficient is set as $1500 \text{ m}^2/\text{s}$ by default.

The increase of electron temperature and the decrease of electron density with increase in the wall radius R_w in the diffusion code may be related to the transport phenomenon. For larger wall radius R_w , large volume may confine the particles better, this may be merely a size effect. From the figure 5.19, it can be seen that for smaller wall radius R_w , the diffusion coefficient increases steeply closer to the wall. For larger wall radius R_w , the increase in Ar neutral diffusion coefficient is rather smooth. This may suggest that particles are better confined in larger wall radius and thus the background plasma is hotter. Thus, transport may be one of the reason why hotter background plasmas are seen at JET.

5.2.7. Iteration time step

In the 1D diffusion model, the iteration step size dt should be defined for which the continuity equation 5.1 is solved. For higher dt , the code undergoes computational error and thus the results are nonphysical. On the other hand, smaller time steps take longer computational time.

Simulations are performed with different iteration time steps : $dt=500$ ns (red dot-dotted), $dt=250$ ns (blue dashed) and $dt=125$ ns with the wall radius $R_w=1.92$ m. It can be seen from the figure 5.20 that iteration time step dt seems to have no effect on the results of the simulation. For $R_w=1.92$ m, $dt < 500$ ns gives nonphysical results. Thus,

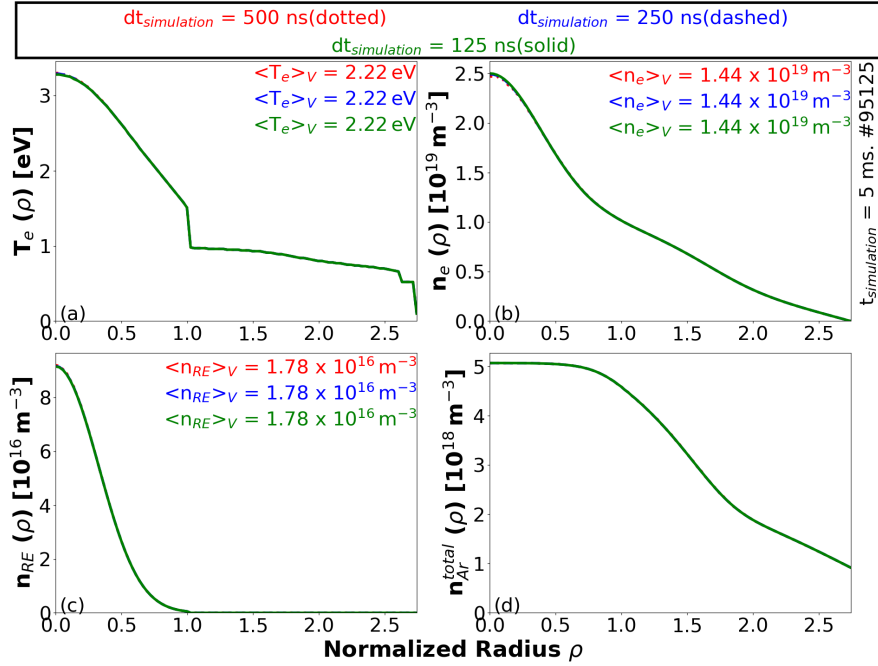


Figure 5.20.: Profiles of (a) Temperature T_e , (b) electron density n_e , (c) RE density n_{RE} and (d) total argon density n_{Ar} , after 5 ms simulation with $dt=500$ ns (red dotted), $dt=250$ ns (blue dashed) and $dt=125$ ns (green solid) time steps. Wall radius $R_w=1.92$ m for all the simulations.

all simulations using the 1D diffusion code are performed with iteration times step $dt=500$ ns for wall radius $R_w=1.92$ m.

However, when 1D diffusion code is run for different wall radii with $dt=500$ ns, it can be observed from the figure 5.21 that for $R_w < 1.91$ m (dashed data), the 1D diffusion code gives a non-physical solution. As seen from the figure 5.21 (d), the argon species are predominantly neutrals. As a consequence, the calculated electron density drops to a very low value as shown in the 5.21(b). Thus, the electron temperature T_e^0 is saturated at $T_e=100$ eV (upper bound of T_e in the model) as shown in the 5.21(a). The estimated RE density n_{RE}^0 is in order of 10^{25} m^{-3} which is non-physical. For $R_w=1.91$ m, the evolution seems to be smooth.

From the figure 5.21 (b), it can be observed that the larger the wall radius, the longer it takes for the n_e to drop to very low value. One possible reason is that with larger wall radius (with larger volume), the diffusion code is less constrained to solve the transport equations. For smaller volumes (smaller wall radius), small iteration time steps dt are needed to resolve smaller volume. For this reason, the iteration times scale is fixed to $dt=250$ ns and this problem was not observed as shown in the figure 5.17.

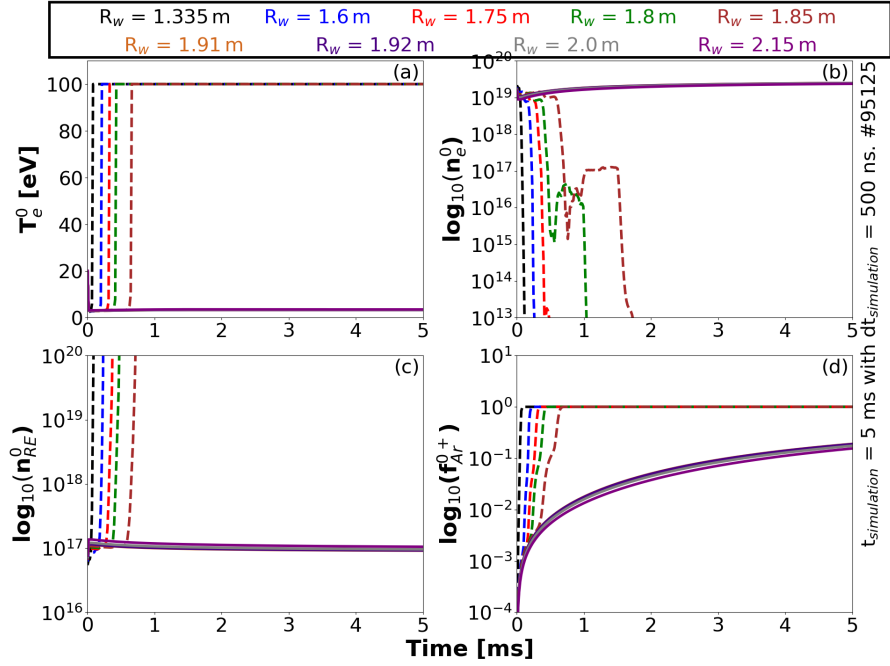


Figure 5.21.: Time evolution of the (a) temperature T_e , (b) electron density n_e , (c) RE density n_{RE} and (d) fractional abundance of Ar neutrals f_{Ar}^0+ for different values of the wall radius R_w , after 5 ms simulation with $dt=500$ ns.

5.2.8. Rate calculations from atomic model

As illustrated in the figure 5.1, the 1D diffusion model computes atomic processes for which rate coefficients (ionization, recombination and cooling rate coefficients) are used as discussed in the section 5.1.2.

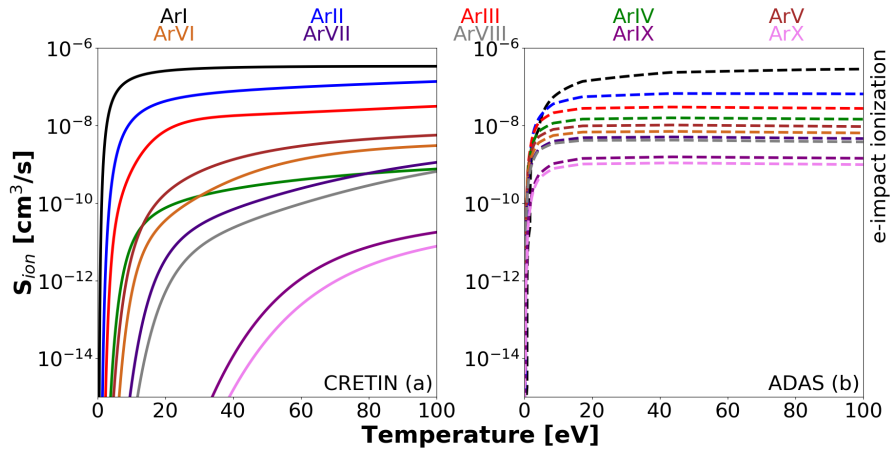


Figure 5.22.: Comparison of ionization rate coefficients from (a) CRETIN and (b) ADAS atomic models

In the 1D diffusion model, the rate coefficients are taken from the CRETIN atomic model. CRETIN is a multi-dimensional radiation transfer code based on non-local

thermodynamic equilibrium (NLTE) (Scott 2001).

The rate coefficients from the CRETIN atomic model is compared with ADAS atomic model (Summers 2004). ADAS atomic model is based on collisional-radiative equilibrium. ADAS atomic data are used in T_e -estimation from the VUV spectroscopy discussed in the section 3.2.

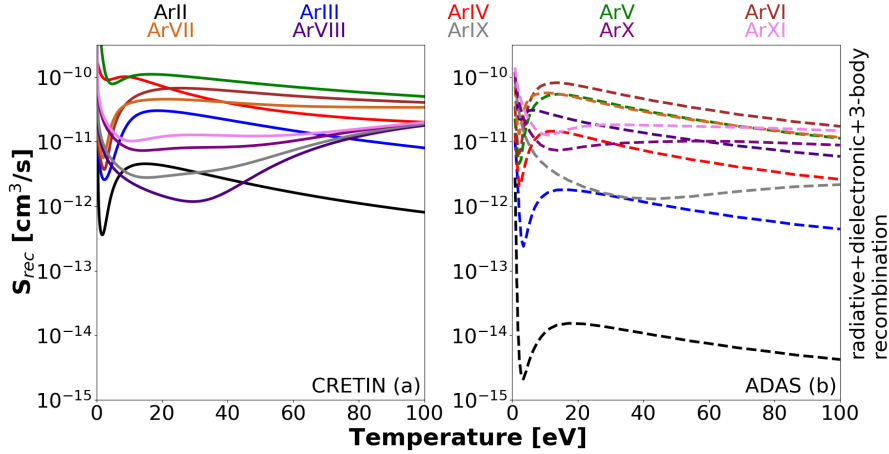


Figure 5.23.: Comparison of recombination rate coefficients from (a) CRETIN and (b) ADAS atomic models

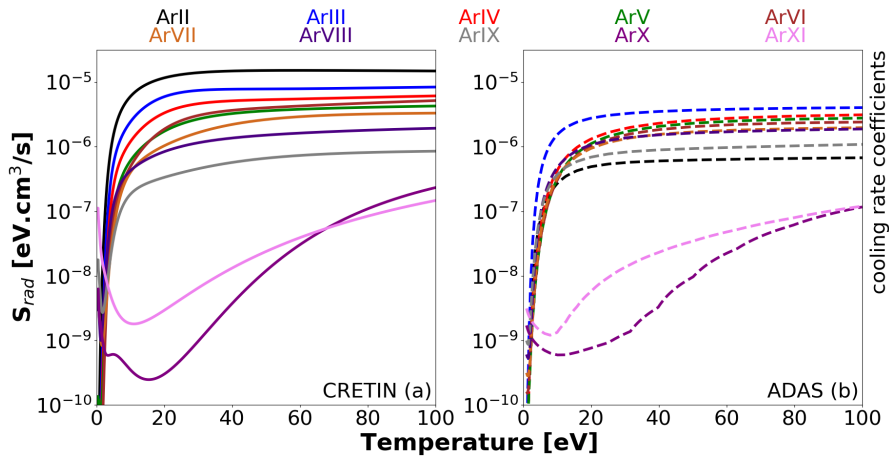


Figure 5.24.: Comparison of cooling rate coefficients from (a) CRETIN and (b) ADAS atomic models

From the figure 5.23, it can be observed that recombination rate coefficients from the CRETIN atomic model are magnitudes higher than that of the ADAS atomic model, for higher ionization states. Therefore, higher ionization maybe more present in the 1D diffusion model using ADAS atomic data as compared to the CRETIN atomic data. It is to be noted that radiative, dielectronic and 3-body recombinations are considered in the figure 5.23.

As shown in the figure 5.24, cooling rate coefficients of CRETIN atomic model are comparable to the ADAS atomic model. The only exception is the cooling rate coefficients of argon neutral (black data line) which are magnitudes higher for CRETIN atomic data as compared to ADAS atomic model.

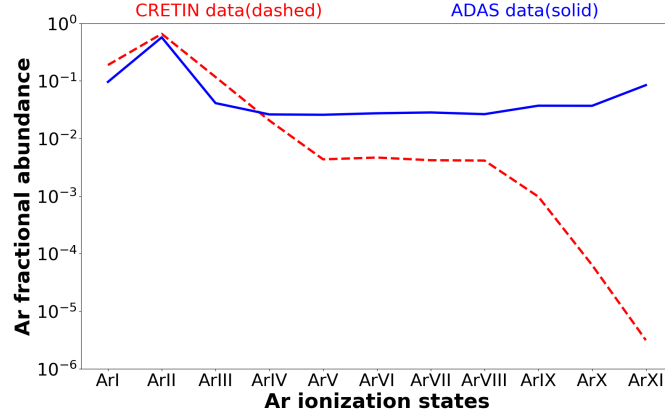


Figure 5.25.: Argon fractional abundance from 1D diffusion model using CRETIN (red dashed) and ADAS (blue solid) atomic models

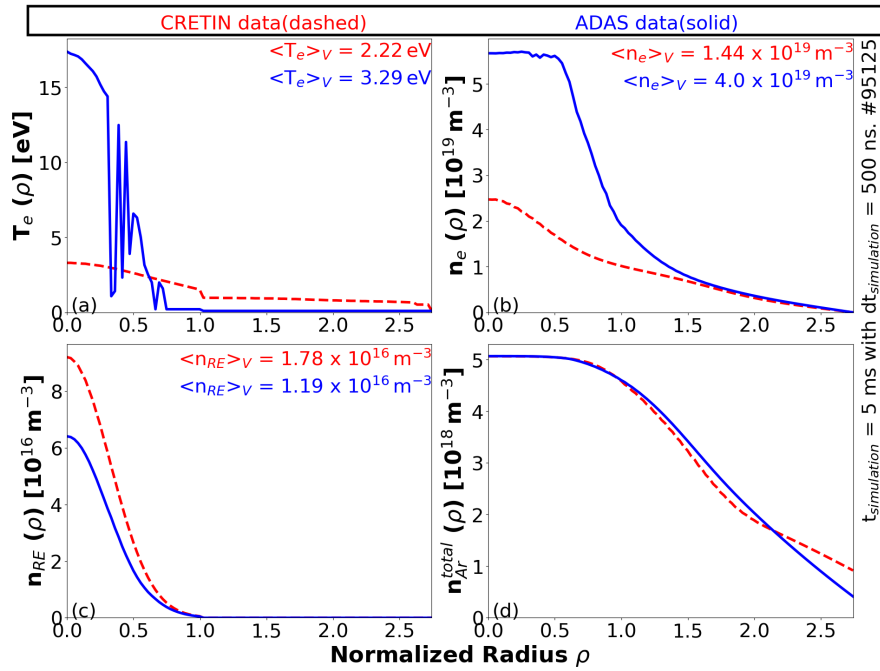


Figure 5.26.: Profiles of (a) Temperature T_e , (b) electron density n_e , (c) RE density n_{RE} and (d) total argon density n_{Ar} , after 5 ms simulation with $dt=500$ ns. Wall radius $R_w=1.92$ m for all the simulations.

From the figure 5.25, it can be observed that at lower ionization states (up to Ar^{2+}), thermal electron-impact ionization rate coefficients are comparable for CRETIN and

ADAS atomic data. However, for higher ionization states, ADAS ionization rates are much higher than CRETIN atomic model. It is to be noted that for higher ionization states, RE impact ionizations are much higher than electron-impact ionization as shown in the figure 5.13 for both the CRETIN and ADAS atomic models. Thus, total ionization rate coefficients may not be sensitive to the atomic model used in the 1D diffusion model.

In the 1D diffusion model, rate coefficients from CRETIN and ADAS atomic models are used and the simulation results are compared as shown in the figure 5.26. It was observed from the figure 5.23 that CRETIN atomic model predicts higher recombination as compared to ADAS atomic model. As a result, ADAS predicts higher fractional abundance of ionization states as compared to CRETIN atomic model as shown in the figure 5.25.

Due to higher argon fractional abundance prediction, ADAS predicts higher electron density profile $n_e(\rho)$ than CRETIN atomic model as shown in the figure 5.26(b). CRETIN predicts higher RE density profile $n_{RE}(\rho)$ than ADAS atomic model as shown in the figure 5.26(c).

As discussed in the section 5.1.5, T_e -profile is estimated from species and electron density profiles using cooling rate coefficients. As shown in the figure 5.24, CRETIN atomic model has higher cooling rate coefficients than ADAS atomic model. Thus, ADAS predicts higher electron temperature profile $T_e^0 \sim 17.5$ eV than CRETIN ($T_e^0 \sim 3.5$ eV) due to the difference in cooling rate coefficients. Thus, the rate coefficients used on the 1D diffusion code may significantly change the results and should be dealt with care.

Now that the sensitivity of different parameters are performed, the argon background background plasmas are simulated using this 1D diffusion model in the section 5.3 for a database of discharges defined in the section 3.3.

5.3. Simulation of argon background plasma

A database of JET discharges of the MGI and SPI experiments from the section 3.3 is simulated using the 1D diffusion code.

For a given discharge, the full simulations are split into "macroscopic" simulations ($t_{simulation}=5$ ms) for which the input parameters of the code (argon and deuterium content, total radiated power, plasma radius R_a and line-integrated electron density measurement from interferometry) are given. For the first simulation, it is assumed that only Ar^{1+} and D^{1+} species are present. From the second simulation, the species density profiles of the previous iterations is carried forward as the initial guesses of the species densities. Using the line-integrated electron density measurement from interferometry (see section 3.1 for more information), the initial guesses of the electron density profile is assumed for each "macroscopic" simulations. Initial guesses of the electron temperature profile is taken as $T_e^0=20$ eV whereas the initial guess of RE

density profile is taken from radiated power emissivity profile.

The background plasmas are simulated starting from quiet current quench until the end of the beam phase. The time step of macroscopic simulations is 5 ms with iteration time step $dt=500$ ns. Since the effect of changing the wall radius is yet to be fully understood, the wall radius is fixed at $R_w=1.92$ for all the simulations. Using the total radiated power $P_{radiated}$ from bolometry measurement, a Gaussian emissivity profile is considered with width 30 cm.

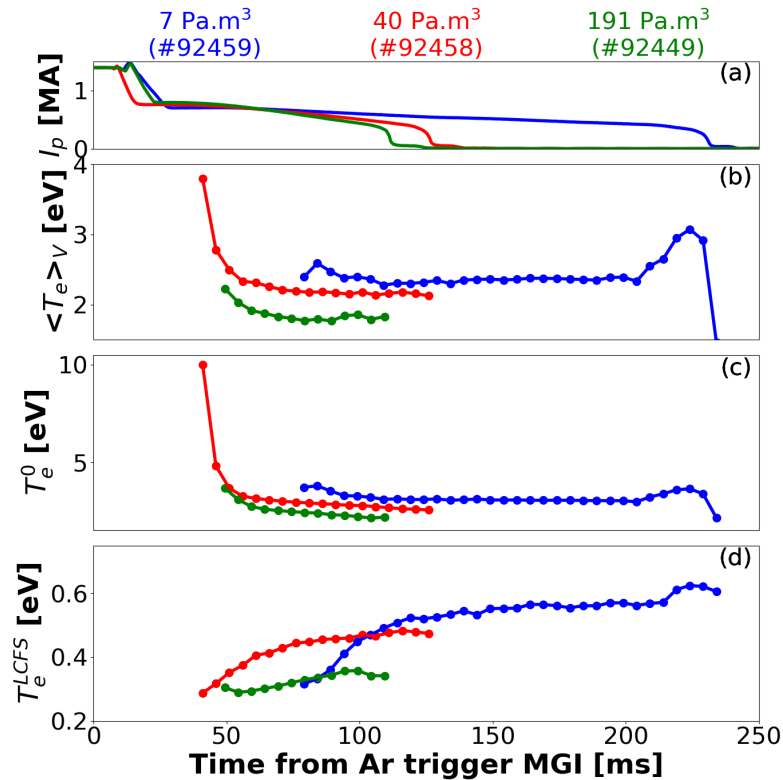


Figure 5.27.: Time evolution of (a) plasma current I_p (from magnetic measurements), (b) simulated volume averaged temperature profile $\langle T_e \rangle_V$, (c) simulated core temperature T_e^0 and (d) simulated temperature at SOL T_e^{LCFS} . Background plasmas are triggered by various amount of Ar MGI and simulated by the 1D diffusion code.

The time evolution of the background plasma characteristics as simulated by the diffusion code is shown in the figure 5.27. It can be observed that during the RE plateau phase, the background plasma temperatures are fairly constant.

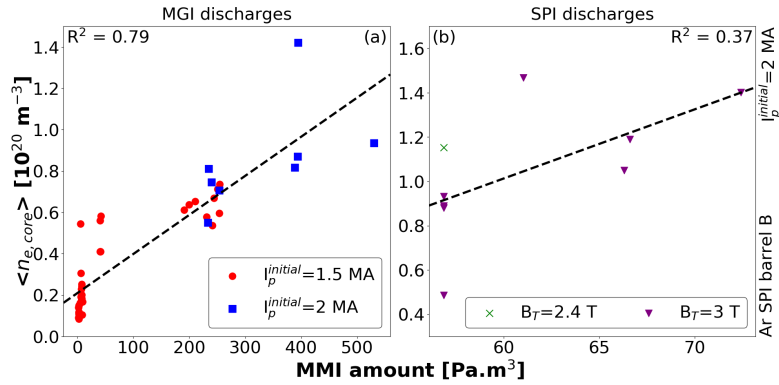


Figure 5.28.: Dependence of the time and volume averaged core electron density $\langle n_{e,core} \rangle$ on the amount of Ar MMI used to trigger the background plasma for (a) MGI and (b) SPI discharges. Core electron density profile $\langle n_{e,core} \rangle$ is estimated from the 1D diffusion code.

As shown in the figure 5.28(a), the core electron density from the 1D diffusion model increases with the Ar MMI amount for the MGI cases. This is consistent with increase of (relative) line-integrated density rise in the core $\langle dn_{e,core} \rangle$ (measured from the interferometry) with Ar MGI amount used to trigger disruption (figure 3.5).

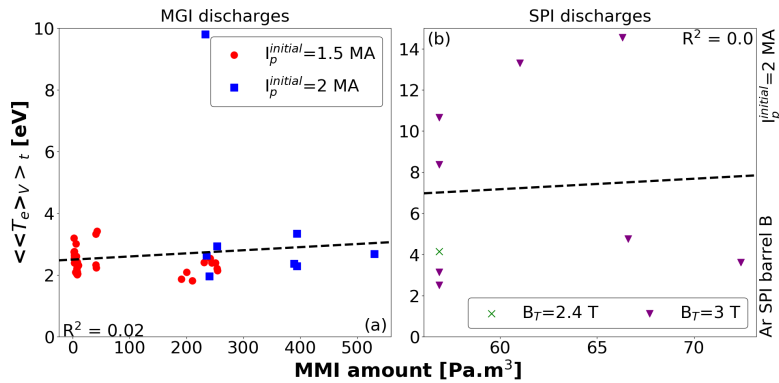


Figure 5.29.: Dependence of the time and volume averaged background electron temperature $\langle\langle T_e \rangle\rangle_t$ on the amount of Ar MMI used to trigger the background plasma for (a) MGI and (b) SPI discharges. Electron temperatures $\langle\langle T_e \rangle\rangle_t$ are estimated from the 1D diffusion model.

The time and volume averaged electron temperature of the background plasma $\langle\langle T_e \rangle\rangle_t$ show very weak correlation with the Ar MMI content used to trigger disruption as shown in the figure 5.29. It can also be observed that some SPI discharges are much hotter than MGI discharges. This trend is opposite to experimental estimations (figure 5.29) where electron temperature of the background plasmas is lower for SPI discharges than MGI discharges.

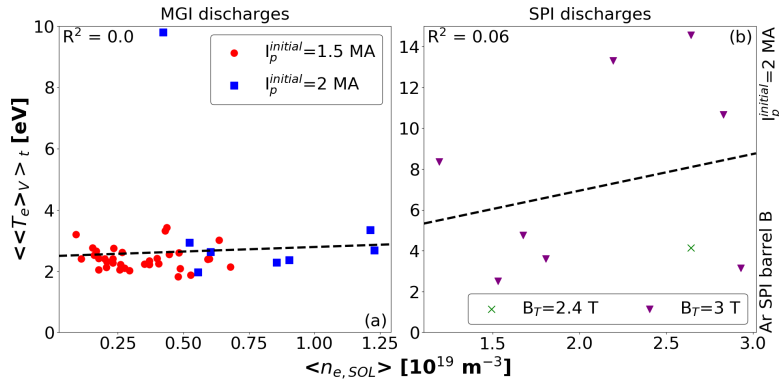


Figure 5.30.: Dependence of the time and volume averaged background electron temperature $\langle\langle T_e \rangle_V \rangle_t$ on the time and volume averaged electron density $\langle n_{e,SOL} \rangle$ at the scrape-off layer (SOL) for (a) MGI and (b) SPI discharges. Electron temperatures $\langle\langle T_e \rangle_V \rangle_t$ and electron density at SOL $\langle n_{e,SOL} \rangle$ are estimated from the 1D diffusion model.

From the figure 5.30, the dependency of the time and volume averaged electron temperature of the background plasmas $\langle\langle T_e \rangle_V \rangle_t$ on the electron density in the SOL is very weak. The volume-averaged electron density value outside the confined region (with $\rho > 1$) is taken as the electron density in the SOL region.

Quantity	Values	
	MGI	SPI
$\langle\langle T_e \rangle_V \rangle_t$	1.82-9.8 eV 78% between 2.02-2.93 eV	2.52-14.55 eV 78% between 2.52-10.67 eV
$\langle T_e^0 \rangle_t$	2.5-38.68 eV 78% between 2.61-3.83 eV	5-45.82 eV 78% between 5-34.97 eV
$\langle T_e^{LCFS} \rangle_t$	0.26-0.8 eV 78% between 0.26-0.65 eV	0.55-0.86 eV 78% between 0.6-0.86 eV

Table 5.1.: Range of background plasma temperatures simulated using the 1D diffusion code for MGI and SPI discharges.

The ranges of background plasma temperatures simulated using the 1D diffusion model are given in the table 5.1. It can be observed that the temperatures of the simulated background plasmas are much lower than the estimated T_e -profiles from the VUV spectrometer for MGI discharges (see table 3.2). For SPI discharges, the simulated background plasma temperature is higher than temperature estimations from VUV spectroscopy. It is to be noted that in the 1D diffusion model, it is assumed that $T_e = T_i$. If $T_e \gg T_i$ may be in reality, the simulated temperature may be a lower bound of the actual electron temperature. Thus, even with comparatively lower temperatures (as

compared to T_e estimation from VUV spectroscopy), JET have hotter background plasma than DIII-D when simulated using the 1D diffusion model (Hollmann 2011).

5.4. Summary

1D diffusion model:

- 1D diffusion considers particle diffusion and atomic processes such as ionization, recombination and charge exchange.
- Input parameters: argon and deuterium content, line-integrated free electron density measurement, total or profile of radiated power
- Output parameters: species densities, electron density, electron temperature and RE density profiles
- Diffusion code is sensitive to initial guesses of the species densities.
- Higher temperatures are predicted by the diffusion code using ADAS atomic data, consistent with the VUV measurements.
- Code predicts higher background plasma temperatures for higher geometrical wall radius.

Database analysis:

- 1D diffusion code predicted much lower temperature (2.02-2.93 eV) than VUV estimations (6-18 eV), using the default CRETIN atomic data.
- Background plasma temperature decreases with increasing argon amounts, reverse trend of T_e estimations from VUV spectroscopy.

5.5. Analysis of D₂ SPI in JET tokamak

As discussed in the section 2.5, Shattered Pellet Injection (SPI) is currently the baseline RE beam mitigation method for ITER. In the JET tokamak, RE mitigation injections were tried using high-Z MMIs as discussed in the section 3.3. During the 2019 JET-SPI experiments, mitigation of the RE beam was attempted using D₂ SPI from barrel A following the experiments in the DIII-D tokamak (Shiraki 2018).

Various RE beam mitigation scenarios in the JET tokamak are shown in the figure 5.31. During a standard RE mitigation scenario using Ar SPI, the high-Z impurities rise the electron density (figure 5.31(a)) and thus mitigate the RE beam which is seen through plasma current decay (figure 5.31(a)) and rise in hard x-ray signal (figure 5.31(d)).

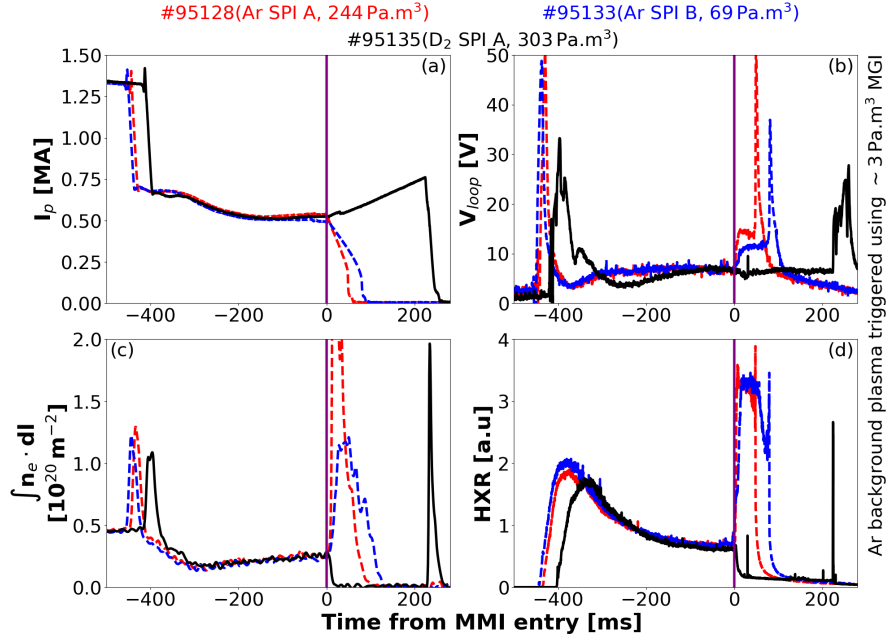


Figure 5.31.: Comparison of RE beam mitigation scenario in the JET tokamak using : Ar SPI from barrel A (red dashed), Ar SPI from barrel B (blue dashed) and D₂ SPI from barrel A (black solid), showing (a) plasma current, (b) loop voltage, (c) line-integrated electron density (interferometry) and (d) hard x-ray signal. RE beams are triggered using $\sim 3 \text{ Pa.m}^3$ Ar MGI.

When D₂ SPI is injected into the Ar background plasma, instead of plasma decay (in the case of high-Z impurities), the RE (plasma) current increases (figure 5.31(a)). The line-integrated free electron density and the hard x-ray signal drops to very low non-measurable values (from figures 5.31(c) and 5.31(d)). The increase in the plasma current after D₂ SPI entry maybe due to the decrease in the resistivity of the RE beam and the background plasma system. D₂ SPI leads to fast benign termination of the RE beam even at high currents without any visible localized wall impact. This benign termination maybe due to the kink instabilities (Paz-Soldan 2019).

The impact of D₂ SPI in the Ar background plasma was also reported in DIII-D tokamak (Shiraki 2018) as shown in the figure 5.32. D₂ SPI impact was also reported in the ASDEX-Upgrade tokamak (Pautasso 2020). However, in the JET tokamak, $\sim 1\text{-}4 \text{ MW}$ of radiated power are measured by the bolometry which was not observed in DIII-D and ASDEX-Upgrade tokamaks.

In DIII-D tokamak, when the 1D diffusion model was applied to the case of D₂ SPI into the argon background plasma (Hollmann 2020), the electron temperature drops to $<1 \text{ eV}$ during which the plasma recombines. As a result, the free electron density drops to very low value as seen from the experimental measurements. It was also observed in DIII-D tokamak that argon line radiation drops after D₂ SPI entry and the appearance of deuterium lines suggests expulsion of argon from the background plasma (Hollmann 2020).

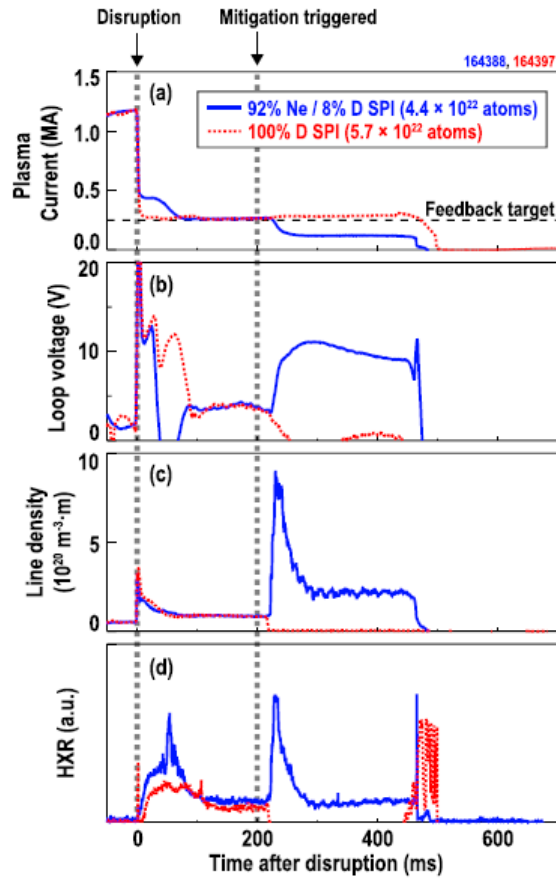


Figure 5.32.: Comparison of RE beam mitigation scenario with 100% D SPI (red dotted) as compared to RE mitigation with 92% Ne+8% D SPI (blue solid) in the DIII-D tokamak (Shiraki 2018), showing (a) plasma current, (b) externally measured loop voltage, (c) line-integrated free electron density and (d) hard x-ray signal. RE beams are triggered by injection of small cryogenic argon pellets.

Using the 1D diffusion model (section 5.1), the effect of D₂ SPI on the argon background plasmas are studied. It should be noted that T_e estimation from the VUV spectroscopy (section 3.2) cannot be applied to D₂ SPI experiments. This is due to the fact that PEC data used in the model assumes pure argon background plasma. The VUV spectra of the argon background plasma after the D₂ SPI entry is also analyzed qualitatively in the section A. The argon background plasma with D₂ SPI in the JET tokamak is simulated using the 1D diffusion model and the results are discussed in this section.

5.5.1. Simulation of the D₂ SPI experiments

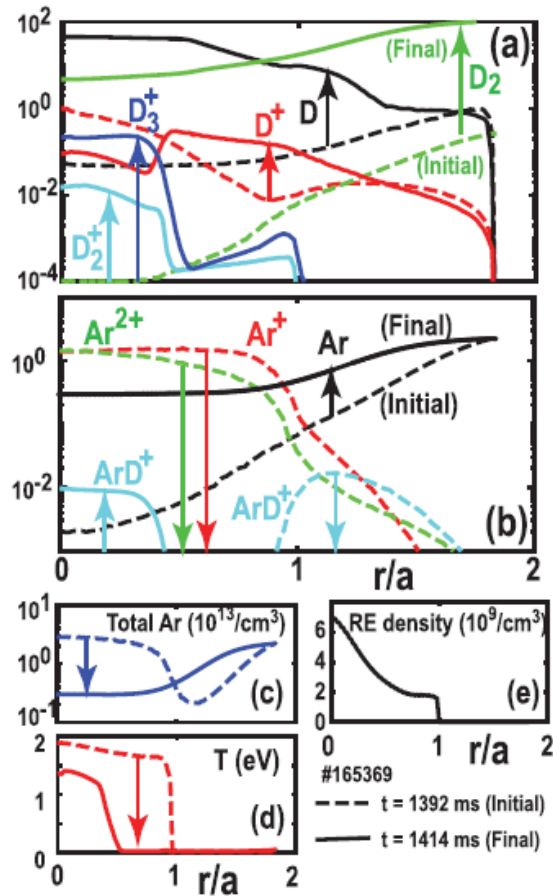


Figure 5.33.: Simulation of argon background plasma (dashed, initial) and Ar+D₂ background plasma (solid, final) in the DIII-D tokamak, showing (a) D ion density profiles, (b) Ar ion density profiles, (c) total Ar density profiles, (d) thermal temperature profile and (e) fixed RE density profile. Densities are given in 10^{13} cm^{-3} (Hollmann 2020).

Using the 1D diffusion model (Hollmann 2019), the rapid expulsion of argon following the low-Z gas injections were studied in the DIII-D tokamak (Hollmann 2020). It was observed that neutral transport to the wall dominated the power loss out of the RE beam. An example of DIII-D simulation using the 1D diffusion model is shown in the figure 5.33. After the D₂ MGI entry, there was a large rise in D and D₂ densities as shown in the figure 5.33(a). There was a strong drop in Ar¹⁺ and Ar²⁺ densities. As shown in the figure 5.33(d), the thermal temperature profile drops after D₂ MGI.

Similar to the DIII-D tokamak, the background plasmas of the JET tokamak during the D₂ SPI experiments are simulated using the 1D diffusion model. Background plasmas are triggered using different quantity of Ar MGI (ranging from 3-42 Pa.m³ Ar) and D₂ SPI from barrel A (~300 Pa.m³ D₂) is injected 400 ms after the Ar trigger MGI.

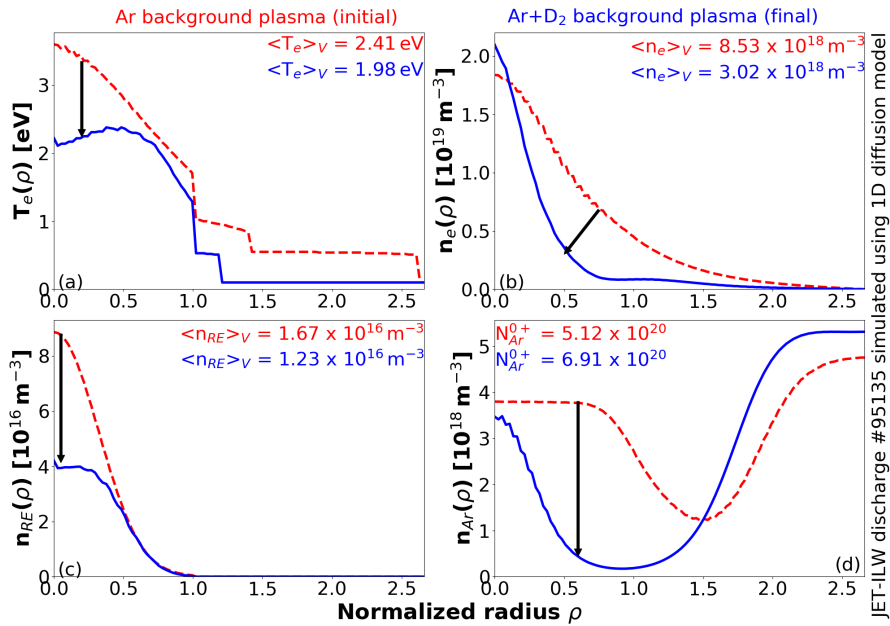


Figure 5.34.: Simulation of argon background plasma (red, dashed) and Ar+D₂ background plasma (blue, solid) in the JET tokamak, showing (a) temperature profile, (b) free electron density profile, (c) RE density profile and (d) total Ar density profile. Simulated using the 1D diffusion model.

One such example is shown in the figure 5.34 for the JET discharge #95135. Similar to DIII-D simulation, the electron temperature and total Ar density profiles are dropped after the D₂ SPI entry. In the DIII-D simulation shown in the figure 5.33, the RE density is frozen (which doesn't evolve in the simulation) whereas for the JET simulation shown in the figure 5.34, the RE density profile evolves.

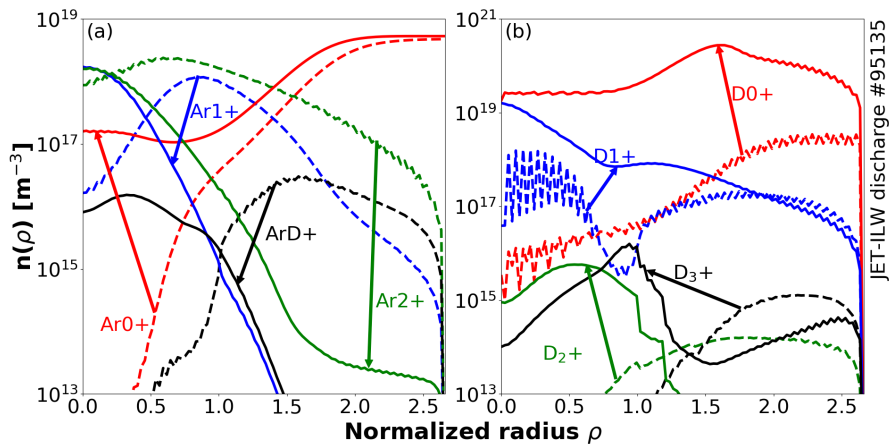


Figure 5.35.: Simulation of argon background plasma (dashed) and Ar+D₂ background plasma (solid) in the JET tokamak, showing (a) D density profiles and (b) Ar density profiles.

Similar to the DIII-D tokamak, there is a significant drop in the Ar ion density

profiles as shown in the figure 5.35(a). The rise in D and D₂ density profiles after D₂ SPI entry shown in the figure 5.35 are consistent with the simulation results of the DIII-D tokamak.

In order to analyze further, the main output parameters from the 1D diffusion code are studied in this section. As discussed in the section 5.1, there are four main output parameters from the 1D diffusion model :

1. species density profiles
2. electron density profile $n_e(\rho)$
3. RE density profile $n_{RE}(\rho)$
4. electron temperature profile $T_e(\rho)$

5.5.1.1. Species density profiles $n_i(\rho)$

As discussed in section 5.1, the density profile of argon charge states is one of the outputs of the code. From the figure 5.36, it can be observed that after the D₂ SPI entry, the volume averaged Ar¹⁺ and Ar²⁺ ion densities drop by almost a magnitude whereas higher ionization states (Arⁱ⁺, $i \geq 4$) drops by several orders of magnitude. From the figure 5.35(a), it can be found that Ar¹⁺ and Ar²⁺ are found even in the SOL ($\rho \geq 1$). After D₂ SPI entry, Ar¹⁺ and Ar²⁺ are present mostly in the confined region with densities around 10^{18} m^{-3} . In DIII-D, Ar¹⁺ and Ar²⁺ drops to really low values ($n_{Ar^{1+}, Ar^{2+}} \leq 10^{16} \text{ m}^{-3}$ from figure 5.33(b)) after D₂ SPI entry.

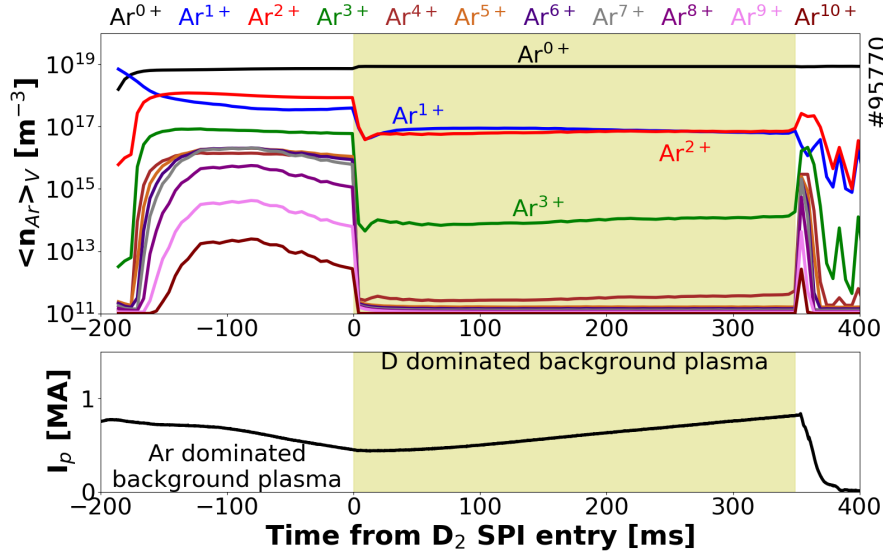


Figure 5.36.: (a) Time evolution of volume averaged Ar ion densities for JET discharge #95770 from the 1D diffusion model and (b) plasma current I_p from magnetic measurements.

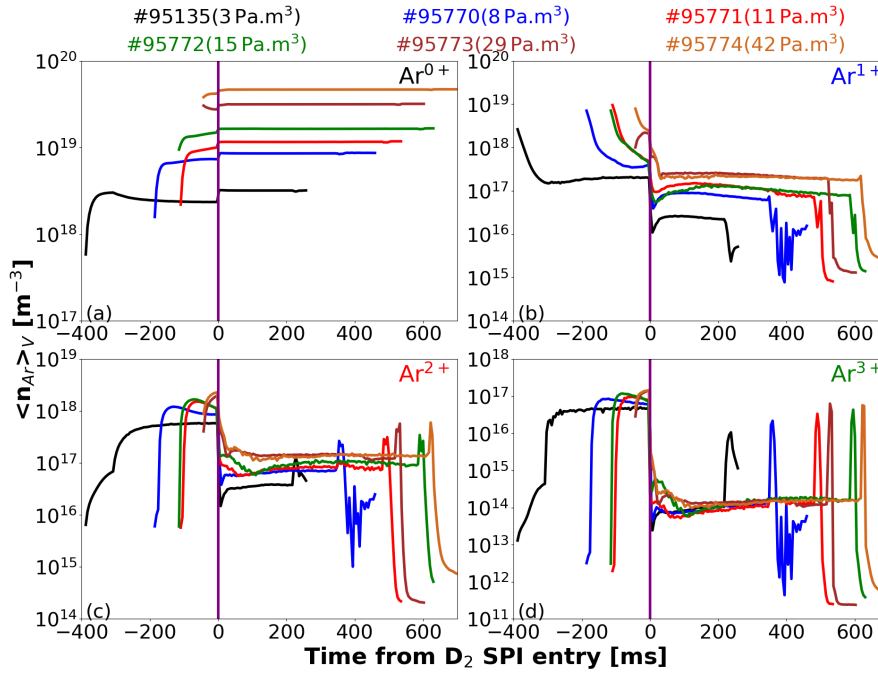


Figure 5.37.: Time evolution of volume averaged ion densities of (a) Ar neutrals, (b)Ar¹⁺, (c)Ar²⁺ and (b)Ar³⁺, for discharges with different Ar MGI amounts.

Background plasma with different initial Ar MGI amount are simulated using the 1D diffusion model. The Ar particles of different ionization states are compared as shown in the figure 5.37. It can be observed from the figures 5.37(b) and 5.37(c) that after the entry of D₂ SPI, Ar¹⁺ and Ar²⁺ drops roughly 1-2 orders of magnitude. On the other hand, Ar³⁺ decreases by almost 4 orders of magnitude after D₂ SPI entry as shown in the figure 5.37(d). As shown in the figure 5.35(b), the rise in the deuterium species densities in JET is qualitatively consistent with DIII-D (figure 5.33(a)).

As shown in the figure 5.38(a), the rise in argon neutral density following the D₂ SPI increases linearly with the Ar MGI amount used to trigger disruptions. On the other hand, the rate at which the densities of Ar¹⁺, Ar² and Ar³⁺ decreases is linearly dependent on Ar MGI amount, as shown in the figures 5.38(b), 5.38(c) and 5.38(d).

It is to be noted that for discharges with higher Ar MGI amounts, initial argon densities are also higher. However, the ratio between the change in argon densities Δn_{Ar} and the initial argon densities is fairly constant of Ar MGI amounts. Therefore, no clear dependency of the Ar purge on the Ar MGI amounts could be established using the 1D diffusion code.

The 1D diffusion model applied to the DIII-D cases predicted almost all of the argon particles recombined to form neutrals. When the 1D diffusion model is applied to the JET background plasmas, it cannot predict total recombination of argon species as shown in the figure 5.37. For instance, Ar³⁺ purged from $\sim 10^{19}$ to $\sim 10^{16}$ after D₂ SPI entry but not to very low value like DIII-D.

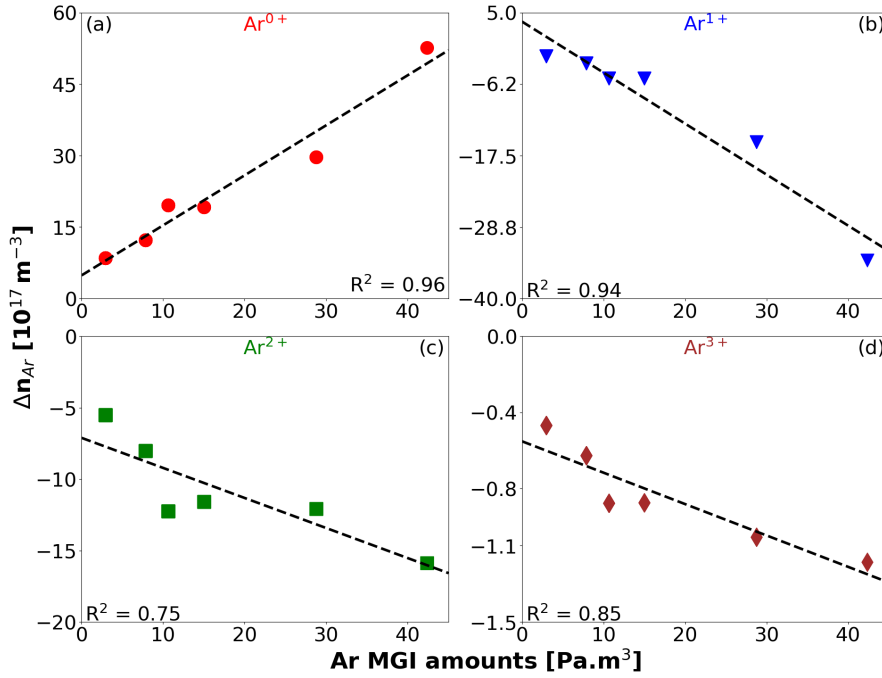


Figure 5.38.: Dependency of the change in volume-averaged density Δn_{Ar} of (a) Ar neutral, (b) Ar^{1+} , (c) Ar^{2+} and (d) Ar^{3+} , on the Ar MGI amounts. Δn_{Ar} is the density difference between the argon dominated and deuterium dominated background plasma. Positive and negative Δn_{Ar} indicates rise and drop in argon densities following the D_2 SPI entry. Densities computed by the 1D diffusion code.

5.5.1.2. Electron density profile $n_e(\rho)$

From the species density profiles, the electron density profile $n_e(\rho)$ is constructed in the 1D diffusion model. Using the free electron density profile $n_e(\rho)$, the line-integrated electron density $\int n_e dl$ can be constructed such that, $\int n_e dl = dr \sum_{\rho} n_e(\rho)$, with dr being the grid radius. For different Ar MGI amounts, the line-integrated electron density from the 1D diffusion model is compared with interferometry measurements as shown in the figure 5.39.

1D diffusion model predicts that after D_2 SPI entry, the line-integrated electron density increases, despite the drop in Ar ions (shown in the figure 5.35). This is inconsistent with the fact that free electrons drop to very low non-measurable value from the interferometry measurements. This may be due to the problem of recombination as shown in the figure 5.37.

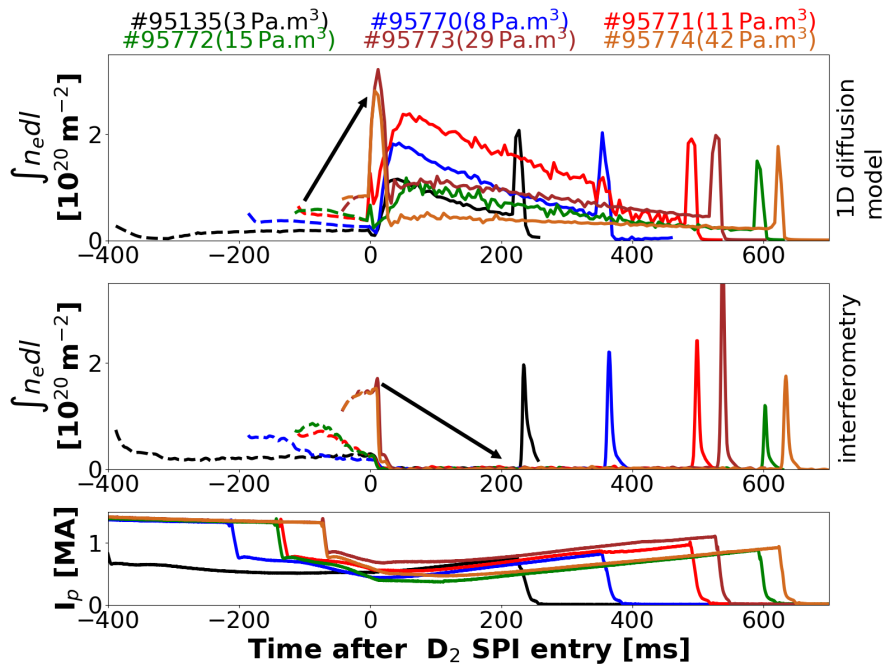


Figure 5.39.: Comparison of line-integrated core electron density $\int n_e dl$ from the 1D diffusion model with the interferometry measurements for the JET discharges with different Ar MGI amounts.

5.5.1.3. Runaway electron density profile $n_{RE}(\rho)$

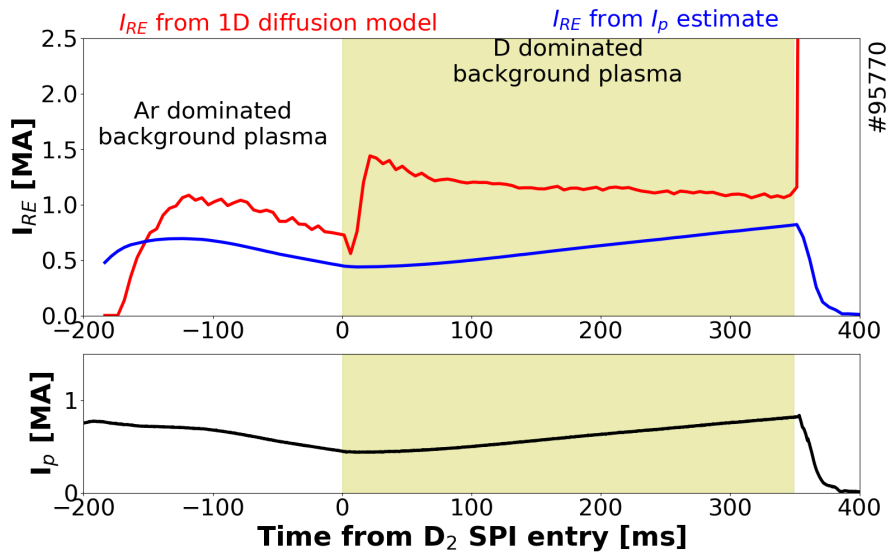


Figure 5.40.: Comparison of current carried by the RE beam I_{RE} from the 1D diffusion model with the estimation from the plasma current for the JET discharges with different Ar MGI amounts.

The estimation of the RE density profile from the species density profiles, free electron density profile and the emissivity profile is already discussed in the section 5.1. Using the RE density profile $n_{RE}(\rho)$ estimated by the 1D diffusion model, the current carried by the RE beam I_{RE} is estimated as, $I_{RE} = \langle n_{RE} \rangle e c A_{plasma}$ with $\langle n_{RE} \rangle$ and A_{plasma} are the volume-averaged RE density and plasma cross-sectional area. From the plasma current I_p , the RE current I_{RE} is estimated assuming ohmic part of the plasma current I_Ω decreases exponentially during the current quench phase.

The RE current I_{RE} predicted by the model (red data line) is in a reasonably good agreement with the RE current from the plasma current measurement (blue data line) as shown in the figure 5.40. The 1D diffusion code is not primary used to predict the RE density. Rather, the RE density predicted by the 1D diffusion code is used to check the consistency of the code. As discussed in the section 5.1.2, the RE density profile n_{RE} is also used in the RE impact ionization of the species. Thus, RE density may significantly impact the charge state distribution and other parameters from the 1D diffusion code.

5.5.1.4. Electron temperature profile $T_e(\rho)$

In the 1D diffusion code, the temperature profile $T_e(\rho)$ is estimated based on the species density profiles, free electron density profile $n_e(\rho)$ and the emissivity profile. From the figure 5.41, it can be observed that after D_2 SPI entry, there is a drop in the background plasma temperature.

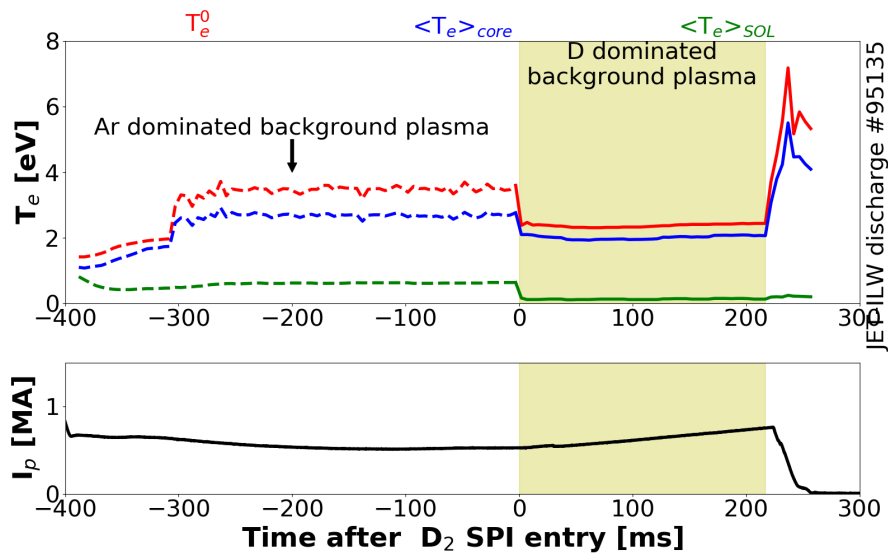


Figure 5.41.: Time evolution of the background plasma temperature simulated using 1D diffusion model for the discharge #95135. The plasma current I_p is from magnetic measurements.

For the JET discharge #95135, after D_2 SPI entry, the core temperature (volume-

averaged T_e -profile in the confined region) $\langle T_e \rangle_{core}$ drops to ~ 3 eV whereas in the SOL, $\langle T_e \rangle_{SOL}$ drops to ~ 0.1 eV as shown in the figure 5.41. Due to the presence of very cold temperatures in the SOL region ($\langle T_e \rangle_{SOL} \sim 0.1$ eV), most of the argon ions recombine to argon neutrals thus confirming what is seen in the figure 5.35. However, in the core, $\langle T_e \rangle_{core} \sim 3$ eV after D_2 may high enough for the presence of Ar_{1+} and Ar_{2+} ions. In the DIII-D tokamak, background plasmas are much colder ($T_e^0 \sim 1.5$ eV from the figure 5.33(d)) and this may explain why Ar_{1+} and Ar_{2+} drops to very low value.

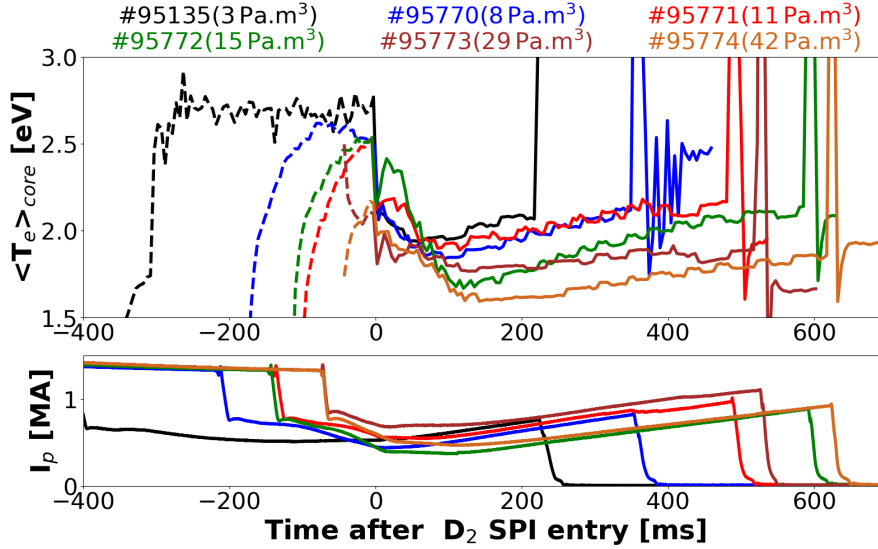


Figure 5.42.: Time evolution of the simulated core background plasma temperature $\langle T_e \rangle_{core}$ for JET discharges with different Ar MGI amounts. The plasma current I_p is measured from magnetic diagnostics.

As shown in the figure 5.42, the core background plasma temperature $\langle T_e \rangle_{core}$ drops after the D_2 SPI no matter how much of Ar MGI amount is used. A steady increase in the background plasma temperature following the temperature drop can be observed from the figure 5.42.

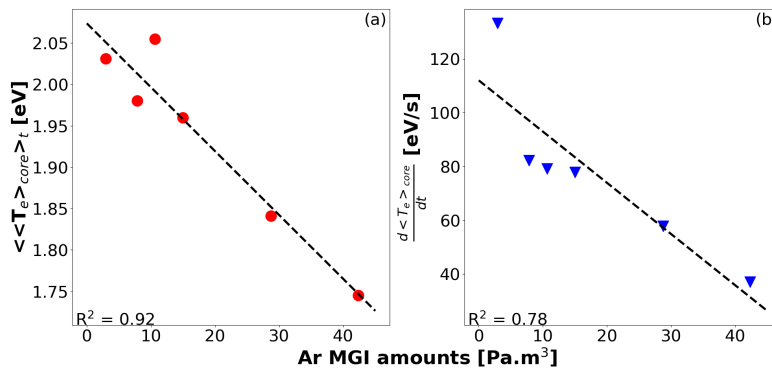


Figure 5.43.: Dependence of the Ar MGI amount on (a) core background plasma temperature following D_2 SPI entry and (b) rate at which the core background plasma temperature drops.

The time-averaged core temperature of the background plasma $\langle T_e \rangle_{core}$ predicted by the 1D diffusion model after the D₂ SPI entry decreases with increase in Ar MGI amounts as shown in the figure 5.43(a). This dependency is similar to the simulations of pure Ar background plasma shown in the figure 5.29.

The rate at which the temperature drops due to D₂ SPI entry $d \langle T_e \rangle_{core} / dt$ also decrease with Ar MGI amount as shown in the figure 5.43(b). One possible explanation for this dependency may be from radiated power following the D₂ SPI. Discharges with lower Ar MGI amount have higher radiated power (figure 5.46, explained later in the section 5.5.2). Consequently, the rate of temperature drop may decrease with Ar MGI amount, since T_e -profile is estimated directly from the radiated power emissivity profile in the 1D diffusion code.

5.5.1.5. Comparison of VUV line intensities

Using the results from the 1D diffusion model, the line intensity ratio of Ar²⁺ ($\lambda_{Ar^{2+}}=47.94$ nm) and D⁰⁺ ($\lambda_{D^{0+}}=102.54$ nm) are estimated from the synthetic line ratio given in the equation 3.18. The line intensity ratio is adjusted according to the VUV spectrometer line of sight.

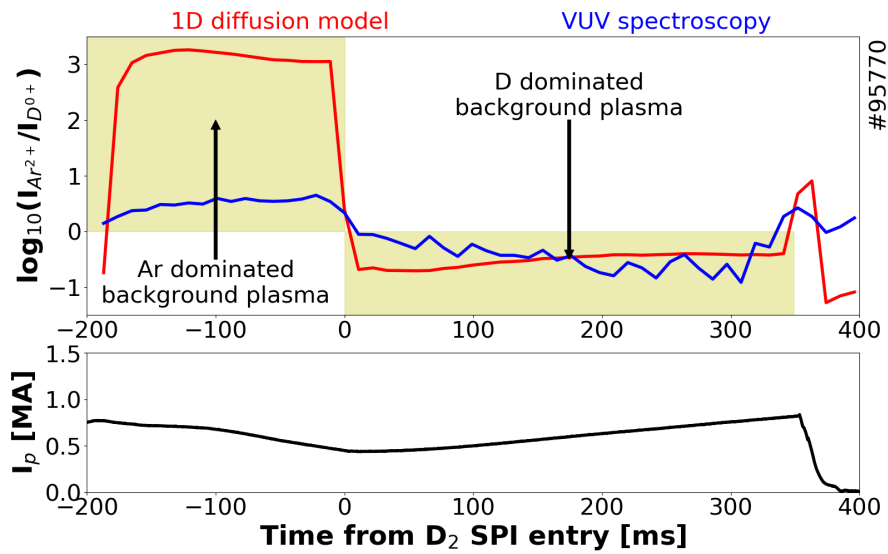


Figure 5.44.: Comparison of the Ar²⁺ and D⁰⁺ line ratio from the 1D diffusion model (red) with VUV spectroscopy (blue) for the discharge #95770.

As shown in the figure 5.44, the 1D diffusion model (red data line) predicts the drop in the Ar line brightness after the D₂ SPI entry. This is qualitatively consistent with the line intensity ratio measured by the VUV spectroscopy (blue data line).

From the figures 5.39, it can be seen that the 1D diffusion model overestimates the electron density of the background plasma as compared to interferometry, probably due to insufficient recombination as shown in the figure 5.37. In spite of the overestimation, the 1D diffusion model could correctly predict the drop in the argon line

brightness for discharges with different Ar MGI amounts as shown in the figure 5.45(a). This predicted drop in the argon line brightness is consistent with the drop measured by VUV spectroscopy shown in the figure 5.45(b), irrespective of initial argon quantity. It can be observed from the figure 5.45 that line ratio remains larger for larger argon amounts after D₂ SPI entry. This may indicate that argon purge may be not complete and some argon impurities still remain in the background plasma.

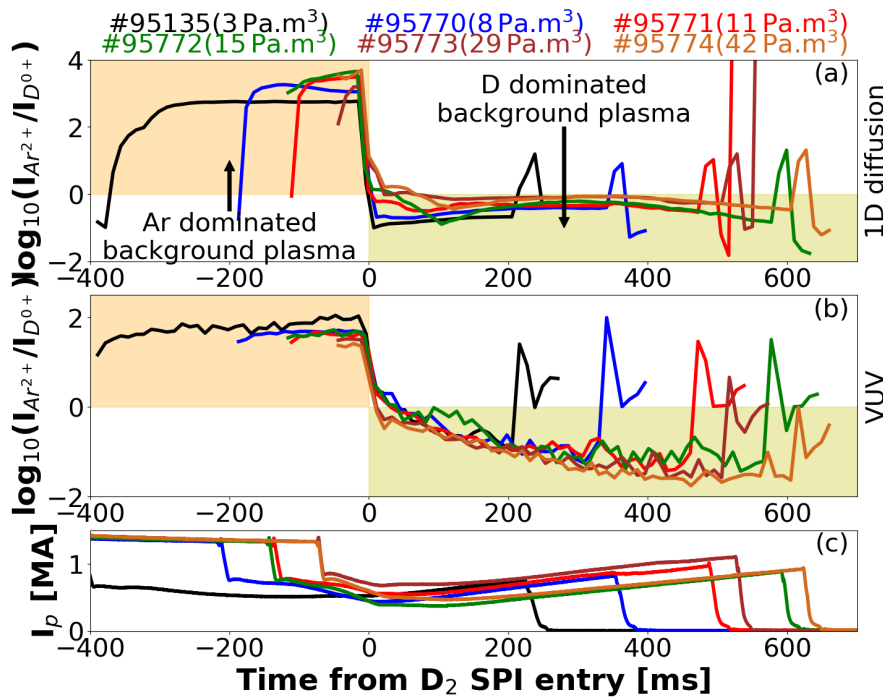


Figure 5.45.: Comparison of Ar²⁺ to D⁰⁺ line ratios for different Ar MGI amounts from (a) 1D diffusion code and (b) VUV spectroscopy, with (c) plasma current I_p .

As discussed in the sections 5.5.1.1, 5.5.1.2 and 5.5.1.4, the 1D diffusion model cannot recombine the argon ions to neutrals and thus predict the drop in electron density in the JET tokamak. A possible reason why this 1D diffusion model overestimates the electron density could be associated to the fact that in the JET tokamak, few MW of radiated power are measured after D₂ SPI entry when very low temperature and density of the background plasmas are expected. Such radiated powers are not observed in DIII-D or ASDEX-Upgrade tokamak.

5.5.2. Non-thermal radiation and 1D diffusion model

In the JET tokamak, the background plasma cools down after D₂ causing higher argon ionization states to drop to very low value. However, the background plasmas may not be cold enough for the Ar¹⁺ and Ar²⁺ to recombine to form argon neutrals.

Thus, the 1D diffusion model overestimates the free electron density and cannot simulate the condition necessary for the total recombination in the JET tokamak.

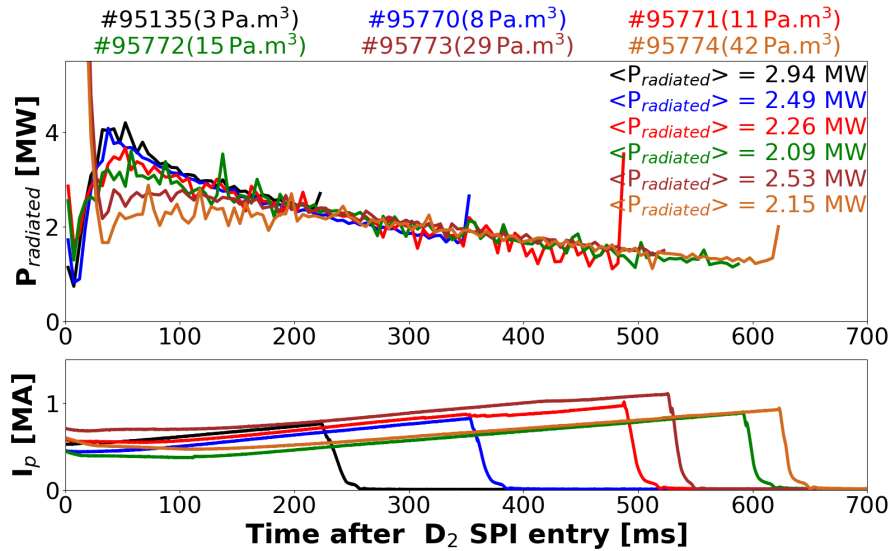


Figure 5.46.: Radiated power of the argon background plasma following D₂ SPI entry for different Ar MGI amounts measured by bolometer in the JET tokamak.

As shown in the figure 5.46, the radiated power is between 2-4 MW after the entry of D₂ SPI in the JET tokamak. The radiated power normally increases with impurity content but from the figure 5.46, the lowest radiated powers are obtained with the highest argon amounts.

When the argon ions recombines to argon neutrals due to plasma cooling following the D₂ SPI entry, the neutrals may not be flushed out. The argon neutrals may be inside the vessel and during the final RE beam termination, the argon neutrals may be re-ionized.

It can also be noted that after the supposed RE beam benign termination, the argon lines reappear in the VUV spectra though with lower intensities as compared to argon background plasma before D₂ SPI entry as shown in the figure 5.47. During the final beam collapse, the magnitude of the radiated power spike increases with argon contents in the plasma.

As the electron density drops to very low value (figure 5.39(b)) and very low electron temperatures are expected favoring recombination conditions after the D₂ SPI entry, the presence few MW of radiated power from the 'thermal' background plasma is highly questionable. One possible explanation for this high radiated power may be due to the contribution of the 'non-thermal' radiation, possibly due to the presence of energetic RE beam.

In the 1D diffusion model, radiated power profile (or emissivity profile) is used to determine the RE density profile and the temperature profile. In turn, the neutral diffusion coefficient is determined by the temperature which in turn affects the species

density profiles. Thus, radiated power may significantly change the results of the 1D diffusion model.

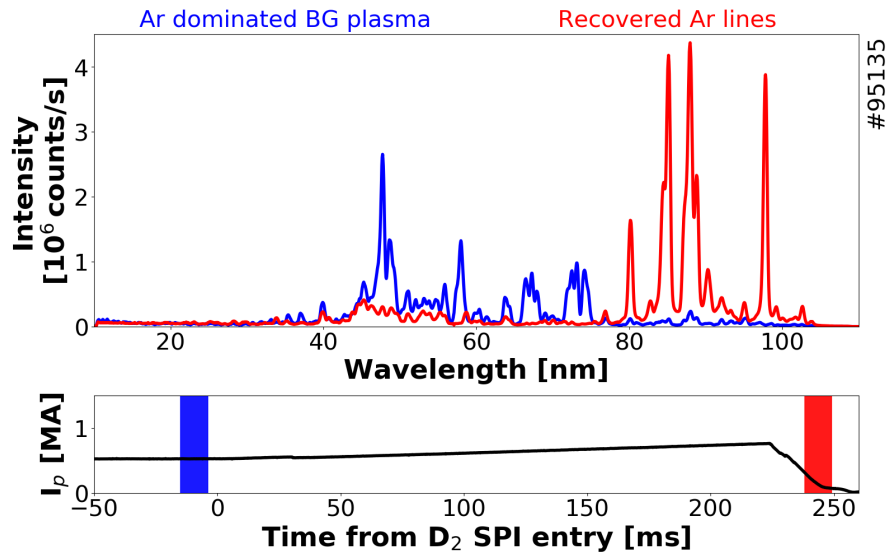


Figure 5.47.: Energy radiated (a) after D₂ SPI before the final collapse and (b) during the final collapse, as a function of Ar MGI amount in the plasma.

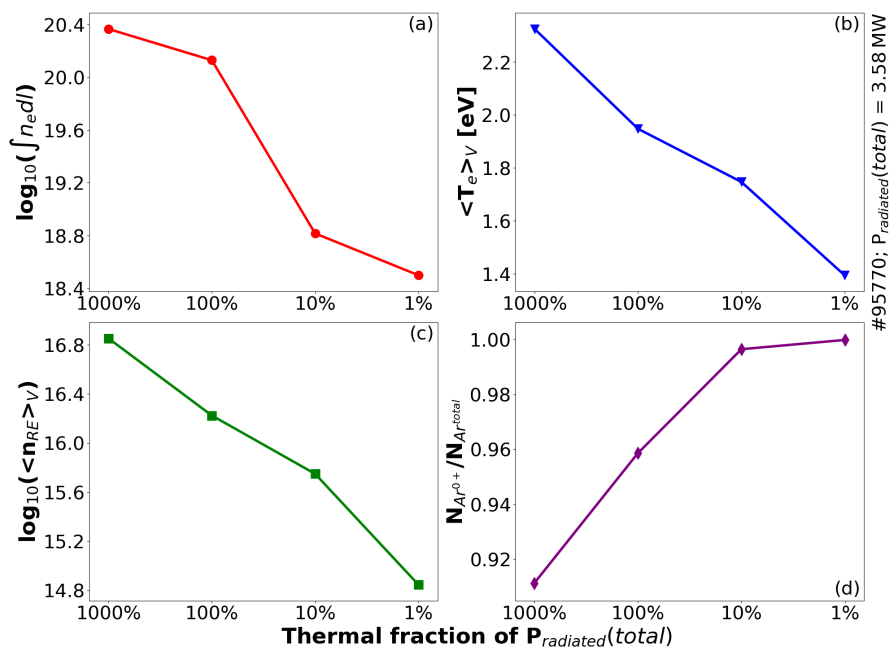


Figure 5.48.: Dependence of (a) line-integrated electron density $\int n_{ed}l$, (b) volume-averaged electron temperature profile $\langle T_e \rangle_V$, (c) volume-averaged RE density profile $\langle n_{RE} \rangle_V$ and (d) fraction of argon neutrals, on the thermal fraction of the total radiated power $P_{radiated}$. The simulations are performed using the data from the discharge #95770.

1D diffusion model simulations are performed by changing the fraction of the thermal contribution in the total radiated power $P_{radiated}$ using the data from the discharge #95770 after the arrival of D2 SPI as shown in the figure 5.48. The line-integrated electron density $\int n_e dl$ and the volume-averaged electron temperature $\langle T_e \rangle_V$ decreases when the thermal fraction of the total radiated power $P_{radiated}$ as shown in the figures 5.48(a) and 5.48(b) respectively. On the other hand, the fraction of argon neutrals in the total argon atoms increases with decrease of the thermal fraction as shown in the figure 5.48(d).

When we assume that only 1% of the total radiated power ($P_{radiated}=0.0358$ MW) are due to the thermal contribution from the background plasma, $\langle T_e \rangle_V \approx 1.4$ eV, $\int n_e dl \approx 10^{18} \text{ m}^{-3}$ and $N_{Ar^{0+}}/N_{Ar^{total}} \approx 1$. Therefore, when the thermal fraction of the total radiated power is just 1% of the total radiated power, almost all the argon ions are recombined as argon neutrals and the line-integrated electron density is closer to the interferometry measurement.

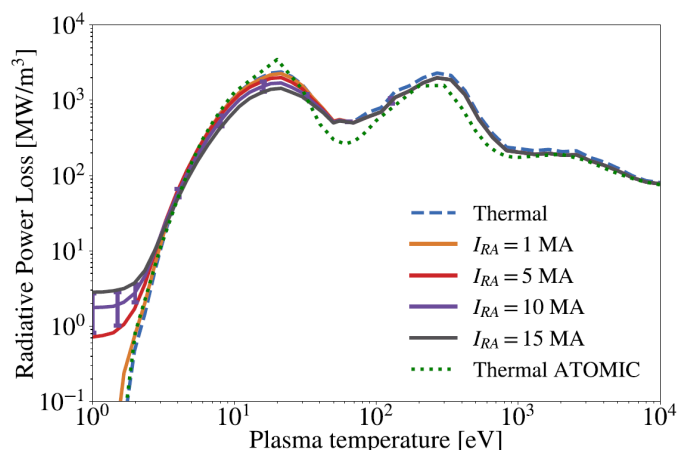


Figure 5.49.: Enhanced radiative power loss of argon due to relativistic electrons (Garland 2020). I_{RA} is the RE current for ITER with $I_{RA}=10$ MA corresponding to $n_{RE} \approx 10^{17} \text{ m}^{-3}$.

At very low temperatures, the presence of energetic RE beam may enhance the radiative power loss of argon impurities according to the results developed in (Garland 2020), as shown in the figure 5.49. At recombination temperatures (around 1 eV), the radiative power loss of argon background plasma is highly dominated by the RE beam. In the JET tokamak, the non-thermal radiation due to the relativistic RE beam may dominate the total radiated power at very low temperature, which is believed to be the case for D₂ SPI entry into the argon background plasma.

In the 1D diffusion model, removal of non-thermal contribution in the total radiated power could create recombination conditions for argon ions, similar to the DIII-D tokamak. As the CRETIN atomic model cannot differentiate the thermal and non-thermal radiation, a more advanced atomic model such as PrismSPECT (MacFarlane 2003) can be used to exclude the non-thermal radiations. This is work in progress.

5.5.3. Conclusions

- Increase in line-integrated free electron density predicted by the diffusion code is inconsistent with experimental measurements.
- Code predicts drop in electron temperature but not low enough for argon recombination.
- Drop in argon line brightness predicted by the code is in qualitative agreement with line intensity drop measured by VUV spectroscopy.
- The over-prediction of electron density and temperature may be due to non-thermal contribution in the total radiated power.
- By removing non-thermal radiation from the total radiated power, the diffusion code may predict the argon expulsion in JET, similar to DIII-D

Summary and Perspectives

Runaway electron beams carry the risk of localized damage to the in-vessel components. For the future large and reactor-scale devices, including ITER, higher plasma current and larger machine size are needed for better confinement and performance. This leads to large avalanche multiplication factor, thus, posing a major threat to robust operation. Therefore, the prevention and control of the runaway electrons are the major concerns of the future larger and reactor-scale tokamaks including ITER, which makes the runaway electron study a hot topic in the field of nuclear fusion. The present strategy for runaway electrons is to first avoid their generation by a massive material injection (MMI) of deuterium or high-Z noble species. As a second line of defense, a second MMI will be used to mitigate the RE beam if their generation cannot be avoided. The impurities from the first MMI form a cold dense background plasma because of which the second MMI aimed at mitigating the runaway electron beam may be inefficient due to poor penetration, as observed in the JET tokamak. Therefore, understanding the physics of the interaction between the runaway electron beam and the mitigation MMI in the presence of a cold background plasma is an essential study for a reliable runaway electron beam mitigation scenario.

The characteristics of the background plasma are poorly known. Using VUV spectroscopy, a method was developed to estimate the electron temperature of the background plasma in JET. In this method, the temperature profile of the background plasma was estimated by fitting synthetic line ratios to experimental line ratios. For this estimation, a peaked temperature profile was parameterized and a pure argon background plasma was assumed. Using this method, the JET-ILW discharges were found to have hotter background plasma ($T_e \approx 6-18$ eV) than on other tokamaks ($T_e \sim 1-2$ eV in DIII-D) where the runaway electron beam mitigation was found to be unconditionally successful. The estimated temperature was consistent with previous estimation of $T_e \approx 5-15$ eV, assuming collisional-radiative equilibrium.

The background plasma due to Ar SPI was found to be colder ($T_e \approx 4-6$ eV) than background plasma due to Ar MGI. The time and volume averaged background plasma temperatures was found to increase with argon gas amount and the electron density in the far-SOL. No clear dependence of the background plasma temperatures with the initial value of the plasma current before disruption was observed. No clear dependence of the background plasma temperatures with the initial value of the plasma temperature $T_e^{initial}$ before disruption was observed.

The background plasma temperature due to Ar SPI was found to increase with the pre-disruption electron density $n_e^{initial}$ and additional heating. Intact Ar pellets were found to have hotter background plasma and they penetrate deeper into the thermal plasma.

In the background plasma temperature estimation from the VUV spectroscopy, the excitation/ionization from the RE beam are not considered. For completeness, including the RE beam as a power source in the temperature estimation might be particularly useful and is allocated as the work for the future.

Using the characterization of the background plasma, a simple 0D/1D power balance was proposed to understand the RE beam interaction with the background plasma.

Using the temperature profile of the background plasma, a more advanced 1D power balance was proposed. For the RE beam, the bremsstrahlung radiation was found to be negligible as compared to synchrotron radiation and collisional power loss. The collisional power transfer between the RE beam and the background plasma was found to be the dominant primary source term which heat the background plasma in the confined region. For the confined background plasma, the ohmic power source and the power source due to γ -ray absorption was found to be negligible. In the open field line region, the heat conducted from the background plasma to the wall was found to be negligible as compared to the radiated power. Also, the radiated power of the background plasma in the open field line region constituted only a fraction of the total radiated power. The measured radiated power was in qualitative agreement with the estimated radiated power of the background plasma for some discharges and the power balance was correct within the uncertainty range of the various power estimations.

On comparing JET discharges #92459 , #92454 ($\langle T_e \rangle_V \approx 3$ eV) and a DIII-D discharge ($\langle T_e \rangle_V = 2$ eV), discharge #92459 with hottest background plasma had highest collisional power transferred per free electron of the background plasma. This was given as a possible explanation for hotter background plasma in JET discharges.

In the power balance, a steady state was considered : constant energies of the RE beam and the background plasmas. The power balance can be further improved by considering a non-steady state power balance. In addition, the Gaussian RE energy distribution can be improved mimicking the energy distribution from experiments.

A 1D diffusion model was adapted for the JET tokamak to simulate the background plasmas. The model considers particle diffusion and atomic processes such as ionization, recombination and charge exchange. The model was found to be sensitive to initial guesses of the species densities. It was also observed that the background plasma temperature estimated by the model increases with geometrical wall radius.

This means that bigger the tokamak size, hotter is the background plasma for a fixed plasma radius and other parameters. When rate coefficients data from the default CRETIN atomic model was replaced by rate coefficients from ADAS atomic model, the code predicted hotter background plasma with higher free electron density as compared to CRETIN, compatible with the VUV measurements, which also use atomic data from ADAS. Due to higher ionization and lower recombination in the ADAS atomic model as compared to CRETIN, higher fractions of argon ions in higher ionization states were predicted in ADAS than CRETIN.

When the argon background plasma was simulated using the 1D diffusion model with CRETIN atomic data, the temperatures were much lower than temperatures estimated from VUV spectroscopy. The time and volume averaged temperatures were found to be decreasing with increasing argon amounts, which was the reverse trend of T_e -profile measurements from VUV spectroscopy.

When the 1D diffusion model simulated the D₂ SPI in argon background plasma, a drop in argon line brightness was predicted by the model which was consistent with experimental VUV measurements. However, the 1D diffusion model predicted an increase in line-integrated free electron density which was inconsistent with experimental measurements. The model predicted a drop in electron temperature but not low enough for argon recombination conditions like in DIII-D.

The over-prediction of electron density and temperature was attributed to the presence of high radiated power in JET tokamak (~1-4 MW) than on DIII-D (≤ 100 kW). By reducing the fraction of thermal contribution in the total radiated power, the electron density and temperature dropped, thereby supporting argon recombination. Thus, a large fraction of the total radiated power was assumed to come from non-thermals (RE beam) in JET. This idea of non-thermal radiation was supported from the results of FLYCHKlite code.

By removing the non-thermal radiation from the total radiation, the 1D diffusion model can be vastly improved for the JET tokamak. To serve this purpose, PRISMspec atomic model can be used in the model to account for non-thermal radiation. Integration of PRISMspec atomic data into the 1D diffusion model is envisaged in the near future to simulate Ar+D₂ background plasma in the JET tokamak.

Bibliography

- [Andersson 2001] F Andersson et al. “Damping of relativistic electron beams by synchrotron radiation”. In: *Physics of Plasmas* 8.12 (2001), pp. 5221–5229 (cit. on pp. [46](#), [112](#), [120](#)).
- [Anicich 1993] Vincent G Anicich. “Evaluated bimolecular ion-molecule gas phase kinetics of positive ions for use in modeling planetary atmospheres, cometary comae, and interstellar clouds”. In: *Journal of Physical and Chemical Reference Data* 22.6 (1993), pp. 1469–1569 (cit. on pp. [138](#), [139](#)).
- [Arnoux 2009] G Arnoux et al. “Heat loads on plasma facing components during disruptions on JET”. In: *Nuclear fusion* 49.8 (2009), p. 085038 (cit. on p. [37](#)).
- [Artola’s PhD 2018] Francisco Javier Artola Such. “Free-boundary simulations of MHD plasma instabilities in tokamaks”. PhD thesis. Aix-Marseille, 2018 (cit. on pp. [39–41](#)).
- [Aston 1936] FW Aston. “New data on isotopes”. In: *Nature* 137.3467 (1936), pp. 613–613 (cit. on p. [17](#)).
- [Bachmann 1995] P Bachmann et al. “Kinetic Description of Elastic Processes in Hydrogen-Helium Plasmas”. In: *Contributions to Plasma Physics* 35.1 (1995), pp. 45–100 (cit. on p. [138](#)).
- [Bakhtiari 2005a] M Bakhtiari et al. “Role of bremsstrahlung radiation in limiting the energy of runaway electrons in tokamaks”. In: *Physical review letters* 94.21 (2005), p. 215003 (cit. on p. [112](#)).
- [Bakhtiari 2005b] M Bakhtiari et al. “Study of plasma termination using high-Z noble gas puffing in the JT-60U tokamak”. In: *Nuclear fusion* 45.5 (2005), p. 318 (cit. on p. [51](#)).
- [Barnsley 2003] R Barnsley et al. “JET beamline with integrated x-ray, VUV, and visible spectrometers, for burning plasma experiments”. In: *Review of scientific instruments* 74.3 (2003), pp. 1969–1973 (cit. on pp. [70](#), [71](#)).
- [Baylor 2010] Larry R Baylor et al. *Shattered Pellet Disruption Mitigation Technology Development for ITER*. Tech. rep. ITR/P1-27, 2010 (cit. on p. [51](#)).

- [Baylor 2017] L Baylor et al. “Developments in shattered pellet technology and implementation on JET and ITER”. In: *PPPL TSD workshop report*. 2017 (cit. on pp. 57, 62).
- [Baylor 2019] LR Baylor et al. “Shattered pellet injection technology design and characterization for disruption mitigation experiments”. In: *Nuclear Fusion* 59.6 (2019), p. 066008 (cit. on p. 51).
- [Berger 1992] Martin J Berger. “ESTAR, PSTAR, and ASTAR: Computer programs for calculating stopping-power and range tables for electrons, protons, and helium ions”. In: *esta* (1992) (cit. on pp. 87, 116, 117).
- [Betti 2016] R Betti et al. “Inertial-confinement fusion with lasers”. In: *Nature Physics* 12.5 (2016), pp. 435–448 (cit. on p. 21).
- [Boboc 2012] A Boboc et al. “Upgrade of the JET far infrared interferometer diagnostic”. In: *Review of Scientific Instruments* 83.10 (2012), 10E341 (cit. on p. 66).
- [Bodin 1980] HAB Bodin et al. “Reversed-field-pinch research”. In: *Nuclear fusion* 20.10 (1980), p. 1255 (cit. on p. 22).
- [Bozhenkov 2008] SA Bozhenkov et al. “Generation and suppression of runaway electrons in disruption mitigation experiments in TEXTOR”. In: *Plasma physics and controlled fusion* 50.10 (2008), p. 105007 (cit. on p. 51).
- [Bretagne 1986] J Bretagne et al. “Relativistic electron-beam-produced plasmas. I. Collision cross sections and loss function in argon”. In: *Journal of Physics D: Applied Physics* 19.5 (1986), p. 761 (cit. on p. 156).
- [Brown 1990] MR Brown et al. “Current drive by spheromak injection into a tokamak”. In: *Physical review letters* 64.18 (1990), p. 2144 (cit. on p. 23).
- [Can 1985] Cüneyt Can et al. “Electron-capture cross sections for low-energy highly charged neon and argon ions from molecular and atomic hydrogen”. In: *Physical Review A* 31.1 (1985), p. 72 (cit. on pp. 138, 139).
- [CCFE] *MAST Upgrade is the UK’s national fusion experiment*. URL: <https://ccfe.ukaea.uk/research/mast-upgrade/> (visited on 08/06/2020) (cit. on pp. 23, 24).
- [CEA] *Laser Mégajoule*. URL: <http://www-lmj.cea.fr/> (visited on 05/04/2020) (cit. on p. 21).
- [Chapman 1970] S Chapman et al. *The Mathematical Theory of Non-Uniform Gases, 3rd edn. Cambridge Math*. 1970 (cit. on p. 137).

- [Commaux 2010] N Commaux et al. “Demonstration of rapid shutdown using large shattered deuterium pellet injection in DIII-D”. In: *Nuclear fusion* 50.11 (2010), p. 112001 (cit. on pp. 51, 55).
- [Connor 1975] JW Connor et al. “Relativistic limitations on runaway electrons”. In: *Nuclear fusion* 15.3 (1975), p. 415 (cit. on p. 45).
- [Deksnis 1997] EB Deksnis et al. “Beryllium plasma-facing components: JET experience”. In: *Fusion Engineering and Design* 37.4 (1997), pp. 515–530 (cit. on p. 37).
- [Dreicer 1958] H Dreicer. *Theory of runaway electrons*. Tech. rep. 1958 (cit. on p. 42).
- [Eidietis 2015] NW Eidietis et al. “The ITPA disruption database”. In: *Nuclear Fusion* 55.6 (2015), p. 063030 (cit. on p. 41).
- [Entrop 2000] Ingneborg Entrop et al. “Scale size of magnetic turbulence in tokamaks probed with 30-MeV electrons”. In: *Physical review letters* 84.16 (2000), p. 3606 (cit. on p. 120).
- [EUROfusiona] *JET: EUROfusion’s flagship device*. URL: <https://www.euro-fusion.org/devices/jet/> (visited on 05/05/2020) (cit. on pp. 25, 27, 29, 30).
- [EUROfusionb] *JET’s salient features*. URL: <https://www.euro-fusion.org/index.php?id=135&L=950> (visited on 08/28/2020) (cit. on p. 28).
- [EUROfusionc] *Tokamak principle*. URL: <https://www.euro-fusion.org/news/detail/tokamak-principle/?> (visited on 05/07/2020) (cit. on pp. 25, 27, 42).
- [Farnsworth 1968] Philo T Farnsworth. *Method and apparatus for producing nuclear-fusion reactions*. US Patent 3,386,883. June 1968 (cit. on p. 21).
- [Fedorczyk 2019] N Fedorczyk et al. “A spectral filament model for turbulent transport and scrape off layer width in circular geometry”. In: *Nuclear Materials and Energy* 19 (2019), pp. 433–439 (cit. on p. 126).
- [Ficker’s Master 2015] Bc Ondrej Ficker. “Generace, ztráty a diagnostika ubíhajících elektronův tokamaciích Generation, losses and detection of runaway electrons in tokamaks”. In: (2015) (cit. on pp. 44, 47).
- [Fonck 1982] RJ Fonck et al. “Multichannel grazing-incidence spectrometer for plasma impurity diagnosis: SPRED”. In: *Applied Optics* 21.12 (1982), pp. 2115–2123 (cit. on p. 70).

- [Frieman 1953] EA Frieman et al. “The proton-proton reaction and energy production in the sun”. In: *Physical Review* 89.3 (1953), p. 648 (cit. on p. 17).
- [Garland 2020] Nathan A Garland et al. “Impact of a minority relativistic electron tail interacting with a thermal plasma containing high-atomic-number impurities”. In: *Physics of Plasmas* 27.4 (2020), p. 040702 (cit. on p. 183).
- [General Fusion] *Magnetized Target Fusion: An Overview*. URL: <https://generalfusion.com/technology-magnetized-target-fusion/> (visited on 05/04/2020) (cit. on p. 22).
- [Gill 2000] RD Gill et al. “Direct observations of runaway electrons during disruptions in the JET tokamak”. In: *Nuclear Fusion* 40.2 (2000), p. 163 (cit. on p. 112).
- [Granetz 1996] RS Granetz et al. “Disruptions and halo currents in Alcator C-Mod”. In: *Nuclear fusion* 36.5 (1996), p. 545 (cit. on p. 40).
- [Granetz 2014] Robert S Granetz et al. “An ITPA joint experiment to study runaway electron generation and suppression”. In: *Physics of plasmas* 21.7 (2014), p. 072506 (cit. on p. 43).
- [Granetz 2019] RS Granetz et al. “Study of Alcator C-Mod discharges that had startup runaways”. In: *Proc. 34th ITPA Meeting on IOS (Garching, Germany, October, 2019) 2019*. 2019 (cit. on p. 43).
- [Greenwald 2002] Martin Greenwald. “Density limits in toroidal plasmas”. In: *Plasma Physics and Controlled Fusion* 44.8 (2002), R27 (cit. on pp. 35, 36).
- [Hender 2007] TC Hender et al. “MHD stability, operational limits and disruptions”. In: *Nuclear fusion* 47.6 (2007), S128 (cit. on pp. 37, 42, 43).
- [Hirshman 1977] SP Hirshman et al. *Neoclassical conductivity of a tokamak plasma*. Tech. rep. Princeton Univ., NJ (USA). Plasma Physics Lab., 1977 (cit. on p. 120).
- [Hollmann 2006] EM Hollmann et al. “Spectroscopic measurement of atomic and molecular deuterium fluxes in the DIII-D plasma edge”. In: *Plasma physics and controlled fusion* 48.8 (2006), p. 1165 (cit. on p. 141).
- [Hollmann 2008] EM Hollmann et al. “Measurements of injected impurity assimilation during massive gas injection experiments in DIII-D”. In: *Nuclear Fusion* 48.11 (2008), p. 115007 (cit. on pp. 51, 55, 145).

- [Hollmann 2011] EM Hollmann et al. *Measurement of Runaway Electron Beam Composition and Estimate of Resulting Collisional Decay of Runaway Electron Currents in DIII-D*. Tech. rep. Oak Ridge National Lab.(ORNL), Oak Ridge, TN (United States), 2011 (cit. on pp. 88, 94, 103, 128, 130, 168).
- [Hollmann 2013] EM Hollmann et al. “Control and dissipation of runaway electron beams created during rapid shutdown experiments in DIII-D”. In: *Nuclear Fusion* 53.8 (2013), p. 083004 (cit. on pp. 55, 68, 77, 128).
- [Hollmann 2015] EM Hollmann et al. “Status of research toward the ITER disruption mitigation system”. In: *Physics of Plasmas* 22.2 (2015), p. 021802 (cit. on p. 144).
- [Hollmann 2019] EM Hollmann et al. “Study of argon assimilation into the post-disruption runaway electron plateau in DIII-D and comparison with a 1D diffusion model”. In: *Nuclear Fusion* 59.10 (2019), p. 106014 (cit. on pp. 135, 136, 141, 142, 144, 152, 153, 171).
- [Hollmann 2020] Eric M Hollmann et al. “Study of argon expulsion from the post-disruption runaway electron plateau following low-Z massive gas injection in DIII-D”. In: *Physics of Plasmas* 27.4 (2020), p. 042515 (cit. on pp. 56, 169, 171, 204).
- [Hubbell 1969] JH Hubbell. “Photon cross sections, attenuation coefficients and energy absorption coefficients”. In: *National Bureau of Standards Report NSRDS-NBS29, Washington DC* (1969) (cit. on p. 122).
- [Huber 2007] Alexander Huber et al. “Upgraded bolometer system on JET for improved radiation measurements”. In: *Fusion Engineering and Design* 82.5-14 (2007), pp. 1327–1334 (cit. on pp. 105, 106).
- [IEA] IEA : *Key World Energy Statistics 2019*. URL: <https://www.iea.org/reports/key-world-energy-statistics-2019> (visited on 04/30/2020) (cit. on p. 16).
- [Iida 2005] H Iida et al. “Nuclear analyses of some key aspects of the ITER design with Monte Carlo codes”. In: *Fusion engineering and design* 74.1-4 (2005), pp. 133–139 (cit. on p. 49).
- [IPB 1999] EDA ITER et al. “MHD stability, operational limits and disruptions”. In: *Nuclear Fusion* 39.12 ITER physics basis (1999), pp. 2251–2389 (cit. on pp. 32, 33, 50).

- [IPP-MPGa] *Introduction: The ASDEX Upgrade tokamak*. URL: <https://www.ipp.mpg.de/16208/einfuehrung> (visited on 06/21/2020) (cit. on p. 52).
- [IPP-MPGb] *Wendelstein 7-X*. URL: <https://www.ipp.mpg.de/w7x> (visited on 05/05/2020) (cit. on p. 24).
- [ITERa] *Disruption mitigation : JET gets an injection*. URL: <https://www.iter.org/newsline/-/3267> (visited on 06/19/2020) (cit. on p. 51).
- [ITERb] *ITER : Fuelling the fusion reaction*. URL: <https://www.iter.org/sci/FusionFuels> (visited on 04/30/2020) (cit. on p. 16).
- [ITERc] *The ITER tokamak*. URL: <https://www.iter.org/mach> (visited on 07/06/2020) (cit. on pp. 25, 29).
- [Jackson 2007] J David Jackson. “Electrodynamics”. In: *The Optics Encyclopedia: Basic Foundations and Practical Applications* (2007) (cit. on p. 112).
- [Jarboe 1994] Thomas R Jarboe. “Review of spheromak research”. In: *Plasma Physics and Controlled Fusion* 36.6 (1994), p. 945 (cit. on p. 23).
- [Jaspers 2001] R Jaspers et al. “A synchrotron radiation diagnostic to observe relativistic runaway electrons in a tokamak plasma”. In: *Review of Scientific Instruments* 72.1 (2001), pp. 466–470 (cit. on pp. 112, 130).
- [Jayakumar 1993] R Jayakumar et al. “Collisional avalanche exponentiation of runaway electrons in electrified plasmas”. In: *Physics Letters A* 172.6 (1993), pp. 447–451 (cit. on p. 50).
- [Keilhacker 1999] M Keilhacker et al. “D–T experiments in the JET tokamak”. In: *Journal of nuclear materials* 266 (1999), pp. 1–13 (cit. on p. 28).
- [Kirkpatrick 1995] Ronald C Kirkpatrick et al. “Magnetized target fusion: An overview”. In: *Fusion Technology* 27.3 (1995), pp. 201–214 (cit. on p. 22).
- [Kolb 1959] AC Kolb et al. “Field mixing and associated neutron production in a plasma”. In: *Physical Review Letters* 3.1 (1959), p. 5 (cit. on p. 23).
- [Kramida 2018] A Kramida et al. “Team 2015, NIST Atomic Spectra Database (ver. 5.3)”. In: *National Institute of Standards and Technology, Gaithersburg, MD (Available at: <http://physics.nist.gov/asd>)* (2018) (cit. on pp. 75, 81, 122, 123).

- [Kruezi 2009] U Kruezi et al. “Massive gas injection experiments at JET-performance and characterisation of the disruption mitigation valve”. In: *Proc. 36th EPS Conf. on Plasma Physics (Sofia, Bulgaria, 29 June–3 July 2009)*. 2009 (cit. on pp. 51, 57).
- [Kruezi 2014] U Kruezi et al. “A new disruption mitigation system for DT operation at JET”. In: *Proc. 28th Symp. on Fusion Technology (San Sebastian, Spain, 29 September–3 October 2014)*. 2014 (cit. on p. 57).
- [Kruskal 1958] M Kruskal et al. “The instability of a pinched fluid with a longitudinal magnetic field”. In: *Proceedings of the Royal Society of London. Series A. Mathematical and Physical Sciences* 245.1241 (1958), pp. 222–237 (cit. on p. 34).
- [Landreman 2014] Matt Landreman et al. “Numerical calculation of the runaway electron distribution function and associated synchrotron emission”. In: *Computer Physics Communications* 185.3 (2014), pp. 847–855 (cit. on p. 45).
- [Lawson 1957] John D Lawson. “Some criteria for a power producing thermonuclear reactor”. In: *Proceedings of the physical society. Section B* 70.1 (1957), p. 6 (cit. on pp. 18, 20).
- [Lehnen 2019 ITPA] M Lehnen. “Progress in validating the ITER Disruption Mitigation Strategy”. In: *Proc. 34th ITPA Meeting on IOS (Garching, Germany, October, 2019) 2019*. 2019 (cit. on pp. 60–62).
- [Li 2018] Y Li et al. “Design of a shattered pellet injection system on J-TEXT tokamak”. In: *Review of Scientific Instruments* 89.10 (2018), 10K116 (cit. on p. 51).
- [Lindl 1995] John Lindl. “Development of the indirect-drive approach to inertial confinement fusion and the target physics basis for ignition and gain”. In: *Physics of plasmas* 2.11 (1995), pp. 3933–4024 (cit. on p. 21).
- [Liu 2018] Chang Liu et al. “The effects of kinetic instabilities on the electron cyclotron emission from runaway electrons”. In: *Nuclear Fusion* 58.9 (2018), p. 096030 (cit. on p. 69).
- [LLNL] *What is NIF?* URL: <https://lasers.llnl.gov/about/what-is-nif> (visited on 05/04/2020) (cit. on pp. 21, 81).
- [Llovet 2014] Xavier Llovet et al. “Cross sections for inner-shell ionization by electron impact”. In: *Journal of Physical and Chemical Reference Data* 43.1 (2014), p. 013102 (cit. on p. 143).
- [Loarte 2005] A Loarte et al. “A new look at JET operation with Be as plasma facing material”. In: *Journal of nuclear materials* 337 (2005), pp. 816–820 (cit. on p. 37).

- [Luxon 2002] James L Luxon. “A design retrospective of the DIII-D tokamak”. In: *Nuclear Fusion* 42.5 (2002), p. 614 (cit. on p. 55).
- [MacFarlane 2003] JJ MacFarlane et al. “Simulation of the ionization dynamics of aluminum irradiated by intense short-pulse lasers”. In: *Proc. Inertial Fusion and Sciences Applications*. Vol. 457. 2003 (cit. on p. 183).
- [Marrero 1972] Thomas Raphael Marrero et al. “Gaseous diffusion coefficients”. In: *Journal of Physical and Chemical Reference Data* 1.1 (1972), pp. 3–118 (cit. on p. 137).
- [Martin-Solis 2017] José Ramón Martíén-Soliés et al. “Formation and termination of runaway beams in ITER disruptions”. In: *Nuclear Fusion* 57.6 (2017), p. 066025 (cit. on pp. 48, 49).
- [McCormick 2005] K McCormick et al. “New bolometry cameras for the JET Enhanced Performance Phase”. In: *Fusion engineering and design* 74.1-4 (2005), pp. 679–683 (cit. on p. 106).
- [Muller 1985] A Muller et al. “An improved crossed-beams technique for the measurement of absolute cross sections for electron impact ionisations of ions and its application to Ar⁺ ions”. In: *Journal of Physics B: Atomic and Molecular Physics* 18.14 (1985), p. 2993 (cit. on p. 142).
- [Murari 1995] A Murari et al. “Multichord calibrated bolometer array for the RFX experiment”. In: *Review of scientific instruments* 66.1 (1995), pp. 665–667 (cit. on p. 105).
- [Murari 2006] A Murari et al. “Real-time recovery of the electron density from interferometric measurements affected by fringe jumps”. In: *Review of scientific instruments* 77.7 (2006), p. 073505 (cit. on p. 66).
- [Nakamura 2002] Y Nakamura et al. “Axisymmetric disruption dynamics including current profile changes in the ASDEX-Upgrade tokamak”. In: *Plasma physics and controlled fusion* 44.8 (2002), p. 1471 (cit. on p. 40).
- [Nelder 1965] John A Nelder et al. “A simplex method for function minimization”. In: *The computer journal* 7.4 (1965), pp. 308–313 (cit. on pp. 73, 74).
- [Osterbrock 1961] Donald E Osterbrock. “On Ambipolar Diffusion in HI Regions.” In: *The Astrophysical Journal* 134 (1961), pp. 270–272 (cit. on p. 138).

- [Papp 2016] G Papp et al. “Runaway electron generation and mitigation on the European medium sized tokamaks ASDEX Upgrade and TCV”. In: *Proceedings of the 2016 IAEA Fusion Energy Conference. EX/9-4. Kyoto, Japan*. 2016 (cit. on pp. 54, 68).
- [Park 2020] SooHwan Park et al. “Deployment of multiple shattered pellet injection systems in KSTAR”. In: *Fusion Engineering and Design* 154 (2020), p. 111535 (cit. on pp. 51, 62).
- [Pautasso 2008] G Pautasso et al. “Disruption mitigation in ASDEX Upgrade with the in-vessel fast valve”. In: *Proc. 22nd Int. Conf. on Fusion Energy 2008 (Geneva, Switzerland, 2008)*. 2008 (cit. on p. 52).
- [Pautasso 2009] Gabriella Pautasso et al. “Disruption studies in ASDEX Upgrade in view of ITER”. In: *Plasma Physics and Controlled Fusion* 51.12 (2009), p. 124056 (cit. on pp. 51, 53, 54).
- [Pautasso 2020] Gabriella Pautasso et al. “Generation and dissipation of runaway electrons in ASDEX Upgrade experiments”. In: *Nuclear Fusion* (2020) (cit. on p. 169).
- [Paz-Soldan 2017] Carlos Paz-Soldan et al. “Spatiotemporal evolution of runaway electron momentum distributions in tokamaks”. In: *Physical review letters* 118.25 (2017), p. 255002 (cit. on p. 130).
- [Paz-Soldan 2019] C Paz-Soldan et al. “Kink instabilities of the post-disruption runaway electron beam at low safety factor”. In: *Plasma Physics and Controlled Fusion* 61.5 (2019), p. 054001 (cit. on pp. 169, 202).
- [Peacock 1969] NJ Peacock et al. “Measurement of the electron temperature by Thomson scattering in tokamak T3”. In: *Nature* 224.5218 (1969), pp. 488–490 (cit. on p. 30).
- [Peng 1986] YM Peng et al. “Features of spherical torus plasmas”. In: *Nuclear Fusion* 26.6 (1986), p. 769 (cit. on p. 23).
- [Peterson 1968] LR Peterson et al. “The relation between ionization yields, cross sections and loss functions”. In: *Journal of Physics B: Atomic and Molecular Physics* 1.6 (1968), p. 1131 (cit. on p. 143).
- [Phelps 1992] AV Phelps. “Collisions of H⁺, H²⁺, H³⁺, ArH⁺, H⁻, H, and H² with Ar and of Ar⁺ and ArH⁺ with H² for energies from 0.1 eV to 10 keV”. In: *Journal of physical and chemical reference data* 21.4 (1992), pp. 883–897 (cit. on pp. 138, 139).
- [Pigarov 1996] A Yu Pigarov et al. “Application of the collisional-radiative, atomic-molecular model to the recombining divertor plasma”. In: *Physics Letters A* 222.4 (1996), pp. 251–257 (cit. on pp. 138, 139, 141).

- [Pigarov 2009] A Yu Pigarov et al. “Coupled plasma–wall modeling”. In: *Journal of nuclear materials* 390 (2009), pp. 192–195 (cit. on p. 140).
- [Pigarov 2012] A Yu Pigarov et al. “Dynamic Models for Plasma-Wall Interactions”. In: *Contributions to Plasma Physics* 52.5-6 (2012), pp. 465–477 (cit. on p. 137).
- [Pitts 2006] Richard Pitts et al. “Fusion: the way ahead”. In: *Physics World* 19.3 (2006), p. 20 (cit. on p. 30).
- [Poline 2004] Bruce E Poling et al. *The properties of gases and liquids*. 2001 (cit. on p. 137).
- [Post 1970] Richard F Post. “Mirror systems: fuel cycles, loss reduction and energy recovery”. In: *Nuclear fusion reactors*. Thomas Telford Publishing, 1970, pp. 99–111 (cit. on p. 22).
- [Press 1992] William H Press et al. *Numerical recipes in Fortran 77: volume 1, volume 1 of Fortran numerical recipes: the art of scientific computing*. Cambridge university press, 1992 (cit. on pp. 74, 82, 84, 94).
- [Reiter 2004] D Reiter et al. “The data file AMJUEL: Additional atomic and molecular data for EIRENE”. In: *Electronic file, FZ Jülich* (2000) (cit. on pp. 139, 141, 144).
- [Reux 2010] C Reux et al. “Experimental study of disruption mitigation using massive injection of noble gases on Tore Supra”. In: *Nuclear Fusion* 50.9 (2010), p. 095006 (cit. on p. 51).
- [Reux 2015] Cédric Reux et al. “Runaway electron beam generation and mitigation during disruptions at JET-ILW”. In: *Nuclear Fusion* 55.9 (2015), p. 093013 (cit. on pp. 58, 65, 81, 87, 144, 153).
- [Reux 2017] Cedric Reux. “Physics of the interaction between runaway electrons and the background plasma of the current quench in tokamak disruptions”. In: *APS 2017* (2017), NI3–003 (cit. on pp. 58–60, 65, 67, 68, 81, 94).
- [Reux’s PhD 2010] Cédric Reux. “Etude d’une méthode d’amortissement des disruptions d’un plasma de tokamak”. PhD thesis. 2010 (cit. on pp. 38, 42).
- [Rider 1995] Todd H Rider. “A general critique of inertial-electrostatic confinement fusion systems”. In: *Physics of Plasmas* 2.6 (1995), pp. 1853–1872 (cit. on pp. 20, 21).
- [Rieke 1972] Foster F Rieke et al. “Ionization cross sections of gaseous atoms and molecules for high-energy electrons and positrons”. In: *Physical Review A* 6.4 (1972), p. 1507 (cit. on p. 143).

- [Robson 1980] AE Robson. “A Conceptual Design for an Imploding-Liner Fusion Reactor”. In: *Megagauss Physics and Technology*. Springer, 1980, pp. 425–436 (cit. on p. 22).
- [Rohrlich 1954] F Rohrlich et al. “Positron-electron differences in energy loss and multiple scattering”. In: *Physical review* 93.1 (1954), p. 38 (cit. on p. 143).
- [Rosenbluth 1997] MN Rosenbluth et al. “Theory for avalanche of runaway electrons in tokamaks”. In: *Nuclear Fusion* 37.10 (1997), p. 1355 (cit. on pp. 49, 50).
- [Salop 1974] Arthur Salop. “Multi-ionization of neon, argon, and xenon and their ions by high-energy-electron impact”. In: *Physical Review A* 9.6 (1974), p. 2496 (cit. on p. 143).
- [Sandquist 2006] Patrik Sandquist et al. “Relativistic electron distribution function of a plasma in a near-critical electric field”. In: *Physics of plasmas* 13.7 (2006), p. 072108 (cit. on p. 114).
- [Sauer 2015] Stephan PA Sauer et al. “The mean excitation energy of atomic ions”. In: *Advances in Quantum Chemistry*. Vol. 71. Elsevier, 2015, pp. 29–40 (cit. on p. 143).
- [Schioler 2011] Tyge Schioler et al. “Dynamic response of the ITER tokamak during asymmetric VDEs”. In: *Fusion engineering and design* 86.9-11 (2011), pp. 1963–1966 (cit. on p. 40).
- [Scott 2001] Howard A Scott. “Cretin—a radiative transfer capability for laboratory plasmas”. In: *Journal of Quantitative Spectroscopy and Radiative Transfer* 71.2-6 (2001), pp. 689–701 (cit. on pp. 139, 141, 142, 144, 145, 162).
- [Shafranov 1956] VD Shafranov. “Stability of plasmas confined by magnetic fields Sov”. In: *J. At. Energy* 5 (1956), p. 38 (cit. on p. 34).
- [Shiraki 2018] D Shiraki et al. “Dissipation of post-disruption runaway electron plateaus by shattered pellet injection in DIII-D”. In: *Nuclear Fusion* 58.5 (2018), p. 056006 (cit. on pp. 56, 168–170).
- [Smith 2008] Hakan M Smith et al. “Hot tail runaway electron generation in tokamak disruptions”. In: *Physics of Plasmas* 15.7 (2008), p. 072502 (cit. on pp. 47, 48).
- [Sokolov 1979] IUA Sokolov. “Multiplication of accelerated electrons in a tokamak”. In: *JETP Letters* 29 (1979), pp. 218–221 (cit. on p. 49).
- [Son 2016] J Son et al. *Current status of density limit studies in KSTAR*. Tech. rep. 2016 (cit. on p. 36).
- [Spitzer 1958] Lyman Spitzer Jr. “The stellarator concept”. In: *The Physics of Fluids* 1.4 (1958), pp. 253–264 (cit. on p. 24).

- [Sridhar 2020] Sundaresan Sridhar et al. “Characterization of cold background plasma during the runaway electron beam mitigation experiments in the JET tokamak”. In: *Nuclear Fusion* (2020) (cit. on pp. 57, 86).
- [Stahl 2015] Adam Stahl et al. “Effective critical electric field for runaway-electron generation”. In: *Physical Review Letters* 114.11 (2015), p. 115002 (cit. on pp. 46, 47).
- [Stahl 2017] Adam Stahl. *Momentum-space dynamics of runaway electrons in plasmas*. Chalmers University of Technology, 2017 (cit. on p. 110).
- [Stangeby 2000] Peter C Stangeby et al. *The plasma boundary of magnetic fusion devices*. Vol. 224. Institute of Physics Pub. Philadelphia, Pennsylvania, 2000 (cit. on pp. 125, 126).
- [Summers 2004] HP Summers. “The ADAS user manual, version 2.6”. In: <http://www.adas.ac.uk/> (2004) (cit. on pp. 80, 123, 124, 145, 162).
- [Thomas 1997] EW Thomas et al. “Deuterium atomic cross section uncertainties and molecular recycling effects in the divertor region of tokamaks”. In: *Physics of Plasmas* 4.3 (1997), pp. 678–689 (cit. on p. 138).
- [Thonemann 1958] PC Thonemann et al. “Controlled release of thermonuclear energy: production of high temperatures and nuclear reactions in a gas discharge”. In: *Nature* 181.4604 (1958), pp. 217–220 (cit. on p. 21).
- [Thornton 2011] AJ Thornton et al. “Disruption mitigation studies on the Mega Amp Spherical Tokamak (MAST)”. In: *Journal of nuclear materials* 415.1 (2011), S836–S840 (cit. on p. 51).
- [Torre 2019] Alexandre Torre et al. “Tore Supra/WEST toroidal field coil quench following a plasma disruption with runaway electrons”. In: *IEEE Transactions on Applied Superconductivity* 29.5 (2019), pp. 1–5 (cit. on p. 43).
- [Troyon 1984] Francis Troyon et al. “MHD-limits to plasma confinement”. In: *Plasma physics and controlled fusion* 26.1A (1984), p. 209 (cit. on p. 34).
- [Tuszewski 1988] M Tuszewski. “Field reversed configurations”. In: *Nuclear Fusion* 28.11 (1988), p. 2033 (cit. on p. 23).
- [UWM] *Inertial Electrostatic Confinement Fusion*. URL: <https://iec.neep.wisc.edu/operation.php> (visited on 04/30/2020) (cit. on p. 18).

- [Wesson 2004] JA Wesson. *Tokamaks*. 3rd ed. Clarendon Press, 2004 (cit. on pp. [20](#), [27](#), [32](#), [34](#), [35](#), [65](#), [66](#), [69](#)).
- [Whyte 2007] DG Whyte et al. “Disruption mitigation on Alcator C-Mod using high-pressure gas injection: experiments and modeling toward ITER”. In: *Journal of nuclear materials* 363 (2007), pp. 1160–1167 (cit. on p. [51](#)).
- [Xu 2016] Yuhong Xu. “A general comparison between tokamak and stellarator plasmas”. In: *Matter and Radiation at Extremes* 1.4 (2016), pp. 192–200 (cit. on p. [24](#)).
- [Yu 1994] Guoyang Yu. “Parametrization study of the decay index of tokamak equilibrium magnetic fields”. In: *Nuclear Fusion* 34.10 (1994), p. 1408 (cit. on p. [39](#)).

A. VUV spectra analysis for D₂ SPI experiments

After the entry of D₂ SPI in the argon background plasma, the argon line brightness drops and the VUV spectra are dominated by deuterium lines.

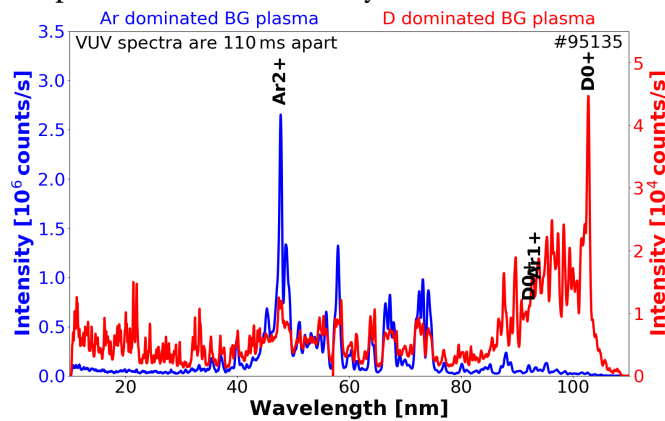


Figure A.1.: Change of a typical Ar VUV spectrum (blue) into deuterium dominated VUV spectrum (red) after the entry of D₂ SPI for the JET discharge #95135. The two VUV spectra are 110 ms apart.

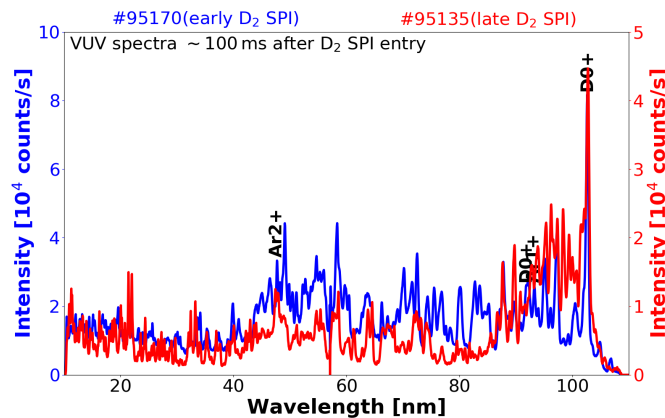


Figure A.2.: Comparison of deuterium dominated Ar VUV spectrum for early D₂ (blue) and late D₂ (red) cases. The two VUV spectra are taken ~100 ms after D₂ SPI.

One such example is shown in the figure A.1 for the JET discharge #95135. The blue data line in the figure A.1 shows a typical VUV spectrum of argon background

plasma. After the entry of D₂ SPI, ~110 ms later, the VUV spectrum is dominated by the deuterium lines as shown as red data line in the figure A.1. It can also be noted that the line intensities loses almost two orders of magnitude after D₂ SPI entry.

Deuterium dominated Ar VUV spectra are compared for early and late D₂ SPI in the Ar background plasma. It can be observed from the figure A.2 that irrespective of when the D₂ SPI arrives at the Ar background plasma, there is no significant change in the VUV spectra. This may be because the background plasma may evolve the same way after D₂ SPI entry. It is to be noted that at ~100 ms after D₂ SPI entry, plasma current is roughly the same, $I_p \sim 0.65$ MA.

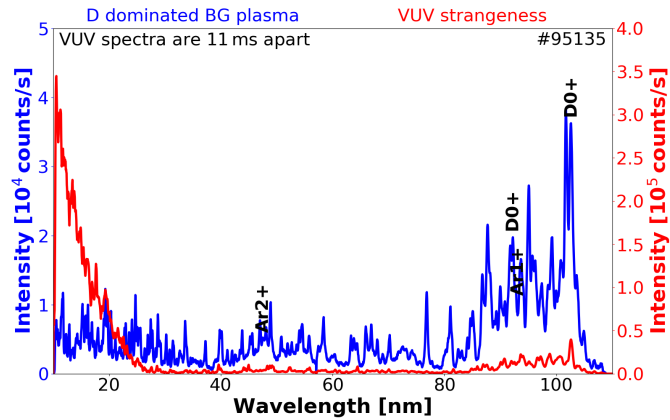


Figure A.3.: Sudden change in the VUV spectrum within 11 ms for the discharge #95135, few tens of ms before the benign RE termination

Few tens of ms before the benign termination of the RE beam, the VUV spectrum changes suddenly within few milliseconds. For instance, within 11 ms, the VUV spectrum of the JET discharge #95135 changes drastically as shown in the figure A.3. The VUV spectrum gains almost a magnitude of line intensities and a continuum towards lower wavelength (usually between 10-30 nm) is observed. This is not a recombination continuum (see figure 3.28(i) for example of recombination continuum) nor a molecular spectra (BeD and ArD maybe possible during this phase, but nether of them has molecular band between 10-30 nm).

Not just the JET discharge #95135, this sudden change can be seen in all the discharges with benign termination of the RE beam as shown in the figure A.4. In some spectra, in addition to continuum at lower wavelengths, additional lines can also be found for some discharges as shown in the figure A.4.

The time vector of the VUV spectroscopy was checked for and this sudden VUV change occurs few tens of ms before the benign termination, 2-3 VUV time points before the final collapse. However, there are no other measurement suggesting for a rapid change in the background plasma or the RE beam. It may be that this sudden VUV change may be caused due to kink instability in the post-disruption systems (Paz-Soldan 2019) during the final RE beam collapse but further analysis may be required to understand this better.

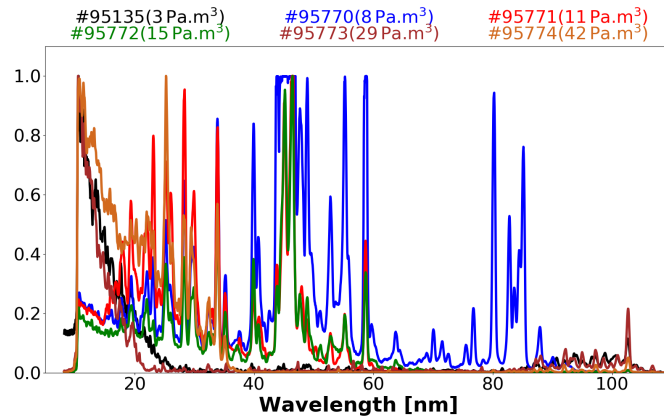


Figure A.4.: Sudden change in the VUV spectra few tens of ms before the benign termination for different Ar MGI amounts.

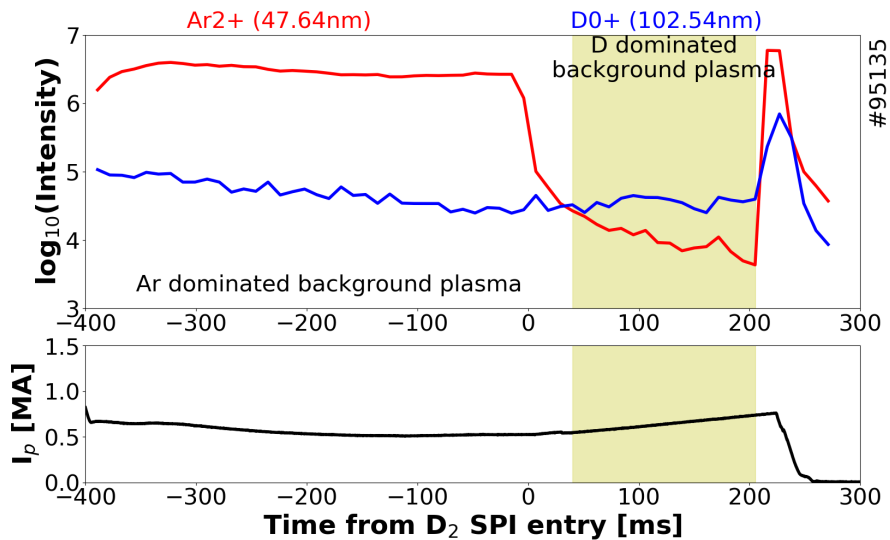


Figure A.5.: Time evolution of Ar^{2+} and D^{0+} VUV lines for the discharge #95135 from the VUV spectroscopy.

Using the VUV spectra, the time evolution of the argon and deuterium VUV lines are analyzed. For this analysis, Ar^{2+} VUV line around 47.64 nm and D^{0+} VUV line around 102.54 nm are used. The line intensities of the VUV lines are taken from the Gaussian fitting of the lines as discussed in the section 3.2.2.2. It can be found from the figure A.5 that after the entry of D_2 SPI, the line brightness of the Ar^{2+} lines drops few orders of magnitude. On the other hand, there is a slight increase of the D^{0+} line intensity. As a result, argon dominated background plasma soon becomes deuterium dominated background plasma.

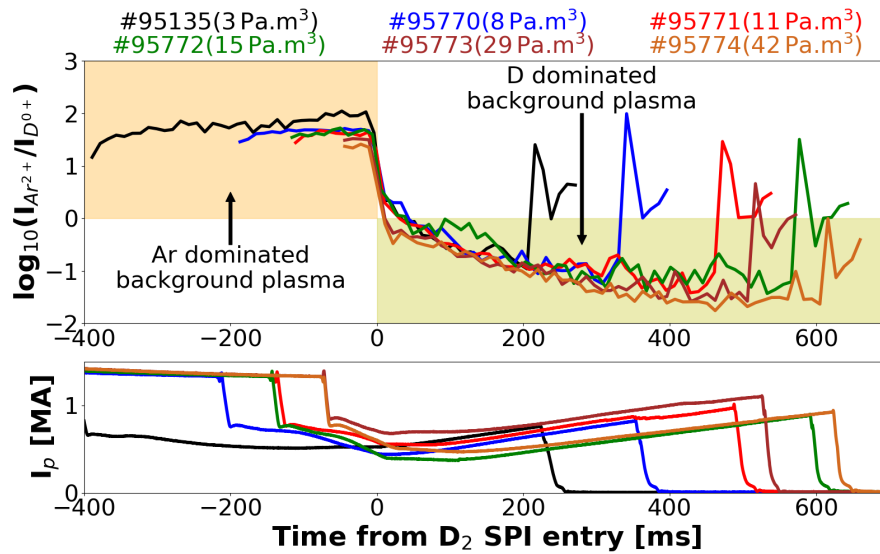


Figure A.6.: Time evolution of Ar²⁺ and D⁰⁺ VUV line ratio from the VUV spectroscopy.

Irrespective of the argon content in the background plasma during the D₂ SPI entry, argon line brightness drops after the entry of D₂ SPI entry as shown in the figure A.6. It can be observed that just before the final collapse, the argon lines are recovered. This may suggest that argon may not be flushed out from the background plasma, but rather, background plasma cools down to very low temperature that argon ions are recombined to form argon neutrals. These argon neutrals are still present in the background plasma in very large quantities

It is to be noted that the rise in the argon to deuterium line ratios take place just after the sudden change in the VUV spectra. The rise in the line ratios are also correlated with the spike in the radiated power measurement which are usually proportional to the argon content in the background plasma.

The drop in Ar line brightness was also observed in the DIII-D tokamak (Hollmann 2020). The expulsion of argon from the background plasma was suggested due to this drop in argon line brightness was explained using the 1D diffusion model in the section 5.5.

Acknowledgments

I would like to take a moment to thank those who have helped me along the way on this journey. Firstly, I am deeply indebted to my supervisor Dr. Cédric Reux (CEA, IRFM) for his unconditional support starting the day of my application to this PhD position and guiding me to this successful PhD completion. I would like to express my sincere gratitude to my PhD director Prof. Peter Beyer (PIIM, CNRS) for providing his valuable time and wisdom during our discussions. I am extremely grateful to Dr. Michael Lehnen (ITER Organization) for mentoring me and motivating scientific conversations. I cannot begin to express my thanks to Dr. Eric Hollmann (UCSD), who helped me in my PhD thesis by sharing his code and also for the fruitful contribution.

I would like to extend my deepest appreciation to my reviewers and jury members for their insightful comments and discussion during the thesis defense. I would also like to extend my sincere thanks to my contributions, Dr. Remy Guirlet (CEA, IRFM), Dr. Ivor Coffey (CCFE, UKAEA), Dr. Nicolas Fedorczak (CEA, IRFM), Dr. Jan Mlynar (IPP Prague), Dr. Ryan Sweeney (MIT), Dr. Carlos Paz-Soldan (GA), Dr. Philippe Moreau (CEA, IRFM), Dr. Eric Nardon (CEA, IRFM), Dr. Ondrej Ficker (IPP Prague) and JET contributors for their fruitful interactions.

I would also like to thank administrative staffs of CEA, IRFM for extending a great amount of assistance during my stay. My special thanks to the administrative staffs for the ITER Organization for their financial help. I also wish to thank the administration of the doctoral school ED352.

I would like to extend my deepest gratitude and thanks to Mr. Sankar Raman Sridhar for his eternal support and guidance throughout my life as my big brother. Another person who deserves a special thanks is Ms. Vaishali Easwaran for continuously tolerating me and joining me in this adventure together. I also wish to thank my friends for pleasant moments during PhD days: Mykola Ialovega, Arvydas Sepetys, Iaroslav Morgal, Yulia Mukha, Aleksandra Chikulaeva, Yeseul Park, Xiao Song, Yan Sun, Jinyu, Ekaterina Matveeva.

Last but not the least, I would like to thank my parents for their relentless support and guidance without whom this journey would not have been possible. I would also like to acknowledge Swaminathan Nageswaran, Niranjana Sampath, Praveena Krishnan, Swathi, Vignesh Kumar for their profound belief in me. I would like to appreciate Mr. Bing and family for being the best entertainment during the hard working days.